# DEVELOPMENT AND CHARACTERIZATION OF REMOTE RADIATION DOSIMETRY SYSTEMS USING OPTICALLY STIMULATED LUMINESCENCE OF $Al_2O_3$:C AND KBr:Eu

By

DAVID MATTHEW KLEIN

Bachelor of Science in Physics
Oklahoma State University
Stillwater, Oklahoma
2002

Submitted to the Faculty of the
Graduate College of the
Oklahoma State University
in partial fulfillment of
the requirements for
the Degree of
DOCTOR OF PHILOSOPHY
December, 2008

DEVELOPMENT AND CHARACTERIZATION OF

REMOTE RADIATION DOSIMETRY SYSTEMS

USING OPTICALLY STIMULATED

LUMINESCENCE OF $Al_2O_3$:C

AND KBr:Eu

Dissertation Approved:

Dr. Stephen W. S. McKeever

Dissertation Adviser

Dr. Bruce J. Ackerson

Dr. Don A. Lucca

Dr. James P. Wicksted

Dr. A. Gordon Emslie

Dean of the Graduate College

ACKNOWLEDGMENTS

In my career as a student, I've had incredible interactions with many, many people. It would be quite impossible for me to now list all of the people to whom I owe my thanks. Still, there are several that I feel obliged to mention here by name.

First and foremost, I would like to thank my boss, mentor, and good friend over these last seven years, Dr. Stephen W. S. McKeever. Dr. McKeever is one of the most driven, understanding, and kind people I've ever had the pleasure to have met. I could always rely on both his outstanding scientific ability and his unending encouragement. I take his example as the gold standard for considerate and expert professionalism. If I have one regret about (finally) receiving my doctoral degree, it is that I will soon have to work under or alongside somebody else.

Next, I would like to thank the students and professors that are and were ever a part of Dr. McKeever's Optically and Thermally Stimulated Phenomena Laboratory, now called the Radiation Dosimetry Laboratory. In particular, I would like to thank Dr. Eduardo Yukihara for his friendship and countless invaluable discussions, both technical and non-technical. I would also like to thank some of my fellow researchers and friends from this lab who provided so many insights to performing good experimental research, and so many good times: Dr. Von Whitley, Dr. Ken Lepper, Dr. Jerimy Polf, Dr.s Ramona and Razvan Gaza, Dr. Enver Bulur, Dr. Michael Blair, Dr. Regina DeWitt, Dr. Juan Mittani, Dr. Kasim Kurt and Dr. Gabriel Sawakuchi. I owe much to Tammy

Austin for all of her help with all things administrative and for her light-hearted attitude.

Over the years I've had the pleasure of learning from and collaborating with many other laboratories. Many thanks go to Dr. Mark Akselrod and all of the people at Landauer Inc. Crystal Growth Division providing many of the $Al_2O_3$:C samples used in this research as well as helpful discussions concerning the properties of $Al_2O_3$:C and experimental techniques. I would like to thank Dr. Eric Benton for his advice and many conversations concerning practical and effective experimentation and for his expertise on radiation dosimetry. Thanks also to Dr. Benton's students, Joel DeWitt and Carl Johnson for many discussions of physical theory and electronics design, but mainly for their friendship and much needed levity. I am indebted to Dr. Art Lucas for the use of his standard radiation sources at the Lucas Newman Science & Technologies laboratory. I feel it more important, however, to recognize Dr. Lucas' encyclopedic knowledge and experience over the history of radiation dosimetry, and his enthusiasm in providing historical perspective – something that is often regrettably lacking in the classroom. I thank my good friends and collaborators from Risø National Laboratory in Roskilde, Denmark. Particularly, I would like to thank to Dr. Claus Andersen and Dr. Jens Edmund for interesting conversations about remote dosimetry using $Al_2O_3$:C, and for graciously hosting my wife and I while we visited Roskilde and Copenhagen.

I would like to express my deepest gratitude to Oklahoma State University, and specifically to the faculty and staff of the Department of Physics. I feel incredibly lucky to have been able to learn from the top-notch professors of this department. My thanks go to Dr. Bruce Ackerson and Dr. James Wicksted from Physics, and to Dr. Don Lucca from the School of Mechanical and Aerospace Engineering for sitting on my graduate advisory

committee. Much appreciation and admiration go to Susan Cantrell, Cindy Raymond, Stephanie Hall, Danyelle Talbot, Warren Grider, and Charles Hunt. I believe that the department would fall into utter chaos within minutes if not for this incredibly capable staff. I would also like to credit Mike Lucas and his staff in the Physics and Chemistry Instrument Shop for the master craftsmanship of the many unique pieces of instrumentation that I've asked them to build for various experimental setups. I am also grateful for the help of Mr. William A. Holloway of the Department of Electrical Engineering Technology in designing and building the portable version of the environmental monitoring system.

The work on medical dosimetry discussed in this work was made possible by the kind invitation for collaboration from the faculty and students of the Oklahoma University Health Sciences Center (OUHSC) and the Loma Linda University Medical Center (LLUMC). I would like to thank Dr. Nolan Newkirk, Dr. David Peakheart, Dr. George Mardirossian, and Dr. John Rong from OUHSC, and Dr. Mike Moyers and Dr. George Coutrakon of LLUMC. Each of these individuals was very accommodating and enthusiastic about our collaboration, even though most of our work was done after hours.

Finally, I would like to express my deepest thanks and love for my family and those dear friends not associated with the laboratory. To my mother and father, I owe you more than I could ever give. Thank you for all the love, support, and encouragement. Most importantly, I would like to thank my beautiful wife Helen. I don't know how she even puts up with me, much less how she always gives her full love and support. Nothing has as bolstering an effect on me as when my thoughts run to her, which they very often do. I would truly be lost without her.

TABLE OF CONTENTS

Chapter Page

I. INTRODUCTION ..... 1

1.1 Ionizing Radiation and Reasons for Measurement ..... 1
1.2 Approaches to Environmental Monitoring and Medical Dosimetry ..... 8
1.3 Current Work: Solutions Using Remote OSL Dosimetry ..... 13

II. MODELS OF THERMALLY AND OPTICALLY STIMULATED LUMINESCENCE ..... 15

2.1 The Single Charge Trap – Single Recombination Center Model ..... 20
2.2 Thermal and Optical Stimulation ..... 23
2.3 A Note on Energies ..... 29
2.4 Advanced Models of TL and OSL ..... 31

III. PROPERTIES OF DOSIMETRIC MATERIALS ..... 40

3.1 Aluminum Oxide Doped with Carbon ($Al_2O_3$:C) ..... 40
3.2 Potassium Bromide Doped with Europium (KBr:Eu) ..... 48

IV. HIGH-SENSITIVITY *IN-SITU* ENVIRONMENTAL MONITORING SYSTEM ..... 53

4.1 The Bench-top System ..... 56
4.1.1 Description of the System and Experimental Details ..... 56
4.1.2 System Optimization ..... 61
4.1.3 System Performance Results ..... 64
4.1.4 Conclusions based on the Bench-top System ..... 68
4.2 The Portable System ..... 69
4.2.1 System Optimization ..... 69
4.2.2 Calibration Testing I: Low-activity Measurements ..... 71
4.2.3 Calibration Testing II: Dose Calculations ..... 79

Chapter Page

V. REMOTE NEAR-REAL-TIME MEDICAL DOSIMETRY SYSTEM BASED ON OSL FROM KBr:Eu ..... 91

5.1 KBr:Eu System Description ..... 93
5.2 Performance under X-Rays I: Fluoroscopy ..... 96
5.2.1 Continuous Fluoroscopy ..... 96
5.2.2 Pulsed Fluoroscopy ..... 103
5.3 Performance under X-Rays II: Computed Tomography Scanning ..... 115
5.4 Performance under High Dose Rate (HDR) Brachytherapy using an $^{192}$Ir Seeds ..... 128
5.5 Performance under 232 MeV Proton Therapy Beam ..... 136
5.6 Further Characterization of KBr:Eu Towards a Simple Model for Describing OSL Mechanisms ..... 144

VI. CONCLUSIONS AND FUTURE WORK ..... 155

REFERENCES ..... 160

APPENDICES ..... 170

A. $^{192}$Ir Dose Plans Calculated for October 20$^{th}$ and 25$^{th}$ ..... 170
B. Energy Absorption Computer Models for $^{232}$Th and $^{226}$Ra Experiments ..... 177

LIST OF TABLES

Table Page

1.1 Estimates of the thresholds for tissue effects in adult humans .....4

1.2 Range of doses associated with specific radiation-induced syndromes and death in humans exposed to uniform whole body radiation .....4

4.1 Results of the last six of seven consecutive POSL measurements of the pulled fiber α-$Al_2O_3$:C sample. .....68

4.2 Comparison of deviations of the original signal backgrounds to the backgrounds after normalizing by the laser power tracking signal. The standard deviation of the mean, $\sigma_{mean,}$ is shown as a percentage of the average, $\mu$, for each case in blue italics. .....78

4.3 Normalized POSL data compared to 3$\sigma$, or the signal corresponding to the minimum detectable dose. All but one of the measurements are greater than 3$\sigma$. .....78

5.1 Values of peak voltages and tube currents applied to the GE Advantx fluoroscopic system, as well as the exposure registered by a thimble IC during an energy dependence experiment.....97

5.2 Values of tube currents applied to the GE Advantx fluoroscopic system, as well as the exposure registered by a thimble IC during a dose response experiment.....101

5.3 Means of the ratios of OSL versus exposure for all seven tube currents at a particular peak voltage. Standard error is also represented as a percentage of the mean under the % symbol. .....120

5.4 Percent difference comparison of averaged BSOSL data taken in the 'front' and 'face to face' geometries ($\mu_{front}$ and $\mu_{ftof}$, respectively) on October 20$^{th}$.....134

5.5 Data from Nucletron dose planning reports showing different values pertaining to source decay.....136

B1 Coefficients for Thorium-232 and Daughters .....178

B2 Coefficients for Radium-226 and Daughters .....180

LIST OF FIGURES

Figure Page

1.1 Photos depicting different waste storage methods; a) and b) show underground liquid waste tank construction while c) shows shallow burial of sealed drums(from www.hanford.gov). .....6

1.2 Single fluoroscopic x-ray comparing the transparency of different dosimetry systems. (1: KBr:Eu, 2&4: micro-MOSFET, 3&5: standard MOSFET). .....12

2.1 a) Delocalized energy bands of an insulating crystal are separated by regions forbidden to electrons called band gaps. b) A close up of the region shared by the highest valence band and the lowest conduction band reveals localized energy levels in the band gap resulting from crystal defects. Defect levels below the Fermi level are occupied by electrons and so are capable of trapping holes, whereas the levels above the Fermi level are empty and are potential electron traps. .....16

2.2 Configurational coordinate diagram depicting the transitions required for radiative non-radiative recombination. .....18

2.3 Examples of a) TL and b) OSL signals from KBr:Eu.. .....19

2.4 Energy band diagram illustrating electron-hole pair production by ionizing radiation, electron ( ●) and hole ( ○) migration into and out of defect centers, and recombination producing luminescence. Here, defect center *1* is an electron trap with a trap depth of *E*, while center *2* is a recombination center. .....20

2.5 Schematic illustration of the build up and decay of POSL for stimulation pulse widths ranging from .22 to 1.61 s. A luminescence lifetime $\tau_e$ = 1 s is used, and the stimulation intensity is identical for each pulse width. Inset shows the ratios of build up OSL to decay OSL for the different stimulation periods. .....28

Figure Page

2.6 Diagram of energy versus configurational coordinate Q showing lattice potentials for an electron trap (dashed parabola) and the neighboring portion of the conduction band (solid parabola). The assorted values of energy related to electron trapping during irradiation, and thermal and optical activation required for TL or OSL production are specified.....30

2.7 Band diagram depicting the multiple traps and transitions considered in the generalized model of OSL of McKeever et al. (1997a).....36

2.8 CW-OSL simulations using the 5-center model shown in figure 2.7 made by varying a) the temperature at which the OSL is measured, b) the optical stimulation intensity *p* (or *f* in this figure), and c) the dose *D* given before measurement. From McKeever et al. (1997b).....38

3.1 Crystal structure of $\alpha$-$Al_2O_3$. a) Perspective view of lattice looking between oxygen (large blue atoms) layers at the distorted aluminum (small grey atoms) sublattice. b) Above view of each plane with left to right following bottom to top planes of a). Two thirds occupation of $Al^{3+}$ ions is clarified by faint crosses marking absences in the aluminum planes.....41

3.2 Energy level diagram depicting the electronic transitions during *F* and $F^+$ center photostimulation. Dotted lines indicate non-radiative transitions. From Lee and Crawford (1979). .....42

3.3 TL signals from four $\alpha$-$Al_2O_3$:C samples shown with a) linear intensity and b) logarithmic, normalized intensity scales.....44

3.4 OSL signals from four $\alpha$-$Al_2O_3$:C samples shown with a) original and b) normalized-to-maximum intensities. .....45

3.5 OSL dose response of four $\alpha$-$Al_2O_3$:C samples normalized to the lowest dose value and shown against a linear fit of the first four datum points of sample 2. .....47

3.6 Crystalline structure of KBr, consisting of two interlocking face-centered cubic lattices of $K^+$ ions (silver) and $Br^-$ ions (maroon). .....49

3.7 Depiction of the effect of ionizing radiation. a) An electron-hole pair is formed and the hole gets captured by nearby anions, forming a $V_k$ center. b) the $V_k$ center migrates along the $\langle 110 \rangle$ axis, while the electron moves into the newly created anion vacancy. c) The $V_k$ center is converted into an *H* center away from the site of ionization (now an *F* center), and an *F-H* pair is formed. After McKeever (1985).....50

3.8 a) Energy band diagram depicting energy levels and optical transitions of the $Eu^{2+}$ ion (adapted from Rubio, 1991). b) Optical absorption spectrum and photoluminescence signal of KBr:Eu. The PL signal results from stimulation with 250 nm light.....51

4.1 Schematic representation of the portable optical fiber dosimeter system showing reader system components and a detector probe. The internal construction of the ground probe containing a 5 mm diameter $\alpha$-$Al_2O_3$:C dosimeter and light discrimintation via the dichroic mirror are detailed in exploded views. .....56

4.2 Timing scheme used for the Pulsed Optically Stimulated Luminescence (POSL) measurements. The laser is pulsed with a frequency of 4 kHz and the PMT counter gate is open between the laser pulses to detect the OSL luminescence from the $\alpha$-$Al_2O_3$:C dosimeter.....59

4.3 Different $\alpha$-$Al_2O_3$:C dosimeters investigated for use as radiation sensor on the probe, with thickness varying between 1 mm and 10 mm.....59

4.4 POSL decay curves obtained with the same sensor and same gamma dose (20 mGy) using different materials around the aluminum oxide crystal. .....62

4.5 Comparison between the POSL signals from samples of different sizes, measured with different types of reflective surfaces. The POSL signal was defined as the total luminescence (integrated over 120s of stimulation). The background was estimated before the irradiation and appropriately subtracted. The “chip” has a thickness of 1mm, but it is from a growth different from that of the set of samples of length between 2 mm and 10 mm. .....63

4.6 Gamma dose response using a $^{137}Cs$ source. By comparing the signal corresponding to the minimum detectable dose (MDD, calculated from signal background) to the linear fit of the OSL data, a MDD of ~2.5 µGy was found. Inset: The entire dose response is shown using log-log scaling.....65

4.7 Dose response of the system of a detector probe using a 1mm-thick aluminum oxide dosimeter. Graph (a) shows typical POSL decay curves obtained during the experiment, and graph (b) shows the dose response curve with error bars on the first two data equal to the standard deviation of three measurements. The POSL signal was defined as the total luminescence in the first 30s of stimulation minus the background signal during the same period, evaluated after extended optical stimulation (bleaching). .....67

4.8 Modified, portable version of the environmental radiation monitoring system with a 30 cm detector probe directly attached to the FiberPort connecter (left) and control PC. Inset: View of rear panel showing power connection, fuse holder, and DAQ-Card connection. .....71

4.9 Photographs of the same experimental setup for the measurement of POSL due to $^{226}$Ra irradiation. The radium vial and dosimeter centers were separated by 10 cm. The blue line on the steel probe marks the position of the dosimeter inside the probe. .....72

4.10 POSL signal results from two 24 hr $^{226}$Ra irradiations, after integrating over 30 s intervals. .....73

4.11 POSL signal results from figure 4.10 after being normalized to laser power tracking signal. .....73

4.12 Experimental setup for testing the portable system against thorium-enriched epoxy blocks. Above: Wooden box housing the $^{232}$Th-enriched blocks in two rows of four. Bottom left: View of the inside of wooden housing with probe 1 inserted between the two rows of blocks. Bottom right: Blank epoxy blocks with probe 2 inserted in the center. .....75

4.13 OSL results from probe 1 after a) two 24 hr and b) two 72 hr dose periods in the $^{232}$Th-enriched blocks, and from probe 2 after c) two 24 hr and d) two 72 hr dose periods in the blank epoxy blocks. Percent differences between each two measurements are also given. .....76

4.14 OSL results from probes 1and 2 after normalization to the laser power tracking signal, presented in the same fashion as figure 4.12. .....77

4.15 Decay series for $^{226}$Ra (above) and $^{232}$Th (below). From DECAY.exe, version 2, written in 1997 by Charles Hacker, Griffith University, Gold Coast, Australia. .....82

4.16 Diagram depicting the line formed by two pseudo-randomly chosen points (*A* and *B*, hollow circles) in the x-z plane, as well as the angles and lines used for calculating a photons paths through steel and Teflon, and the entrance and exit points of the photon on the dosimeter ($E_1$ and $E_2$, hollow squares).....85

4.17 Diagram depicting the xz-y plane transformation, with lines detailing the isosceles triangles used for calculating the area of the dosimeter's profile for calculating the probability that a photon emitted at a point $D_i$ would strike the dosimeter. .....87

4.18 Deconstruction of the area of an orthographic projection of a cylinder similar to the shape of an $Al_2O_3$:C dosimeter. The sum of the area of the ellipse ($A_{el}$) and the area of the skewed rectangle would be used to calculate the efficiency of the dosimeter if an emission were to occur at point $D_2$ in figure 4.16.....87

5.1 Drawing of remote medical dosimetry system based on KBr:Eu. Detail of both the internal construction of the reader box and the distal end of the fiber with dosimeter attached.....94

5.2 Example of an OSL signal decay taken using the KBr:Eu system. PMT signal was recorded for 5 ms before and after the laser was on. .....95

5.3 Averaged OSL responses to various x-ray energies, normalized to IC exposure readings that all equal close to 2.5 R/min. Error bars represent the standard deviation of the mean, and are ~1 % or less in all cases. The average value for the results is plotted, and clarifies the OSL signal dependence on x-ray energy. .....98

5.4 Mass-energy absorption coefficients for KBr that have been normalized by those for air. The peak of the coefficients occurs at ~40 keV. .....98

5.5 Spectral distributions of x-rays generated by bombarding a thick tungsten target with 200 keV electrons. Dashed line A represents the unfiltered spectrum, while curves B, C, D, and E represent spectra filtered through various layers of Al, Cu, and Sn. Reproduced from Johns and Cunningham (1983). .....99

5.6 Exposure response of the KBr:Eu system using 80 kVp x-rays from the GE Advantx fluoroscopic system. Error bars represent the standard deviation of the mean of all OSL signals taken over each 30 second exposure and equal ~1% or less for all measurements. .....101

5.7 Dependence of the KBr:Eu system response on gantry tilt angle with the dosimeter's long axis a) perpendicular and b) parallel to the rotational axis of the fluoroscopy machine gantry. Inset to b): Diagram depicting gantry tilt planes and directions relevant todata shown in a) (blue) and in b) (red). Error bars represent standard deviation of the mean for each measurement. .....102

5.8 Close-up detail of a portion of the ~220 measurement data set of initial OSL intensities from taken under fluoroscopic x-rays in 30 PPS cine mode. Inset: Initial intensities measured over the entire irradiation period. .....104

5.9 One of the ~220 OSL decays obtained under fluoroscopic x-rays in 30 PPS cine mode. An irregular 'bump' in the signal, due to an incoming x-ray pulse, occurs between ~9 and ~14 ms. .....105

5.10 Timing scheme showing OSL measurement occurring between two x-ray pulses incoming at 30 PPS. .....107

5.11 Three-dimensional a) perspective and b) contour view representation of all OSL signals taken during measurement frequency tuning experiment. The signals are arranged in order of acquisition. .....108

5.12 Three-dimensional a) perspective and b) contour view representation of all OSL signals taken with signal acquisition frequency of 9.92 Hz. No x-ray pulse interaction with the OSL signals is observed. .....109

5.13 Three-dimensional a) perspective and b) contour view representation of all OSL signals taken with signal acquisition frequency of 9.92 Hz. In this case, the x-ray pulses occur during the OSL measurement, but all at the same point. .....110

5.14 Three-dimensional a) perspective and b) contrast-increased contour view representation of OSL signals taken with the active RL tracking control program. X-ray pulses (via a characteristic RL signal) are shown occurring ~5 ms after the OSL signal is completed. .....112

5.15 Initial intensity and OSL per pulse results for a continuous x-ray exposure. OSL measurements were made after the KBr:Eu system counted 5, 10, 20, 10, and 20 RL peaks (due to x-ray pulses), each during a single minute of the continuous exposure. The blue dotted line shows the average of all OSL per pulse data. .....113

5.16 Photograph of a partially disassembled Rando® phantom. Clearly depicted are the grids of plugged holes used for dosimeter placement, as well as the human skeleton. Reproduced with permission of The Phantom Laboratory - www.phantomlab.com. .....117

5.17 Initial OSL intensities of signals taken at 10Hz for ~90 s while capturing groups of five axial CT slices at 100 kVp in a current ramping experiment. Inset: Close up of last three scans, revealing a dipping feature of the data. .....118

5.18 Average initial intensities (solid) plotted against x-ray tube current for the four available peak voltages. Pencil IC exposure readings (hollow) taken under identical circumstances are also shown. The y axes are loosely scaled for comparison. .....119

5.19 Averaged background-subtracted integral OSL results of a high-resolution axial slice profile experiment. ..... 120

5.20 Results of the gantry tilt dependence tests for the KBr:Eu dosimeter located at the CT isocenter a) in air, and b) centered in the CT body phantom. Error bars are equivalent to the standard error for six measurements. c) Diagram depicting CT gantry tilt with respect to patient table and centered on the CT body phantom, as in the case for the results of a). ..... 122

5.21 Initial OSL intensities taken over three consecutive routine 16 cm chest exam with the KBr:Eu dosimeter placed at the center of the CT body phantom. $A_i$ represents the areas under the curves for the first (i = 1), second (i = 2), and third (i = 3) scans.. ..... 123

5.22 Photograph of Rando® phantom used for testing performance under helical scanning during a routine abd/pel exam. The positions of the slice in the phantom, and the dosimeter in the slice, are detailed. Also shown is a list of CT scanning parameters used for the scans. Used with permission from Peakheart (2006). ..... 124

5.23 Photograph of Rando® phantom used for testing performance under helical scanning during a routine chest exam. The positions of the slice in the phantom, and the dosimeter in the slice, are detailed. Also shown is a list of CT scanning parameters used for the scans. Used with permission from Peakheart (2006). ..... 125

5.24 Initial OSL intensity results from simulated abdominal/pelvic scans using the Rando® phantom. The dosimeter was subject to three consecutive scans while placed in the a) pancreas portion of slice 2-2, b) the left kidney area of slice 2-5, and c) the linea alba of slice 2-5. Integrals of the area under the three results from each position in the phantom are shown as $A_{n=1,2,3}$. ..... 126

5.25 Initial OSL intensity results from simulated routine chest scans using the Rando® phantom, in the fashion of figures 5.21 and 5.24. The dosimeter was subject to three consecutive scans while placed in the heart region of slice 1-6. ..... 127

5.26 Schematic drawings of initial source and dosimeter positioning. ..... 128

5.27 Schematic drawings of alternate positioning schemes ..... 129

5.28 Comparison of 10-20-2006 OSL results to Nucletron dose plan values for the ‘above’ and ‘below’ experimental geometries. All data in each curve were normalized to the maximum of the curve. ..... 128

5.29 Comparison of 10-20-2006 OSL results to Nucletron dose plan values for the 'face to face' and 'front' experimental geometries. All data in each curve were normalized to the maximum of the curve. .....131

5.30 Comparison of 10-25-2006 OSL results to Nucletron dose plan values for the profile above the $^{192}$Ir source as in figures 5.28 and 5.29. .....132

5.31 Ratios of BSOSL over dose plan value using dose profile data taken in all positioning geometries on the 20$^{th}$ and above profile data taken on the 25$^{th}$. (Note: Only the profile above the source was taken on the 25$^{th}$, and at lower resolution than on the 20$^{th}$.).....132

5.32 Reproducibilty results after taking repeated OSL measurements at different distances above the $^{192}$Ir source. The error bars represent one standard deviation of the data taken over 60 s. .....134

5.33 BSOSL values obtained on Oct. 20$^{th}$ compared to the results obtained on Oct. 25$^{th}$. Inset: Expanded view of results obtained at larger distances.....135

5.34 Dose deposition curve (a.k.a. Bragg curve) measured with an ionization chamber for 232 MeV protons in water show the distinct Bragg peak at 33.9 cm.. .....137

5.35 Schematic drawings of initial source and dosimeter positioning.....138

5.36 OSL measurement timing scheme (not to scale) used during proton irradiation: proton spills were identified using the RL from KBr:Eu, and then an OSL measurement (50 ms, in this case) was made after a wait period of 500 ms.....139

5.37 RL signal due to a single proton spill, captured during active RL observation. Inset: The OSL signal from the measurement triggered by the spill RL. .....139

5.38 Average a) BSOSL and b) initial OSL intensity results show sub-optimal dose deposition response when plotted against the normalized Bragg curve. .....141

5.39 Examples of RL signals obtained as the proton spill occurred completely within (black) and partially (red) within the RL observation period. .....142

5.40 Average a) BSOSL and b) initial OSL intensity results that have been normalized RL signal due to previous proton spills. The data show much better correlation than the data of figure 5.38 when plotted against the normalized Bragg curve. Hollow points represent the averages of the solid points. .....143

5.41 Normalized initial intensity and total integral data for single measurements under a) $^{192}$Ir gamma and b) proton irradiation show sensitivity changes that occur at different rates. ..... 146

5.42 OSL curves taken after step-annealing to various temperatures and stimulated with a) 700 nm and b) 650 nm light from a broadband lamp. Inset: Integrated area under the OSL curves as a function of anneal temperature. ..... 148

5.43 Representative TL curves taken after step-bleaching with **700** nm light show both increasing and decreasing features. TL was measured a) immediately after bleaching and b) 1500 s after irradiation, regardless of bleach period. ..... 150

5.44 Representative TL curves taken after step-bleaching with **650** nm light show both increasing and decreasing features. TL was measured a) immediately after bleaching and b) 1500 s after irradiation, regardless of bleach period. ..... 150

5.45 Energy band diagram representing the proposed model of electronic processes during the measurement of OSL from KBr:Eu. Solid lines represent optical transitions of electrons ($e^-$) out of and into electron traps 1 and 2 and into the recombination center, which is populated with holes ($h^+$). The dotted line represents fading of trap 1 due to thermal detrapping of electrons. ..... 153

5.46 Schematic illustration of OSL signal including the fast and slow components (dotted lines). The fast component is due to the release of charge from trap 2, and decays quickly. The slow component is due to trap 1, and grows initially due to charge transfer from trap 2. It then decreases slowly after trap 2 empties and charge transfer stops. Note: Illustration is not based on numerical evaluations of the proposed model. ..... 154

# CHAPTER I

# INTRODUCTION

## 1.1 Ionizing Radiation and Reasons for Measurement

Ionizing radiation is the term used to describe electromagnetic waves or particles such as electrons or atomic nuclei that possess energy high enough to rend atoms or molecules into multiple charged components. Light in the visible spectrum at ~2 eV is powerful enough to strip electrons from atoms in processes like photosynthesis and photovoltaic electricity generation. Of course, at higher energies the radiation readily breaks stronger atomic and molecular bonds, having such effects as contributing to biological mutation via disruption of deoxyribonucleic acid (DNA) molecules (as well as wholesale cell death), malfunction or destruction of sensitive electronics due to extensive electron excitation or structural damage in materials used in electronics, production of secondary radiation that may be more harmful than the primary, and even activation of stable nuclei into radioactive isotopes. The effects can be harmful, but also beneficial, and over the last 100+ years many technologies have been developed to take specific advantage of ionizing radiation for industrial, medical, and military applications.

The fundamental quantity of ionizing radiation measurement is absorbed dose, or absorbed energy per unit mass. The SI unit for absorbed dose ($D$) is the gray (Gy), after

Louis Harold Gray (Suit, 2002), and is defined as one joule per kilogram, or $1\ \mathrm{Gy} = 1\ \mathrm{J/kg}$. With respect to radiobiology and radiation protection, absorbed dose alone does not adequately account for biological effects. Radiation quality and the different susceptibilities of various tissues represent other contributing factors. Thus, three dose-like quantities are defined to encompass these factors. The dose equivalent ($H$) was developed in the early 1960s for weighting dose to a point, and is and given by

$$H = QD \qquad \text{(J/kg)}, \tag{1.1}$$

where $Q$ is the radiation quality factor. $Q$ is a unitless number that pertains to a specific energy and type of radiation and expresses the absorbed dose's impact on, for example, organic tissue relative to other radiation types. For x-rays, gamma rays, and electrons, $Q = 1$, while for neutrons and protons, $Q \geq 2$. The equivalent dose $H_T$ adjusts the absorbed dose by averaging over the volume of a certain organ or tissue $T$ (due to a type of radiation $R$) by the radiation weighting factor $\omega_R$:

$$H_T = \sum_R \omega_R D_{T,R} \qquad \text{(J/kg)}. \tag{1.2}$$

$\omega_R$ equals unity for photons and electrons of all energies, while $5 \leq \omega_R \leq 20$ for different energies of neutrons. The effective dose $E$ goes one step further by adjusting the equivalent dose by a tissue weighting factor $\omega_T$:

$$E = \sum_T \omega_T H_T \qquad \text{(J/kg)}. \tag{1.3}$$

This quantity encompasses the contributions of each type of radiation absorbed by each type of tissue in the context of a uniform irradiation of the whole body (ICRP, 1990; 2007). Though the equivalent and effective doses share dimensions of absorbed dose,

they are not fundamental quantities, and require a unit distinct from the gray. This special unit is the sievert (Sv), after Rolf Sievert (Morgan, 1976)[1].

The annual dose received by a person by all man-made and natural background radiation, averaged over the whole population, is ~3 mGy (Johns and Cunningham, 1983). Table 1.1 lists thresholds of different effects to humans due to different radiation doses given in a short period of time (acute doses) and table 1.2 lists dose ranges that lead to human death after periods of days (ICRP, 1984; ICRP, 2007). Appropriate measurement of dose, or dosimetry, is paramount for determining any potential for harm when dealing with situations involving increased or unknown levels of ionizing radiation.

Nuclear waste storage facilities represent a type of environment with unnaturally elevated levels of radiation. The U. S. Nuclear Regulatory Commission (NRC) uses three categories to classify regulated radioactive waste: low-level waste (LLW), high-level waste (HLW), and uranium mill tailings, which are wastes generated during the mining of uranium ore and contains small amounts of long-lived uranium, radium, and thorium isotopes (NRC, 2002). LLW consists of many things, including contaminated gloves, shoe covers, and other protective garments, as well as mops, tools and used parts from nuclear industry and medical facilities.

The NRC defines three sub-classes for LLW (A, B, and C) which increase in strength going from Class A to C and are differentiated by the concentration of radionuclides, defined as average activity by volume (curies per cubic meter, $Ci/m^3$) or by mass (nanocuries per gram, nCi/g). Considerations are also made for whether the waste contains long-lived or short-lived radionuclides. Though LLW of Class A-C is suitable

[1] Though the gray superseded the *rad* unit (1 *Gy* = 100 *rad*) and the sievert superseded the röntgen equivalent man (*rem*, 1 *Sv* = 100 *rem*) as the SI derived units for absorbed dose and dose equivalent, respectively (Jennings, 2007), the *rad* and *rem* are still in use today.

**Table 1.1** Estimates of the thresholds for tissue effects in adult humans

| Time and effect | Threshold | | |
|---|---|---|---|
| | Total dose received in a single brief exposure (Gy) | Total dose received in highly fractionated or protracted exposures (Gy) | Annual dose if received yearly in highly fractionated or protracted exposures for many years (Gy) |
| Testes | | | |
| Temporary sterility | 0.15 | Not applicable | 0.4 |
| Permanent sterility | 3.5-6.0 | Not applicable | 2.0 |
| Ovaries | | | |
| Sterility | 2.5-6.0 | 6.0 | >0.2 |
| Lens | | | |
| Detectable opacities | 0.5-2.0 | 5 | >0.1 |
| Visual impairment | 5.0 | >8 | >0.15 |
| Bone marrow | | | |
| Depression of hematopoiesis | 0.5 | Not applicable | >0.4 |

*From ICRP 41*

**Table 1.2** Range of doses associated with specific radiation-induced syndromes and death in humans exposed to uniform whole body radiation

| Whole body absorbed dose[a] (Gy) | Principal effect contributing to death | Time of death after exposure (days) |
|---|---|---|
| 3-5 | Damage to bone marrow | 30-60 |
| 5-15 | Damage to the gastrointestinal tract | 7-20 |
| 5-15 | Damage to the lungs and kidneys | 60-150 |
| >15 | Damage to the nervous system | <5, dose dependent |

[a] Some data included from partial body irradiations

*From ICRP 103*

for long-term disposal by near-surface burial, the storage criteria for preventing toxic release by evaporation, leakage, or detonation become more stringent with class (NRC, 2007).

HLW contains spent fuel from nuclear reactors and highly radioactive wastes from nuclear weapons production. Typical radioisotopes found in HLW include $^{90}Sr/^{90}Y$, $^{99}Tc$, $^{131}I$ and $^{137}Cs$, which are products of nuclear fission, as well as $^{239}Pu$ and $^{240}Pu$ from reprocessing spent fuel for weapons production. The dose rate at one meter away from a spent nuclear fuel assembly can exceed 200 Sv/hr, ten years after it's been removed from the reactor (NRC, 2002). This extreme intensity of radioactivity, along with the long half-lives of the radioisotopes, warrants much stricter storage/disposal schemes than those of LLW. The Department of Energy (DOE) is responsible for the safe handling and management of HLW in the U. S., with assistance from the Environmental Protection Agency (EPA), and the departments of Transportation (DOT) and Interior (DOI).

Two-thirds of all DOE-managed nuclear waste resides in the Columbia River Basin of Washington state at the Hanford Site, formerly known as the Hanford Engineer Works. Originally built to support the Manhattan Project with extraction of plutonium from uranium, the complex at Hanford grew quickly until 1964 when production phase-downs were implemented. However, nuclear research and production operations for the U. S. Nuclear Weapons Program continued through to the end of the Cold War. Over this time an prodigous amount of radioactive waste was produced and stored in various ways (see figure 1.1) including using large underground storage tanks. Most of these methods were never designed for long-term or permanent storage. As a result, the region of the Columbia Basin has suffered many accidental releases of concentrated HLW into the


**Figure 1.1** Photos depicting different waste storage methods; a) and b) show underground liquid waste tank construction while c) shows shallow burial of sealed drums (from www.hanford.gov).

local environment. Remediation efforts at the Hanford Site began in the late 1980s, and continue today. Underground waste storage tanks represent one of the larger problems facing the remediation effort. As of late 2000, there were 177 tanks containing millions of gallons of HLW in liquid form at Hanford. Sixty-eight of these are known or are suspected to have leaked, creating plumes of migrating waste throughout the environment (Gerber, 2002). If left untreated more tanks are bound to leak in time, and could present dangerously high levels of ionizing radiation to nearby human populations.

Radiotherapy, radiodiagnosis, and nuclear medicine are techniques in which intense fields of ionizing radiation are created intentionally and specifically for improving medical treatment to a patient. Ionizing radiation is exploited in these situations to kill cancer cells, or to penetrate into and/or be absorbed by different tissues so that anatomy

may be discerned without surgery. Typical radiation sources for medical purposes include x-ray machines of various designs and energies, which are used primarily in radiodiagnostics; gamma sources $^{125}$I and $^{192}$Ir, and radium capsules, which are used in brachytherapy; and particle accelerators such as linacs, cyclotrons and synchrotrons that produce beams of high-energy electrons, protons, and atomic nuclei for radiation therapy.

A routine chest x-ray gives a small dose of ~0.17 mGy (Warren-Forward and Bradley, 1993) which is equivalent to a few weeks of normal background radiation and is not normally monitored in any way other than the relative contrast of the resultant image. However, the technique of fluoroscopy often requires a rapid succession of x-ray images so that surgeons may indirectly view the internals of a patient and operate accordingly without heavy lacerations. Tracking the patients anatomy and the surgical tools within the body require near-real-time imaging, and x-ray images are taken at up to 30 frames per second. Since these operations can last many hours, the patient can receive a significant dose from the x-rays with the potential for skin burns as well as an increased probability for developing cancer later in life.

Radiotherapy is a non-surgical technique that uses beams of high-energy photons, electrons, and heavy charged particles (HCPs) in order to irradiate and destroy cancerous tissue. This technique exploits the higher susceptibility of cancerous tissue to ionizing radiation relative to normal tissue. Using proton therapy for prostate treatment, the dose to the tumor can reach 78 Gy. This is given using thirty nine 2 Gy fractions over several weeks using different delivery geometries so that the dose to the surrounding normal tissue is considerably less than that given to the tumor (Pollack, 2002). By its very nature

radiotherapy is devastating to biological tissues, and the margins of error for these procedures are decreasing as the techniques and technologies improve.

Medical uses of ionizing radiation depend on delivering precise doses so that enough energy is applied to kill the majority of cancer cells or obtain useful diagnostic images, while doing as little harm to normal tissues as possible. Correct delivery of these doses requires accurate testing, characterization, and calibration through proper dosimetry.

## 1.2 Approaches to Environmental Monitoring and Medical Dosimetry

Many techniques have been developed and used for radiation monitoring and dosimetry, and at the center of each approach lies a particular measurement technology. Most of the subsurface contaminant monitoring performed at nuclear waste remediation sites such as the Hanford Site is done by chemical analysis or gamma spectroscopy of waste and environmental samples taken from bore holes in the contaminated areas. These techniques are used to determine exactly which radioisotopes are present in the soil sample, and provide information related to waste migration, if any, throughout the local environment as well as evolution of the waste as the constituents decay and the elemental makeup of the waste changes. However, there are many disadvantages to sample extraction and subsequent lab analysis. Extracting subsurface soil samples may affect the integrity of the environment in which contaminants may be migrating and is an inefficient way to profile or map the distribution of radioactive plumes underground. Also, subsequent monitoring of the same location becomes difficult due to the previous removal of material. Lastly, soil sampling is costly and labor intensive due to extraction,

delivery, preparation and lab analysis, as well as the need for additional management of the samples as radioactive waste after analysis. For these reasons, this form of environmental monitoring may not be performed as often as effective remediation may require.

Recently, *in-situ* subsurface monitoring devices have been proposed, such as: NaI scintillators and Ge semiconductors for gamma spectroscopy (DOE, 2001; Hult et al., 2006); a laser-heated thermoluminescence dosimetry (TLD) system (Braunlich et al., 1983); and an optically stimulated luminescence (OSL) dosimetry system based on doped glass dosimeters (Huston et al., 2001). Each has the ability to remotely detect radiation via optical or electronic means, but they also each have drawbacks. NaI scintillators and Ge semiconductors provide more information than absorbed dose; they also report the particular energies of the detected gamma rays. Since the energies are characteristic of the radioisotope that emitted them, NaI and Ge devices can identify unique contaminants. However, in order to obtain the sensitivity needed to quickly determine natural background dose levels and/or any increase above natural background levels, the crystals must be very pure, large (i.e. expensive), and attached directly to sensitive electronics needed to convert the scintillations to electrical signals. Using these subsurface scintillator installations to provide meaningful tracking of large-scale contamination at a dynamic remediation site could prove prohibitively expensive. The laser-heated TLD approach relies on remotely interrogating a dosimeter that has been allowed to integrate the environmental dose over a prescribed period with a high-power laser beam. The resulting thermoluminescence (TL) travels back to a reader over a fiber optic cable. While the level of complexity is low with respect to gamma spectrometers, the thallium

bromo-iodide light guide used in these systems is toxic and has a short lifetime, and application of high laser power into an existing or potentially volatile waste plume may be problematic. Glass dosimeters show promise as inert and inexpensive subsurface monitors, but they suffer from darkening due to prolonged radiation exposure. They are also insensitive to the point of needing several weeks to accumulate a detectable signal at environmental dose rates, which leads to a similar frequency (or rather, infrequency) of measurement to that of soil sampling.

Medical dosimetry takes advantage of many different technologies. Among the oldest are photographic films and ionization chambers. Photographic film was used to make the first diagnostic images shortly after Wilhelm Konrad Röntgen discovered x-rays (Pais, 1986), and technology has long since evolved to address issues such as x-ray scatter and the originally high x-ray intensities and exposure times needed to produce useful images. Today, photographic film is still used as a reliable, effective, and quick diagnostic tool. Medical dosimetrists also regularly use ionization chambers as standards by which they calibrate both diagnostic and therapeutic machines. Two of the most common configurations of ionization chambers in the hospital are the thimble and pencil chambers. The thimble chamber is typically ~ $1cm^3$ in volume and is used for isodose curve construction and depth dose profiling. The 10 cm long, 1 cm diameter pencil chamber is used for computed tomography (CT) machine characterization. Its length allows an entire axial CT slice with penumbra to be integrated when placed perpendicular to the plane of rotation with the CT gantry centered on the middle of the chamber. TLDs and metal oxide-silicon field effect transistor (MOSFET) detectors represent more contemporary dosimeters. TLDs are relatively small yet very sensitive passive dosimeters

that can be placed in a variety of configurations that would be too awkward for ionization chambers or films. MOSFET detectors are solid state electronic devices that provide real-time dose readings and may be built very small so that they may be placed *in-vivo* during therapy or fluoroscopic procedures. More recently, a small electret-based transponder has been proposed as an *in-situ* medical dosimeter implant (Son and Ziaie, 2006). This device operates by means of a variable capacitor that is partially filled with a Teflon electret. As air between the capacitor plates is ionized, the electret collects charge and the capacitance changes. Changes in capacitance may be read wirelessly by monitoring the impedence of an interrogating coil placed close to the implanted transponder. This dosimeter is a simple collection of coils and capacitors, and can be made very small and may be implanted into patients for long-term use. However, the device is passive and is constructed from materials such as gold and titanium that may pose problems for radiotherapy dose planning and delivery due to their high atomic numbers relative to tissue.

Advances in modern radiation delivery techniques are outpacing dosimetry development. With the advent of therapy techniques like high dose rate (HDR) brachytherapy, intensity modulated radiation therapy (IMRT) and image guided radiotherapy (IGRT), and diagnostic techniques like cone-beam CT, the complexity and spatial detail of radiation fields are rapidly increasing. Passive dosimeters like films and TLDs are becoming less relevant or even useless in these areas. The ionization chamber, while a sound active detector, cannot be miniaturized to the point of reporting modern dose gradients effectively. Some MOSFET detectors are small enough to resolve these fields, but they may depend on source-to-patient skin distance (Tao et al., 2000) and need

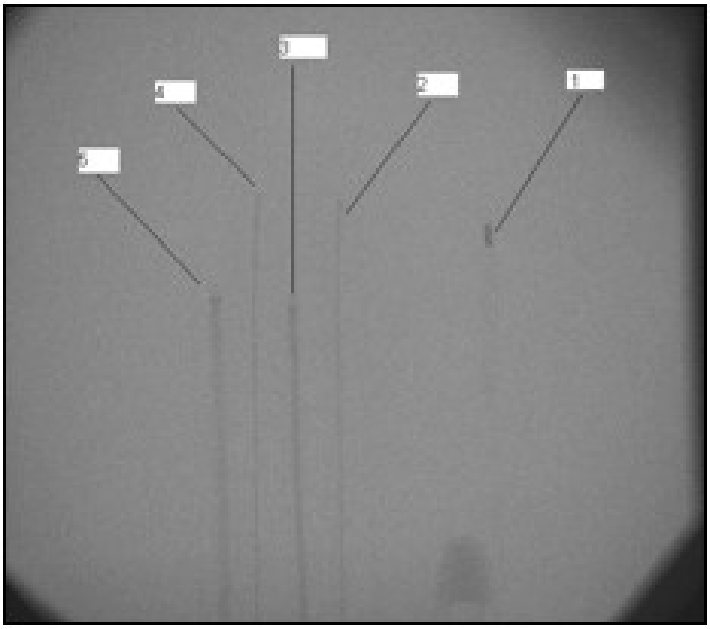

**Figure 1.2** Single fluoroscopic x-ray comparing the transparency of different dosimetry systems. (1: KBr:Eu, 2&4: micro-MOSFET, 3&5: standard MOSFET)

to be recalibrated often. MOSFETs also require radio-opaque metal wires for signal transmission that could complicate dose planning and fluoroscopic procedures. Figure 1.2 shows a fluoroscopic image of an assortment of MOSFET detectors and a single fiber optic cable with a small KBr:Eu OSL dosimeter at the end.

Doses delivered to patients during IMRT, IGRT, and HDR brachytherapy are not directly measured. They are calculated using sophisticated computer codes that are based on simulations and empirical data, and that can interpret patient–specific information (e.g. the location and shape of a tumor) from CT scans. The lack of actual dose measurement is a direct result of the inadequacies of existing dosimeters. As the race for faster and more effective (and potentially more harmful) radiotherapy and radiodiagnosis procedures continues, so does the need for real-time direct dose measurement that can be included into the procedures both innocuously and transparently.

## 1.3 Current Work: Solutions Using Remote OSL Dosimetry

The work presented in the following chapters is an attempt to address particular problems in environmental and medical dosimetry by using OSL of $Al_2O_3$:C for high-sensitivity measurements suitable for subsurface environmental monitoring, and of KBr:Eu for near-real-time measurements useful for *in-vivo* medical dosimetry. Two systems were built and optimized for remote interrogation of these crystal dosimeters by sending stimulation light and receiving the resulting luminescence over single fiber optic cables. The next chapter discusses the basic principles of OSL and TL, while the third chapter details dosimetric properties and characteristics of $\alpha$-$Al_2O_3$:C and KBr:Eu.

Chapter 4 discusses on the environmental system, which was built with the main focus of remote interrogation of high-sensitivity $\alpha$-$Al_2O_3$:C dosimeters so that a discernable signal from natural background radiation could be obtained in as short a time as possible. Much of the system's sensitivity is due to the use of the pulsed optically stimulated luminescence (POSL) technique, discussed in chapter 2. The system was also designed for portability so that one reader system could measure signals from multiple dosimeters installed throughout any arbitrary environment. The dosimeters themselves are placed at the bottom of steel ground probes and coupled to an optical fiber that runs to the surface. This scheme represents a useful supplement to existing remediation efforts as it has many clear advantages over other environmental monitoring systems. The simplicity and economy of the dosimetry probes allows for many more to be installed (unlike subsurface scintillators), the probes maintain the environment's integrity, can give

dose results frequently (perhaps more often than once per day), and reading them does not produce additional waste management concerns, unlike soil sampling. The $Al_2O_3$:C crystal dosimeter is robust, inert and is more sensitive and radiation hard than doped glass dosimeters. Also, the POSL procedure is relatively low power, unlike laser-heated TLDs.

Initial bench top development and testing of the environmental system is reported, as well as further development into a fully functional and portable field prototype. Initial testing relevant to environmental monitoring is also presented.

Chapter 5 focuses on the KBr:Eu-based medical OSL system and further characterization of the KBr:Eu material, respectively. Initially developed by Gaza (Gaza and McKeever, 2006) the medical system takes advantage of the fast optical bleaching of KBr:Eu so that 10 full continuous-wave OSL (CW-OSL) signals can be read every second. Thus, the rapid succession of traditional OSL signals qualifies the KBr:Eu system as a near-real-time dosimetry system. Extensive testing was conducted in clinical settings including radiotherapy, brachytherapy, and radiodiagnostic procedures. In some cases, dose delivery and system measurement patterns conflicted, so appropriate modifications were made to provide measurement compatibility. Also, complex sensitization behavior of the medical system was noted. This prompted a deeper investigation into the fundamental properties of KBr:Eu and a simple model is proposed that gives an explanation to the material's behavior.

Chapter 6 briefly summarizes the results of this dissertation in the context of the applicability of the systems to the fields for which they were intended. It also suggests ways in which the systems may be improved. Finally, future work necessary for further understanding and completion of the systems is discussed.

# CHAPTER II

## MODELS OF THERMALLY AND OPTICALLY STIMULATED LUMINESCENCE

A single atom in its ground state features discrete energy levels that confine valence electrons. When many atoms are grouped together in close proximity, as in crystalline solids, these discrete energy levels are split into nearly continuous, yet finite ranges of energies referred to as energy bands (Eisberg and Resnick, 1985). In semiconductors and insulators, the highest energy valence bands are completely filled with electrons (at 0 kelvin). Also, there is a band gap, or range of energy forbidden to the electrons, that separates the highest valence band from the next available empty band, called the conduction band (see figure 2.1a). This configuration holds for ideal crystals. However, real crystals are defective and may include cation or anion vacancies, impurity atoms with atomic numbers and/or valencies differing from the host atoms, as well as ions or molecular forms caught interstitially between regular lattice sites. Defects and impurities cause misalignments from the ideal crystal structure and introduce localized energy levels within the band gap (figure 2.1b) which can act as electron or hole traps, depending on their energy relative to the Fermi level (McKeever, 1985). The presence of these defect levels is of vital importance to solid-state radiation dosimetry.

When a crystalline solid is subjected to ionizing radiation, valence electrons within the solid may absorb enough energy to overcome the band gap and migrate through the

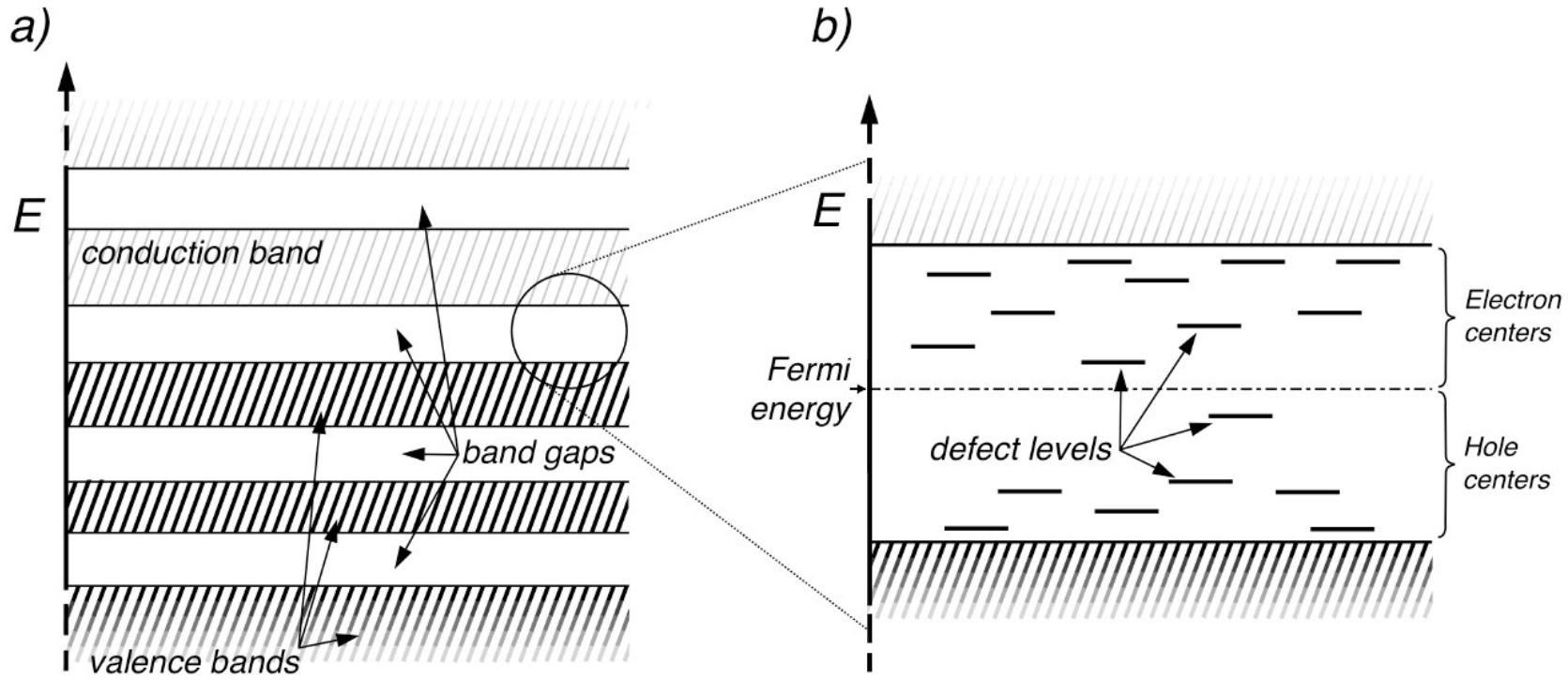


**Figure 2.1** a) Delocalized energy bands of an insulating crystal are separated by regions forbidden to electrons called band gaps. b) A close up of the region shared by the highest valence band and the lowest conduction band reveals localized energy levels in the band gap resulting from crystal defects. Defect levels below the Fermi level are occupied by electrons and so are capable of trapping holes, whereas the levels above the Fermi level are empty and are potential electron traps.

crystal with energies in the conduction band. Liberated electrons leave vacancies, or 'holes', behind. It is reasonable and convenient for discussion to treat holes as discrete positive charge carriers that can 'conduct' through the valence band. In their journey to settle into the lowest energy configuration, electrons and holes may recombine with each other directly or indirectly immediately after ionization, or they may transition into meta-stable defect energy levels within the band gap. A defect level is classified as a either a charge trap or a recombination center, depending on the probabilities of a charge carrier to transition between the defect level and the valence or conduction bands (McKeever, 1985). For example, if it is more likely for an electron trapped at an electron center (see figure 2.1b) to transition into the conduction rather than the valence band, then that defect level is considered a trap. However, if it is more probable that the electron transition to the valence band (i.e., a valence band hole transition to the electron center), then the defect level is considered a recombination center.

Direct recombination consists of a charge crossing the entire band gap from one band to the other to recombine with an opposite charge, and is also known as band-to-band recombination. Recombination that takes place at a defect level is called indirect, or band-to-center recombination. Trapped electrons and holes may be released if they absorb enough energy from stimulation with ionizing or non-ionizing radiation, or thermal energy. The freed charge may travel through the crystal as before, getting retrapped or recombining.

No matter which transitions the charges make, luminescence is produced if recombination and subsequent relaxation of the excited defect center results in the emission of light. However, electron-hole recombination does not guarantee

luminescence. Recombination may be radiative or non-radiative, with the luminescence efficiency of a material given as

$$\eta = \frac{P_r}{P_r + P_{nr}}, \tag{2.1}$$

where $P_r$ and $P_{nr}$ are the probabilities of radiative and non-radiative recombination, respectively. Both radiative and non-radiative recombination may be described using the Mott-Seitz approach, by which the electronic energy states are represented as lattice potentials versus configurational coordinate of the defect with respect to the crystal lattice. Figure 2.2 illustrates the case of an electron transitioning from the conduction band into a recombination center, leaving the electron in an excited state at point A of the diagram. The recombination is radiative if the transitions A→B→C→D are made, with the luminescence being produced from the B→C transition. Transitions A→B and C→D involve energy losses due to phonon interaction of amounts $E_1$ and $E_2$, respectively. Non-radiative recombination can occur if the excited electron absorbs enough thermal energy $\Delta E$ such that the transition series B→E→D takes place. All of these transitions

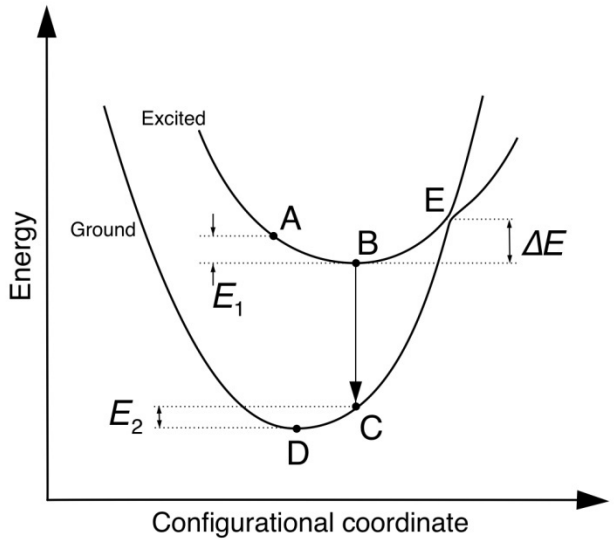


**Figure 2.2** Configurational coordinate diagram depicting the transitions required for radiative and non-radiative recombination.

result from phonon interaction, i.e., heat is either absorbed from (B→E) or dissipated to (E→D) the lattice by the electron (Braunlich et al., 1979, McKeever, 1985).

Radioluminescence (RL) is produced during irradiation and results from the immediate recombination that occurs when one or both recombining charges avoid getting trapped after ionization. Because it is produced promptly and only during irradiation, RL intensity is proportional to the rate at which dose is absorbed. Optically stimulated luminescence (OSL) is emitted after trapped charges are released from their meta-stable defect states via absorption of certain wavelengths of visible light. Recombination of trapped charges that were released by means of added thermal energy produces thermoluminescence (TL). Ignoring trap saturation effects, the amount of charge trapped during irradiation increases linearly over time. Thus, the irradiated crystal is effectively integrating absorbed dose information. Since optical and thermal stimulation empties the accumulated trapped charge, OSL and TL intensity measurements provide signals (see figure 2.3) that are proportional to the absorbed dose given to the material. A simple model to describe the mechanisms of charge transfer during irradiation, OSL, and TL can help to elucidate the structure of these signals.

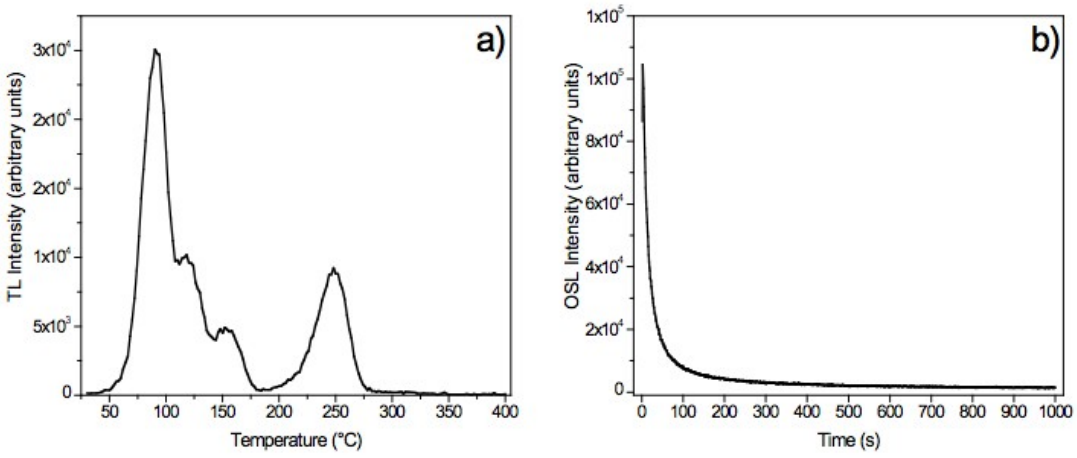


**Figure 2.3** Examples of a) TL and b) OSL signals from KBr:Eu.

## 2.1 The Single Charge Trap – Single Recombination Center Model

The simplest model of TL and OSL can be described using a band diagram like that shown in figure 2.4. The model features a band gap of energy $E_g$ containing one electron trap situated between the conduction band at $E_c$ and the Fermi level $E_F$, and one hole trap/recombination center that lies between $E_F$ and the top of the valence band at $E_v$. Figure 2.4 also indicates the various transitions that electrons and holes may undergo during irradiation and subsequent thermal or optical stimulation. Trapped electrons must absorb at least an amount of energy equal to $E$ in order to be released and allowed to recombine. So, $E$ is interpreted to be the trap "depth" below the conduction band.

Both OSL and TL phenomena may be described mathematically by using a set of equations that represent the rates of change in concentrations of charge at different energy levels. To meet charge neutrality conditions, the concentration of electrons and

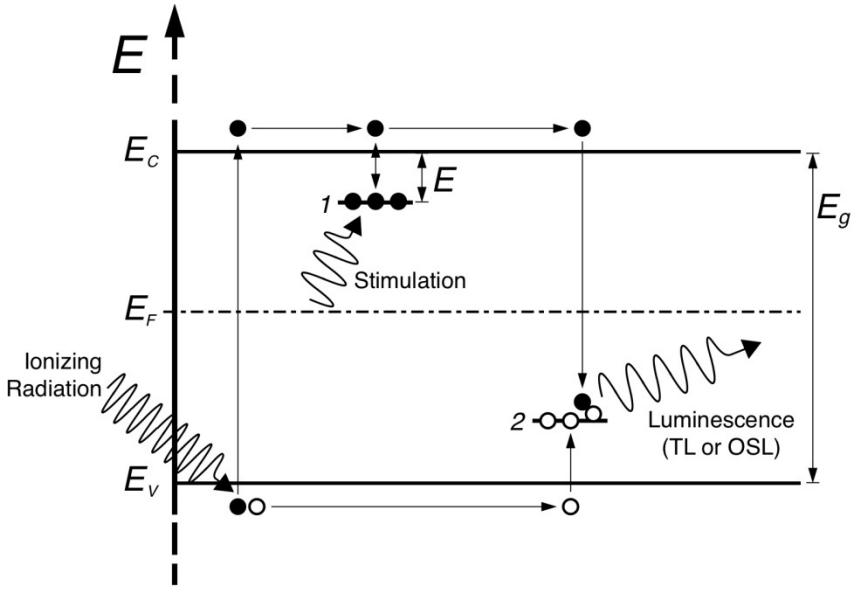


**Figure 2.4** Energy band diagram illustrating electron-hole pair production by ionizing radiation, electron ( ● ) and hole ( ○ ) migration into and out of defect centers, and recombination producing luminescence. Here, defect center *1* is an electron trap with a trap depth of *E*, while center *2* is a recombination center.

holes, at any time, must be equal. Thus,

$$n + n_c = m + m_v, \tag{2.1}$$

where $n$ and $m$ are the concentrations of trapped electrons and holes, respectively, and $n_c$ and $m_v$ are the concentrations of electrons in the conduction band and holes in the valence band, respectively. During irradiation, the rate of change of $n_c$ is equal to the electron-hole pair production rate $f$ minus the rate of electron-hole recombination at center *2* and minus the rate of electron trapping, or

$$\frac{dn_c}{dt} = f - n_c A_r m - n_c (N - n) A_e, \tag{2.2}$$

where $A_r$ is the probability of electron-hole recombination, $A_e$ is the probability of electron trapping, and $N$ is the total concentration of electron traps. Assuming that trapped electrons are not stimulated out of the trap during irradiation, the change in trapped electrons is the same as the last term of equation 2.2, or

$$\frac{dn}{dt} = n_c (N - n) A_e. \tag{2.3}$$

The concentration of holes in the valence band changes as the rate of pair production minus the hole trapping rate,

$$\frac{dm_v}{dt} = f - m_v (M - m) A_h, \tag{2.4}$$

where $M$ is the total concentration of hole traps and $A_h$ is the probability of hole trapping from the valence band. Since center *1* is a trap, holes and electrons do not recombine there, and thus equation 2.4 has no equivalent to the recombination term in equation 2.2. Finally, $m$ increases as more holes are trapped, and decreases when recombination occurs,

$$\frac{dm}{dt} = m_v(M-m)A_h - n_c A_r m. \tag{2.5}$$

After irradiation and during stimulation, these equations are altered as they pertain to trap emptying and the resetting of the crystal to its pre-irradiated state. In this treatment, both TL and OSL phenomena result from the stimulation of electrons out of electron traps and the subsequent recombination of electrons with holes at recombination centers. It is assumed that no holes are stimulated out of hole traps into the valence band $(dm_v/dt = 0)$, and that neither hole trapping $(A_h = 0)$ nor direct recombination takes place. Thus, with negligible re-trapping (or $n_c A_e(N-n) \approx 0$), only the excitation of electrons out of traps accounts for any change in *n*:

$$\frac{dn}{dt} = -np \tag{2.6}$$

where *p* is the probability per unit time of electrons being released into the conduction band due to stimulation. The change in concentration of trapped holes can be written as

$$\frac{dm}{dt} = -n_c A_r m \tag{2.7}$$

since no more hole traps are being filled. From equation 2.1, the rate equation for electrons in the conduction band becomes

$$\frac{dn_c}{dt} = -\frac{dn}{dt} + \frac{dm}{dt} = np - n_c A_r m. \tag{2.8}$$

However, the crystal can be considered to be in quasi-equilibrium under stimulation in that $n_c$ changes much less than *n* and *m*. So, because

$$\frac{dn_c}{dt} << \frac{dn}{dt}, \frac{dm}{dt} \tag{2.9}$$

and using equation 2.8, we may write an expression for the intensity of luminescence

$$I = -\frac{dm}{dt} = -\frac{dn}{dt} = np \tag{2.10}$$

as the luminescence is the end product of electron-hole recombination which is concomitant with change in trapped hole concentration. Integrating equation 2.10 gives

$$I = I_0 \exp(-pt) \tag{2.11}$$

where $I_0 = n_0 p$ and the subscript 0 denotes initial values at $t = 0$ of the stimulation period (Bøtter-Jensen et al., 2003). So far, a simple model of stimulated luminescence has been given, and a relation for the luminescence intensity derived without regard to the type of applied stimulation. Further developments of the model for the specific cases of TL and OSL follow.

## 2.2 Thermal and Optical Stimulation

The important distinction to be made between the solutions of equation 2.10 for OSL ($I_{OSL}$) and TL ($I_{TL}$) is in the choice of an appropriate value of $p$ for each case. For both cases, and at any temperature $T > 0$ kelvin, there exists a probability of thermal excitation of trapped electrons $p_{TL}$ such that

$$p_{TL} = s \exp(-E_T / k_b T). \tag{2.12}$$

Here, $s$ is the frequency factor, or attempt-to-escape frequency, and accounts for the interaction between a trapped electron and lattice phonons; $E_T$ is the thermal activation energy; and $k_b$ is Boltzmann's constant. Of course, at low temperatures or for electrons in thermally stable traps (i.e. large $E_T$), this probability is low. TL is obtained by increasing $T$ such that $p_{TL}$ increases to a point at which luminescence is amply produced.

Thus, we can simply combine equations 2.10 and 2.12 to produce the TL intensity relation

$$I_{TL} = -\frac{dn}{dt} = sn\exp\left(-E_T/k_bT\right). \tag{2.13}$$

This equation follows first-order kinetics, due to the dependence of the rate of change on the first power of the concentration *n*. TL signals are normally acquired by heating materials linearly at a rate $\beta$ (K/s) such that $T = T_0 + \beta t$ and it is helpful to obtain a solution of TL intensity as a function of temperature only. Equation 2.13 may be put into the temperature domain by integrating using a change in variables ( $dt = dT/\beta$), which gives

$$I_{TL} = sn_0\exp\left(-E_T/k_bT\right)\exp\left[-\frac{s}{\beta}\int_{T_0}^{T}\exp\left(-E_T/k_bT\right)\right]. \tag{2.14}$$

This result is the TL peak shape equation for first-order kinetics developed by Randall and Wilkins (1945) and is dependent on the previous assumption of negligible electron retrapping once thermally stimulated. Garlick and Gibson (1948) proposed that retrapping and recombination could occur with approximately equal probabilities $\left(A_e \approx A_r\right)$. In this case, the change in trapped electrons follows

$$\frac{dn}{dt} = -np_{TL} + n_cA_e(N-n). \tag{2.15}$$

Inserting equations 2.7 and 2.15 into equation 2.10, solving for $n_c$ gives

$$n_c = \frac{np_{TL}}{A_e(N-n) + A_rm}. \tag{2.16}$$

Putting this back into equation 2.15 produces the analog to equation 2.13, assuming that the concentrations of trapped electrons and recombination centers are equal $\left(n = m\right)$,

$$I_{TL} = -\frac{dn}{dt} = \frac{n^2}{N} s \exp\left(-E_T / k_b T\right). \tag{2.17}$$

This is the second-order kinetics form of the TL peak equation, as $dn/dt$ is now dependent on the second power of *n*. Integrating equation 2.17 while allowing for a linear heating rate produces the solution

$$I_{TL} = \frac{s n_o^{\ 2}}{N} \exp\left(-E_T / k_b T\right) \left[1 + \int_{T_o}^{T} \frac{s n_o}{\beta N} \exp\left(-E_T / k_b T\right) dT\right]^{-2}. \tag{2.18}$$

In order to account for cases in which first- or second-order kinetics inadequately describes the TL peaks, May and Partridge (1964) proposed a purely empirical general-order kinetics expression of the form

$$I_{TL} = -\frac{dn}{dt} = n^b s' \exp\left(-E_T / k_b T\right), \tag{2.19}$$

where *b* is the kinetic order term and is usually in the range $1 < b < 2$. However, under dimensional analysis, the pre-exponential factor $s'$ is found to require units of $m^{3(b\text{-}1)}s^{-1}$. The mutability of the dimensions of this constant with the general-order term hinders any meaningful physical interpretation of $s'$. Rasheedy (1993) suggested a revision to equation 2.19 that retained the original frequency factor *s*, giving

$$I_{TL} = -\frac{dn}{dt} = \frac{n^b}{N^{b-1}} s \exp\left(-E_T / k_b T\right), \tag{2.20}$$

with the linear heating rate solution of

$$I_{TL} = \frac{s n_o^b}{N^{b-1}} \exp\left(-E_T / k_b T\right) \left[1 + \frac{s(b-1) n_o^{b-1}}{\beta N^{b-1}} \int_{T_o}^{T} \exp\left(-E_T / k_b T\right) dT\right]^{-\frac{b}{b-1}}. \tag{2.21}$$

which reduces to the Garlick-Gibson expression for $b = 2$ and to the Randall-Wilkins expression as $b \to 1$.

OSL is not generally dependent on the thermal excitation of trapped electrons, and so a different form of the excitation probability $p$ from that of equation 2.12 is needed. Whereas TL is primarily governed by the thermal activation energy $E_T$ of the electron trap, OSL is mostly contingent on the photoionization cross-section $\sigma$, and the electron excitation probability most applicable to OSL takes the form

$$p_{OSL} = \Phi\sigma(h\nu, E_o), \tag{2.22}$$

where $\Phi$ is the intensity of incident photons. The photoionization cross-section has the units of area ($m^2$) and represents the probability that an interaction between a trapped electron and an incident photon of energy $h\nu$ will provide enough energy $E_o$ to stimulate the electron out of the trap. Though several expressions for $\sigma(h\nu, E_o)$ have been put forth following differing assumptions, one that is used regularly follows

$$\sigma = C\sqrt{E_o}\,\frac{(h\nu - E_o)^{3/2}}{h\nu\left[h\nu + E_o(m_o/m_e - 1)\right]^2} \tag{2.23}$$

where $C$ is a constant, $m_o$ is the rest mass of the trapped electron, and $m_e$ is the effective mass of the electron in the conduction band (Grimmeiss and Ledebo, 1975).

Under the assumptions made in section 2.1, namely quasi-equilibrium and first-order kinetics (negligible retrapping), the expression for OSL intensity follows directly from equation 2.11:

$$I_{OSL} = I_0 \exp(-tp_{OSL}) = I_0 \exp(-t/\tau). \tag{2.24}$$

where again $I_0 = n_0 p_{OSL}$, and the denominator in the exponent on the right-hand side is the inverse of the electronic excitation probability, called the luminescence lifetime $(\tau = 1/p_{OSL})$. Equation 2.24 reveals that the luminescence produced by emptying a single

electron trap under stimulation produces an exponentially decaying signal characterized by $\tau$. This may be surmised by another look at the OSL signal from KBr:Eu in figure 2.3.

One can develop an OSL intensity expression that considers appreciable retrapping in the same fashion as for TL. In fact, only a slight modification to the derivation by Garlick and Gibson (equation 2.17) is needed. By disregarding their assumption that $A_e \approx A_r$ and adding a term $R = A_e / A_r$, the second-order OSL intensity is written as

$$I_{OSL} = -\frac{dn}{dt} = \frac{n^2 p_{OSL}}{NR}. \tag{2.25}$$

Integrating equation 2.25 gives

$$I_{OSL} = I_0 \left( 1 - \frac{n_0 p_{OSL} t}{NR} \right)^{-2}, \tag{2.26}$$

where $I_0 = n_0^2 p_{OSL} / NR$ (Chen and McKeever, 1997).

So far, the discussion of OSL has been based on the notion that the optical stimulation is applied at a constant intensity over the luminescence read out period. This mode is called continuous-wave OSL (CW-OSL). However, optical stimulation may be applied in different ways, such as ramping the intensity at a given rate while monitoring the OSL, as is done in linearly-modulated OSL (LM-OSL) mode (Bulur, 1996). Another method is to pulse the stimulation light and read the OSL between laser pulses. This is called the pulsed OSL (POSL) method (McKeever et al., 1996).

The POSL method takes advantage of the inherent delay that exists between the excitation of a recombination center and the subsequent luminescence-producing relaxation of the center to the ground state. The lifetime of the excited center $\tau_e$ is normally very short and therefore plays no significant part in the development of OSL models concerned with CW-OSL, since the duration of stimulation *T* is much larger than

$\tau_e$. It is when $T$ is made to approach $\tau_e$ that the POSL is most effective. Assuming that during short stimulation periods the change in the number of trapped electrons is much less than the total number, or $\Delta n << n$, the number of excited recombination centers $n_e$ builds up as long as stimulation light is applied (Bøtter-Jensen et al., 2003). When stimulation ends, the build-up stops and only decay of the existing excited centers occurs. This process is illustrated in figure 2.5 for several different stimulation periods of constant intensity.

An important characteristic of the curves in figure 2.5 is that the areas under the curves are proportional to the amount of detrapped charge that has recombined and produced OSL, i.e., to the absorbed dose that initially populated the charge traps. The two features that make POSL most interesting for dosimetry are the area under the build up and the area under the decay. As the stimulation pulse is shortened the ratio of

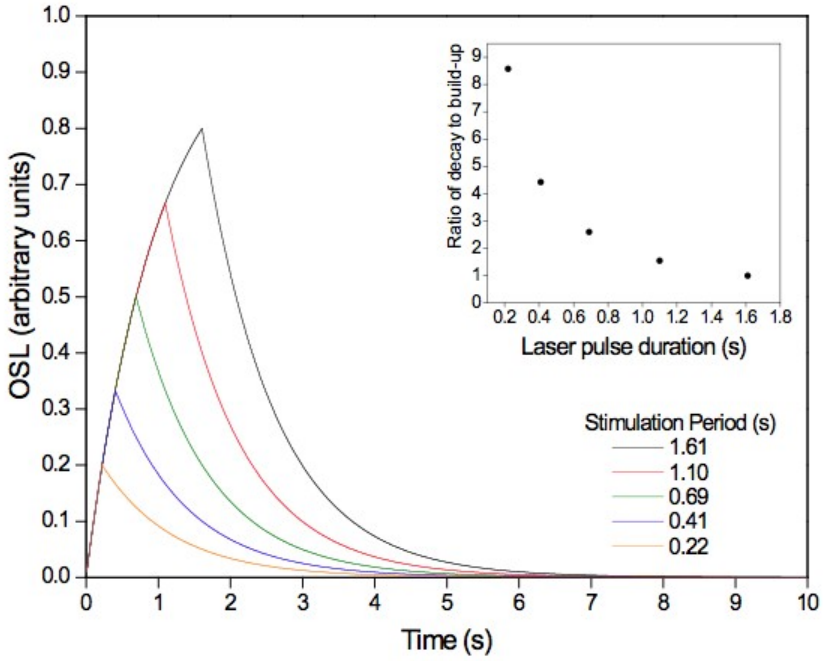


**Figure 2.5** Schematic illustration of the build up and decay of POSL for stimulation pulse widths ranging from .22 to 1.61 s. A luminescence lifetime $\tau_e$ = 1 s is used, and the stimulation intensity is identical for each pulse width. Inset shows the ratios of build up OSL to decay OSL for the different stimulation periods.

luminescence produced during the decay to that produced during the build up increases rapidly (inset of figure 2.5). Increasing the stimulation intensity while decreasing the pulse width is possible with an appropriate choice of simulation source (e.g. a q-switched laser), and significantly increases the decay-to-build-up ratio. In lieu of these developments, a dosimetry system may be developed that takes advantage of a timing scheme such that the greater part of the OSL may be read between short pulses laser light. The POSL detection system may therefore disregard any signal that comes during the intense light pulse. This effectively removes background signal from the stimulation source, as well as allowing for less optical filtration before the detector (Akselrod and McKeever, 1999).

## 2.3 A Note on Energies

When discussing models of TL and OSL in the contexts of energy band and configurational coordinate diagrams, it is necessary to introduce many different terms defining the energy values of the features inherent to these models. Therefore, it is constructive to detail the relationship between certain energy terms, especially those that deal with electron-trap transitions. Figure 2.6 depicts the conduction band and an electron trap as parabolic lattice potentials in a configurational coordinate diagram, and can be compared directly with the representation of the conduction band and center *1* in figure 2.4. The model of trap filling during irradiation described above relies on the trapping transition to be non-radiative. Therefore, a trap may capture an electron from the conduction band only if the electron possesses an amount of energy $U$ such that

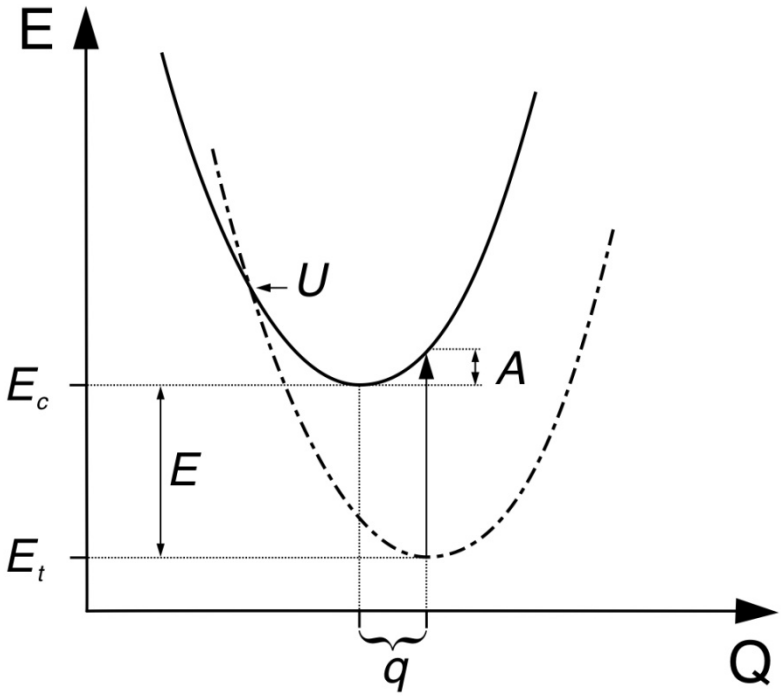


**Figure 2.6** Diagram of energy versus configurational coordinate Q showing lattice potentials for an electron trap (dashed parabola) and the neighboring portion of the conduction band (solid parabola). The assorted values of energy related to electron trapping during irradiation, and thermal and optical activation required for TL or OSL production are specified.

it may reach the intersection of the conduction and trap potentials. This transition is analogous to the transition B→E→D of figure 2.2. At equilibrium, an occupied trap lies at energy $E_t$ at a trap depth of $E$ below $E_c$ (Braunlich et al., 1979).

In order to produce TL, trapped electrons must be released via electron-phonon interactions of sufficient magnitude. In other words, enough thermal energy from lattice vibrations caused by heating the material must be imparted to the electrons so that it can traverse the intersection of the two potentials at $E_c + U$ and be ejected back into the conduction band. Thus, the thermal activation energy of the trapped electron is given as

$$E_T = E + U \ . \tag{2.27}$$

OSL production relies on optical transitions that occur without change in the configurational coordinate (shown as vertical transitions in figure 2.2 and 2.6), and so the

trapped electrons need not be constrained to travel along the lattice potentials for release as in thermal activation. However, because the equilibrium positions of the lattice potentials are generally located at different coordinates (separated by $q$ in figure 2.6), the amount of energy needed to transition optically from trap equilibrium to the conduction band is normally greater than the trap depth $E$. The additional energy needed for this transition is called the lattice-readjustment energy $A$ (Braunlich et al., 1979) given as

$$A = S\hbar\omega_p \tag{2.28}$$

where $S$ is the Huang-Rhys factor, or mean number of photons emitted during equilibration after the optical transition, $\hbar$ is the reduced Planck's constant, and $\omega_p$ is the frequency of phonon vibration (Curie, 1960; Bøtter-Jensen et al., 2003). The optical activation energy can now be written as

$$E_o = E + A\,. \tag{2.29}$$

The important point to be made here is that the trap depth does not alone govern the release of trapped electrons for TL or OSL production. Additional energies must be considered that depend on the configuration of the lattice structure as well as the stimulation mode used, whether thermal or optical.

## 2.4 Advanced TL and OSL models

The models discussed above pertain to the simple case of a single electron trap and single recombination center and provide an introduction to the essential mechanisms of TL and OSL. Under certain circumstances, these models can be expanded in a straightforward manner to incorporate the presence of distributions of thermally (in the

case of TL) or optically (for OSL) active electron traps by superposing multiple instances of first-order TL peaks

$$I_{TL,total} = \sum_i s_i n_{0i} \exp\left(-E_i/k_bT\right)\exp\left[-\frac{s_i}{\beta}\int_{T_0}^{T}\exp\left(-E_i/k_bT\right)\right], \qquad (2.30)$$

or OSL decay curves

$$I_{OSL,total} = \sum_i n_{0i}\, p_{OSL,i} \exp\left(-tp_{OSL,i}\right). \qquad (2.31)$$

However, this superposition is only effective when the TL or OSL structures form independently of any other structure, obeying first-order kinetics. The assumption of non-negligible retrapping for kinetic orders of $b > 1$ does not address the possibility of interaction between traps. Bull et al. (1986) considered several cases in which simulated TL glow curves were calculated numerically using the rate equations governing an insulator with three electron and three hole trapping levels. They found that fitting multi-peak TL curves via superposition worked well only when the curves were calculated using parameters that satisfied negligible retrapping, and only when the fitting was also of first-order. Fittings of calculated TL curves of higher order and of mixed electron and hole traps showed poor results with superposed peak fits of any order.

Simulations carried out by Chruścińska (2008) showed that fitting OSL decays by superposition can lead to erroneous results when the aim is to determine the photoionization cross-section. The model was comprised of a shallow, optically inactive trap; a single optically active OSL trap; and two recombination centers of differing recombination probabilities. By varying the relative concentrations of optically active and inactive traps, trapping probabilities, dose period, and probabilities of recombination, it was shown that the simulated LM-OSL signal deviated from first-order. This deviation

could possibly mislead an experimenter into thinking that the signal is comprised of a convolution of components from multiple first-order, optically active traps. Thus, in general, first-order fitting does not provide an accurate means for finding the photoionization cross-section of traps responsible for OSL production in cases where first-order kinetics do not apply.

In moving to a more advanced and realistic picture of TL and/or OSL, it is common to introduce deep localized defect levels that are unaffected by thermal or optical stimulation, yet participate in charge transfer. In TL, these traps are located deep enough below the conduction band so as to be thermally disconnected from the heating process. Adding a concentration of these deep traps $n_d$ to the one-trap, one-recombination center model changes the charge neutrality condition to

$$n + n_d = m, \tag{2.32}$$

and $n_d$ changes during TL readout as the probability of deep trapping $A_d$ multiplied by the number of unoccupied deep traps

$$\frac{dn_d}{dt} = A_d (N_d - n_d), \tag{2.33}$$

where $N_d$ is the total number of deep traps. The change in free electrons can now be written as

$$\frac{dn_c}{dt} = -\frac{dn}{dt} + \frac{dm}{dt} - \frac{dn_d}{dt}. \tag{2.34}$$

Under quasi-equilibrium $\left(n_c << n,\ dn_c/dt << dn/dt\right)$, and for the special condition that the deep traps are full $\left(n_d \approx N_d,\ dn_d/dt \approx 0\right)$, we can combine equations 2.7, 2.32, and 2.34 to produce (Dussel and Bube, 1967)

$$\frac{dn_c}{dt} + \frac{dn}{dt} = -n_c(n + N_d)A_r. \tag{2.35}$$

Solving equations 2.8 and 2.35, following Kelly and Braunlich (1970), gives

$$I_{TL} = -\frac{dn}{dt} = \frac{ns\exp[-E_T/k_bT](n + n_d)A_r}{(N-n)A_e + (n + n_d)A_r}, \tag{2.36}$$

which is easily shown to match the first-order Randall-Wilkins equation 2.13 when assuming slow retrapping ($(N-n)A_e << (n + n_d)A_r$). However, when considering fast retrapping ($(N-n)A_e >> (n + n_d)A_r$) and with $n << N$, equation 2.36 becomes

$$I_{TL} = -\frac{dn}{dt} = \frac{ns\exp[-E_T/k_bT](n + n_d)A_r}{NA_r}. \tag{2.37}$$

This expression may be expanded to the form

$$I_{TL} = s'\left(nn_d\exp[-E_T/k_bT] + n^2\exp[-E_T/k_bT]\right), \tag{2.38}$$

where $s' = sA_r/NA_e$. From equation 2.38, it seems that the introduction of thermally disconnected traps leads to a TL signal that exhibits a mixture of first- and second-order behaviors (Chen and McKeever, 1997).

In the context of OSL, the additional traps are not only thermally stable at the temperature of measurement, but are also optically inactive. The inclusion of these traps changes the simple OSL equation 2.25 to

$$I_{OSL} = I_{01}\exp(-t/\tau_1) - n_c(N_2 - n_2)A_{e2}. \tag{2.39}$$

where subscript *1* refers to features of the optically active trap, and subscript *2* refers to the second, optically inactive trap. Depending on the values of $N_2$ and $n_2$, the OSL signal may be altered from a pure exponential form. For instance, if $N_2 >> n_2$, then the optically inactive trap could compete the recombination centers for the duration of the measurement. This would introduce a slowly decreasing component to simple OSL decay

with $n_c(N_2 - n_2)A_{e2} \to 0$ as $t \to \infty$. If $n_2 \approx N_2$ the deep traps are filled and the OSL decay would be practically unaffected by the optically inactive trap, since $n_c(N_2 - n_2)A_{e2} \approx 0$.

Other adjustments to the simple models have been made to produce more realistic pictures of TL and OSL mechanisms. Lewandowski and McKeever (1991) introduced a purely general model of TL that circumvents the need for the quasi-equilibrium and kinetic order approximations. These two approximations are difficult to justify physically for all but the simplest arrangements of traps and recombination centers, arrangements which are not typically found in natural or even synthetic materials. The model describes the physically meaningful functions

$$Q = \frac{R_{ex} - R_{recap}}{R_{recom}} = \frac{ns\exp[-E_T/k_bT] - n_c(N-n)A_e}{n_c A_r m} \tag{2.40}$$

and

$$P = \frac{R_{recap}}{R_{recom}} = \frac{(N-n)A_e}{A_r m}. \tag{2.41}$$

The TL rate equations concerning the one trap, one recombination, and one thermally disconnected trap were solved using $Q$ and $P$ and by making no assumptions concerning quasi-equilibrium and kinetic order, giving

$$I_{TL} = \frac{sn_0}{Q+P}\exp(-E_T/k_bT)\exp\left[-\frac{1}{\beta}\int_{T_0}^{T}\frac{Q}{Q+P}s\exp(-E_T/k_bT)\right]. \tag{2.42}$$

This expression reverts to the Randall-Wilkins relation when $Q \approx 1$ and $P >> 1$. An analytical from of equation 2.42 has been developed that may be expressed in terms of measurable parameters for the case of slow-retrapping, and its ability to fit curves

generated from exact, numerical solutions to the TL rate equations compare favorably to that of the Randall-Wilkins equation (Lewandowski et al., 1994).

An even more realistic OSL model has been proposed that incorporates more defect center types than the optically active traps, competing optically inactive deep traps and radiative recombination centers mentioned in the discussion above. Figure 2.7 shows an energy band diagram detailing the different trap types and transitions of this model. Note that the transitions pertain to what happens during optical stimulation. As such, the model consists simultaneously of the standard thermally stable (at room temperature) OSL trap, out of which electrons are optically stimulated; a deep trap that electrons can transition into but out of which they cannot be optically or thermally stimulated, a recombination center that produces luminescence; as well as a thermally unstable shallow trap that can both capture and release electrons under thermal or optical stimulation; and a non-radiative recombination center (McKeever et al, 1997a).

The flow of charge between these five traps is described using a set of six coupled

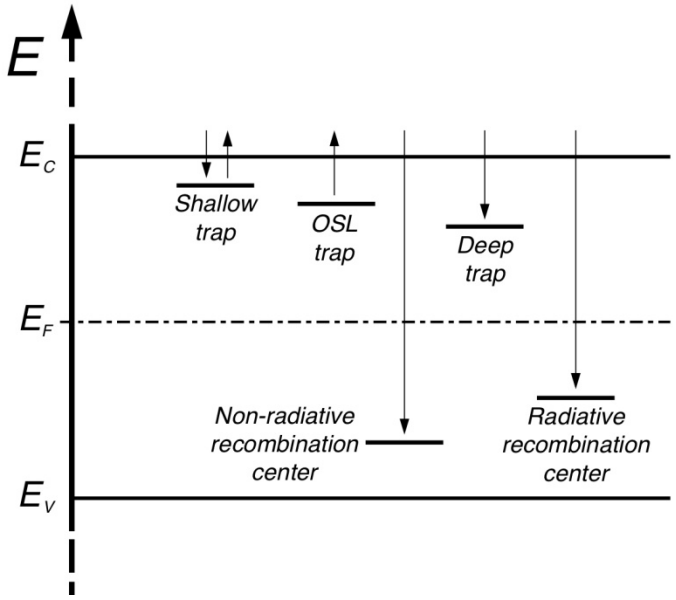


**Figure 2.7** Band diagram depicting the multiple traps and transitions considered in the generalized model of OSL of McKeever et al (1997a).

rate equations, with the OSL intensity equaling the negative rate of change of the radiative recombination center. McKeever et al. solved these rate equations numerically and simulated CW-OSL curves that would result from varying the temperature of OSL readout, the optical stimulation intensity, and the dose given prior to read out. (McKeever et al., 1997a, b). These curves are reprinted in figure 2.8.

By varying the temperature at which the OSL is measured (figure 2.8a), the influence of the shallow traps is made clear. At low temperatures, the shallow traps are thermally stable over the 100 s measurement period and act as competitors to the recombination centers for the optically stimulated electrons coming out of the OSL trap. At the intermediate temperatures, the shallow traps become thermally unstable and a peak appears in the initial portion of the OSL decay curve. This peak is due to a combination of shallow traps filling with electrons at the beginning of the stimulation, and a relatively slower emptying via thermal activation. As the temperature increases, the thermal instability of the shallow traps increases to the point at which the traps cannot keep charges trapped for any significant amount of time before they are thermally released. Thus, at high temperatures, the OSL decay is more intense and loses its peak since the shallow traps are no longer able to trap charge. It is necessary to point out that each of these OSL curves are also influenced by retrapping of charge into the optically inactive deep traps and by recombination at the non-radiative recombination center. These traps alter the luminescence decay into a non-exponential form, but the intermediate temperature peaks result from the shallow traps.

Figure 2.8b shows CW-OSL curves that were calculated at one of the intermediate temperatures of figure 2.8a, but using various stimulation intensities. As the

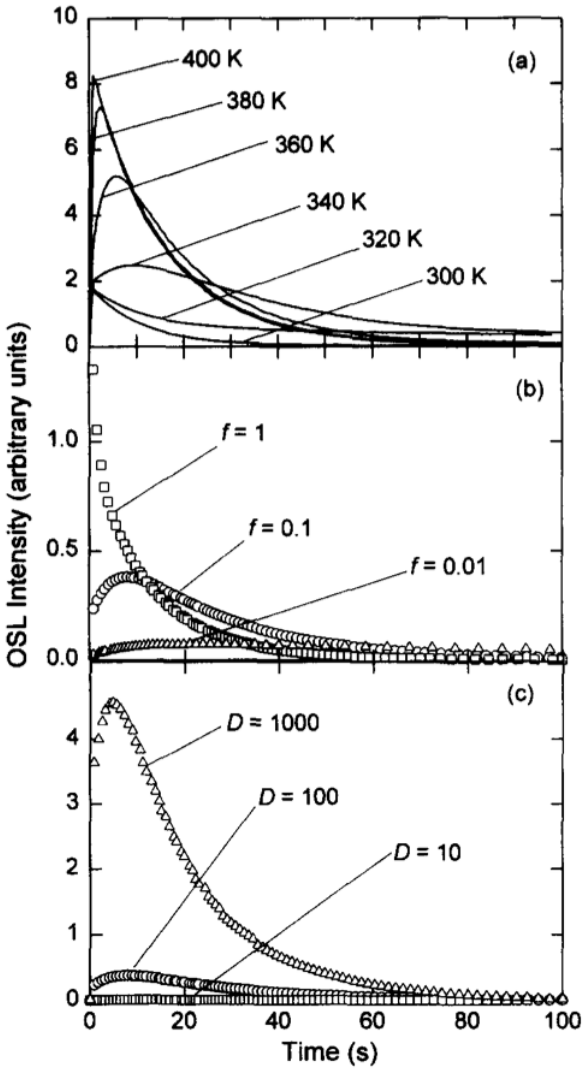


**Figure 2.8** CW-OSL simulations using the 5-center model shown in figure 2.7 made by varying a) the temperature at which the OSL is measured, b) the optical stimulation intensity *p* (or *f* in this figure), and c) the dose *D* given before measurement. From McKeever et al. (1997b).

intensity increases, the peak due to shallow traps occurs at shorter times until, at high intensity, the peak disappears since the shallow traps are immediately overwhelmed by the large number of electrons from the OSL traps. Figure 2.8c displays the effect of absorbed dose on the OSL signal at intermediate temperatures and stimulation intensities. The signal increases linearly with dose and the OSL peak shifts to shorter times with increasing dose, but only slightly.

This model has been used by McKeever et al. (1997b) to explain the behaviors of OSL signals from quartz and feldspar materials. It was shown that by measuring the OSL at different temperatures and at different intensities, the signals exhibited behavior in line with the shallow trap peak formation of the simulated curves in figure 2.8. By taking another look at figure 2.3b, a peak in the beginning of the signal indicates the possibility that the OSL of KBr:Eu is also influenced, to a certain extent, by the presence of shallow traps. This will be discussed further in the KBr:Eu results of chapter 5.

CHAPTER III

# PROPERTIES OF DOSIMETRIC MATERIALS

## 3.1 Aluminum Oxide doped with Carbon ($Al_2O_3$:C)

Aluminum oxide in its single crystalline form is known as corundum and designated $\alpha$-$Al_2O_3$. It is a versatile material: it ranks second behind diamond on the Mohs scale of relative mineral hardness, is transparent and inert, and has a high melting point at >2275 K (CRC, 1987). $\alpha$-$Al_2O_3$ is also an excellent electrical insulator and a good thermal conductor. These properties have made the material useful for a variety electronics, optics, and industrial applications.

The crystal structure of $\alpha$-$Al_2O_3$ can be seen in figure 3.1. The arrangement consists of oxygen ions ($O^{2-}$) in a rigid, hexagonal close-packed array with the ions having $C_2$ symmetry. The octahedral interstices of the oxygen lattice are occupied by aluminum ions ($Al^{3+}$). Only two thirds of these lattice interstices are occupied by $Al^{3+}$ ions so that overall charge neutrality is satisfied. Two different Al-O bond lengths (0.186 nm and 0.197 nm) cause the aluminum sublattice to be distorted such that the $Al^{3+}$ ions lie in two closely separate planes between the surrounding oxygen planes.

Investigations of the thermoluminescent properties of $\alpha$-$Al_2O_3$ were made as early as the 1950's by Reike and Daniels (1957) as part of an effort to better understand the

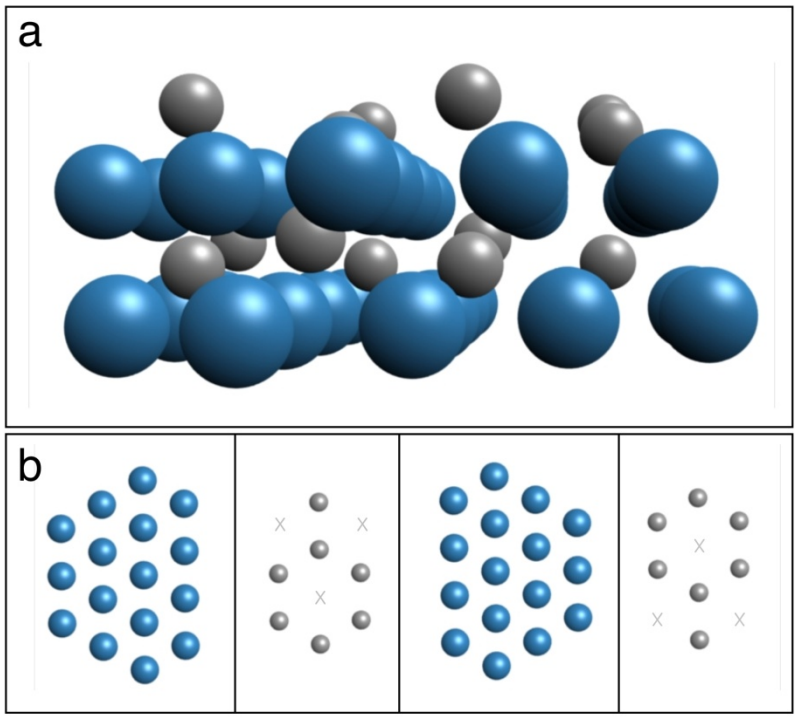


**Figure 3.1** Crystal structure of $\alpha$-$Al_2O_3$. a) Perspective view of lattice looking between oxygen (large blue atoms) layers at the distorted aluminum (small grey atoms) sublattice. b) Above view of each plane with left to right following bottom to top planes of a). Two thirds occupation of $Al^{3+}$ ions is clarified by faint crosses marking absences in the aluminum planes.

details of TL emission from a wide range of crystals. Though many properties of high-grade $\alpha$-$Al_2O_3$ were found to be attractive for application as a TL dosimeter (TLD), its sensitivity to ionizing radiation was low compared to other materials known at the time, such as lithium fluoride (LiF). It wasn't until relatively recently that a form of $\alpha$-$Al_2O_3$ was found to possess TL sensitivity high enough to garner significant consideration as a capable TLD.

Akselrod et al. (1990) synthesized anion-defective $\alpha$-$Al_2O_3$:C by growing $\alpha$-$Al_2O_3$ from a melt at ~2325 K in a highly reducing atmosphere and in the presence of graphite (Akselrod et al., 1993). This so-called Stepanov process allows for the deliberate introduction of selected impurities (in this case, carbon) into an otherwise high-purity crystal. The presence of carbon in the form of $C^{2+}$ ions catalyzes the formation of oxygen

vacancies, hence the 'anion-defective' nomenclature. Oxygen vacancies are crucial to luminescence production in $\alpha$-$Al_2O_3$:C and take multiple forms, with the two most important forms being the *F* and $F^+$ centers. *F* centers get their name from the German word *farbe* (color), and are oxygen vacancies that contain two electrons and so maintain the local charge equilibrium of the lattice. $F^+$ centers contain only one electron, and are formed as charge compensators to $C^{2+}$ impurities that have supplanted $Al^{3+}$ ions during the crystal growth process. The interplay of these two color centers is responsible for the production of TL and OSL.

When photo-stimulated with 205 nm light, *F* centers emit at 410-420 nm, the same emission that is observed during TL and OSL measurement. An energy band diagram shown in figure 3.2 depicts the multiple transitions that take place during this process, as suggested by Lee and Crawford (1979). When an *F* center electron in its $^1S$ ground state absorbs 205 nm ($h\nu$ = 6.1 eV) light it is promoted to an excited $^1P$ state. This level is thought to be very close to or perhaps inside the conduction band due to photoconductivity observed while bleaching with 6.1 eV light (Draeger and

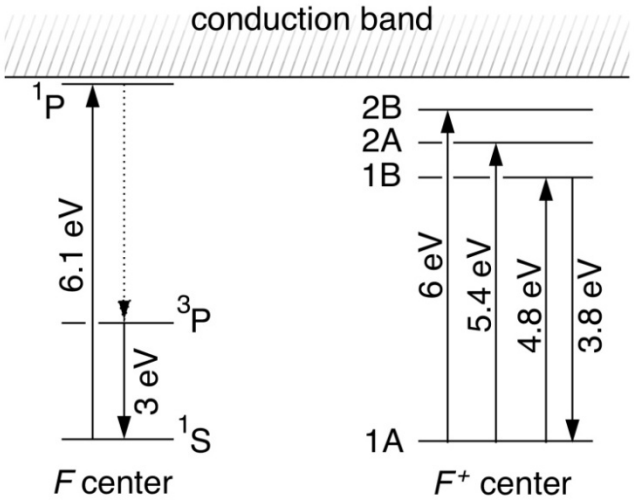


**Figure 3.2** Energy level diagram depicting the electronic transitions during *F* and $F^+$ center photostimulation. Dotted lines indicate non-radiative transitions. From Lee and Crawford (1979).

Summers, 1979). During relaxation, the electron transitions non-radiatively into a $^3$P state, and from this level transitions back to the $^1$S ground state with the emission of a ~420 nm ($h\nu$ = 3eV) photon. This emission is observed to have a lifetime of ~35 ms (Evans and Stapelbroek, 1978; Brewer, et al., 1980). $F^+$ center absorption primarily occurs at ~230 nm ($h\nu$ = 5.4 eV) and ~255 nm ($h\nu$ = 4.8 eV), with another at $h\nu \geq 6$ eV that overlaps the 205 nm *F* center absorption. All three of these absorptions lead to the emission of 326 nm light ($h\nu$ = 3.8 eV) with an emission lifetime of ≤ 7 ns (Evans and Stapelbroek, 1978). The electronic transitions occurring during $F^+$ center stimulation are represented in figure 3.2. The single $F^+$ center electron in its ground state gets excited into a $^3$P-like state that results from the low $C_2$ symmetry of the oxygen vacancy. The electron then undergoes a relaxation transition from 1B to 1A, producing a 3.8 eV photon (Evans and Stapelbroek, 1978; Lee and Crawford, 1979).

Dosimetry-grade $\alpha$-$Al_2O_3$:C contains concentrations of *F* centers on the order of $10^{17}$ cm$^{-3}$ and concentrations of $F^+$ centers of (5-10)×$10^{15}$ cm$^{-3}$ (Akselrod et al., 1990; McKeever et al., 1999). These concentrations change when *F* centers lose electrons (i.e., gain holes) and convert into $F^+$ centers. Conversely, electrons may recombine with $F^+$ centers and reform *F* centers. Thus, the concentrations are reciprocally related. *F* to $F^+$ center conversion may take place by stimulating with UV light, say at 205 nm. As previously discussed, this will excite an *F* center electron into a $^1$P-like state that is in or near the conduction band. If this electron is released from this delocalized state into the conduction band it will leave the original color center as an $F^+$ center. Ionizing radiation can also significantly modify color center concentrations by inducing hole migration into existing *F* centers to form $F^+$ centers, as well as exciting electrons into the conduction

band to be trapped or to recombine with $F^+$ centers to form $F$ centers (McKeever et al., 1999). The key mechanisms for TL and OSL dosimetry using α-$Al_2O_3$:C are: the release of electrons trapped during irradiation using optical and thermal stimulation, and the recombination of electrons at $F^+$ centers to produce luminescence via the conversion

$$F^+ + e^- \rightarrow F^* \rightarrow F + h\nu_{420\,nm}, \tag{3.1}$$

where $F^*$ is an excited $F$ center. Indeed, the TL and OSL sensitivity of α-$Al_2O_3$:C have been shown to track with $F^+$ center concentration (McKeever et al., 1999)

TL signals of four α-$Al_2O_3$:C samples of the TLD-500 type are shown in figure 3.3. Each sample was given a 0.53 Gy $\beta$ dose and were heated at a rate of 5 K/s. The signals are generally similar, but sample-to-sample variation is evident. The dominant feature is the main peak centered at ~490 K and this is of most interest to TL dosimetry. Figure 3.3a clearly displays sample-to-sample differences in sensitivity as well as peak position and shape. For example, sample 3 shows a peak at ~480 K that is narrower than the similarly intense peak from sample 4 centered above 500 K. The main dosimetric 'peak' is actually comprised of multiple superposed components, rather than a single peak. The

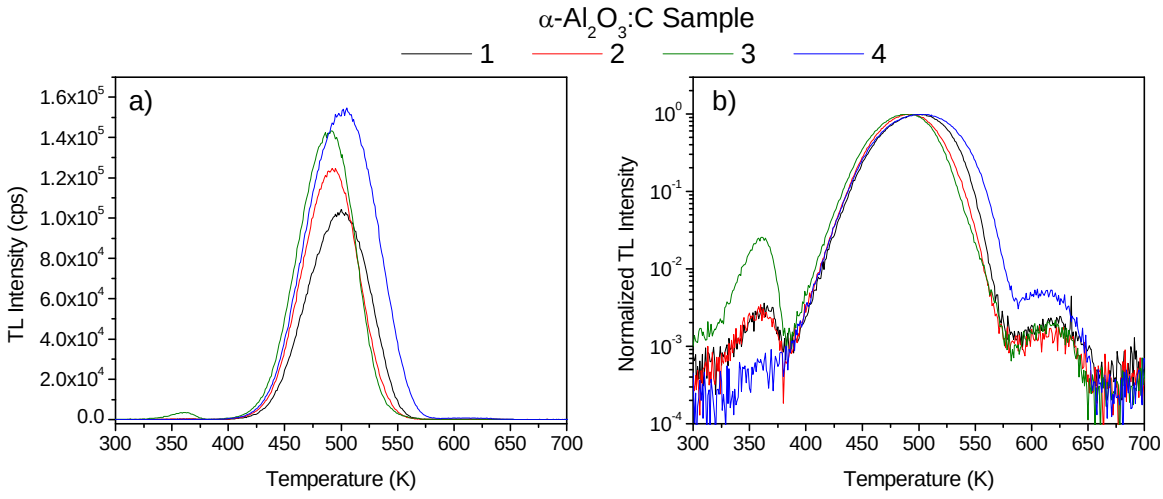


**Figure 3.3** TL signals from four α-$Al_2O_3$:C samples shown with a) linear intensity and b) logarithmic, normalized intensity scales.

distribution of peak components differs between samples, and each component responds differently to irradiation. Thus, the main dosimetric peak may be broad or narrow, depending on sample, and alters shape and shifts position with respect to dose (McKeever et al., 1999). Figure 3.3b shows the same signals shown in figure 3.3a after normalization to the signal maximum. Here it can be seen that the samples also differ in their concentrations of shallower traps, responsible for the ~360 K peaks, and deeper traps that produce the ~620 K peaks. TL peaks have also been observed below room temperature at ~260 K (Akselrod et al., 1998) and above the temperature range shown in figure 3.3 at ~730 K and ~880 K (Milman et al., 1998; Polf, 1998).

Figure 3.4 presents OSL signals from the same four samples used in figure 3.3 measured using green ($\lambda$ = 532 nm) stimulation after each was given the same 0.53 Gy $\beta$ dose. As with the TL signals, the OSL signals reveal sample-to-sample differences with the most obvious being the sensitivity of the samples, shown in figure 3.4a. It is important to note that the OSL maxima in 3.4a vary in intensity in a similar fashion to the variation of TL peak maxima in figure 3.3a. This shows that a close correlation between

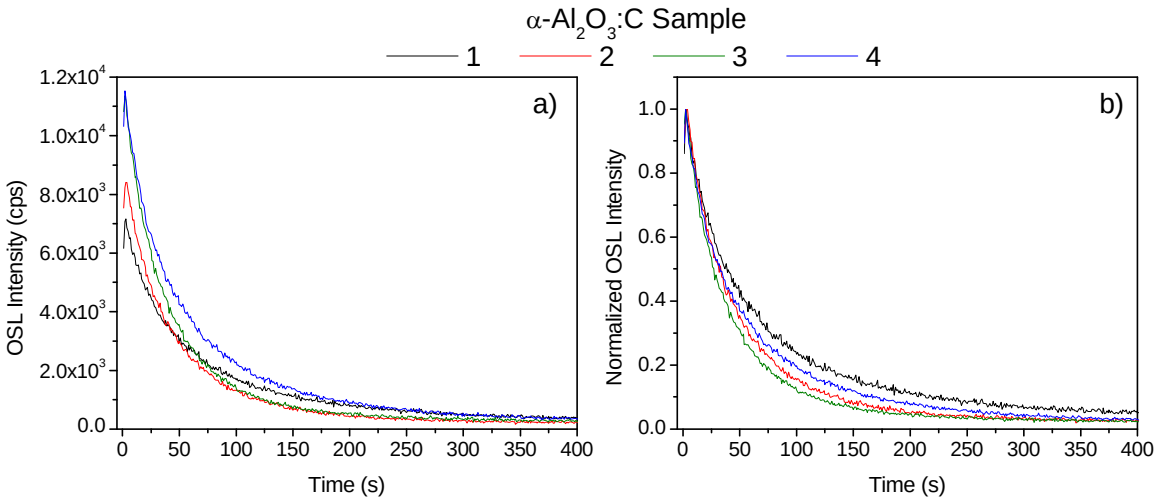


**Figure 3.4** OSL signals from four $\alpha$-$Al_2O_3$:C samples shown with a) original and b) normalized-to-maximum intensities.

TL and OSL exists in $\alpha$-$Al_2O_3$:C. Akselrod and Akselrod (2002) report that bleaching irradiated $\alpha$-$Al_2O_3$:C samples prior to TL measurement significantly reduces the lower temperature component of a broad main TL dosimetric peak, demonstrating that the traps responsible for this portion of the TL peak have a higher photoionization cross-section $\sigma$ than the higher temperature components. As a result, the lower temperature components make the greatest contribution to the OSL process. The rate of decay of the OSL signals can also be correlated to the TL signals. Since the low temperature TL component has a higher $\sigma$, the OSL from this component should decay faster. Consequently, samples that exhibit higher TL signal at the lower temperature edge of the main dosimetric peak should also exhibit faster OSL decay. Yukihara et al. showed that exposing $\alpha$-$Al_2O_3$:C to high doses shifts the TL peak to lower temperatures (Yukihara et al., 2003). They also observed that normalized OSL decays from high doses decayed faster than those from lower doses, and suggest that this may result from a complex dosimetric trap structure, or possibly from the kinetics of the process (Yukihara et al., 2004). A comparison of figure 3.4b to figure 3.3a supports this claim, as the samples with the lowest temperature TL peaks (2 and 3) have the fastest OSL decays.

The nature of the charge traps responsible for TL and OSL production has been investigated using several methods (Akselrod et al., 1990; Akselrod et al., 1993; Whitley and McKeever, 2000; Molnár et al., 2002). Polf (2002) used two methods to track the concentrations of $F$ and $F^+$ centers in several $\alpha$-$Al_2O_3$:C samples. The first method repeatedly measured the absorption spectrum at room temperature, from 190-270 nm, of an irradiated sample after it had been incrementally annealed (step-annealing) from 323 K to 973 K. The next method monitored the absorption of the 205 nm ($F$) and 255 nm

($F^+$) absorption lines as an irradiated sample was linearly heated from 323 K to 973 K. Both methods showed an anti-correlation to the $F$ and $F^+$ center concentrations over different temperature ranges. $F$ centers increased while $F^+$ centers decreased in the range of the main dosimetric peak (423-473 K). Similar changes occurred in the range of 573-673 K, while over the range of 773-973 K the $F$ centers decreased and the $F^+$ centers increased. These results confirm that the charge traps responsible for the main dosimetric TL peak, as well as the OSL signal, are electron traps. The thermally or optically released electrons recombine with $F^+$ centers to form $F$ centers and release 420 nm luminescence. Using this reasoning, the 573-673 K activated trap must also be an electron trap, while between 773-973 K, holes are released from hole traps, converting $F$ centers to $F^+$ centers.

The TL and OSL response of $\alpha$-$Al_2O_3$:C to absorbed dose extends over several orders of magnitude and exhibits supralinearlity at higher doses before the signal is

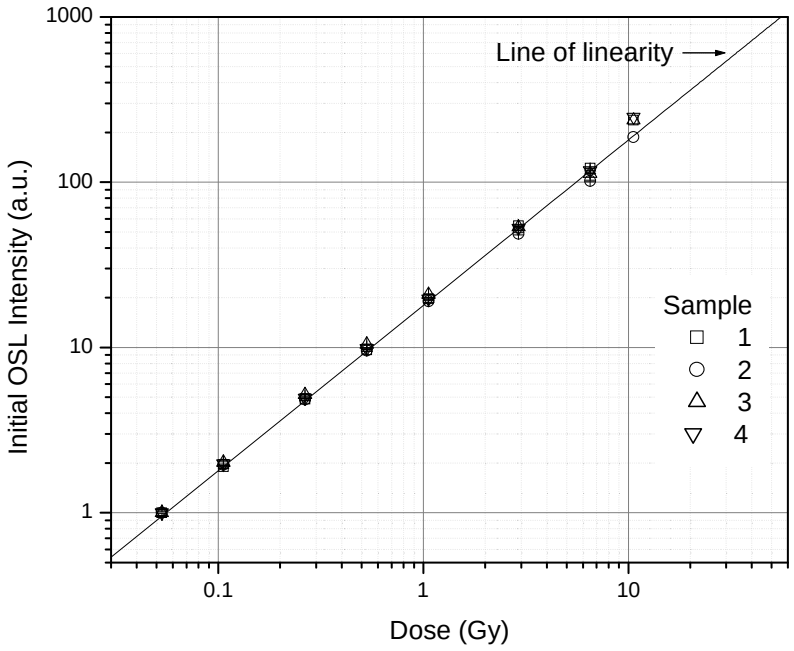


**Figure 3.5** OSL dose response of four $\alpha$-$Al_2O_3$:C samples normalized to the lowest dose value and shown against a linear fit of the first four datum points of sample 2.

finally saturated (Akselrod et al., 1990; Akselrod and McKeever, 1999). This response is, of course, dependent on the sample, and the dose responses of the four samples used in figures 3.3 and 3.4 are shown in figure 3.5. The responses of samples 1, 3, and 4 show the onset of supralinearity at ~10 Gy, while sample 2 stays more or less linear. Minimum detectable doses have been measured on the orders of microgray using a various measuring systems. One such report follows in the next chapter of this work.

### 3.2 Potassium Bromide doped with Europium (KBr:Eu)

Potassium bromide (KBr) is a member of the well-known alkali halide family that includes regular table salt (NaCl), as well as LiF - one of the most important materials in the realm of thermoluminescence dosimetry. Recently, KBr:Eu has been under investigation as the basis for alternatives to x-ray radiographic imaging plates, optical memory devices, and medical dosimeters (Nanto et al., 2000; Pedroza-Montero et al., 2000; Gaza and McKeever, 2006).

The structure of KBr follows that of a typical alkali halide – a face-centered cubic lattice of alkali metal ions interlocked with a face-centered cubic lattice composed of halogen ions. This structure is shown in figure 3.6. As with any real crystal, defects exist in KBr. The most common type is the Schottky defect, which consists of equal numbers of cation and anion vacancies. When $Eu^{2+}$ ions are added as a dopant, the divalent impurities are charge compensated by anion vacancies ($\alpha$ centers). A host of other defects may also be found, including interstitial halogen atoms ($H$ centers), anion vacancies occupied by one or two electrons ($F$ and $F'$ centers, respectively), holes

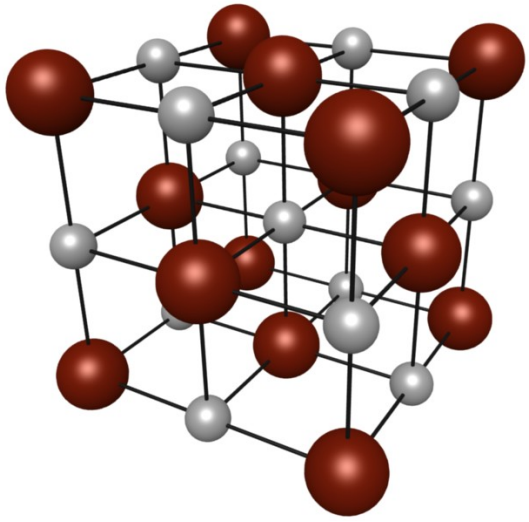

**Figure 3.6** Crystalline structure of KBr, consisting of two interlocking face-centered cubic lattices of $K^+$ ions (silver) and $Br^-$ ions (maroon).

trapped between two adjacent halide ions ($V_k$ centers), or halogen ion interstitials ($I$ centers), just to name a few (Townsend and Kelly, 1973; McKeever, 1985).

Under ionizing irradiation, the primary defect production mechanism in KBr:Eu begins with the creation of self-trapped excitons, or electron-hole pairs held together through the Coulombic force. The holes become bound by neighboring anions forming $V_k$ centers. The $V_k$ centers may become displaced and travel along the close-packed anion row in the ⟨110⟩ direction to form $H$ centers away from original anion site. At room temperature, single $H$ centers are not stable, and may continue migrating until aggregating with other $H$ centers to form interstitial clusters in dislocation loops (Hobbs et al., 1972). They may also become trapped at $Eu^{2+}$ impurities, forming $H_z$ centers. Meanwhile, the freed electrons get localized back into the now vacant anion sites and $F$ centers are formed (McKeever, 1985). This process is presented schematically in figure 3.7. After $F$-$H$ pairs are formed, optical and thermal stimulation may be used to mobilize the electrons from the $F$ centers. If these electrons recombine with holes located at $H_z$ centers, the $Eu^{2+}$ becomes excited, and its relaxation leads to an emission at ~420 nm.

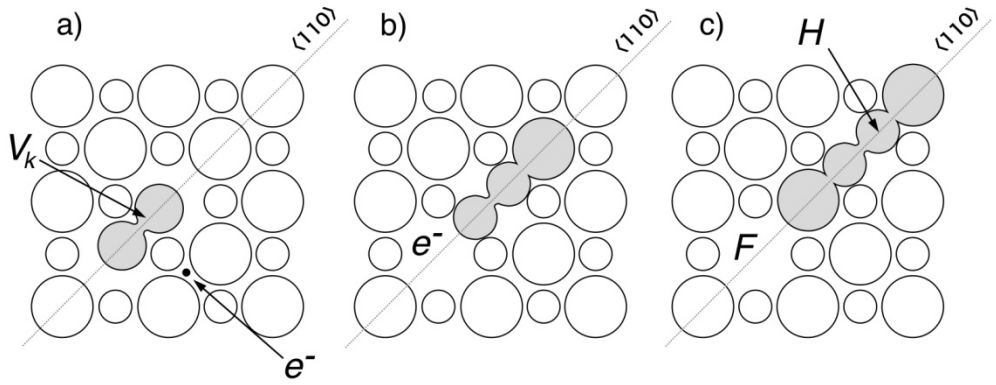


**Figure 3.7** Depiction of the effect of ionizing radiation. a) An electron-hole pair is formed and the hole gets captured by nearby anions, forming a $V_k$ center. b) the $V_k$ center migrates along the ⟨110⟩ axis, while the electron moves into the newly created anion vacancy. c) The $V_k$ center is converted into an *H* center away from the site of ionization (now an *F* center), and an *F*-*H* pair is formed. After McKeever (1985).

The transition responsible for the luminescence is the $4f^6 5d \rightarrow 4f^7$ relaxation which is described in figure 3.8a. Optical absorption and emission spectra of KBr:Eu are shown in figure 3.8b, and the relationship between the $Eu^{2+}$ energy band diagram and the absorption/emission of KBr:Eu follows.

A divalent europium ion in its ground state contains seven electrons which may be excited into states in the $4f^6 5d$ configuration. Here, six electrons will occupy the $4f^6$ state, hence the split level feature on the left side of 3.8a. The other electron will occupy the 5*d* level which is split by the crystal field into the $T_{2g}$ and $E_g$ bands. The absorption band centered at ~250 nm in figure 3.8b is associated with the $T_{2g}$ band, and an electron stimulated at this wavelength would make the 'a' transition in figure 3.8a. The longer wavelength bands from ~330-380 nm are associated with the $E_g$ band, and electrons excited by light in this range will make the 'b' transition. The $T_{2g}$ absorption band is relatively featureless, while the $E_g$ band has a characteristic 'staircase' pattern. This structure is a result of spin-orbit splitting of the $4f^6 5d$ configuration, coulomb interactions, and a weak interaction between the six $4f^6$ electrons and the single

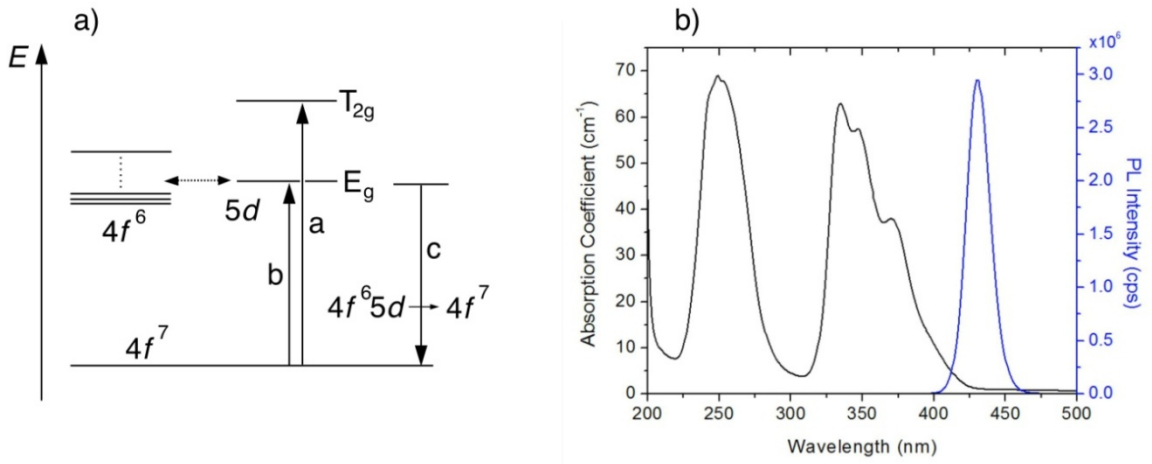


**Figure 3.8** a) Energy band diagram depicting energy levels and optical transitions of the $Eu^{2+}$ ion (adapted from Rubio, 1991). b) Optical absorption spectrum and photoluminescence signal of KBr:Eu. The PL signal results from stimulation with 250 nm light.

5*d* electron. Regardless of which excitation transition is made, the relaxation of the 5*d* electron back to the $4f^7$ ground state results in the emission of ~430 nm light (Hernandez et al., 1981; Rubio, 1991). Optical absorption measurements of other $Eu^{2+}$ doped alkali halides (KCl:Eu, KI:Eu, NaBr:Eu, NaCl:Eu, RbCl:Eu, and RbBr:Eu) show similar double broad peak spectra, and all with emissions peaking in the 400-450 nm range (Hernandez et al., 1980; Nanto et al., 2000).

Dosimetric properties of KBr:Eu that have been investigated include TL and OSL dependences on irradiation dose and type, environmental conditions, and after different thermal treatments. Buenfil and Brandan (1992) observed a strong TL peak in gamma-irradiated KBr:Eu at 383 K, as well as a TL dose response that was linear over approximately three orders of magnitude. However, they also noticed significant fading of the TL signal of ~80 % after only a few minutes. Other authors noticed fading as well, but at varying degrees (Pedroza-Montero et al., 2000; Gaza, 2004). Nanto et al. (1993, 2000) monitored the OSL and OSL fading of KBr:Eu and found that the OSL stimulation spectrum peaks around ~620 nm, while the emission peaks at ~420 nm, consistent with

the relaxation of excited $Eu^{2+}$ ions. The lifetime of the luminescence is reported by Nanto et al. to be ~1.6 μs, while Rubio reports a lifetime of 1.33 μs. The group studied the effects on OSL fading of x-irradiated samples due to ambient temperature, humidity, x-ray energies, and $Eu^{2+}$ concentrations. Their results showed that a concentration of 0.01 mol% faded the least. Lesser fading was observed under low humidity and higher energy x-rays. Perez-Salas et al. (1996) reported a TL signal with a complex structure comprised of as many as 6 peaks. This structure was seen to change with respect to the wavelength of UV light used to irradiate the sample. This complex structure was also reported by Castaneda et al. (2000). Perez-Salas et al. also showed that the main peak (in this case found at ~380 K) was significantly reduced by photostimulation with 600 nm light. This shows a clear correlation between TL and OSL using 600 nm light. Further TL/OSL correlations will be explored in chapter 5 of this work.

# CHAPTER IV

## HIGH-SENSITIVITY *IN-SITU* ENVIRONMENTAL MONITORING SYSTEM

As discussed previously in section 1.2, well-established techniques used currently for subsurface monitoring of environmental background radiation levels include chemical analysis of soil samples, and the use of scintillators and semiconductor crystals. Though they provide valuable information, these techniques could be difficult to implement for high resolution (both spatial and temporal) monitoring of a large region due to prohibitive cost, labor, and infrastructure requirements. Instead, a large array of simple and inexpensive radiation sensors may be better suited. These sensors would be remotely interrogated at regular periods with little or no human intervention and are easy to install, operate, and maintain. Such devices may operate, for example, as quiescent "trigger" detectors for subsequent intervention with more detailed analytical technologies.

One application that could benefit from such a system is the monitoring of radioactive plumes from nuclear waste storage sites such as those found at the Hanford Site in the state of Washington, discussed in section 1.1. This application could be extended to include continuous verification that the containment integrity of remediated waste sites is maintained. Besides application for the detection of stored radiological materials and contaminants, the system can also be used as a sensitive remote dosimeter for difficult to access or hazardous locations, such as "high-radiation-level areas in and around nuclear

reactors", as suggested by Huston et al. (2001). It could be deployed to monitor industrial, commercial, or private pipework and ductwork for low concentration radiological contaminants, or for surveillance purposes in high-security buildings. Yet another potential use is for on-site determination of the gamma component of the natural dose rate in soils for general environmental monitoring applications.

This chapter details the potential of the POSL technique for use with an effective and inexpensive sub-surface radiation sensor utilizing $\alpha$-$Al_2O_3$:C crystal dosimeters. The detector crystals are installed into ground probes, and passively integrate dose information via the electronic processes similar to those discussed in section 2.1.1. In this sense, the dosimeters may be considered always "on" - absorbing dose until connected to a stimulation/detection system for OSL read-out. $\alpha$-$Al_2O_3$:C is the basis for the personal dosimetry system Luxel™ (Landauer, Inc.), successfully used on a large commercial scale since 1998. The probes by themselves are simple and inexpensive, consisting simply of stainless steel tubes each containing a single crystal dosimeter coupled to an optical fiber. Multiple probes, installed at different locations covering a large area or structure, can all be connected to a single multiplexing reader configured for periodic readouts of each probe. An integrated sensor network could thus be constructed that monitors the radiation level at these locations with a low-level autonomy, only alerting higher level systems (e.g. a human operator) when significant deviations from nominal readings are detected. Each probe can also be independently read using a portable reader, for environments ill-suited to a large networked infrastructure, or for impermanent monitoring of a site. This chapter details the design and development of a portable system that could be used for probe-by-probe investigation.

Similar concepts of remote OSL dosimetry using α-$Al_2O_3$:C have been developed and tested for radiation protection (Ranchoux et al., 2002) and for dose evaluation of radiotherapy treatments (Andersen et al., 2003; Edmund, 2007; Polf et al., 2002, 2004). The long luminescence lifetime (~35 ms) of the main emission from α-$Al_2O_3$:C presents a key challenge for applying the OSL of α-$Al_2O_3$:C to radiotherapy dosimetry, as it takes upwards of minutes to read the entire OSL signal. Alternatively, radioluminescence (RL) may be monitored in real-time during treatment, while the OSL signal is measured afterwards as a check against the RL results (Andersen et al., 2003). The time constraints on environmental monitoring are much less demanding than for radiotherapy, and obtaining an environmental measurement every 24 hours may be considered near-real-time monitoring. Further improvement to sensitivity (and concomitantly, reduction in measurement time interval) may make the system discussed in this chapter useful for a number of other potential applications in homeland security, including radiation detection in buildings, in air, in soils, and on or in shipping containers.

A proof-of-concept design of a portable system based on optical fiber dosimetry is discussed, as well as results on system optimization efforts. The performance of the bench-top system was tested mainly by multiple determinations of the lower detection limits using several different methods. Reproducibility and radiation type discrimination were also tested. The proof-of-concept design was migrated into a more refined, truly portable form, which included modifications intended to improve the capabilities of the system. Results of this final prototype are discussed in the second section of this chapter.

## 4.1 The Bench-top System

### *4.1.1 Description of the System and Experimental Details*

The remote radiation monitoring system consists of a POSL-based reader unit to which a detector probe is connected via a light guide. Figure 4.1 represents schematically the proof-of-concept design of the reader with a probe attached. The reader provides both the stimulation light to interrogate the radiation sensor on the tip of the probe, and the light detection capability to measure the OSL emitted by the $\alpha$-$Al_2O_3$:C crystal dosimeter. The optical fiber cable carries both the stimulation light to the dosimeter and the emitted OSL, which is proportional to the radiation dose absorbed by the crystal, back to the reader for detection. The optical fiber is attached to the reader using a standard fixed connection (FC) optical fiber connector, allowing multiple probes to be used

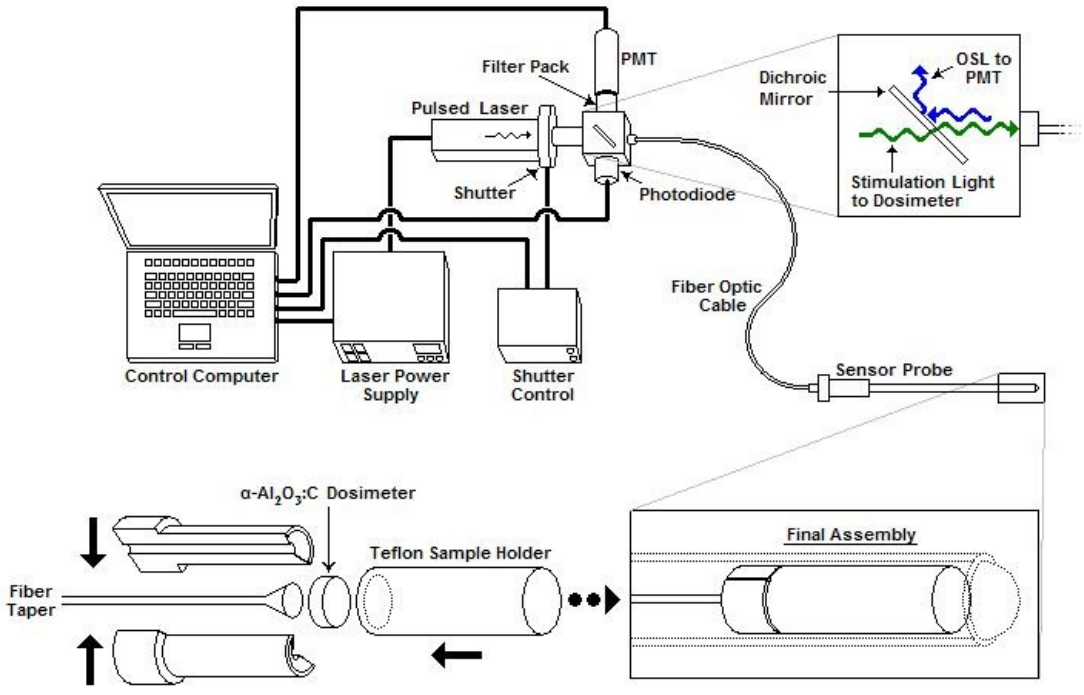


**Figure 4.1** Schematic representation of the portable optical fiber dosimeter system showing reader system components and a detector probe. The internal construction of the ground probe containing a 5 mm diameter $\alpha$-$Al_2O_3$:C dosimeter and light discrimintation via the dichroic mirror are detailed in exploded views.

reproducibly with a single reader.

The 532 nm line of a Q-switched Nd:YAG diode-pumped laser (model GSQAOM32-25 from MeshTel/Intelite, Inc.) was used for optical stimulation. The laser was operated at a frequency of 4 kHz with an average output power of ~40 mW with laser pulses 15 ns wide. A 1-mm thick dichroic mirror (OptoSigma Corporation, 95% transmission at 532 nm, 90% reflectivity at 420nm) allowed the green stimulation light to pass to the attached optical fiber connecting the probe, and reflected the radiation-induced blue light from the sensor probe into the photomultiplier tube (PMT) within a P10PC Ultra High Speed Photon Counting Detector from Electron Tubes, Inc. A 4-mm thick Corning 5-58 filter (bandpass filter centered at 410 nm with full-width at half maximum of 80 nm) was used in front of the PMT to prevent the green stimulation light from reaching the PMT while allowing the detection of the characteristic 420 nm luminescence of the $\alpha$-$Al_2O_3$:C dosimeter.

Output TTL pulses from the P10PC corresponding to detected luminescence photons were counted using two National Instruments DAQCard$^{TM}$-6062Es according to the gating scheme described in figure 4.2. In this scheme, a DAQ card triggered the laser and the PMT counter gate every 250 μs. The duty cycle of the counter gate was set to 85%, so that the gate was open with a 37.5 μs delay in relation to the laser pulse. The PMT is on during the laser pulse and the 5-58 filters do not perfectly block the green light. So, this small gate delay grants the PMT some relaxation time and reduces laser background in the recorded OSL signal. Only the TTL pulses arriving when the gate is open, i.e., between the laser pulses, were counted. The intensity of the emitted OSL signal (with a luminescence lifetime of ~35 ms) was practically constant on the timescale of figure 4.2.

However, the pulsed stimulation continuously depleted the charge previously trapped in the crystal due to exposure to ionizing radiation, causing a decrease in the OSL signal at longer timescales. After a certain period, the optical stimulation reduces the OSL signal to background levels, resetting the dosimeter. The total integration time for each data point is 0.5 s.

Laser stimulation was controlled with an Oriel shutter and controller (models 79663 and 79665, respectively). Not all of the laser light was transmitted through the dichroic mirror, and the small fraction of reflected laser light that was directed into an EG&G photodiode for monitoring general fluctuations in the laser power, if any. Data acquisition, analysis, and storage - as well as electronic and mechanical component control - were performed using a laptop computer into which the two DAQ cards were installed, and using a custom software interface developed using National Instruments LabView$^{TM}$ 6.1.

Several forms of $\alpha$-$Al_2O_3$:C crystal, of different sizes and growths, were investigated. Some were of 5 mm diameter with a thickness of 1 mm, of the type generally known as TLD-500, that were grown in the Urals Polytechnic Institute, Russia. Similar crystals with diameter of 5 mm and lengths varying between 2 and 10 mm (shown in figure 4.3) were grown and provided by Stillwater Crystal Growth Division of Landauer, Inc., USA, as was a pulled $\alpha$-$Al_2O_3$:C fiber having a 0.9 mm length and a 2 mm diameter. In order to allow remote reading of the radiation sensor, the $\alpha$-$Al_2O_3$:C dosimeters were mechanically coupled to the distal ends of silica optical fibers. The proximal ends of the fiber cables were fitted with FC connectors, and the coupled cable-dosimeters were then placed into prototype ground probes measuring 30 cm in

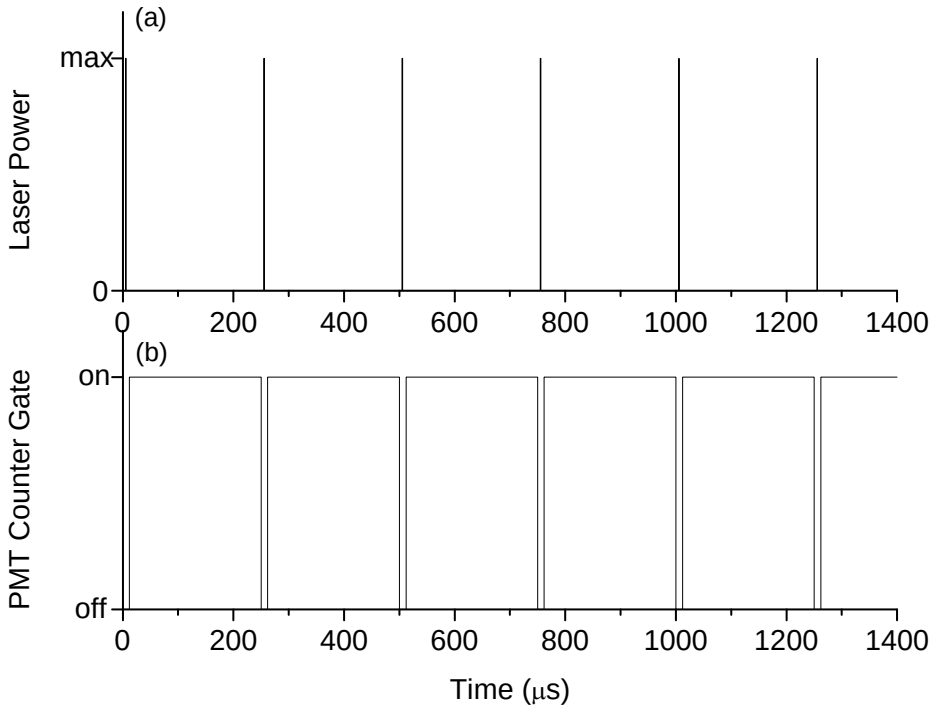


**Figure 4.2** Timing scheme used for the Pulsed Optically Stimulated Luminescence (POSL) measurements. The laser is pulsed with a frequency of 4 kHz and the PMT counter gate is open between the laser pulses to detect the OSL luminescence from the $\alpha$-$Al_2O_3$:C dosimeter.

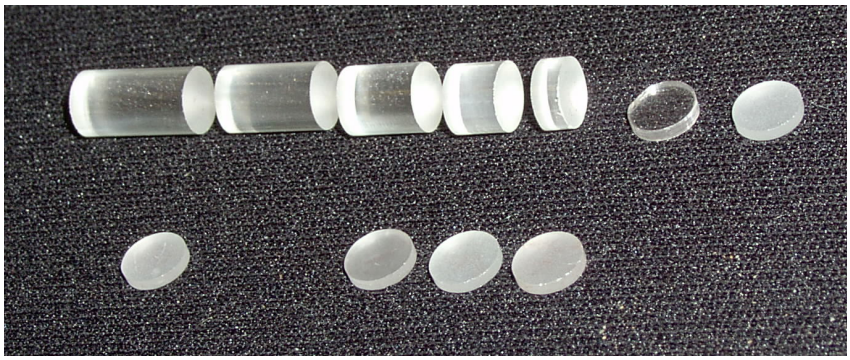

**Figure 4.3** Different $\alpha$-$Al_2O_3$:C dosimeters investigated for use as radiation sensor on the probe, with thickness varying between 1 mm and 10 mm.

length. For the pulled fiber dosimeter, the internal optical fiber is a straight length of silica connected directly to the end of the dosimeter. The pulled fiber was placed into an aluminum end cap (bored aluminum cylinder with inner diameter of ~2 mm, out diameter 12 mm, bore length 15 mm and outer length 20 mm) to test whether beta and gamma rays could be discriminated when the pulled fiber was exposed to both types of radiation. For the chip, a fused-silica taper was used to improve the collection efficiency of emission light (see lower portion of figure 4.1). The off-the-shelf fiber taper (from Polymicro Technologies, LLC; NA: ~0.11, Attenuation: ~40 dB/km @ 410nm and ~15 dB/km @ 532nm) has a diameter at its widest part of 3 mm and was used to improve the optical coupling between the optical fiber cable (1 mm diameter) and the aluminum oxide dosimeter (5 mm diameter). The intended function of the taper was to increase the luminescence collection efficiency. Sample holders were used to mechanically couple the chip to the fiber taper. These were made from Teflon® for high reflectivity of both green and blue light, significantly improving both optical stimulation and collection of luminescence by the optical fiber. The choice of Teflon is discussed in the next section.

For irradiation of dosimeters of different sizes, a $^{60}$Co GammaCell source - delivering a dose rate of 7 mGy/s at the sample location - was used. The samples were wrapped in aluminum foil to attain charge particle equilibrium. Two button sources, one $^{60}$Co and one $^{137}$Cs (both part of a gamma source set from The Nucleus, Inc.), were used for the dose responses of dosimeters in assembled probes. Another weak $^{137}$Cs source was used for POSL measurement reproducibility. A $^{90}$Sr/$^{90}$Y beta source from DayBreak was used in conjunction with the $^{60}$Co GammaCell for beta/gamma radiation discrimination testing. Additional irradiation and OSL measurements were performed using a Risø

TL/OSL-DA-15 from Risø National Laboratory (Denmark) equipped with a $^{90}Sr/^{90}Y$ beta source providing 55.2mGy/s to the dosimeter (Bøtter-Jensen et al., 2000).

### *4.1.2 System Optimization*

The material used to construct the sample holder has a significant influence on OSL measurements. Dark materials absorb both the stimulation light and the OSL from the dosimeter, whereas materials with high reflectivity increase the stimulation light inside the sample and also reflect portions of the OSL signal that would otherwise be absorbed by the sample holder.

The influence of the sample holder material was investigated by placing a 5 mm diameter, 6 mm long $\alpha$-$Al_2O_3$:C single crystal irradiated with a 20 mGy gamma dose in contact with the fiber taper and performing the OSL readout. The OSL curve obtained is shown in figure 4.4 as “blank”. The dosimeter was then annealed at 1273 K for 15 min and irradiated with the same dose, but this time the OSL was performed using a metallic reflective surface on the side of the dosimeter opposite the taper. The sample was again annealed and irradiated in the same conditions using Teflon tape around the dosimeter for the OSL measurement. This resulted in an increase of almost 400% in the OSL initial intensity. The integrated OSL signal (area under the curve) increased 230%, showing that the light scattering by the Teflon improves the light collection by the taper. The normalized curves shown in the inset of figure 4.4 indicate that the stimulation is also improved with the Teflon, since the OSL decay curve obtained with the Teflon decays faster than the OSL in the other cases. The results of this investigation led to the design of the sensor probe using the Teflon sample holder shown in the lower portion of figure 1.

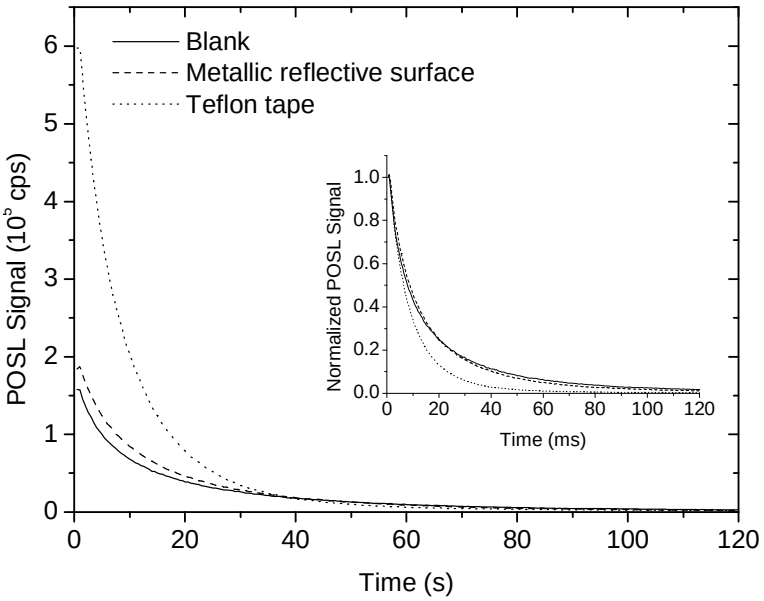


**Figure 4.4** POSL decay curves obtained with the same sensor and same gamma dose (20 mGy) using different materials around the aluminum oxide crystal.

The effect of the size of the $\alpha$-$Al_2O_3$:C detectors used in the sensor probe was investigated by irradiating a set of samples of different sizes with a gamma dose of 20 mGy. A 1 mm thick sample (called the 'chip') and the set of samples of length varying between 2 mm and 10 mm were used. All samples had a diameter of 5 mm. The samples were placed in the detector probe for the POSL readout one at a time. A second and a third irradiation of the set of dosimeters were performed, but this time the POSL measurements were performed with a metallic reflective surface or with Teflon tape around the dosimeters, as described above. The resultant POSL signals, defined as the integrated luminescence over 120 s of stimulation minus the background, are compared in figure 4.5. To guarantee that the same dose was delivered in the different irradiation runs, a set of three 1 mm thick aluminum oxide dosimeters (chips) were included in the irradiations. These crystals were read in the Risø TL/OSL reader and the OSL signals

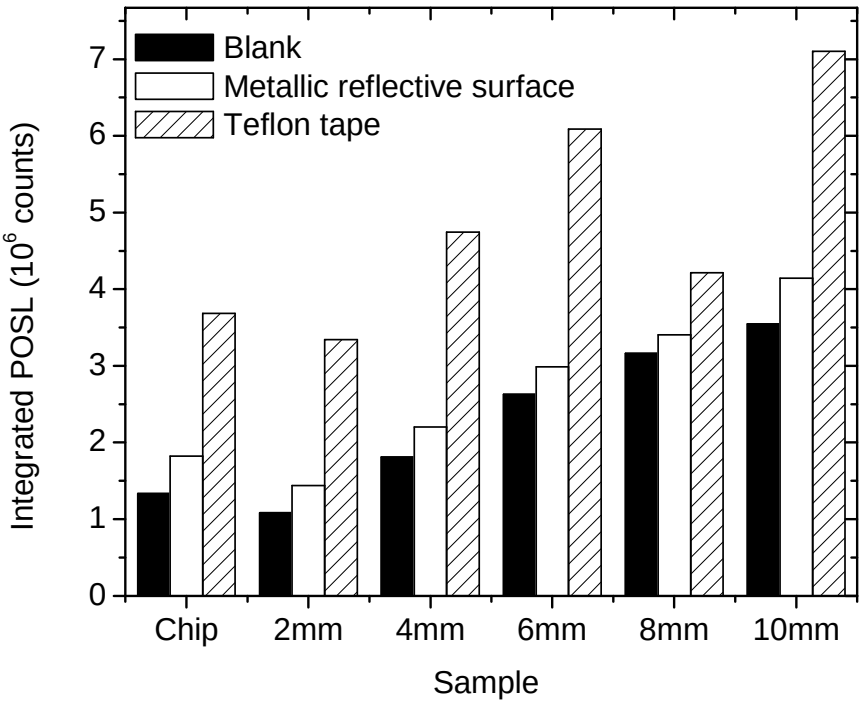


**Figure 4.5** Comparison between the POSL signals from samples of different sizes, measured with different types of reflective surfaces. The POSL signal was defined as the total luminescence (integrated over 120s of stimulation). The background was estimated before the irradiation and appropriately subtracted. The "chip" has a thickness of 1mm, but it is from a growth different from that of the set of samples of length between 2 mm and 10 mm.

varied little between irradiations, having standard deviations of 3.2%, 4.5%, and 8.0% for the first, second, and third crystals, respectively. In this case, the OSL signal was defined as the total luminescence during the initial 20 s of stimulation minus the background, estimated by measuring the OSL signal for 20 s after 100 s of stimulation.

The comparison in figure 4.5 indicates that the sensitivity can be improved by the use of larger α-$Al_2O_3$:C crystals, but the gain is not proportional to the volume. If the thickness of the crystal is increased from 2 mm to 10 mm, the gain in total OSL signal is approximately 2 to 3 times, depending on the type of reflective surface. This is related to the fact that the light stimulation and OSL collection is less efficient for the larger crystals volumes. The 1 mm thick chip used in the study is from a different growth and

exhibited a larger sensitivity than the set of crystals of thickness between 2 mm and 10 mm. The discontinuous low intensity of the 8 mm long rod measured with Teflon tape is believed to have been caused by poor coupling of this dosimeter to the fiber taper. The mismatch of fiber taper diameter to dosimeter diameter represents an area for further optimization. As noted in the previous section, the use of Teflon tape causes a significant increase in the POSL signal in all cases.

### *4.1.3 System Performance Results*

The minimum detectable dose (MDD) - defined as the dose that would give a signal at least $3\sigma$ above the signal background, where $\sigma$ is the standard deviation of the signal background - is one of the most important performance metrics for a system designed to measure radiation at low dose rates such as those from natural environmental background sources. An initial MDD measurement of the system was calculated from data taken using both a 1 mm chip and the 2 mm diameter pulled fiber sample. For the chip, a dose response curve was obtained using a $^{137}$Cs source giving a dose rate of 0.88 μGy/s. Comparison with the linear fit of the dose response shows that 3σ is equivalent to ~2.5 μGy. This result is presented in figure 4.6.

Another dose response of a sensor probe was measured using a 5 mm diameter, 1 mm thick α-$Al_2O_3$:C dosimeter. The system was setup as shown in figure 4.1, and a $^{60}$Co button source was placed above the probe directly above the portion housing the dosimeter. An initial 5 min bleach of the crystal was performed. The dosimeter was then allowed to absorb dose from the source for three 160 s periods, and three 360 s periods.

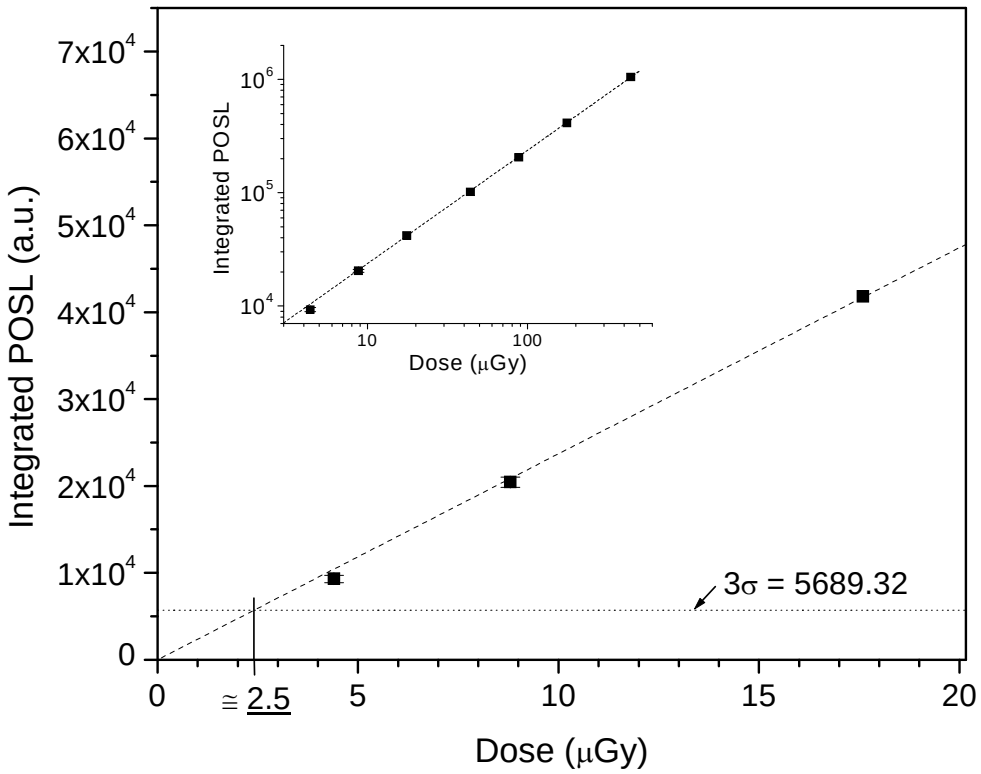


**Figure 4.6** Gamma dose response using a $^{137}$Cs source. By comparing the signal corresponding to the minimum detectable dose (MDD, calculated from signal background) to the linear fit of the OSL data, a MDD of ~2.5 μGy was found. Inset: The entire dose response is shown using log-log scaling.

Then single dose periods of 1,060 s, 3,060 s, and finally 15,060 s in duration were given. Between each and every dose period, the POSL was measured for 5 min, with 30 s dark count measurements before and after the POSL measurement. Representative POSL curves obtained in the study are shown in figure 4.7(a).

Following the last POSL measurement, the dosimeter was allowed to absorb radiation for an additional 30,000 s. The dosimeter was then extracted from the probe and OSL was read using the Risø reader. Using the Risø reader's calibrated source, a dose of 110.4 mGy was then given to the dosimeter and OSL was again measured, The ratio of the total integrated, background-subtracted OSL provided the calibration for calculating

the dose rate provided by the $^{60}$Co button source while over the probe (~19μGy/hr). The results of the dose response may be seen in figure 4.7(b).

Ten background signal measurements were made before the $^{60}$Co dose response was performed, and these were used to obtain an average integral background of 1690 counts over 30 seconds. The standard deviation of these ten measurements equaled 33.9 counts, or ~2% of the background. This background was subtracted from the POSL signal, defined as the integrated luminescence of the first 30 s of stimulation. By the definition above, any POSL signal that measures larger than $3\sigma$ (101.6 counts) is considered signal due to ionizing radiation. Figure 4.7(b) shows a horizontal line marking $3\sigma$, which corresponds to a minimum detectable dose of <1 μGy. However, this result is interpreted as representing an order of magnitude estimate and is not claimed to be the absolute MDD. A look back to Figure 4.7(a) shows that for the 0.84 μGy dose, the POSL signal may not seem conclusive. However, the signal due to the 1060s (5.6 μGy) dose is clearly well above the level needed to discriminate statistically from background.

The system's reproducibility was tested by repeating the irradiation and subsequent POSL of the pulled fiber sample readout six times. An initial POSL measurement bleached any residual signal of the fiber to the background level. The following 6 measurements were all taken after irradiation from a $^{137}$Cs source for eight hours at a dose rate of approximately 7.2 μGy/hr. The results are shown in table 4.1, which lists the integrated POSL signals. The POSL signal integrated over the first 20 seconds has a standard deviation of 3.3% of the average value, indicating good reproducibility. MDD calculations from these measurements ranged from 2.68 μGy to 5.57 μGy, with the average being 4.18 μGy.

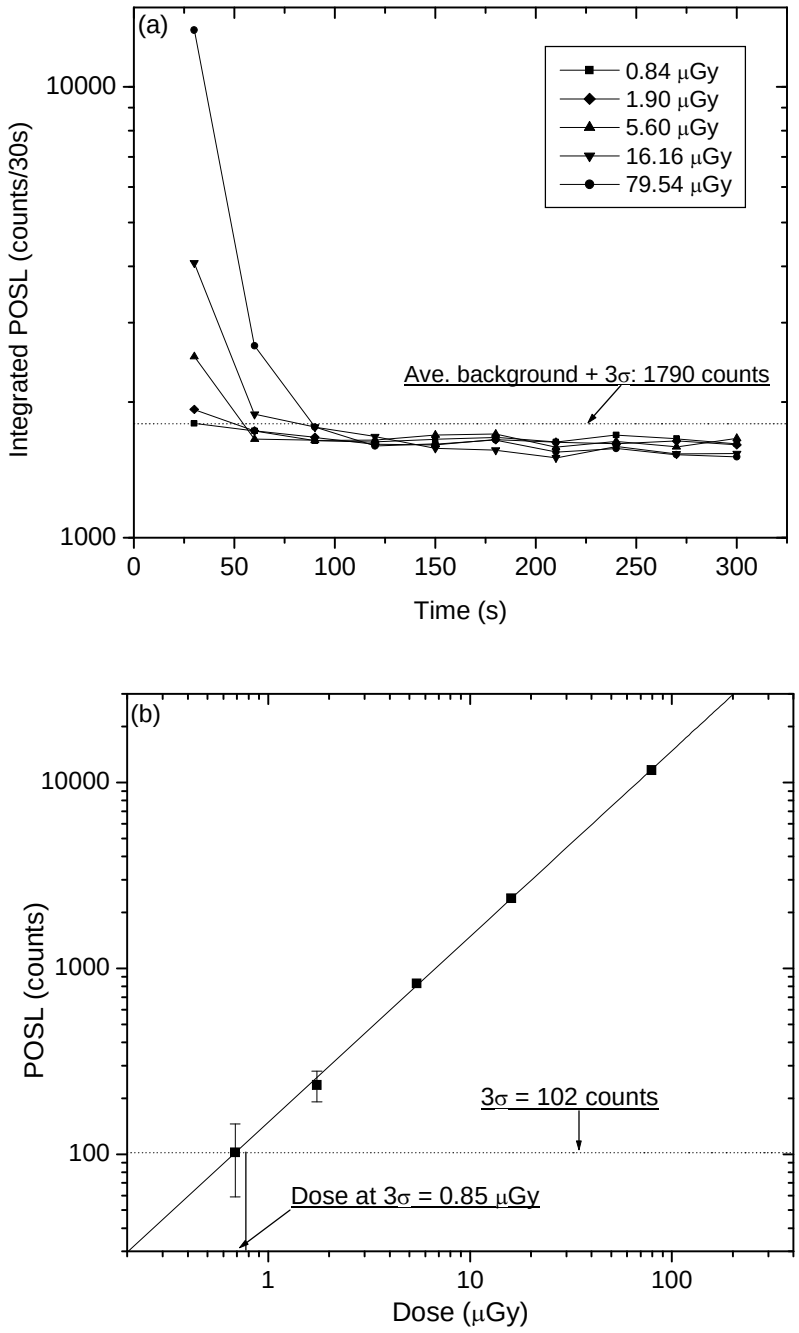


**Figure 4.7** Dose response of the system of a detector probe using a 1mm-thick aluminum oxide dosimeter. Graph (a) shows typical POSL decay curves obtained during the experiment, and graph (b) shows the dose response curve with error bars on the first two data equal to the standard deviation of three measurements. The POSL signal was defined as the total luminescence in the first 30s of stimulation minus the background signal during the same period, evaluated after extended optical stimulation (bleaching).

**Table 4.1** Results of the last six of seven consecutive POSL measurements of the pulled fiber α-$Al_2O_3$:C sample.

| **POSL measurement:** | **Integral POSL:** (counts per 0.5 s) | **Calculated MDD:** (μGy) |
|---|---|---|
| 2 | 1605 | 4.44 |
| 3 | 1644 | 5.57 |
| 4 | 1497 | 4.87 |
| 5 | 1619 | 2.68 |
| 6 | 1599 | 4.13 |
| 7 | 1555 | 3.41 |
| ***Average:*** | **1587** **σ = 53** | **4.18** **σ=0.14** |

### *4.1.4 Conclusions based on the Original Bench-top System*

Currently the system is capable of an MDD of ~5 μGy. This is a conservative estimate based on the largest of the calculated MDDs, although much lower values were found under certain circumstances. An MDD of 5 μGy would be already satisfactory for applications such as the monitoring of radioactive plumes in radioactive waste sites. The computer code Varskin 2 was used to calculate minimum exposure times necessary to measure the MDD due to various radionuclides at a given concentration of radioactivity. This exposure time was calculated by dividing the MDD value by soil contamination dose rate. Based on an MDD of 5 μGy, it was determined that the sensor can measure the contaminant concentration at which soil can be released for unrestricted use (1.85 $Bq/cm^3$) for the radionuclides $^{137}Cs$, $^{90}Sr/^{90}Y$ and $^{99}Tc$ in 50 h, 67 h, and 1520 h (63 days), respectively (Klein et al., 2006). Thus, the monitor is clearly adequate for measuring $^{137}Cs$ and $^{90}Sr/^{90}Y$. The monitor may be suitable for measuring $^{99}Tc$ in soil because the exposure time is comparable to the time between soil samples. These

exposure times will provide rapid notification of the possibility of radioactive contamination entering the soil. Furthermore, a minimum detectable dose of 5 μGy is one order of magnitude lower than the detection limit of the optical fiber dosimetry system based on the OSL of $Al_2O_3$:C reported by Ranchoux et al. (2002).

Significant improvement can still be made to enhance the capabilities of the environmental monitoring system. Correctly-matching the taper termination diameter with the diameter of the crystal dosimeter could improve the sensitivity of the system, as this would grant more efficient use of detector material. Index-matching gels could be used in the interface between the silica fiber taper (index of refraction 1.45) and the aluminum oxide dosimeter (index of refraction 1.77) to improve the optical coupling. In previous testing, the use of index-matching gel introduced a significant background, however, apparently due to spurious effects associated with the high intensity of the laser pulses. This may be due to processes induced by the high laser power being delivered in such short intervals (laser pulse periods of 15 ns). Better tracking of the laser power may also lead to MDD improvements by providing data by which the POSL signals may be corrected for laser power fluctuations. Improvements such as these were implemented and the results of such modifications are discussed in the next section.

## 4.2 The Portable System

### *4.2.1 Changes to the Bench-top System*

The motivation for developing a high-sensitivity subsurface radiation dosimetry system originated from a search for alternative methods for monitoring large environments having broad, dynamic ranges of radionuclide containment and/or

contamination. The POSL technique offers an effective, inexpensive way to provide a relatively high spatial and temporal resolution for this type of monitoring. As discussed in the previous section, a single POSL reader system can interrogate multiple subsurface detector probes. This may be accomplished by having a centralized reader station that remains connected to all ground probes over long distances via a network of optical fibers, or by having a portable reader system that can be taken into the field and connected to ground probes individually. The POSL system was designed to accommodate the latter readout scheme, and this section details the transition of the proof-of-concept, bench-top system into a more robust, fully portable, prototype reader.

The design of the portable environmental system follows the same general layout as that of the bench-top system shown in figure 4.1. The GSQAOM32-25 Q-switched laser and the discriminating optics and filters remain the same. The P10PC photon detection system was replaced with a P25PC system from Electron Tubes, Inc. The P10PC had been made obsolete and the P25PC was the updated equivalent. The fiber-optic cable connector was upgraded with a PAF-X-5-A FiberPort FC collimator from Thorlabs that features six-degrees of freedom for alignment. A custom electronics board was developed by Mr. William A. Holloway – a senior research engineer with Oklahoma State University's Electrical Engineering Technology department. – that regulates power between dedicated power supplies and the various components. The board also contains TTL circuitry that can output a digital pulse train that is delayed by ~10 μs. This is necessary for controlling the gate timing between the triggering of the laser pulse and the activation of PMT counting (see section 4.1.1). It also replaces the functionality of one of the two National Instruments DAQCard$^{TM}$-6062E cards, and so the total complexity and

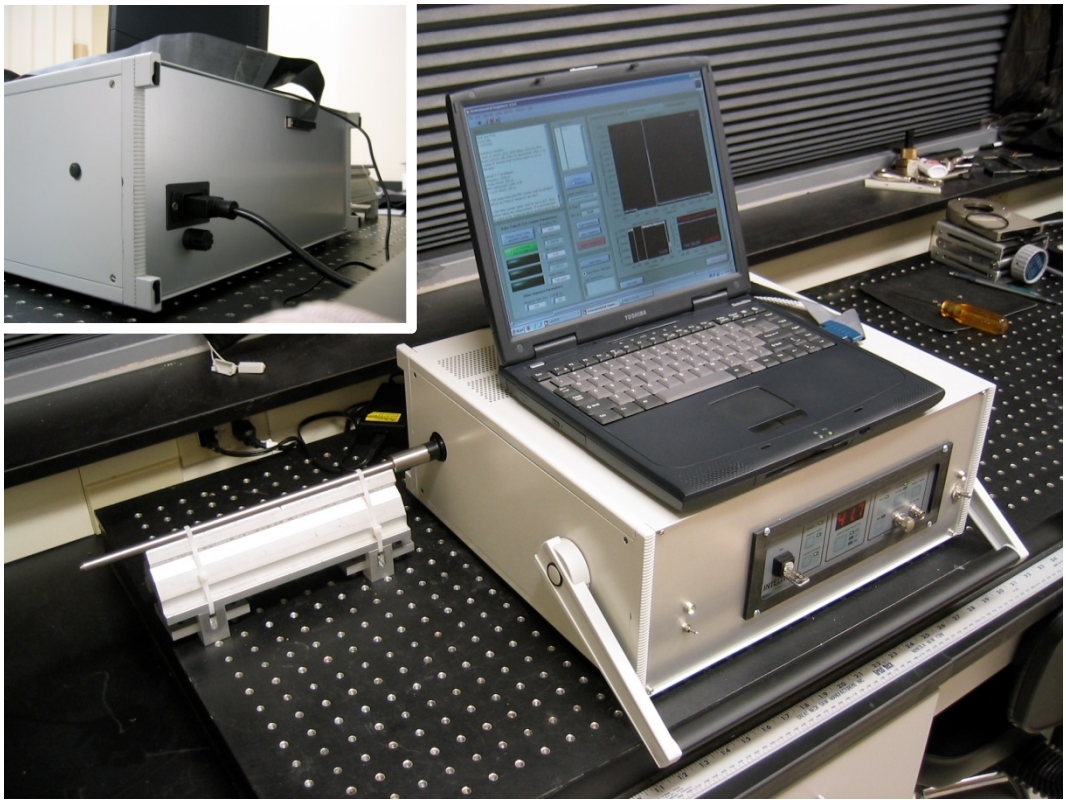

**Figure 4.8** Modified, portable version of the environmental radiation monitoring system with a 30 cm detector probe directly attached to the FiberPort connecter (left) and control PC. Inset: View of rear panel showing power connection, fuse holder, and DAQ-Card connection.

cost of the system is reduced. The two National Instruments shielded SCB-68 connector blocks were also replaced with a single, simpler CB-68LPR connector block. All components were installed into a model 15B0544-33 portable desktop enclosure from ELMA Electronic, Inc. Photographs of the portable system are given in figure 4.8.

### *4.2.2 Calibration Testing I: Low-activity Measurements*

With the migration of the portable system complete, a thorough calibration was needed. The calibration process began with the measurement of signals obtained using a fully assembled 30 cm ground probe that had been exposed to a low-activity $^{226}$Ra source under the supervision of Dr. Art Lucas at the Lucas Newman Science & Technologies

(LNST) laboratory in Stillwater, Oklahoma. The NIST-certified $^{226}Ra$ source (Standard Reference Material 4967) is in liquid form - 5 mL of 1.4 mol/L HCl solution containing 8.9 mg $BaCl_2$ and $Ra^{2+}$ - inside a flame-sealed borosilicate glass vial. The activity concentration of the source is 2729 Bq/g. The source and probe were placed 10 cm apart and horizontally level, with the probe lying tangential to the cylindrical source vial (see figure 4.9). Two POSL measurements (labeled 'ra226cal1' and 'ra226cal2') were made, each after the dosimeter in the probe was irradiated for approximately 24 hours. The POSL signal was recorded for 300 s at 500 ms per datum point. However, the final analysis treated the POSL signal as ten consecutive 30 s integrations, as shown in figure 4.10. The first two 30 s periods were considered to contain the whole of the POSL from the $Al_2O_3$:C dosimeter. The latter 8 integrals were used to calculate the average background, which was then subtracted from the first integral. The background-subtracted POSL values of the two measurements differ by 18.4%. This large discrepancy between the two measurements led to an investigation of the method of background subtraction. The two signals in figure 4.10 show significant variability in the background. Thus, a correction to this variability was applied by normalizing the POSL data by

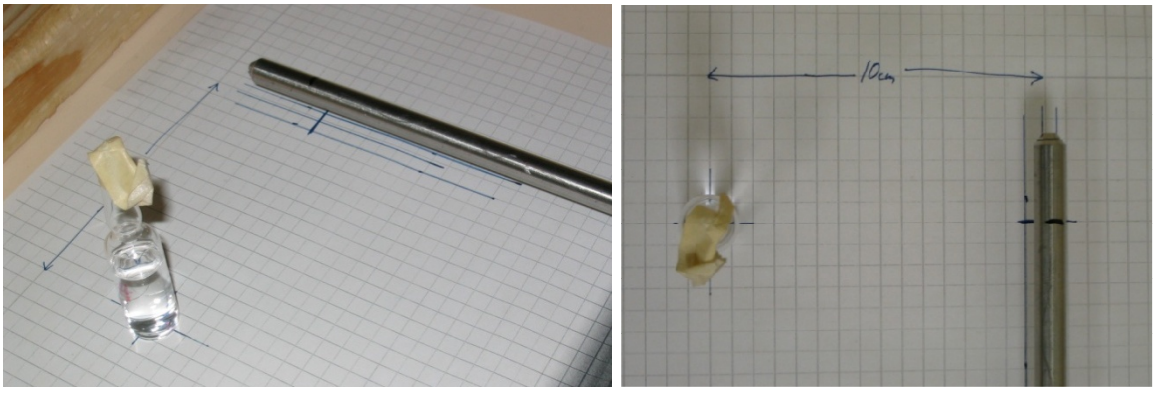


**Figure 4.9** Photographs of the same experimental setup for the measurement of POSL due to $^{226}Ra$ irradiation. The radium vial and dosimeter centers were separated by 10 cm. The blue line on the steel probe marks the position of the dosimeter inside the probe.

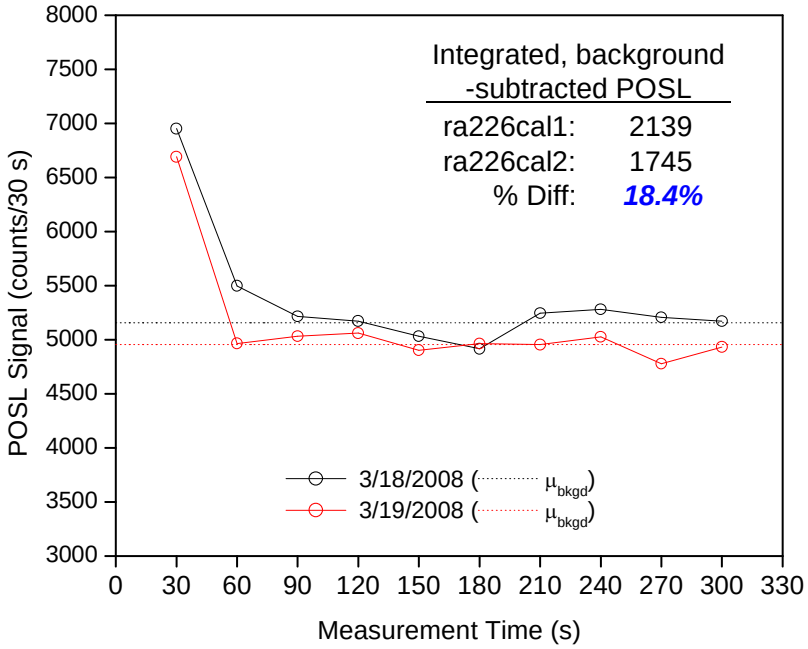


**Figure 4.10** POSL signal results from two 24 hr $^{226}$Ra irradiations, after integrating over 30 s intervals.

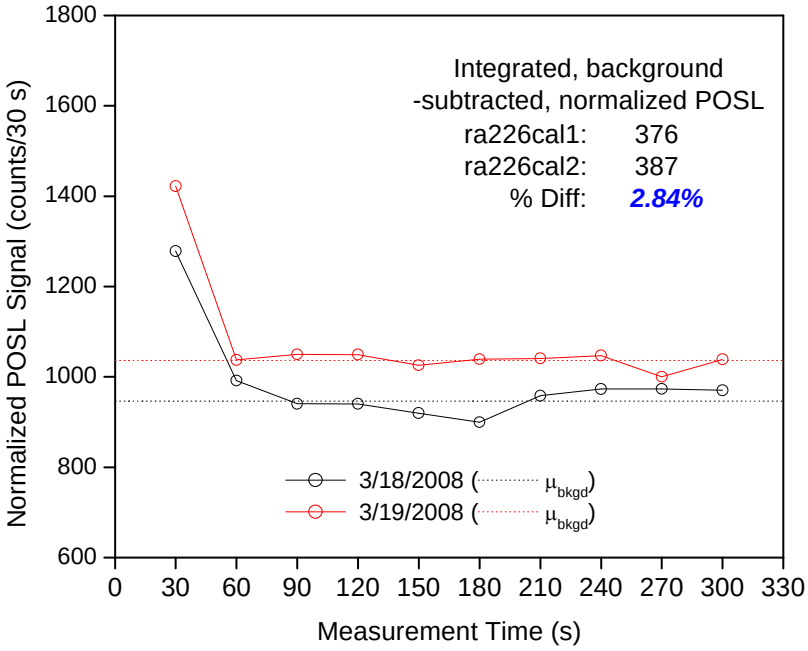


**Figure 4.11** POSL signal results from figure 4.10 after being normalized to laser power tracking signal.

the signal from the photodiode that tracks the laser power alongside each POSL measurement. Figure 4.11 shows that this normalization brings the percent difference between the two measurements to 2.84%.

The next step in the calibration process tested the portable system under simulated environmental conditions in the LNST laboratory using two sets of eight epoxy blocks manufactured as surface monitor check sources at the Kerr-McGee (KM) Technical Center in Cushing, Oklahoma. One set of blocks was enriched with thorium-232 to achieve an activity of 10 pCi/g, while the second set was left un-enriched for use as background blanks. Each block is 4" tall, 9" wide, and 18" deep, and weighs 18.2 kg on average. Two dosimeter probes were used. Probe 1 was placed at the center of the enriched blocks that were housed in a wooden box with two rows of four blocks. Probe 2 was used for an experimental control and was placed at the center of the blank blocks, which were stacked in 4 rows of 2 blocks. Figure 4.12 shows photographs of the two setups. The dosimeters in the probes were both single crystal $Al_2O_3$:C 'chips', 5 mm in diameter and 1 mm thick. Both probes were left accumulating dose for two periods of 24 hr and two periods of 72 hr before being removed from the blocks and connected to the portable system to be read out. Each probe placement and dosimeter read times were noted to the minute. The results of these four measurements, for each probe, are shown in figure 4.13. The data were analyzed in the same fashion as the $^{226}$Ra results. The POSL signals from probe 1 in the thorium-enriched blocks were labeled 'th232*x*' and the signals from probe 2 were labeled 'control*x*', where *x* = 'a' denotes the signal acquired after the first 24 hr dose accumulation period, 'b' for the second 24 hr period, 'c' for the first 72 hr period, and 'd' for the second 72 hr period. The percent differences between the

**Figure 4.12** Experimental setup for testing the portable system against thorium-enriched epoxy blocks. Above: Wooden box housing the $^{232}$Th-enriched blocks in two rows of four. Bottom left: View of the inside of wooden housing with probe 1 inserted between the two rows of blocks. Bottom right: Blank epoxy blocks with probe 2 inserted in the center.

repeated measurements are also show in figure 4.13, and range from 1.78% to 13.3%. In some of the signals, the background data appear to follow a decreasing trend that may be due to a systematic error in the portable system. This is especially apparent in the signals from probe 2 measured after the two 24 hr periods spent in the blank blocks (‘controla’ and ‘controlb’ in figure 4.13c). Since the decreasing trend of the POSL background may be due to laser power fluctuation, the photodiode signal was again used, as with the $^{226}$Ra data, to normalize the POSL signals in an attempt to correct for the downward trend. Figure 4.14 shows the normalized data in the same fashion as figure 4.13, and table 4.2 compares the standard deviations of the normalized background to those of the original

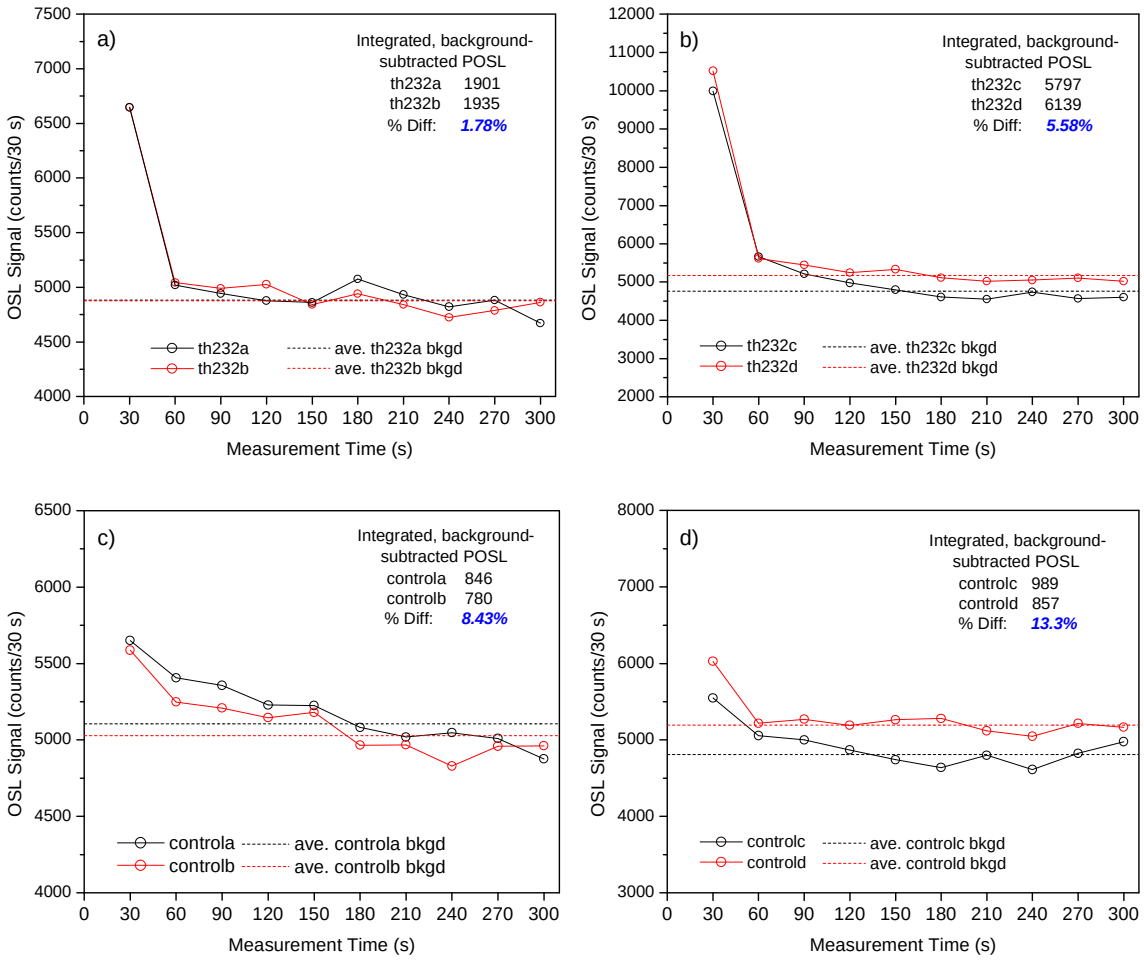


**Figure 4.13** OSL results from probe 1 after a) two 24 hr and b) two 72 hr dose periods in the $^{232}$Th-enriched blocks, and from probe 2 after c) two 24 hr and d) two 72 hr dose periods in the blank epoxy blocks. Percent differences between each two measurements are also given.

POSL background. Figure 4.14 shows that the normalization does improve the flatness of the controla and controlb data with respect to the averages of the data, and table 4.2 shows that the laser power correction improves the standard deviation of the mean of the background in every case.

Next, the dosimeters from probes 1 and 2 were used to compare the dose rates of the thorium blocks to a $^{90}$Sr/$^{90}$Y beta source from DayBreak giving a dose rate of 0.584 mGy/s. The Daybreak source was calibrated against a $^{90}$Sr/$^{90}$Y beta source integrated into a Risø TL/OSL-DA-15 reader, which was itself calibrating against a NIST $^{60}$Co gamma

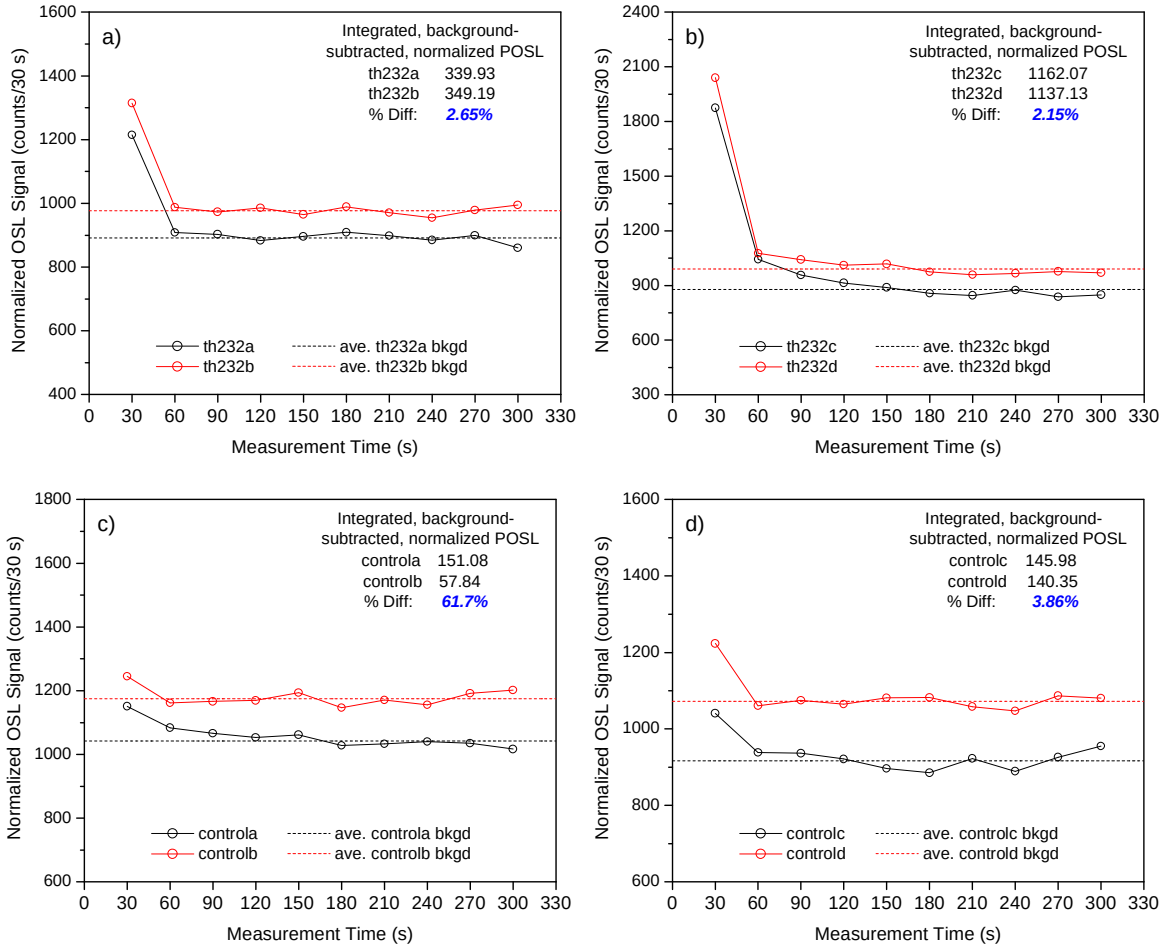


**Figure 4.14** OSL results from probes 1and 2 after normalization to the laser power tracking signal, presented in the same fashion as figure 4.12.

ray source. Doses are quoted as dose to water.

These comparison measurements were independent of the portable environmental monitoring system and were performed using a green LED-based POSL system developed by Dr. Eduardo G. Yukihara. Both probes were left in the epoxy blocks for approximately 3 weeks. After this dose period, the probes were taken out of the blocks, disassembled, and the POSL from each dosimeter was read for 600 s by the LED-based system. The bleached dosimeters were then irradiated in the Daybreak source for 10 s and read again in the LED-based system. The probes were reassembled and the process was

**Table 4.2** Comparison of deviations of the original signal backgrounds to the backgrounds after normalizing by the laser power tracking signal. The standard deviation of the mean, $\sigma_{mean,}$ is shown as a percentage of the average, $\mu$, for each case in blue italics.

| Measurement | Original Data | | | Normalized Data | | |
|---|---|---|---|---|---|---|
| | $\mu$ | $\sigma_{mean}$ | % | $\mu$ | $\sigma_{mean}$ | % |
| th232a | 4883.6 | 114.7 | ***2.35%*** | 891.8 | 15.3 | ***1.71%*** |
| th232b | 4877.3 | 102.7 | ***2.10%*** | 976.6 | 13.3 | ***1.36%*** |
| th232c | 4758.4 | 232.7 | ***4.89%*** | 878.2 | 40.7 | ***4.63%*** |
| th232d | 5168.1 | 157.9 | ***3.06%*** | 990.0 | 18.7 | ***0.63%*** |
| controla | 5105.5 | 153.9 | ***3.01%*** | 1041.9 | 17.2 | ***1.65%*** |
| controlb | 5027.4 | 134.1 | ***2.67%*** | 1174.6 | 19.5 | ***1.66%*** |
| controlc | 4807.9 | 141.8 | ***2.95%*** | 916.6 | 24.4 | ***2.66%*** |
| controld | 5194.4 | 81.3 | ***1.56%*** | 1072.1 | 13.9 | ***1.30%*** |

**Table 4.3** Normalized POSL data compared to $3\sigma$, or the signal corresponding to the minimum detectable dose. All but one of the measurements are greater than $3\sigma$.

| Measurement | Normalized POSL integral | $3\sigma$ | Above MDD? |
|---|---|---|---|
| th232a | 339.93 | 45.85 | Yes |
| th232b | 349.19 | 39.87 | Yes |
| th232c | 1162.07 | 121.95 | Yes |
| th232d | 1137.13 | 89.74 | Yes |
| controla | 151.08 | 51.61 | Yes |
| controlb | 57.84 | 58.50 | No |
| controlc | 145.98 | 73.28 | Yes |
| controld | 140.35 | 41.73 | Yes |

repeated after a nearly 10 week dose period in the epoxy blocks.

This comparison shows that the $^{232}$Th-enriched blocks gave a dose rate of $1.044\times10^{-7}$ mGy/s (± 4.14%) and the blank blocks gave $1.223\times10^{-8}$ mGy/s (± 4.92%). Using these dose rates, the calculated dose received by the $Al_2O_3$:C crystal in probe 1 over 24 hours was 7.995 ± 0.060 µGy, and 23.900 ± 0.022 µGy over 72 hours. For probe 2, the dose given by the blank blocks was found to be 1.065 ± 0.001 µGy over 24 hours and 3.185 ± 0.002 µGy for 72 hours. The response of the portable system in terms of PMT signal versus dose was calculated using the data from probe 1 to be 45.6 ± 1.5 counts/µGy. Finally, table 4.3 shows a comparison between the normalized POSL integrals and the calculated signals corresponding to the minimum detectable doses (MDDs), defined as $3\sigma$ (see section 4.1.3). All of the epoxy block measurements produced POSL results well above than that needed for the MDD, with the exception of 'controlb', which resulted in a signal equal to 98.9% of the MDD signal. Because the doses given to probe 2 during the two 24 hr periods in the blank blocks were just over 1 µGy, and since 'controla' exceeded the MDD signal calculation at this dose (with 'controlb' nearly matching the MDD signal), the MDD of the portable environmental monitoring system is conservatively estimated at 3 µGy.

### *4.2.3 Calibration Testing II: Dose Calculations*

In order to further validate the calibration of the portable system, two simple computer models were developed to calculate the dose deposited in the $Al_2O_3$:C by $^{232}$Th and $^{226}$Ra using the Monte-Carlo method and incorporating the geometries of the epoxy blocks and the radium source vial. The code was developed using National Instruments

LabVIEW 8.5, and is given with all relevant parameters in Appendix B. The first function of the models is to pseudo-randomly generate two points; one within the radiation source and the other in the volume of the single crystal dosimeter. These two points are then used to define a line along which the gamma rays emitted by the radiation source travel. Beta and other particles are ignored, as they are assumed to be totally attenuated by the stainless steel tubing of the detector probe. Path lengths through the source material (and container, for the case of the radium vial), the steel tubing, the Teflon holder, and the dosimeter are calculated according to a geometry defined to closely match the experimental setups described in the previous section. Along all paths except for that of the dosimeter, the linear attenuation of photons was calculated using

$$I = I_0 e^{-\mu t}. \tag{4.1}$$

where $I$ is the final photon intensity, $I_0$ is the initial photon intensity, $\mu$ is the material-specific mass attenuation coefficient for a single photon energy, and $t$ is the thickness, or path length, of material through which the photon is passing (Johns and Cunningham, 1983). The initial photon intensity used for the source material is $I_0 = 1$. The final intensity calculated to survive the source material is used as the initial intensity for the linear photon attenuation calculation through the next material, and so on until the final intensity of the Teflon is used as the photon intensity $I$ for the calculation of energy absorption in the $Al_2O_3$:C, given as

$$E = I\ h\nu\ \mu_{abs}\ \Delta x.. \tag{4.2}$$

Here, $E$ is the energy absorbed, $h\nu$ is the photon energy, $\mu_{abs}$ is the mass-energy absorption coefficient at energy $h\nu$, and $\Delta x$ is the path length through the dosimeter. These calculations are made for each different path length and for each energy of photon

that is emitted via the $^{232}$Th, $^{226}$Ra, or any of their respective daughter nuclides. Figure 4.15 depicts the decay series of both $^{232}$Th and $^{226}$Ra. The total number of energies emitted from $^{226}$Ra and its daughter products is 85, while for $^{232}$Th the number is 137. Mass attenuation and mass-energy absorption coefficients were obtained using a power ($y = Ax^b$) interpolation of coefficients provided by NIST[2].

All but one of the materials used in these experiments have well-known physical characteristics. For example, the stainless steel used for the detector probe is of the typical 304 variety, and so the fractions by weight of iron (72.5%), chromium (18%), nickel (8%), manganese (1%), and silicon (0.5%) can be found in references such as the Chemical Rubber Company Handbook of Chemistry and Physics (CRC Press, 1987). This information is necessary to calculate the proper mass attenuation coefficients for the model calculations. However, the composition of the thorium-enriched epoxy blocks is unknown from a chemical standpoint. The epoxy blocks were made in 1998 at the KM Technical Center using a proprietary silica-filled epoxy from the Ciba company (Lucas, 2008), which no longer makes the epoxy. Due to the lack of specific information concerning the true chemical composition of the blocks, the properties were estimated using a generic epoxy molecule, along with the $SiO_2$ structure of silica to simulate silica-filled epoxy. The epoxy molecule consists of *n* groups of bisphenol-A, having a chemical structure of $C_{15}H_{16}O_2$, and is terminated on each end by $C_3H_5O$ epoxide. The value of *n* can range from 1 to 25, and with $n$ = 10, the fractions by weight of the constituent

[2] Mass attenuation and energy absorption coefficients can be found for Teflon, borosilicate glass, and water at http://physics.nist.gov/PhysRefData/XrayMassCoef/cover.html, while all other coefficients can be found by entering the compound or mixture constituents in the XCOM Photon Cross Sections Database at http://physics.nist.gov/PhysRefData/Xcom/Text/XCOM.html

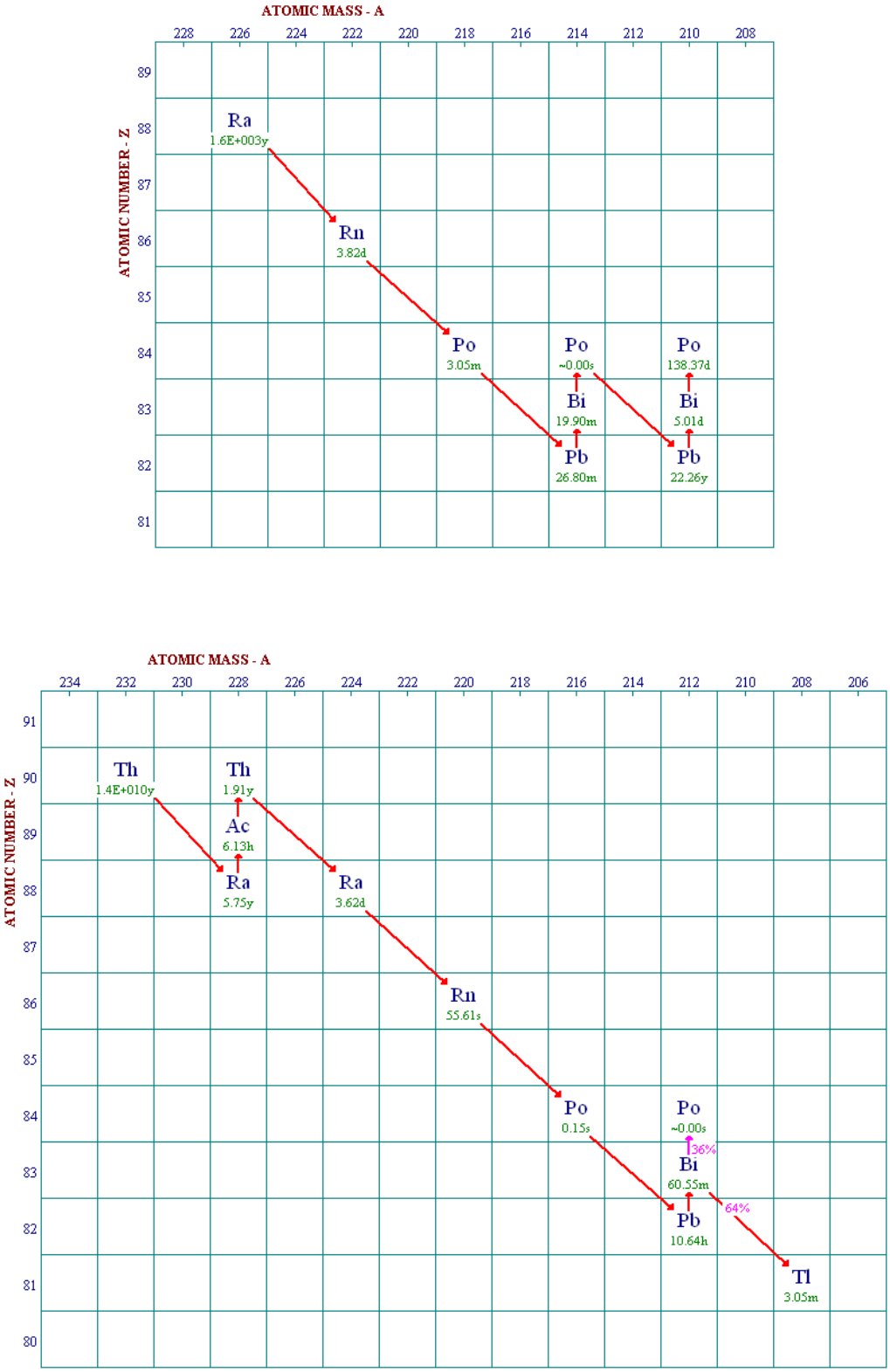


**Figure 4.15** Decay series for $^{226}$Ra (above) and $^{232}$Th (below). From DECAY.exe, version 2, written in 1997 by Charles Hacker, Griffith University, Gold Coast, Australia.

elements are found to be 75.9% carbon, 7.1% hydrogen, and 17% oxygen. The ratio of silica to epoxy is unknown, so the mass attenuation coefficients were calculated assuming a 50/50 mix. The values of these estimated mass attenuation coefficients can be found in Appendix B, preceding the computer model code.

Fortunately, the materials involved in the $^{226}$Ra experiments (dilute HCl source solution, glass vial, steel probe, Teflon holder, and $Al_2O_3$:C dosimeter) are all relatively well-known. Photon attenuation in air was found to be negligible, and was ignored. Also, since the dose calculations are in the end going to be compared to the cross-calibration data of the $^{232}$Th blocks to an effective $^{60}$Co source gamma dose to water, the mass-energy absorption coefficients for water are used in the energy absorption calculation of equation 4.2, instead of those for $Al_2O_3$.

An example of a model-generated photon path between pseudo-randomly chosen dosimeter and source points is shown in figure 4.16, and follows the geometry of the thorium-enriched epoxy block experiment. The coordinate axes are chosen such that the x-axis lies in the horizontal direction along the width of the blocks, the y-axis lies horizontal along the depth of the blocks, and the z axis is directed vertically along the height of the blocks. In this coordinate system, the circular faces of the dosimeter lie parallel to the x-z plane, which is shown in figure 4.16, and the dosimeter is centered on the origin. The points chosen by the random number generator are depicted as hollow circles, one within the circular bounds of the dosimeter, and one in the space occupied by epoxy block material (*A* and *B*, respectively). The angle that the line *AB* makes with the x direction is labeled $\theta_1$, and the angle formed between the x axis and the line *a* that connects point *A* to the origin is labeled $\theta_2$. The angle $\gamma$ is equal to the difference of $\theta_1$ and

$\theta_2$. Using $a$ and γ, the line $d$ can now be determined using $d = a\sin(\gamma)$. The Pythagorean theorem is then be used to find $s$ (and $q_1$ as well, by using $d$ and the radius of the dosimeter, $r1$, instead of $a$). The photon's entrance and exit points to the dosimeter (hollow square points, labeled $E_1$ and $E_2$, respectively) can be found by adding or subtracting the x and z components of $s$ and $q_1$ to the coordinates of point $A$ using

$$E_{1,x} = A_x + s_x + q_{1,x}\ , \qquad E_{1,z} = A_z + s_z + q_{1,z} \tag{4.3}$$

and

$$E_{2,x} = A_x - q_{1,x} + s_x\ , \qquad E_{2,z} = A_z - q_{1,z} + s_z. \tag{4.4}$$

The y coordinates for the entrance and exit points of the dosimeter are calculated by using the parametric vector equation for a line in 3-dimensional space:

$$\begin{pmatrix} x \\ y \\ z \end{pmatrix} = \begin{pmatrix} x_2 \\ y_2 \\ z_2 \end{pmatrix} + \begin{pmatrix} x_2 - x_1 \\ y_2 - y_1 \\ z_2 - z_1 \end{pmatrix} p. \tag{4.5}$$

The path lengths through steel and Teflon are found by another application of the Pythagorean theorem using $d$ and the known inner and outer radii of each structure. For example, in figure 4.16 the path length through the Teflon sample holder (in the x-z plane) is equal to the difference of $q_2$ and $q_1$, which are found by using the inner diameter ($r_1$, which is equal to the diameter of the dosimeter) and the outer diameter of the Teflon holder, $r_2$. The total path length through the Teflon is extended into the y dimension by using the relation

$$path\bullet\ length\bullet = \frac{\sqrt{(B_x - A_x)^2 + (B_y - A_y)^2 + (B_z - A_z)^2}}{\sqrt{(B_x - A_x)^2 + (B_z - A_z)^2}} \cdot (q_2 - q_1)\ . \tag{4.6}$$

This same relation is used for finding the total path length through the steel tubing. In the case of the radium vial, the same methods used to determine the entrance and exit points

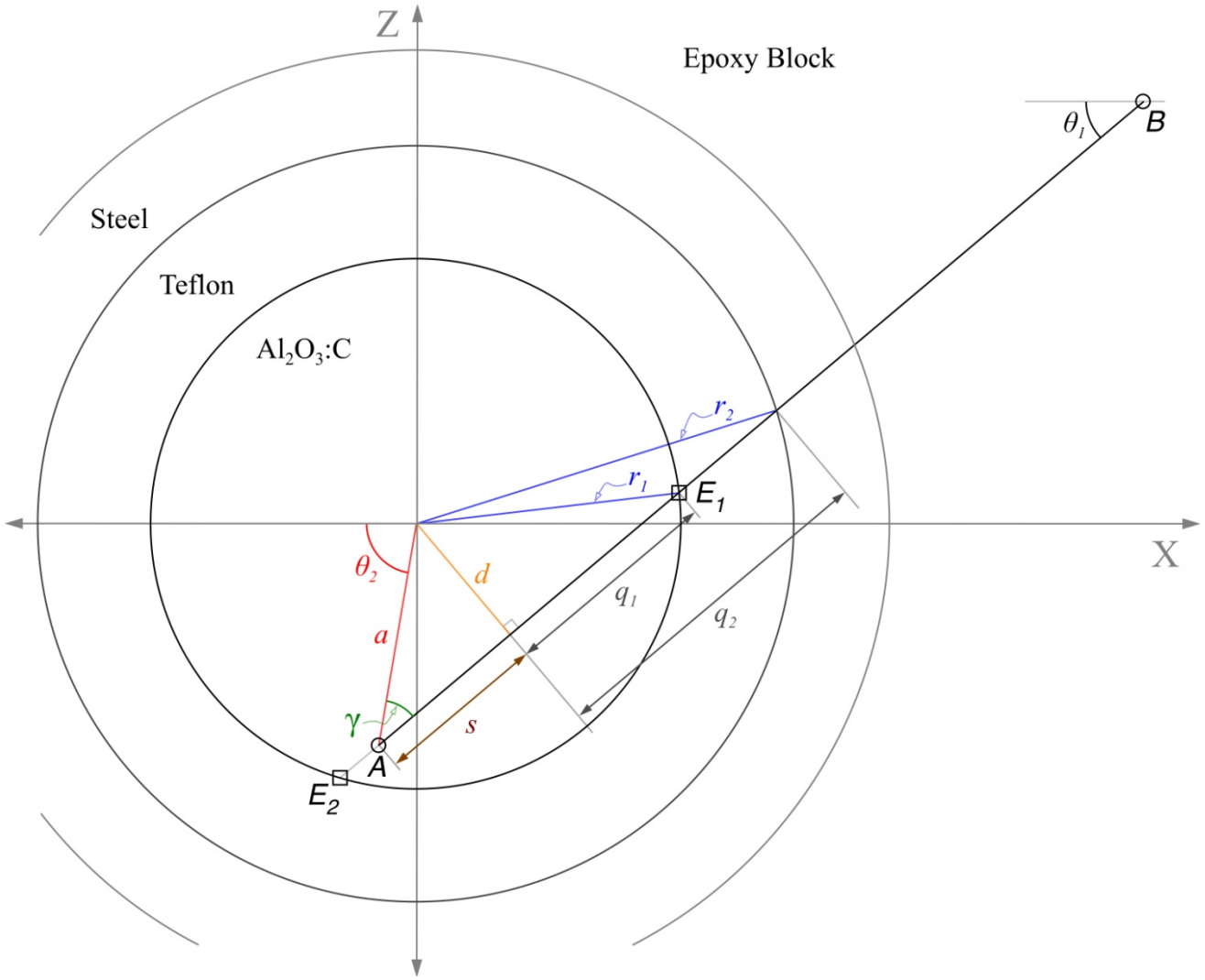


**Figure 4.16** Diagram depicting the line formed by two pseudo-randomly chosen points (*A* and *B*, hollow circles) in the x-z plane, as well as the angles and lines used for calculating a photons paths through steel and Teflon, and the entrance and exit points of the photon on the dosimeter ($E_1$ and $E_2$, hollow squares).

on the dosimeter in the x-z plane are used to find the photon's exit point from the vial, and the attenuation through the glass wall of the vial is found by using a path length calculation similar to that of 4.6. However, the x-y plane is used for these calculations, as the radium vial is an upright cylinder.

So far, the model assumes that every emission by the source will pass through the dosimeter. This is clearly not the case for either of the calibration experiments, as the photons are emitted in random directions and only seldom hit the relatively small $Al_2O_3$:C dosimeter. Thus, the efficiency of the dosimeter, i.e. the ratio of photon emissions that hit the dosimeter to the total number of emissions, is calculated in this model by dividing the area of the profile of the dosimeter (as seen from the point of emission) by the surface area of a sphere with a radius equal to the distance separating the point of emission and the dosimeter. Figures 4.17 and 4.18 detail how the model finds the area of the dosimeters profile by using orthographic projections of the dosimeter. Since the dosimeter is rotationally symmetric in the x-z plane, the profile of the dosimeter will look exactly the same from all emission points that share a given y coordinate and have x and z coordinates such that the distance from the origin $r = \sqrt{x^2 + z^2}$ is constant. Therefore, the calculation of the area of the dosimeter's profile may be simplified by defining a new plane - the xz-y plane of figure 4.17 – and by taking advantage of the symmetry of the crystal centered at the origin. For the thorium block geometry, emission points may be generated in any of the three regions (I-III) shown in figure 4.17. The coordinates of the emission point are transformed to the absolute value in the y dimension, and to $'xz' = \sqrt{x^2 + z^2}$ in the xz dimension. Note that the label 'xz', as used here and from now on, refers not to the product of x and z, but to a coordinate. In region

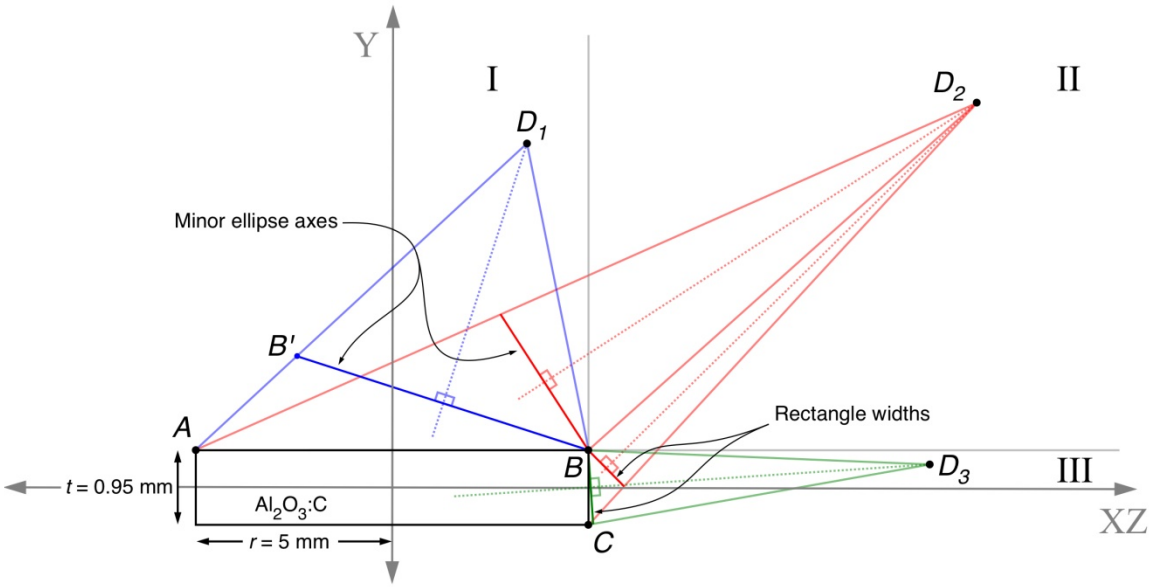


**Figure 4.17** Diagram depicting the xz-y plane transformation, with lines detailing the isosceles triangles used for calculating the area of the dosimeter's profile for calculating the probability that a photon emitted at a point $D_i$ would strike the dosimeter.

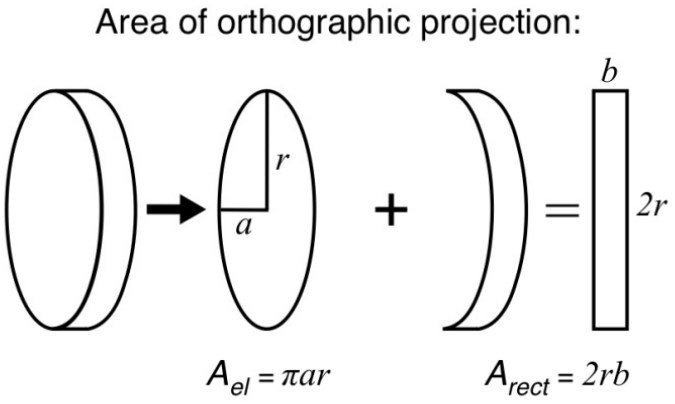


**Figure 4.18** Deconstruction of the area of an orthographic projection of a cylinder similar to the shape of an $Al_2O_3$:C dosimeter. The sum of the area of the ellipse ($A_{el}$) and the area of the skewed rectangle would be used to calculate the efficiency of the dosimeter if an emission were to occur at point $D_2$ in figure 4.16.

I, an emission from point $D_1$ will 'see' only an elliptical profile of the circular face of the dosimeter. Therefore, the cross-sectional area of the dosimeter, as seen from the $D_1$, is the area of an ellipse with a major axis equal to the diameter of the dosimeter and a minor axis equal to the base of the blue isosceles triangle ($BB'$) with side length $BD_1$. This minor axis is found by calculating the angle $\theta = AD_1B$ and by using the law of cosines for the case of an isosceles triangle,

$$BB' = \sqrt{2(BD_1)^2(1-\cos\theta)}\,. \tag{4.7}$$

The efficiency of the dosimeter for an emission from $D_1$ is then taken by using the area of an ellipse ($A_{el}$, from figure 4.18) as

$$\text{efficiency} = \frac{A_{el}}{A_{sph.surf}} = \frac{\pi ar}{4\pi r_{sph.}{}^2} = \frac{rBB'}{8BD_1{}^2}\,, \tag{4.8}$$

where $A_{sph.surf}$ is the surface area of a sphere of radius $r_{sph} = BD_1$, and $a = BB'/2$ is half the minor axis of the ellipse. For region III of figure 4.17, an emission from point $D_3$ is confronted only by the rectangular edge profile of the dosimeter. In this case, as in the case of region I, the cross-sectional area of the dosimeter's profile is dependent on finding the base length of an isosceles triangle. This length is calculated in the same fashion as in region I, but the area to be used in the numerator of equation 4.8 is now that of a rectangle with a length equal to the diameter of the dosimeter, and width equal to the base of the green isosceles triangle of figure 4.17. The majority of emissions take place in region II, and here both the elliptical and rectangular profiles of the dosimeter are in the line of sight of the emission point $D_2$. Thus, the efficiency calculation for an emission in this region uses the area-finding schemes of both regions I and III. Figure 4.18 shows the profile of the dosimeter as it would appear from an emission point similar to $D_2$. The area of the ellipse is added to that of the skewed rectangle (which is easily shown to equal the

area of a right rectangle of the same length and width), and this sum is used as the numerator in equation 4.8.

The model was built to iteratively calculate the photon attenuation and energy absorption of all emitted energies along five million randomly generated paths. The calculated energy absorbed (in MeV) by the dosimeter was multiplied by the calculated efficiency for each path, and the summation of all five million products of absorbed energy and efficiency was then divided by the number of iterations. The end result provided an average energy absorbed by the dosimeter per decay event. The five million iteration calculation was then repeated for a total of twenty times, so that an estimate of deviation about a mean could be determined.

The model corresponding to the materials and geometry of the $^{232}$Th measurements calculated an average absorbed energy of $1.385\times10^{-7}$ MeV per decay. The total activity of the blocks is found - using the activity concentration of the 10 pCi/g, the total mass of the blocks and a curie to becquerel conversion - to be 53909 Bq. The dose rate is calculated by converting MeV to joules and dividing by the mass of water that would fill the volume of the dosimeter (0.0177 g), and is equal to $6.759\times10^{-11}$ Gy/s. The mass of water is used instead of $Al_2O_3$ because of the quoted $^{60}$Co dose to water from the NIST calibration of the $^{90}$Sr/$^{90}$Y source used to estimate the dose rates of the epoxy blocks. The average dose period for the th232a and th232b measurements is 86790 s, so the model estimates that the dosimeter in probe 1 received a dose of 5.87 μGy, which is 73.4% of the 7.995 μGy dose found from the calibration measurements of section 4.2.2.

No measurements were made to verify the dose given to the dosimeter under $^{226}$Ra irradiation, as in the case of the $^{232}$Th measurements. However, a comparison of

measured POSL signal to the absorbed energy calculations of the $^{226}$Ra-specific model may be made by dividing the POSL results from the radium measurements by the 45.6 counts/μGy system response determined by the thorium-enriched block data analysis. This results in an absorbed dose of 8.367 μGy. The model corresponding to the experimental setup using the $^{226}$Ra source vial returned an absorbed energy of $7.092\times10^{-7}$ MeV per radium decay. Applying the same conversions as for the thorium calculation above gives an absorbed dose of 7.766 μGy, or 92.8% of the dose reported by actual measurements.

The energy absorption models seem to work well, especially in the case of $^{226}$Ra. This is not surprising, as both the geometry and the materials making up the experimental setup for the radium measurements are well known. The 26.6% difference seen in the thorium calculations are most likely due to incorrect values of the mass attenuation coefficients for the epoxy blocks. The average distances that the photons travel through the blocks is very large compared to the distances through all the other materials involved. Thus, the energy absorption calculations based on this geometry are very sensitive to the block material composition.

# CHAPTER V

# REMOTE NEAR-REAL-TIME MEDICAL DOSIMETRY SYSTEM BASED ON OSL FROM KBr:Eu

Ionizing radiation has become one of the most useful and effective tools available to the medical community. Radiologists use it for patient imaging so that correct diagnoses may be made quickly with little to no harm to the patient, as well as to image patients during surgical procedures that would normally be highly invasive, so that the only incisions needed are those by which small surgical tools may enter. This greatly reduces both recovery time and the likelihood of infection to the patient. Ionizing radiation is also used to supplant the surgical scalpels, lancets, and scissors themselves for non-reparative procedures such as cancer removal.

While ionizing radiation provides significant advantages to modern medicine, it is not without its drawbacks. Incorrect usage can endanger not only the patient, but the physicians and other medical personnel assisting the procedure. There is generally a narrow range in which the application of radiation gives the desired diagnostic or therapeutic result, and poses the least danger to the people involved. This is particularly true for radiation therapy. If too little radiation is delivered, radiotherapies may result in only partial remissions, increasing the chance for relapses and further expensive treatments. Conversely, if too much radiation is given, therapy procedures can disrupt or

kill normal, healthy tissues along with the cancerous tissue. Radiation therapy procedures are designed to give doses in multiple fractions instead of all at once. The multiple fractions (as many as 40 - 50) deliver large doses over short periods of time, and from many different directions, so that the sum of the fractions gives a high uniform dose to the target volume while minimizing the dose to surrounding tissues. In this context a 'figure of merit' for radiotherapy may be defined as

$$\text{figure of merit} = \frac{\text{energy imparted to the target volume}}{\text{total energy imparted to patient}}$$

where the best treatment plan would be the one that gives figure of merit closest to unity (Johns and Cunningham, 1983).

Fortunately, radiodiagnostic and radiation therapy technologies are constantly under development to produce better and better results, while keeping in consideration the reduction of danger to patients and doctors. One of the more important consequences of this rapid technology development is that modern medical systems can now produce dynamic radiation fields having very complex geometries with large dose gradients over small areas or volumes. Clearly, the nature of these fields make it difficult to obtain real and accurate dose verification using existing medical dosimetry technologies such as thermoluminescent dosimeters and ionization chambers.

One example of an increasingly complex radiation field is that of a modern computed tomography (CT) scanner. These machines produce x-ray beams that rotate and translate, are output in fans and cones, and may modulate x-ray intensities during patient scans. However, the volume CT dose index (CTDI) continues to the most important radiation dose descriptor (McCollough, 2008). CTDI is measured using a 100 mm pencil-type ionization chamber (IC) that integrates the dose profile of a single axial

CT scans with a thickness much less than that of the IC. Axial scanning is approaching obsolescence in favor of helical and multi-slice scanning, and so new methods for obtaining CTDI in modern heterogeneous scanning beams may soon be necessary.

Appropriate characterization and monitoring of these fields calls for a dosimeter to be small, so that it is able to spatially resolve the dose profile; to be active, so that changes of the field over time can be distinguished in real time; and to be inconspicuous, so that an optimized radiation field need not lose effectiveness or be modified due to the presence of the dosimeter.

In the current work, a near-real-time, remote dosimetry system based on the OSL from a small single crystal KBr:Eu dosimeter has been tested under interventional and diagnostic fluoroscopy fields, axial and helical computed tomography (CT) scanning fields, high dose rate (HDR) brachytherapy fields, and 232 MeV proton therapy beams. The results of these tests and comparisons to conventional ionization chamber readings are given in the following sections.

## 5.1 KBr:Eu System Description

The medical dosimetry system used in this work is the same as that developed by Gaza and McKeever (2006), and is similar in design to that of the α-$Al_2O_3$:C dosimetry system discussed in chapter 4. Figure 5.1 shows a drawing of the various components of the KBr:Eu system. Red laser light (λ = 658 nm) emitted from a PPMT-LD1360 diode laser (Power Technology Inc.) is reflected by a mirror through an Edmund Industrial Optics NT52-543 dichroic mirror, so that it passes into the proximal end of 10 m long, 1

mm diameter plastic Mitsubishi ESKA fiber optic cable via a fixed connection (FC) fiber coupler. The red light stimulates a KBr:Eu single crystal which is placed inside a black plastic casing and mechanically coupled to the distal end of the fiber cable. OSL produced by the KBr:Eu passes back through the fiber cable and reflects off of the dichroic mirror into the PMT of an Electron Tubes, Inc. P25PC photon detection package. A set of Kopp 5-58 filters (glass #5113, transmission window centered at 410 nm) precedes the P25PC, for discriminating background light.

The stimulation power at the KBr:Eu crystal is ~20 mW, which is enough to fully deplete the OSL in tens of milliseconds. An OSL signal decay measured using the KBr:Eu system is shown in figure 5.2. In most cases, a stimulation period of 20 ms is sufficient to bleach the crystal to background. Thus, the normal operating procedure for the KBr:Eu system consists of an 80 ms dose period, in which the diode laser

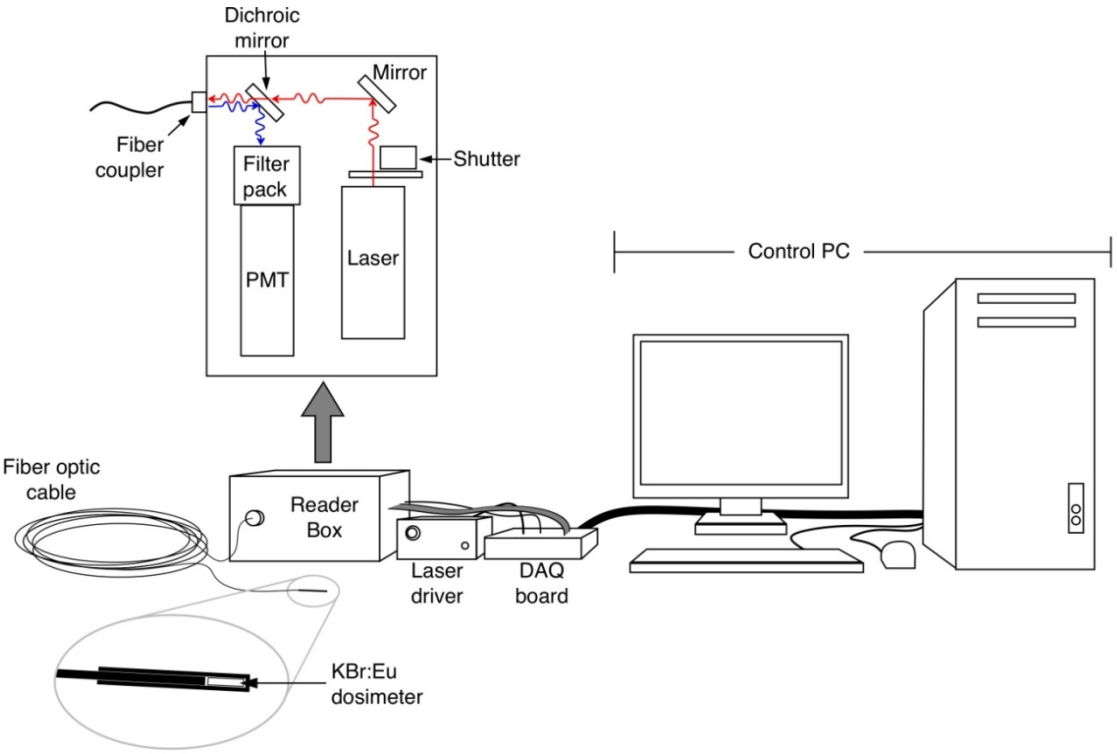


**Figure 5.1** Drawing of remote medical dosimetry system based on KBr:Eu. Detail of both the internal construction of the reader box and the distal end of the fiber with dosimeter attached.

is turned off, followed by a 20 ms stimulation period. This 100 ms measurement is performed repeatedly, one after another, so that full OSL signals may be obtained at a rate of 10 Hz. The OSL decay is resolved by summing the number of PMT counts that have accumulated over periods ranging from 100 to 500 µs, so that the decay consists of 40-200 data points.

The KBr:Eu dosimeter used in this work was cleaved from a bulk crystal grown using the crystal which had a concentration of $Eu^{2+}$ of ~1700 ppm. The crystal is approximately 1×1×2 mm in dimension, and this allows for a low profile so that interference with medicalradiation fields is reduced and for high spatial resolution of fields that contain high dose gradients.

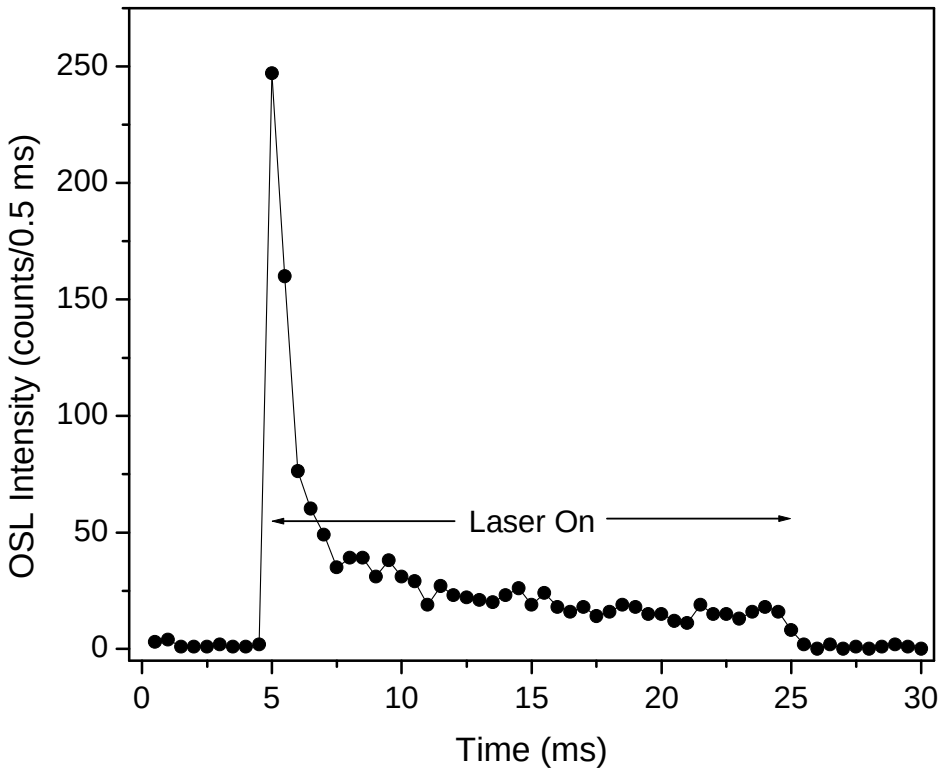


**Figure 5.2** Example of an OSL signal decay taken using the KBr:Eu system. PMT signal was recorded for 5 ms before and after the laser was on.

## 5.2 Performance under X-Rays I: Fluoroscopy

### *5.2.1 Continuous Fluoroscopy*

The KBr:Eu system was first tested at the Oklahoma University Health Sciences Center (OUHSC) under an Advantx system from General Electric (GE), which delivered x-rays continuously. The KBr:Eu dosimeter was positioned in air, level to a thimble ionization chamber (IC) in the horizontal plane. The two detectors were placed so that they shared the center of the fluoroscopic field and were elevated ~10 cm above the patient table for reduction of x-ray scatter.

One characteristic of a good dosimeter is an independence of its performance on the energy of the radiation that it is measuring. It is favorable to have a dosimeter that reports the same value whether a certain dose was given with 50 keV x-rays or 2 MeV gamma rays. The energy dependence of the KBr:Eu dosimeter was examined by exposing the dosimeter to x-ray energies ranging from 60-120 kVp (peak kilovolts) in 10 kV increments for 2 minutes at each step. The OSL was measured over 20 ms at 10 Hz (allowing 80 ms dose periods), with a resolution of 100 µs per data point. At the same time, exposures to the thimble IC were recorded in R/min so that the OSL data could be corrected for variations in exposure levels. The initial intensity[3] of each OSL signal was taken as the representative dose-proportional value resulting from the previous dose accumulation period. The x-ray tube current was altered at each kVp level so that an exposure of ~2.5 R/min was maintained over the entire experiment. Table 1 shows the corresponding values of tube current and exposure read from the thimble IC at each kVp.

[3] As opposed to the total integrals, which showed sensitization effects. These effects will be examined and discussed further in section 5.7 of this work.

**Table 5.1** Values of peak voltages and tube currents applied to the GE Advantx fluoroscopic system, as well as the exposure registered by a thimble IC during an energy dependence experiment.

| Energy (kVp) | Tube Current (mA) | Exposure to IC (R/min) |
|---|---|---|
| 60 | 10.3 | 2.51 |
| 70 | 6.8 | 2.52 |
| 80 | 4.8 | 2.46 |
| 90 | 3.8 | 2.61 |
| 100 | 2.9 | 2.47 |
| 110 | 2.3 | 2.48 |
| 120 | 2.0 | 2.48 |

The average values of the initial intensity measurements were normalized by the reported IC exposure values, and the results are shown in figure 5.3. It is clear from the data that the KBr:Eu dosimeter possesses an energy dependence. However, it is important to note here certain known characteristics of both KBr crystals and x-ray tubes. An important factor in a materials ability to absorb energy (i.e., dose) is the mass-energy absorption coefficient $\mu_{ab}$ of that material for a particular energy. $\mu_{ab}$ depends on several factors including the fluence of incoming photon energy as well as the multiple scattering interactions between the photons and electrons and nuclei of the material. The $\mu_{ab}$ values for KBr can be found by calculating the weighted sum of the coefficients for K and Br, and are plotted in figure 5.4. The Eu dopant of the dosimeter material is in such low concentration that it does not contribute significantly to the overall $\mu_{ab}$ spectrum. Also, x-ray tubes do not produce monoenergetic x-rays, but x-rays over a broad spectrum of energies. The listed kVp used for each measurement represent the highest energy of the x-rays, but the amount of x-rays with this energy is small. Figure 5.5 shows the spectral distribution of x-ray energies emitted from a tungsten target. Each curve represents the

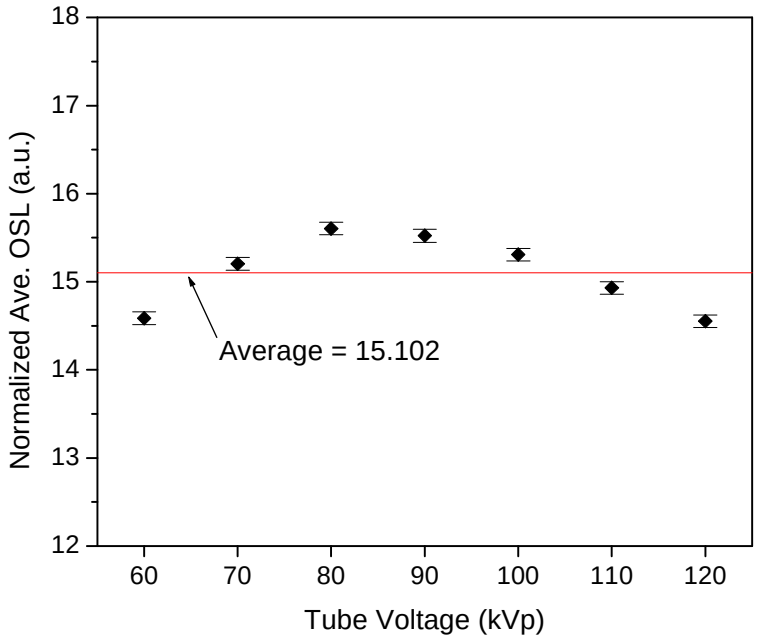


**Figure 5.3** Averaged OSL responses to various x-ray energies, normalized to IC exposure readings that all equal close to 2.5 R/min. Error bars represent the standard deviation of the mean, and are ~1 % or less in all cases. The average value for the results is plotted, and clarifies the OSL signal dependence on x-ray energy.

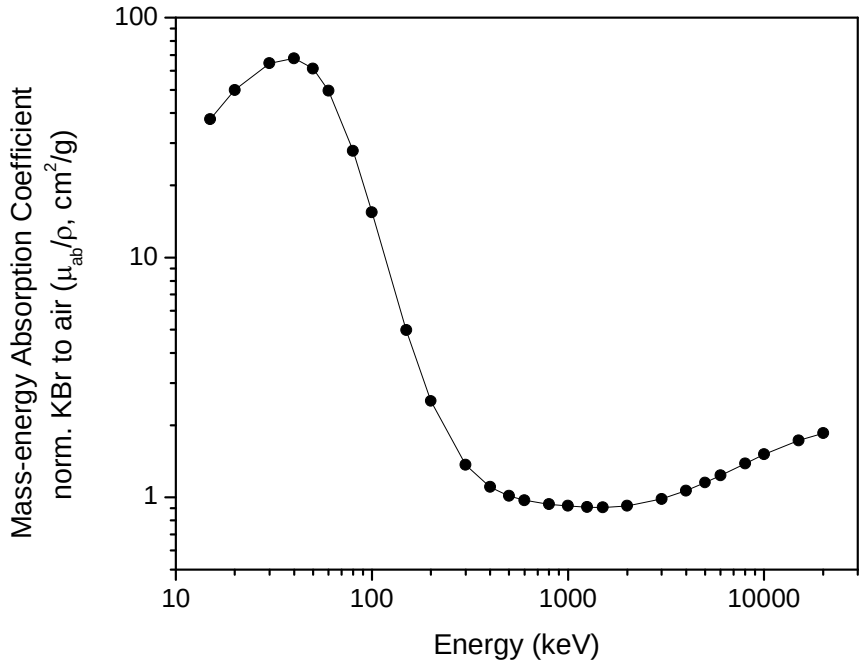


**Figure 5.4** Mass-energy absorption coefficients for KBr that have been normalized by those for air. The peak of the coefficients occurs at ~40 keV.

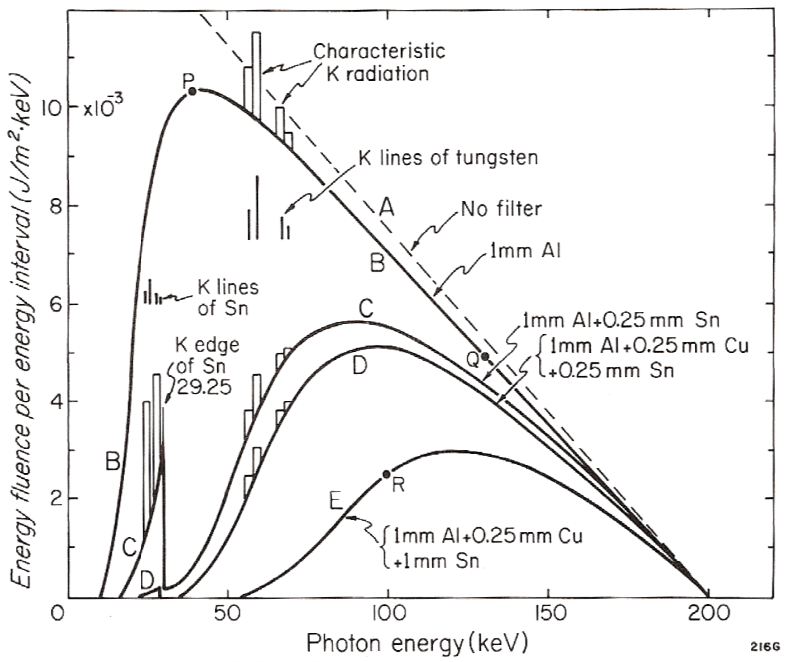


**Figure 5.5** Spectral distributions of x-rays generated by bombarding a thick tungsten target with 200 keV electrons. Dashed line A represents the unfiltered spectrum, while curves B, C, D, and E represent spectra filtered through various layers of Al, Cu, and Sn. Reproduced from Johns and Cunningham (1983).

the spectrum resulting from different attenuating materials and thicknesses placed between the target and the output. This filtration of the spectrum due to materials such as aluminum, copper, and selenium reduces the amount of low energy (soft) x-rays but permits the high energy (hard) x-rays to pass. Thus, the amount of filtration material controls the 'hardness' of the beam. Note that according to figure 5.5, the actual x-ray energy fluence peaks at a photon energy of between about one-quarter to about two-thirds of the maximum energy (which is denoted as the kVp in practice), depending on what filtration is used.

All of these factors can affect how the KBr:Eu system performs under x-ray exposure. The x-ray spectrum from the GE Advantx was not measured, and by comparing figures 5.3 and 5.4, it may be speculated that the energy fluence of the x-rays

peaks well below 80 keV, but may not necessarily match the 40 keV peak of the $\mu_{ab}$ spectrum. A particular convolution of x-ray fluence and $\mu_{ab}$ spectrum could give an OSL response similar to that of figure 5.3. Similarly, if the x-ray energy spectrum of a particular fluoroscopic system was known, a possible correction scheme to the energy dependence of the KBr:Eu system may be developed that incorporated the $\mu_{ab}$ values relevant to the output energies.

The response of the KBr:Eu system was then tested versus exposure rate by fixing the x-ray tube voltage at 80 kVp and incrementally increasing the tube current, which increased the x-ray output and thus the dose rate. The dosimeter and IC were exposed simultaneously for 30 s at a time at each tube current, and the same positional configuration was used for the KBr:Eu and IC as in the energy dependence experiment. The OSL results may be found plotted against the corresponding exposure readings in figure 5.6. Table 5.2 lists the tube currents used and the corresponding exposure rates read from the thimble IC. The table and detectors were moved closer to the x-ray source between the $8^{th}$ and $9^{th}$ measurement so that a higher dose rate could be achieved without further increasing the tube current, which was reaching a maximum safe level The table was moved even closer to the source between the $9^{th}$ and $10^{th}$ measurements for the same reason, though in this case the tube current was lowered to 6.2 mA. The response is linear over all of the tube currents used.

Angle dependence measurements were taken by placing the KBr:Eu dosimeter at the center of rotation of the GE Advantx gantry. The thimble IC was removed for these experiments. First, the dosimeter was placed such that its long axis was placed perpendicular to the rotational axis of the gantry. The KBr:Eu was then exposed to

**Table 5.2** Values of tube currents applied to the GE Advantx fluoroscopic system, as well as the exposure registered by a thimble IC during a dose response experiment.

| Tube Current (mA) | Exposure to IC (R/min) |
|---|---|
| 0.1 | 0.114 |
| 0.6 | 0.356 |
| 1.0 | 0.562 |
| 1.9 | 1.045 |
| 2.9 | 1.555 |
| 3.9 | 2.01 |
| 6.3 | 3.15 |
| 8.5 | 4.15 |
| 8.5 | 6.07 |
| 6.2 | 8.05 |

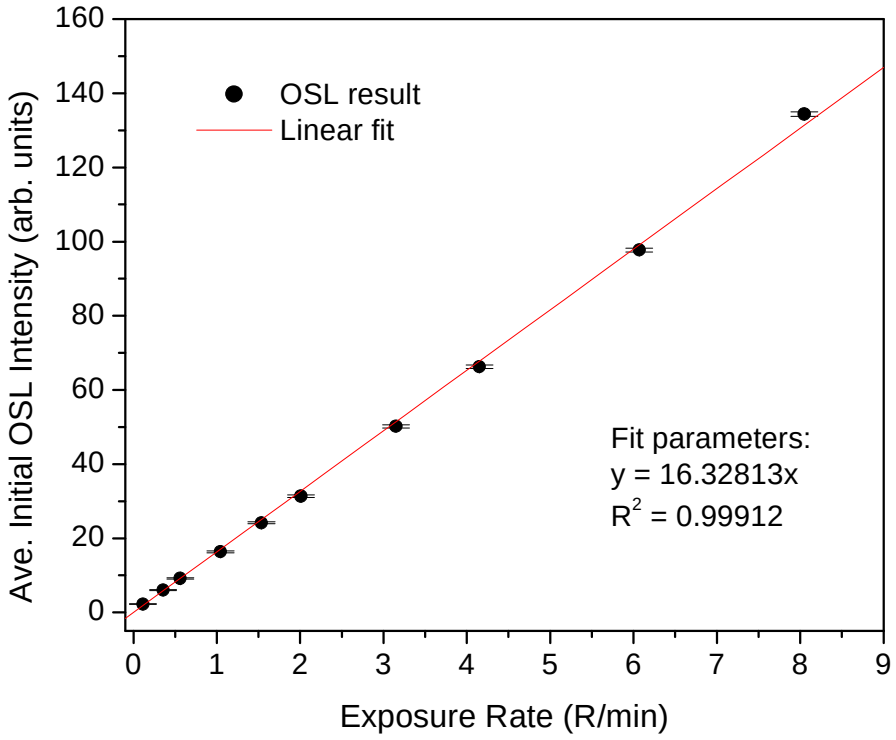


**Figure 5.6** Exposure response of the KBr:Eu system using 80 kVp x-rays from the GE Advantx fluoroscopic system. Error bars represent the standard deviation of the mean of all OSL signals taken over each 30 second exposure and equal ~1% or less for all measurements.

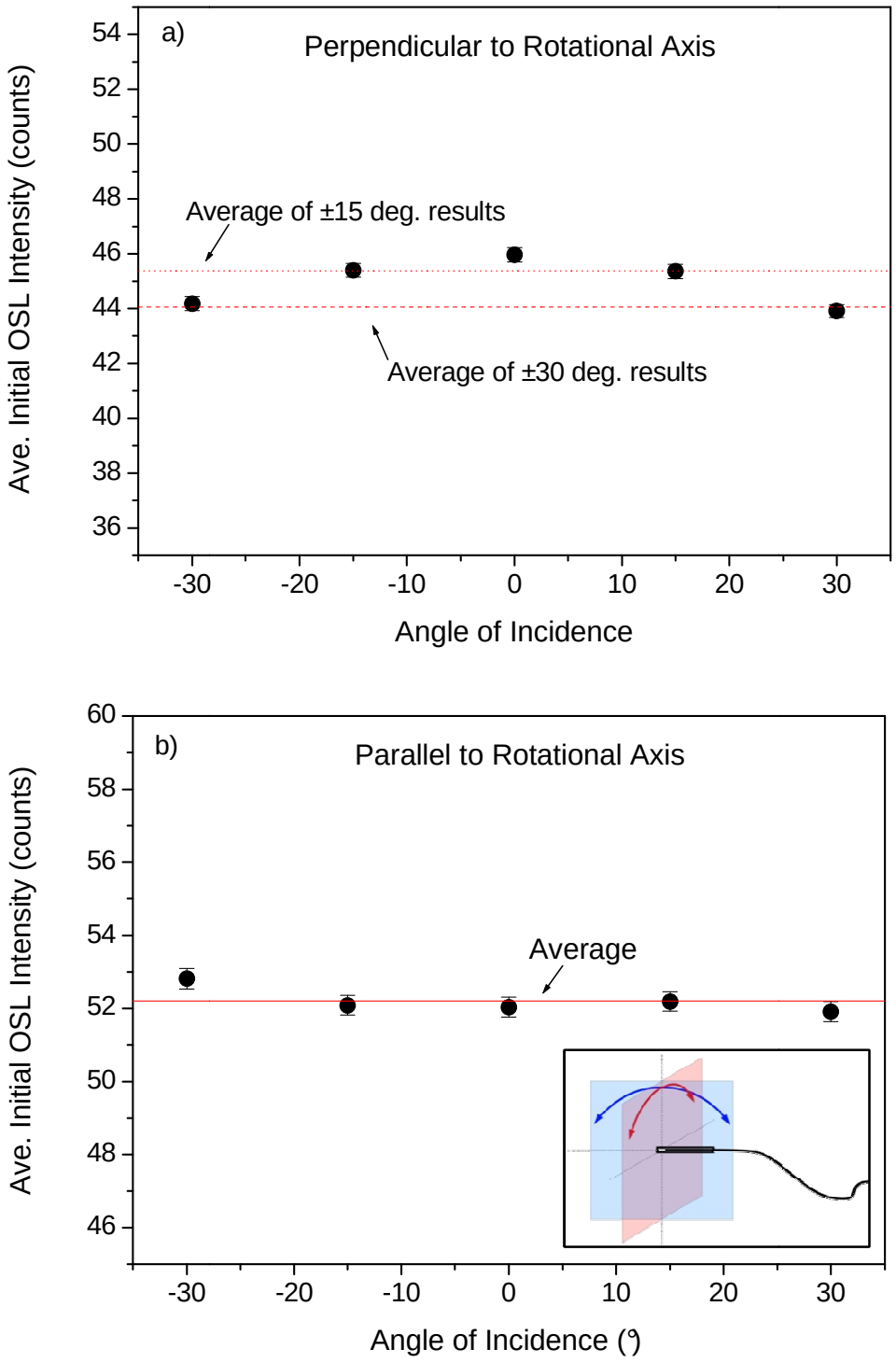


**Figure 5.7** Dependence of the KBr:Eu system response on gantry tilt angle with the dosimeter's long axis a) perpendicular and b) parallel to the rotational axis of the fluoroscopy machine gantry. Inset to b): Diagram depicting gantry tilt planes and directions relevant todata shown in a) (blue) and in b) (red). Error bars represent standard deviation of the mean for each measurement.

80 kVp x-rays at ~8.5 mA for approximately1 min. with the gantry at -30°, -15°, 0°, 15°, and 30° to vertical. Second, the KBr:Eu was repositioned so that its long axis was parallel to the axis of rotation. It was also exposed to ~1 min. of 80 kVp x-rays using tube currents of ~6 mA, and at the same gantry angle as the previous experiment. The results of these angular dependence experiments are shown in figure 5.7.

Figure 5.7a shows that an angular dependence is present when the long axis of the crystal is positioned perpendicular to the axis of rotation. As the gantry rotates away from the vertical position, the cross-section of the KBr:Eu crystal that the x-ray tubes output window 'sees' gets smaller, while the corresponding thickness of the dosimeter increases. Also, the thickness of the plastic casing that surrounds the KBr:Eu also increases from the point of view of the incoming x-rays. These changes in geometry increase the x-ray attenuation of both the dosimeter and the casing, resulting in lower OSL signals. This is supported by figure 5.7b, which shows that when the geometry stays more or less the same, as is the case when the KBr:Eu is placed parallel to the rotational axis, the x-rays are equally attenuated and so the OSL response is flat across the gantry's angle of incidence.

### *5.2.2 Pulsed Fluoroscopy*

The KBr:Eu was then tested under a Philips Bi-plane fluoroscopy system that delivered x-rays in pulses with durations of ~5-8 ms at rates of 30, 15 , and 7.5 pulse per second (PPS). A high dose rate mode of 30 PPS, known as cine fluoroscopy, was also used for some measurements. The KBr:Eu dosimeter was setup in conjunction with the same thimble IC and in a similar configuration as that used in the continuous fluoroscopy

experiments of the previous section. For each measurement, the KBr:Eu system was turned on before radiation was applied, and left to run for a few seconds after irradiation stopped so that the system's background could be measured.

During the first few measurements - intended to test the performance of the system under the pulsed x-ray machine in cine mode - a peculiar pattern was observed in the OSL signals that repeated over time. A cursory analysis of the data showed that the initial intensity of the OSL signals varied with a staggered, seemingly sinusoidal change in amplitude. Figure 5.8 shows an example of this signal behavior. The system was taking 20 ms OSL measurements at 10 Hz with an integration time per data point of 100 μs. Over the course of the ~22 s pulsed irradiation period, the initial intensity varied from a baseline value of ~675 counts to ~1000 counts, but the increase (and subsequent decrease) of the signal only occurs at every other OSL measurement.

Upon further analysis, most of the 20 ms OSL curves showed an uncharacteristic

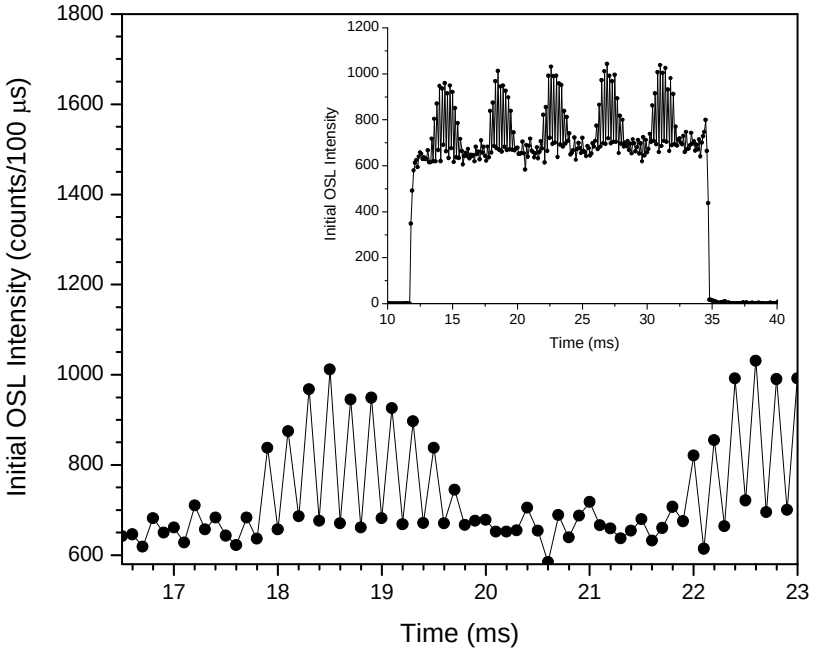


**Figure 5.8** Close-up detail of a portion of the ~220 measurement data set of initial OSL intensities from taken under fluoroscopic x-rays in 30 PPS cine mode. Inset: Initial intensities measured over the entire irradiation period.

'bump' in the signal. This OSL feature occurred at different points along the 20 ms measurement time for different OSL curves, and did not appear in any of the background measurements that were made before or after the ~22 s dose period. It was soon recognized that the periodic change in OSL intensity and the peculiar features were related, and that they were caused by the x-ray pulses and the OSL measurements not being synchronized such that the x-rays were being pulsed at varying times during the OSL measurement (see figure 5.9).

The KBr:Eu system recorded OSL signals at 10 Hz with a period $\tau$ = 100 ms, while the fluoroscopy machine was supposedly pulsing at 30 PPS (i.e. 30 Hz, $\tau$ = 33.3 ms). Since the x-ray pulses were ~5-8 ms long, the KBr:Eu system had a window of only ~25 ms in which it could ideal timing scheme for measuring 30 PPS x-rays using the KBr:Eu system at 10 Hz. Here, each OSL measurement would produce an initial OSL intensity

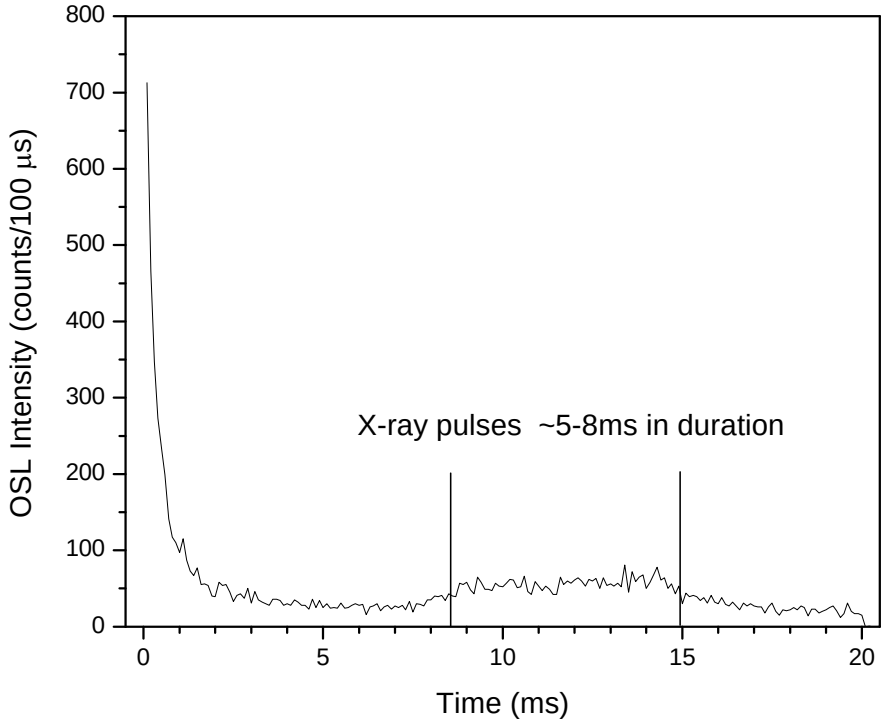


**Figure 5.9** One of the ~220 OSL decays obtained under fluoroscopic x-rays in 30 PPS cine mode. An irregular 'bump' in the signal, due to an incoming x-ray pulse, occurs between ~9 and ~14 ms.

that was proportional to the dose absorbed by the three preceding, complete x-ray pulses. The initial intensities in this case would show only random deviations from an average value, not a clearly systematic deviation as is seen in the data in figure 5.8. However, it can be seen from figure 5.9 that the synchronization of x-ray pulsing to OSL acquisition is not ideal. Furthermore, figure 5.8 reveals another asynchronous trend - the 10 Hz OSL acquisition and the 30 PPS x-ray delivery interfere incoherently. This suggests that either the KBr:Eu system or the fluoroscopy machine, or both, are operating at frequencies other than exactly 10 or 30 Hz, respectively.

Any cyclic phenomenon occurring with a frequency of exactly 10 or 30 Hz should reproduce perfectly identical features over 100 ms periods. Even if the timing scheme were imperfect, so that an OSL acquisition occurred during an x-ray pulse as opposed to between pulses, the initial intensity would still be constant over the measurement. The initial intensity would be lower, due to the fact that the OSL resulting from the dose given by the interfering x-ray pulse would already be depleted before the next measurement, but it would still deviate only randomly about some average value if the operating frequencies were exactly 10 and 30 Hz.

Figure 5.8 shows that the initial OSL intensity varies from ~1000 to ~675 counts. This demonstrates that only rarely does the OSL measurement fall directly between two x-ray pulses, giving the maximum value of 1000 counts from 3 x-ray pulses. Most of the time, an x-ray pulse occurs during the OSL measurement, and when the whole of the pulse falls within the OSL period, the following OSL measurement has an initial intensity of ~675, or ~2/3 of the maximum, which is due to only 2 x-ray pulses contributing to the OSL.

The controls of the Philips Bi-plane did not allow for fine-tuning of the x-ray pulse rate, so the OSL measurement frequency of the KBr:Eu system was altered during several x-ray irradiation periods to find coherence between the x-ray and OSL frequencies. Figure 5.11 shows two three-dimensional representations of all OSL signals (arranged sequentially by time of acquisition, and in their entirety) taken during one such 'tuning' experiment. By adjusting the OSL acquisition frequency, it can be seen that the interference pattern changes as the signal bump from the x-ray pulses travels along the sequential OSL curves. Notice that the initial intensities of the curves occurring between 2.5 s and 7 s, as seen in figure 5.11a, follow a similar pattern to those shown in figure 5.9. Figure 5.12 shows OSL signals measured using an OSL measuring frequency of 9.92 Hz ($\tau$ = 100.8 ms) and in the same fashion as in figure 5.11. At this frequency, no x-ray/OSL interference is observed. The ideal timing scheme had been achieved.

Though an OSL measurement frequency was found that matched the periodicity of the x-ray pulse frequency, there was still no way of ensuring that further measurements would follow the ideal timing scheme of figure 5.10. Sub-optimal measurements were still possible because of the lack of synchronization between the beginning of the 9.92 Hz

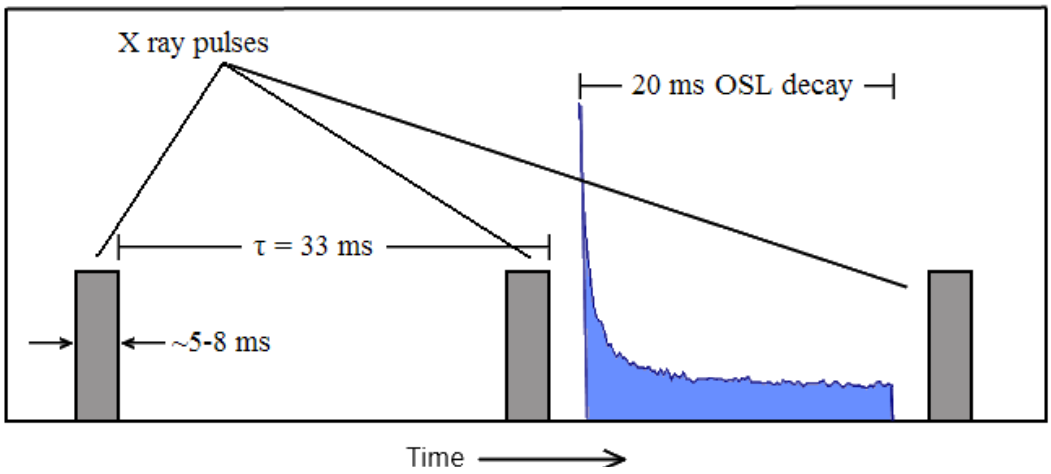


**Figure 5.10** Timing scheme showing OSL measurement occurring between two x-ray pulses incoming at 30 PPS.

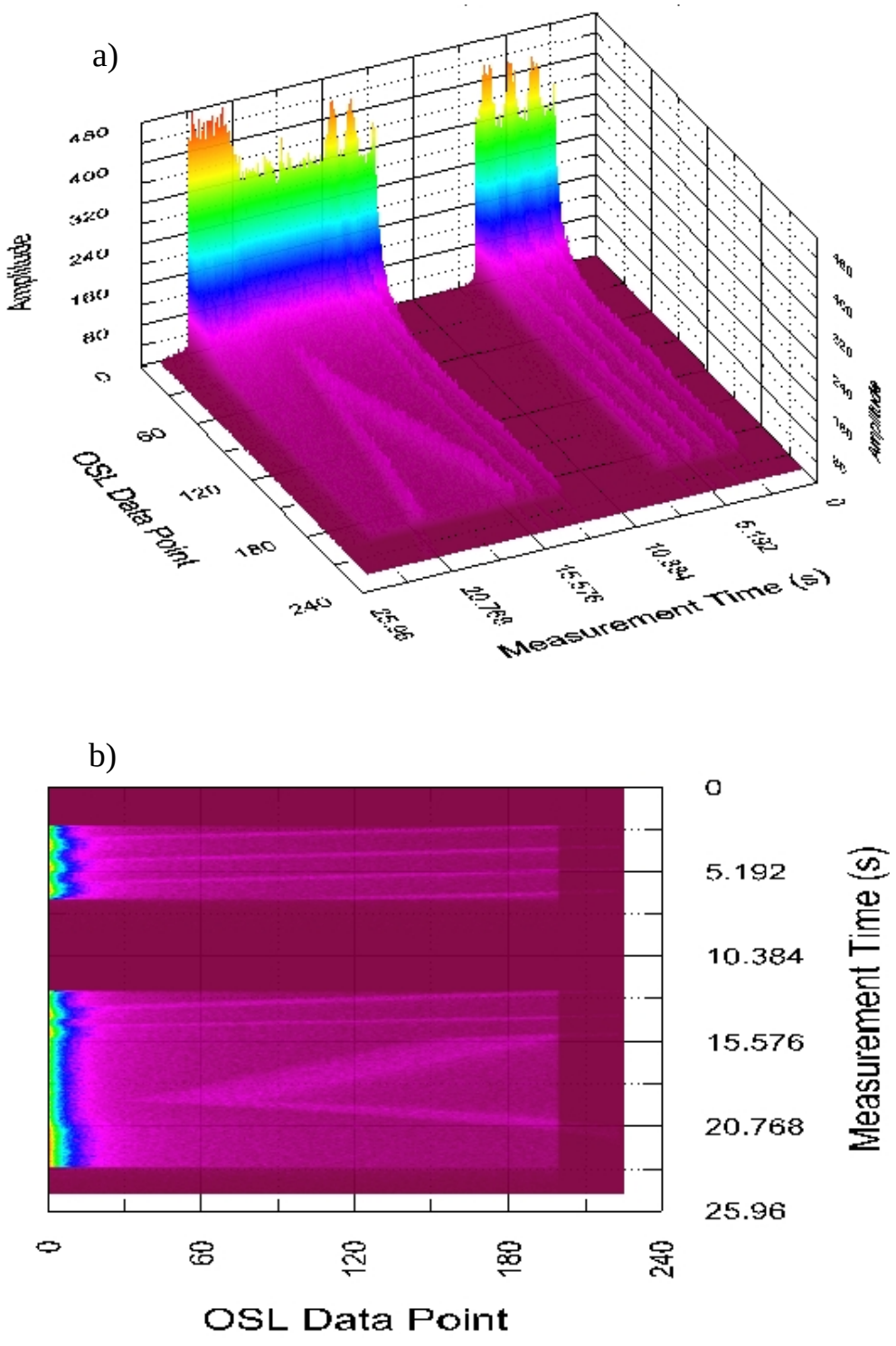


**Figure 5.11** Three-dimensional a) perspective and b) contour view representation of all OSL signals taken during measurement frequency tuning experiment. The signals are arranged in order of acquisition.

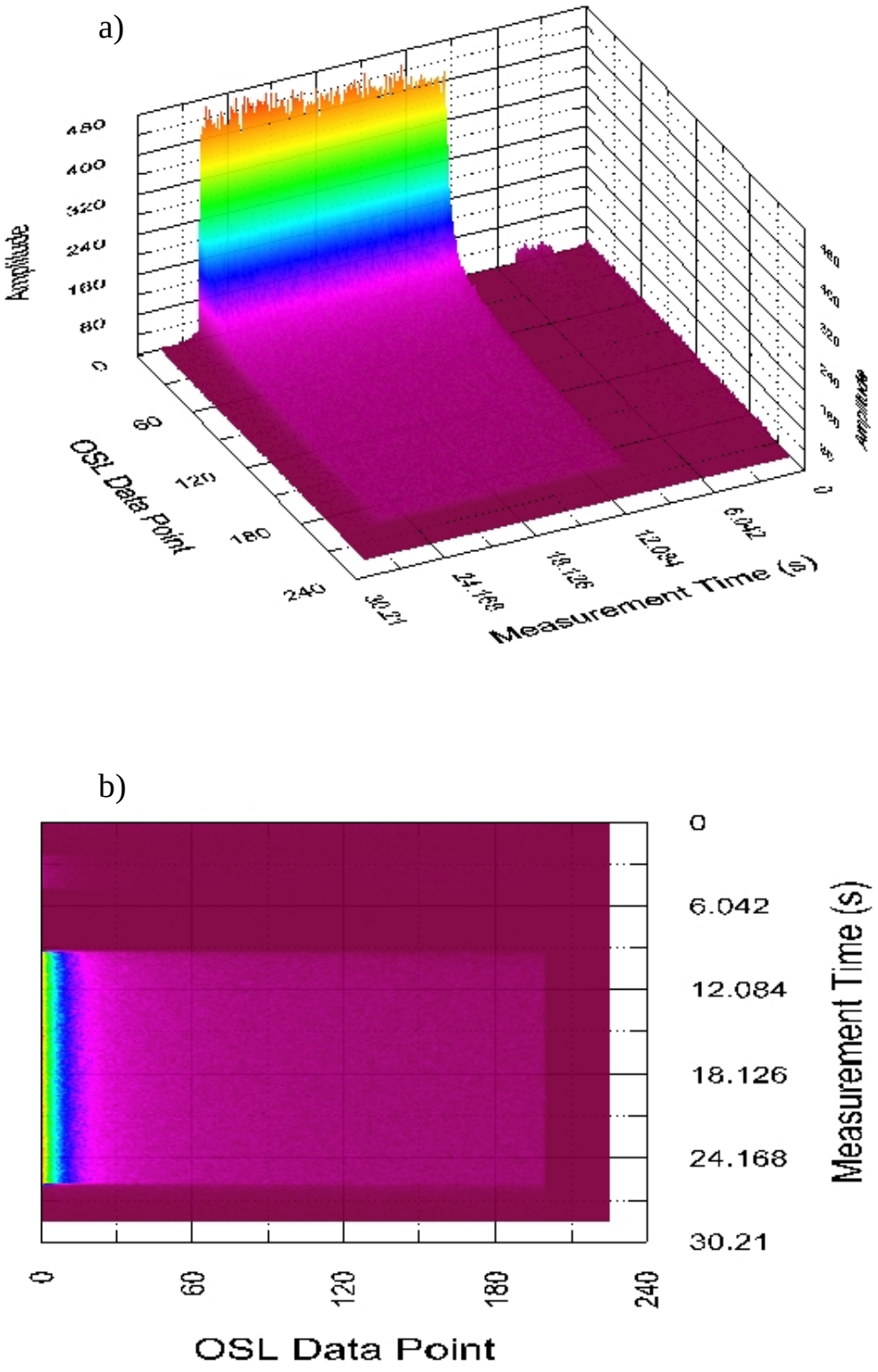


**Figure 5.12** Three-dimensional a) perspective and b) contour view representation of all OSL signals taken with signal acquisition frequency of 9.92 Hz. No x-ray pulse interaction with the OSL signals is observed.

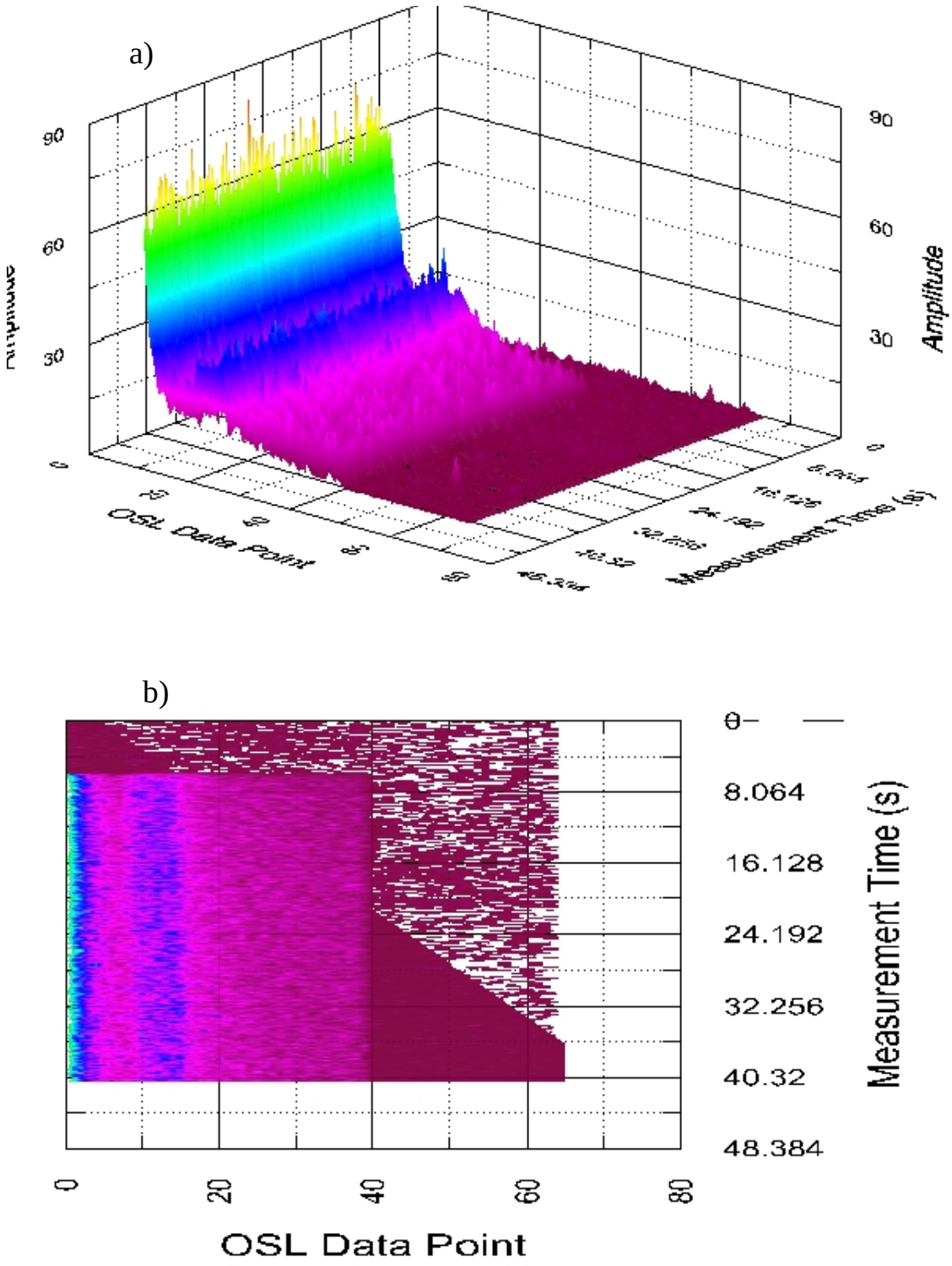


**Figure 5.13** Three-dimensional a) perspective and b) contour view representation of all OSL signals taken with signal acquisition frequency of 9.92 Hz. In this case, the x-ray pulses occur during the OSL measurement, but all at the same point.

OSL acquisition and the beginning of the x-ray pulsing. Figure 5.13 shows a case of where the KBr:Eu system and fluoroscopy machine were started asynchronously. The signals confirm that the 9.92 Hz OSL frequency is coherent with the x-ray output frequency, as the signal bumps due to x-ray pulses occur at the same time on each OSL signal.

In general, fluoroscopy machines do not allow access to the internal electronics that dictate the pulsing of the x-rays, so simply connecting the KBr:Eu system electronically to the fluoroscopy machine to coordinate data acquisition with x-ray pulsing is not possible. As a result, a new measurement scheme was developed that would actively observe the radioluminescence (RL) produced by the KBr:Eu dosimeter during an x-ray pulse. A peak detection algorithm was used that applies a quadratic least-squares fit to the RL data. Once an x-ray pulse is detected, the algorithm instituted a predetermined wait period, to ensure that the pulse had finished, then an OSL measurement was made. Figure 5.14 shows OSL data in the style of figures 5.10-13 that was taken using the active RL-monitoring control program under. The OSL was measured for 18 ms with an integration time of 0.5 ms per data point. In this experiment, the PMT was interrogated for an additional 10 ms after the laser was turned off so that the RL from any following x-rays could be observed. The contrast of figure 5.14b was increased so that the RL due to x-rays could be more clearly discerned after the OSL signals. The algorithm works consistently, and it can be seen that the x-rays arrive at ~8-10 data points (~4-5 ms) after the OSL signal ends. Also, the initial intensities in figure 5.14a do not follow a pattern like that seen in figure 5.8, only random, relatively small fluctuations about an average of ~210 counts. The ideal timing scheme could now be achieved consistently, regardless of

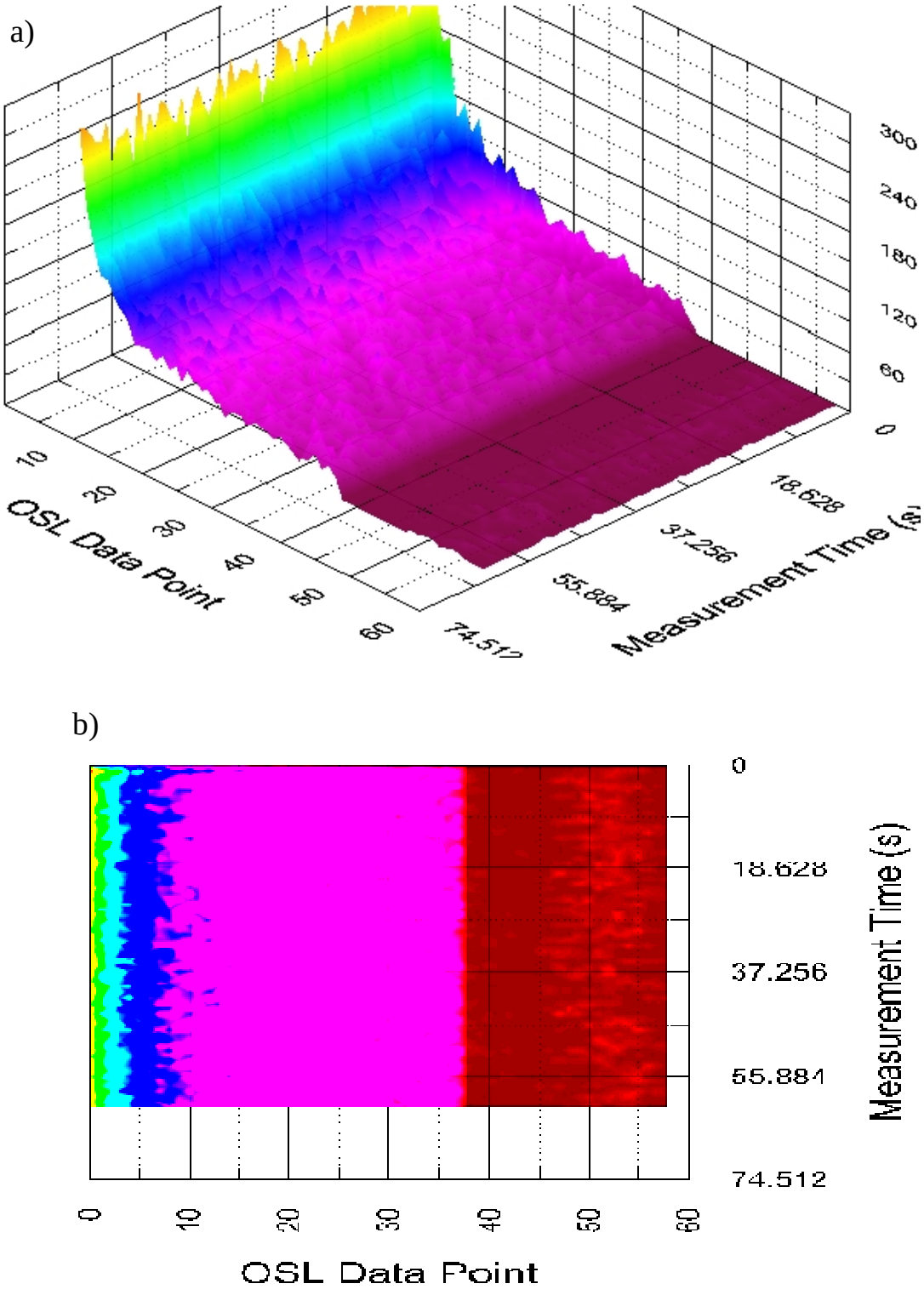


**Figure 5.14** Three-dimensional a) perspective and b) contrast-increased contour view representation of OSL signals taken with the active RL tracking control program. X-ray pulses (via a characteristic RL signal) are shown occurring ~5 ms after the OSL signal is completed.

x-ray pulse frequency.

Another consequence of actively tracking the RL for timing of the OSL measurement is that an arbitrary number of x-ray pulses may be observed before triggering the OSL measurement. This could prove useful for adjusting the sensitivity of the system to lower dose rate fluoroscopy, such as that used for pediatric fluoroscopy. Figure 5.15 shows the results of the KBr:Eu system's performance under lower energy (70 kV) x-rays delivered at 15 PPS. OSL was measured during a continuous exposure that lasted 5 minutes. The system was set up so that over the first minute, the OSL would be measured after at least 5 pulses had been counted. Over the second and fourth minutes, the OSL measurement was triggered after counting 10 pulses, and after 20 pulses during the third and fifth minute. While counting 5 pulses, the rate of

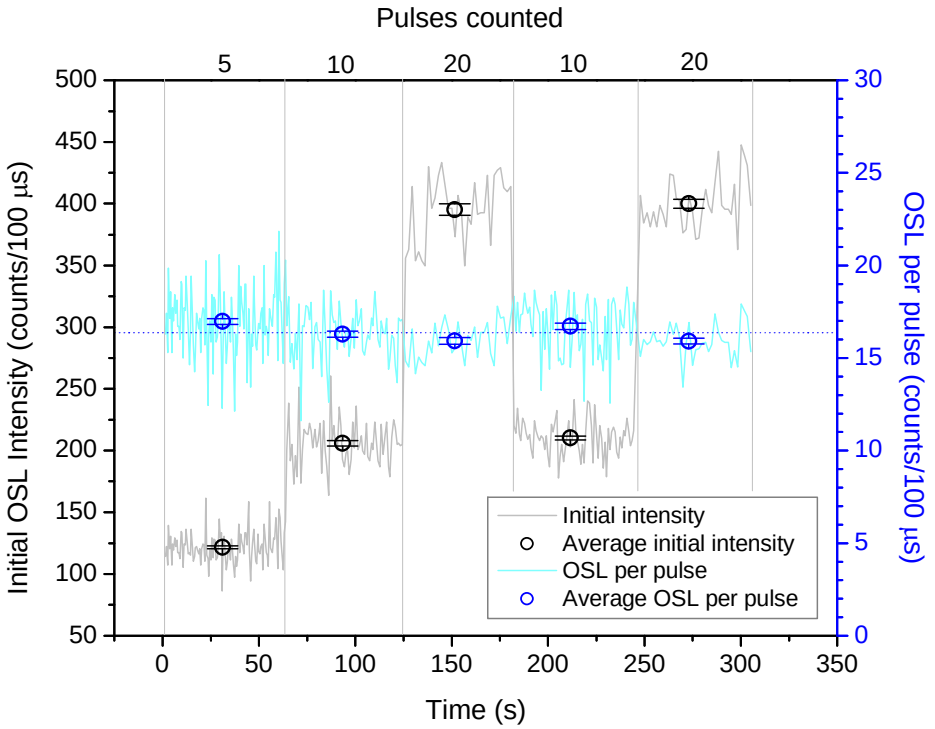


**Figure 5.15** Initial intensity and OSL per pulse results for a continuous x-ray exposure. OSL measurements were made after the KBr:Eu system counted 5, 10, 20, 10, and 20 RL peaks (due to x-ray pulses), each during a single minute of the continuous exposure. The blue dotted line shows the average of all OSL per pulse data.

measurement was ~1.85 Hz; for 10 pulses it was ~1.12 Hz; and for 20 pulses, ~0.6 Hz. The same data are represented using four analysis methods: the light gray line represents the initial intensities of the OSL signals measured after a certain number of pulses had been counted. The black circles represent the average of the initial intensities taken over the minute, with error bars equal to the standard deviation of the mean (a.k.a standard error). The light cyan line represents the same initial intensities as shown by the gray line, each divided by the number of pulses counted before that particular OSL measurement was triggered. This data representation is labeled as 'OSL per pulse'. The blue circles and error bars represent the average OSL per pulse in the same fashion as the average initial intensities.

Due to the set up of the RL monitoring algorithm, the actual number of x-ray pulses that irradiated the dosimeter was usually larger than the prescribed number-to-count by 1 to 5 pulses. The actual number of pulses was found by dividing the time between OSL measurements by the x-ray pulse period, since the peak detection algorithm often failed to count some x-ray pulses. This was especially true for the pulses that came immediately after the OSL signal, as there was a short delay between the end of the OSL signal and the activation of the RL monitoring.

The initial intensity data in figure 5.15 shows no periodic behavior like that seen in figure 5.8, and the error in each case is ~1% of the average value (see table 5.3). This shows that the precision of measurement is practically independent of the number of pulses counted before OSL triggering over any similar time periods. This is understandable, given that any decrease in random fluctuation due to increasing the number of pulses counted (i.e., integration period) will be opposed by a smaller number

of measurements from which to take the inverse square. However, integrating more pulses may prove valuable in low-dose situations, where OSL sensitivity is more important than frequency of measurement. The OSL per pulse data reveals that the x-ray pulse counting functions consistently, as the data closely follows an average of 16.36 ± 0.21 counts of OSL for a single x-ray pulse.

### 5.3 Performance under X-Rays II: Computed Tomography Scanning

**** Disclaimer: The results discussed in section 5.3 on computed tomography scanning are the product of research done in collaboration with Dr. David Peakheart at OUHSC. Dr. Peakheart operated the CT scanner and made all of the pencil ionization chamber measurements, while the author performed all KBr:Eu OSL measurements. Portions of the OSL results have been shown and discussed by Dr. Peakheart as part of a Master's thesis for his degree in medical physics, which he defended successfully in 2006.*

Computed tomography (CT) scanning makes uses of an x-ray source that revolves around a patient, while a system of detectors diametrically opposed to the x-ray source measures the total attenuation of the x-rays along numerous paths through the patient. Tomographic images of the patient are then digitally reconstructed using a computer by comparing the attenuation values with the orientation of the x-ray source at the time of detection. Over the years, CT scanning has advanced from simple step-wise axial scanning to helical scanning to multislice scanning. Modern scanners employ technologies like cone x-ray beams and hundreds of rows of detectors, exposing patients to fast-moving radiation fields with increasingly complicated geometries. New quality assurance (QA) and dosimetry techniques are needed to characterize and calibrate these new systems.

The viablilty of the KBr:Eu system as an alternative to existing QA and dosimetry technique for CT was tested at OUHSC with a GE Lightspeed Ultra CT scanner. This scanner is capable of both axial and helical scanning, and outputs continuous x-rays using peak voltages of 80, 100, 120, and 140 kVp at currents adjustable up to 350 mA. The scanner has 16 rows of detectors of 1.25 mm thickness, and can acquire of up to 8 slices per rotation in an 8×1.25 mm or 8×2.5 mm detector configuration.

For most of the measurements, the KBr:Eu dosimeter was placed within one of two phantoms: a cylindrical CT body dosimetry phantom or a Rando® phantom. The CT body phantom is a right circular cylinder 15 cm in length and 32 cm in diameter. It is composed of soft-tissue-equivalent polymethyl-methacrylate (PMMA), and has a 1 cm diameter channel running along its length at its center. The KBr:Eu dosimeter was typically placed at the center of this channel inside a 15 cm long, 1 cm diameter PMMA plug that had been drilled through the center (~2mm diameter) along its long axis to allow for dosimeter and optical fiber. The CT body phantom was then positioned on the patient table at the isocenter of the CT scanner gantry. A standard, 100 mm pencil IC was used in place of the KBr:Eu dosimeter for obtaining exposure measurements for comparison. The Rando® phantom is an anthropomorphic phantom made from tissue-equivalent material and contains a natural human skeleton (see figure 5.16). This phantom is sliced into 2.5 cm sections, with each slice being perforated with a grid of 6 mm diameter holes that can run from slice to slice, depending on the local skeletal structure. Each channel is filled with a Mix D tissue-equivalent plastic plug, which may be easily removed and replaced (The Phantom Laboratory, 2008).

The first experiment was to check the response of the KBr:Eu system as the x-ray

**Figure 5.16** Photograph of a partially disassembled Rando® phantom. Clearly depicted are the grids of plugged holes used for dosimeter placement, as well as the human skeleton. Reproduced with permission of The Phantom Laboratory - www.phantomlab.com.

source current was ramped from 60 mA to 350 mA in steps of 40 or 50 mA, while the peak voltage of the x-ray source was held constant. Figure 5.17 shows the initial intensities of OSL signals taken at 10 Hz over a ~90 s portion of one of the current ramping tests. During this period, the CT scanner was programmed to sequentially perform five axial scans at one scan per second, using 100 kVp x-rays at four different tube currents. A 4×2.5 mm detector configuration was used, and the slice thickness was set to 5 mm so that the KBr:Eu dosimeter would be totally enveloped. The inset shows a close up of OSL results from the last three axial scans. A clear central dip can be seen in the data, due to attenuation of the incoming x-rays by the patient table. This attenuation effect is most clearly seen when the scanner goes under the table in the middle of the OSL measurement, but is present in every scan.

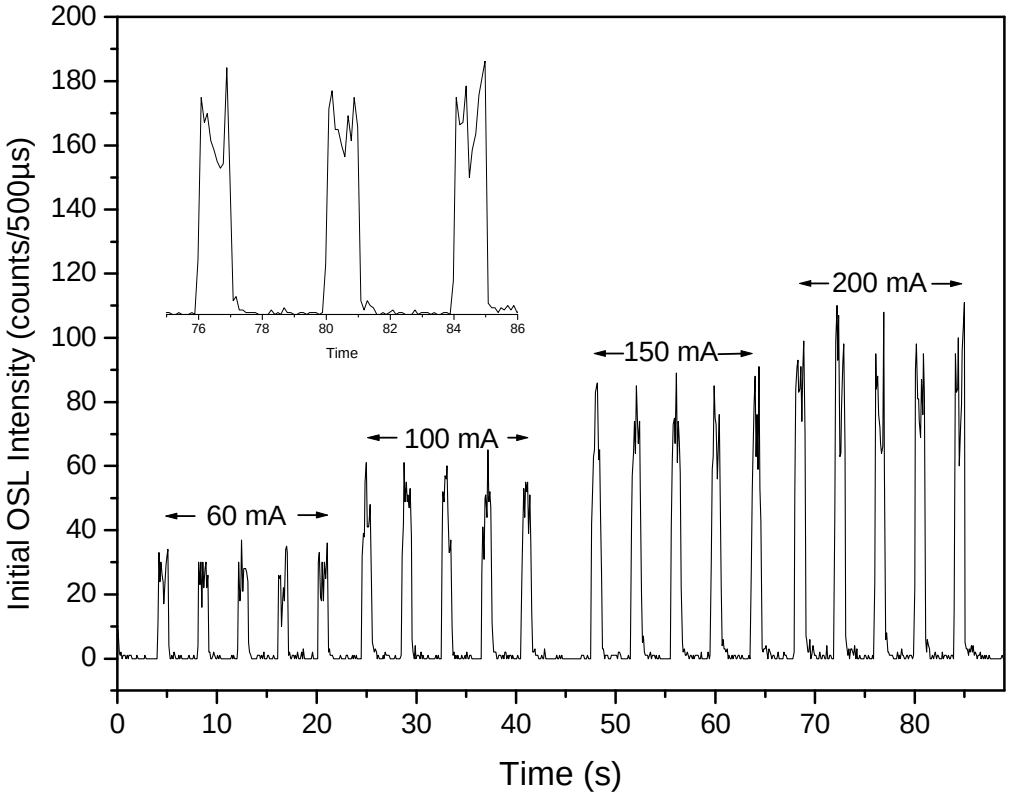


**Figure 5.17** Initial OSL intensities of signals taken at 10Hz for ~90 s while capturing groups of five axial CT slices at 100 kVp in a current ramping experiment. Inset: Close up of last three scans, revealing a dipping feature of the data.

The average values of initial intensity resulting from current ramping experiment are plotted in figure 5.18 for each available peak voltage. Exposure readings from a pencil ionization chamber are also plotted. The two y axes were loosely scaled for comparison. The CT scanner implemented a mechanism that would alter the focal spot of the incident electrons on the x-ray- producing anode to protect the anode at higher voltages and currents. This change in focal spot introduces a small, discontinuous rise the dose rate. Peakheart (2006) showed that the data in figure 5.18 are linear over ranges that correspond to before and after this focal spot changed. Table 5.3 lists the mean ratios of OSL data to exposure readings over all seven tube currents, for each peak voltage. For the most part, the OSL data follow the exposure results well. However, in figure 5.18 the

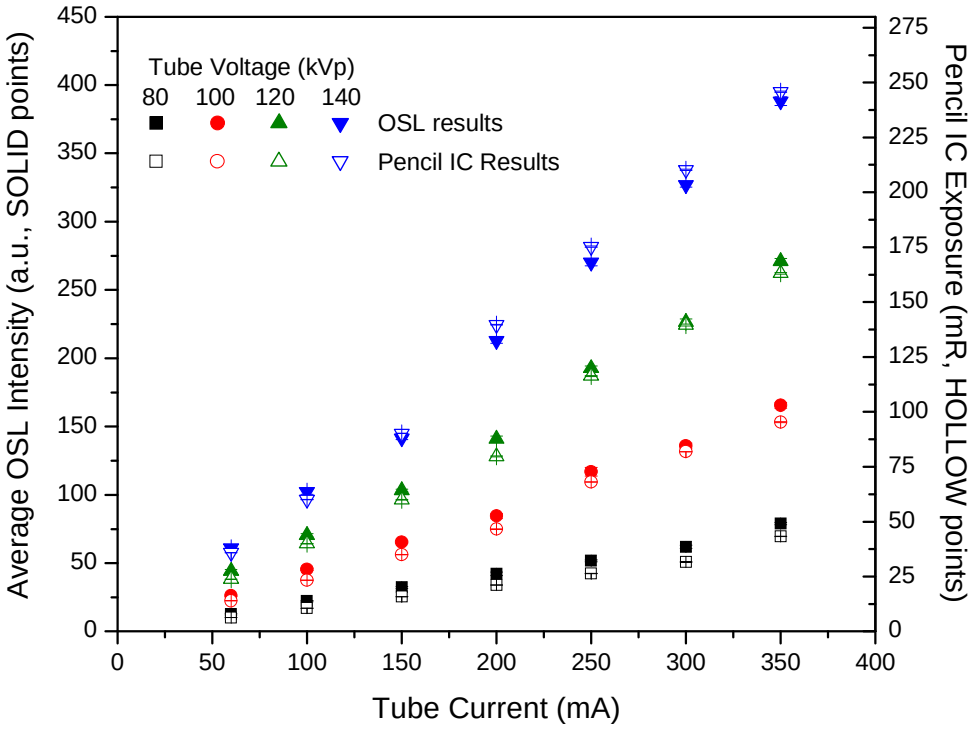


**Figure 5.18** Average initial intensities (solid) plotted against x-ray tube current for the four available peak voltages. Pencil IC exposure readings (hollow) taken under identical circumstances are also shown. The y axes are loosely scaled for comparison.

140 kVp data lies below that of the IC results, whereas for 80, 100, and 120 kVp, the data lie just above the average exposures. This may be evidence of an energy dependence of KBr:Eu near 140 keV. CT machines use relatively high filtration between the x-ray tube and output port (Goldman, 2007). This means that the energy spectra of CT beams are harder, with the energy spectrum peaking at a value closer to the set kVp (as with curve E of figure 5.5). With most of the x-rays closer to 140 kVp, and with a look back at the mass-energy absorption coefficients of KBr (figure 5.4), an under-response of the OSL signal, relative to the response to lower energy x-rays, is not surprising.

Next, the KBr:Eu system was used to measure the beam profile for a collimation of 5 mm. Axial scans were made on the CT body phantom with the dosimeter placed in the center. The patient table was moved in steps of 0.5 mm from 10 mm superior to 10 mm

**Table 5.3** Means of the ratios of OSL versus exposure for all seven tube currents at a particular peak voltage. Standard error is also represented as a percentage of the mean under the % symbol.

| Peak Voltage (kVp) | Mean OSL/exposure ratio | Standard error of ratios | % |
|---|---|---|---|
| 80 | 1.98 | 0.032 | ***1.61%*** |
| 100 | 1.80 | 0.038 | ***2.13%*** |
| 120 | 1.72 | 0.031 | ***1.79%*** |
| 140 | 1.59 | 0.028 | ***1.74%*** |

inferior. From 10 mm to 20 mm (on each side), the table was moved in 1 mm increments, and from 20 mm to 50 mm in 5 mm increments. At each step, the OSL from three axial scans was recorded. The scans were made at 1 rotation per second, 120 kVp, and 250 mA. A 4×2.5 mm detector configuration was used. Figure 5.19 shows the integrated, background-subtracted, and averaged OSL signal with error bars equal to the standard error. The profile exhibits a full-width, half maximum of approximately 8 mm. Of particular interest are the signal levels 50 mm away from scan center, which show that a significant amount of dose is deposited far from the scan center in a CT body phantom.

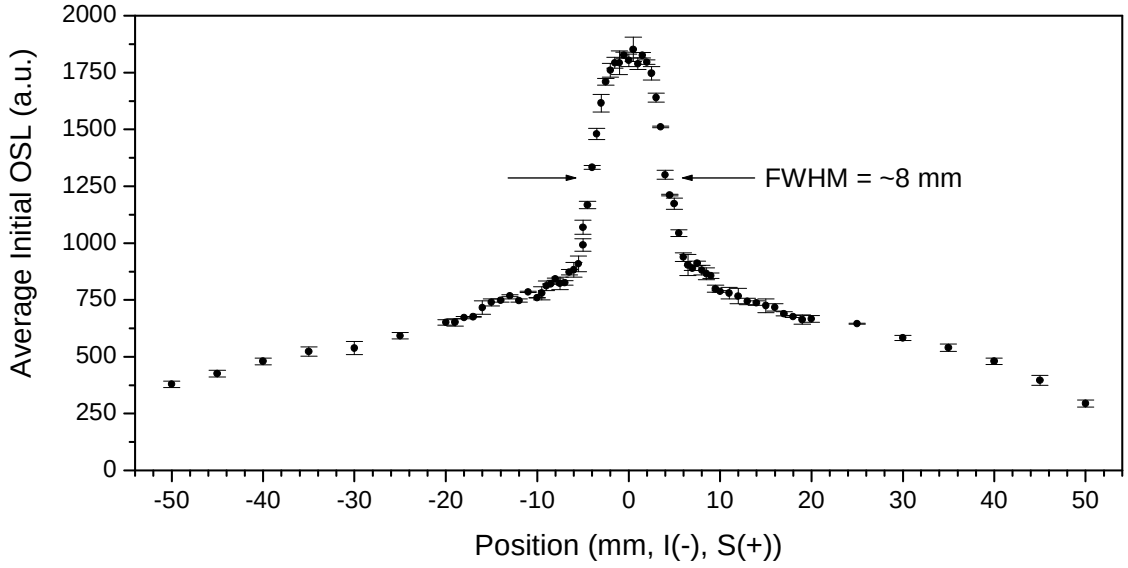


**Figure 5.19** Averaged background-subtracted integral OSL results of a high-resolution axial slice profile experiment.

Gantry tilt angle dependence was tested with the dosimeter placed at the ioscenter of the CT field, either in air or centered in the CT body phantom, and exposed to multiple axial scans at varying gantry angles through a 40° range. The CT gantry was tilted superiorly and inferiorly to the phantom, on the horizontal axis normal to the long axis of the patient table. The scanning and x-ray parameters were the same as those used for the beam profile experiment, with the exception that a total of six scans was used at each tilt angle. Also, the OSL signals were analyzed in an identical fashion to that used for the beam profile experiment, and the results can be seen in figure 5.20. While in air (figure 5.20a) there is no appreciable dependence on tilt, the results obtained using the CT body phantom (figure 5.20b) show decreasing OSL values as the angle increases from the vertical. This is due to attenuation from the increasing thickness of phantom material that the x-rays pass through as the gantry tilts away from vertical.

Helical CT scanning provides a more complicated irradiation field than axial scanning. The CT scanner spins axially while the patient table is moved at a constant rate through the gantry. In this way, scanning large portions of a patient is accomplished much faster than the move-stop-scan-move axial procedures. Figure 5.21 shows the initial OSL intensities during three consecutive helical CT scans on the CT body phantom with the KBr:Eu dosimeter placed in the center. The scan followed a routine chest exam program, and the scanner moved from 80 mm superior to 80 mm inferior at 0.7 seconds per rotation. The beam was collimated to 10 mm and the detectors were configured as 8×1.25 mm. Helical scanning requires a pitch between the patient table movement and the width of the x-ray beam. In this case, the pitch was set to 1.35:1, so that the table moved 13.5 mm for every rotation of the scanner, since the beam had been collimated to

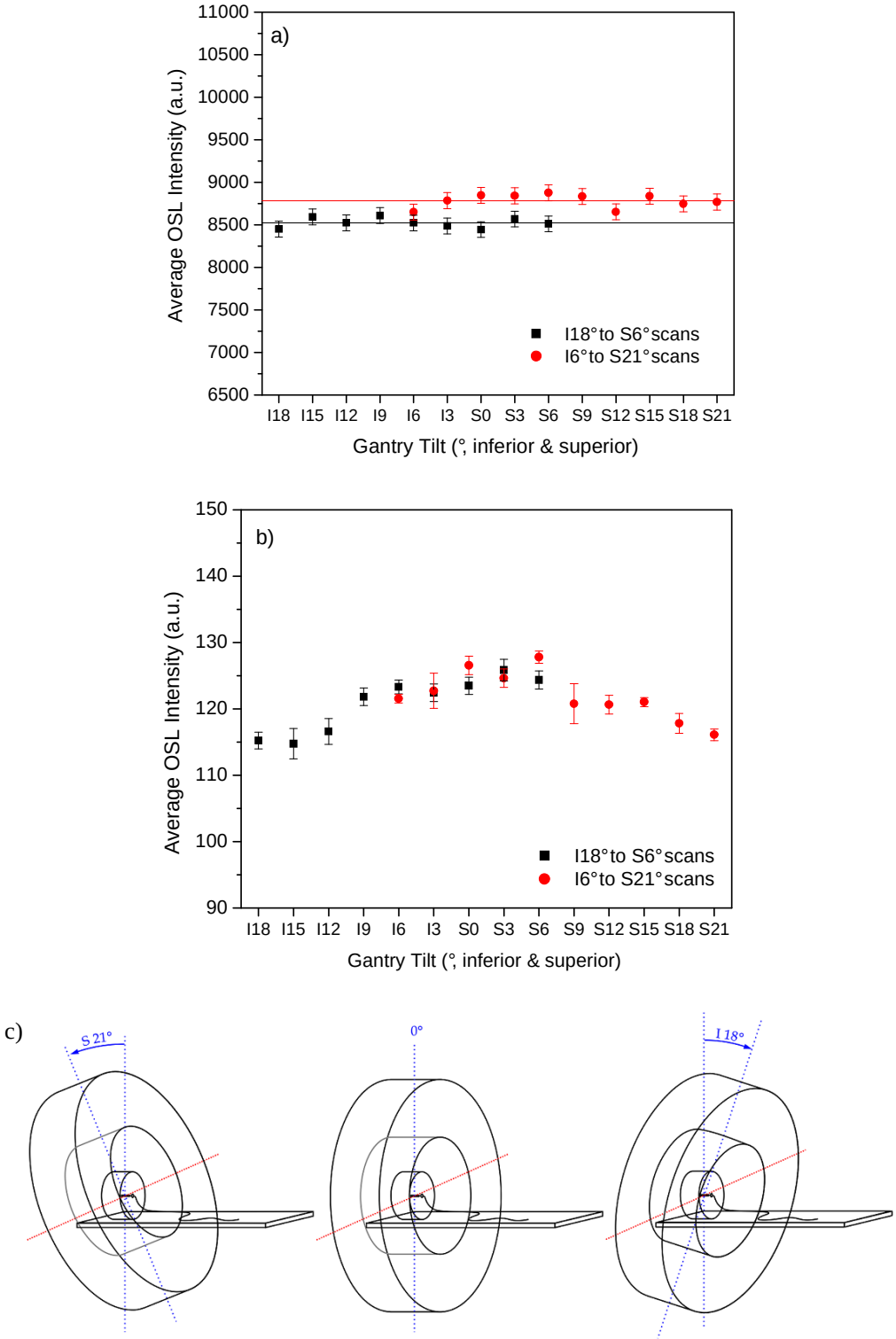


**Figure 5.20** Results of the gantry tilt dependence tests for the KBr:Eu dosimeter located at the CT isocenter a) in air, and b) centered in the CT body phantom. Error bars are equivalent to the standard error for six measurements. c) Diagram depicting CT gantry tilt with respect to patient table and centered on the CT body phantom, as in the case for the results of b).

10 mm. Each scan in figure 5.21 shows a major peak structure, on top of which a finer periodic structure appears. The fine structure has a periodicity similar to that of the rotation of the scanner – there are ~ 11 rotations in each scan – and so it is believed to be due to attenuation by the patient table as the scanner goes underneath. The major structure represents the increasing and decreasing intensity of x-rays as the source spirals closer to and further away from the dosimeter. The integrals under the initial intensity results of figure 5.21 are comparable, even though they have somewhat dissimilar shapes. The average of the three areas is 15201 counts with standard error of 164, or 1.1 % of the average.

Helical scanning of a Rando® phantom introduces even greater complexity to the CT radiation field, due to the non-symmetric shape of the phantom and the presence of both soft andhard tissues (i.e. plastic and bone). Testing of the KBr:Eu system under helical scanning inside a Rando® phantom began with simulated routine ~40 cm abdominal/pelvic (abd/pel) scans that started just below the sternum and ended at the

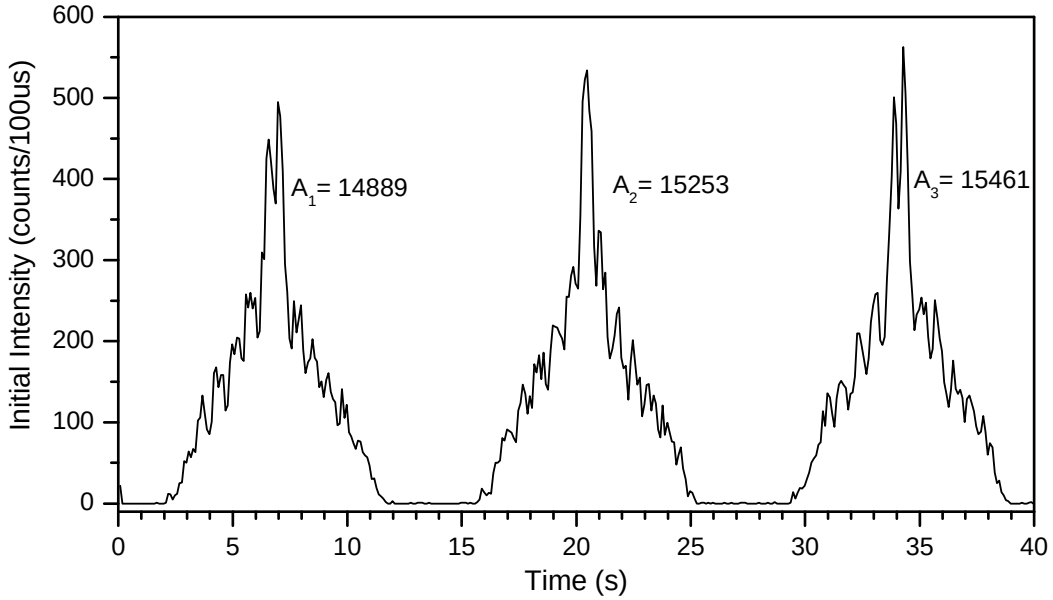


**Figure 5.21** Initial OSL intensities taken over three consecutive routine 16 cm chest exam with the KBr:Eu dosimeter placed at the center of the CT body phantom. $A_i$ represents the areas under the curves for the first (i = 1), second (i = 2), and third (i = 3) scans.

upper thigh of the phantom. The response of KBr:Eu dosimeter was tested at three locations for the abdominal/pelvis scans: in slice 2-2 at the pancreas, in slice 2-5 at the left kidney, and again in slice 2-5 at the linea alba. Figure 5.22 shows a photograph of the slices used and where the dosimeter was positioned in each slice. Also shown is the fully assembled phantom with anindication of where the different slices fit, and a list of parameters used for these scans. Further helical scanning tests were performed using the Rando® phantom by simulating a routine chest examination (~25 cm in length). For this

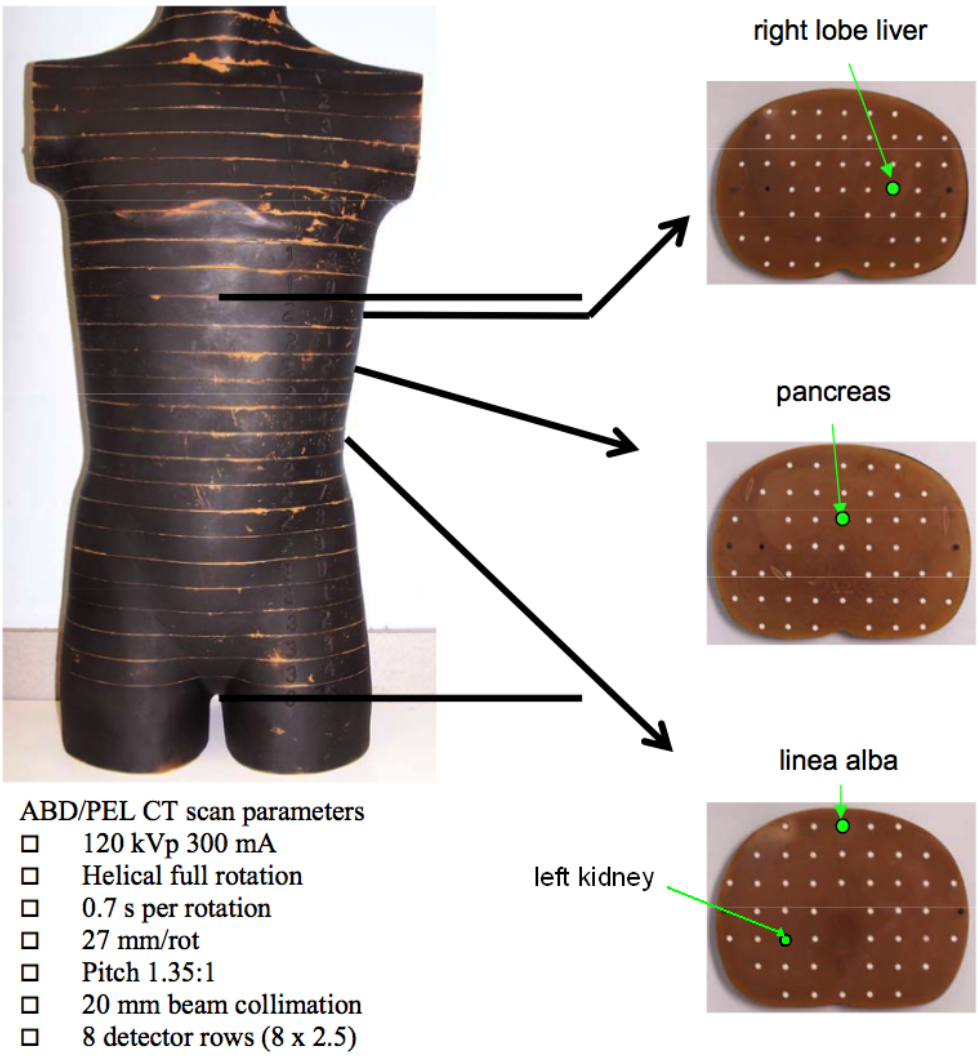


**Figure 5.22** Photograph of Rando® phantom used for testing performance under helical scanning during a routine abd/pel exam. The positions of the slice in the phantom, and the dosimeter in the slice, are detailed. Also shown is a list of CT scanning parameters used for the scans. Used with permission from Peakheart (2006).

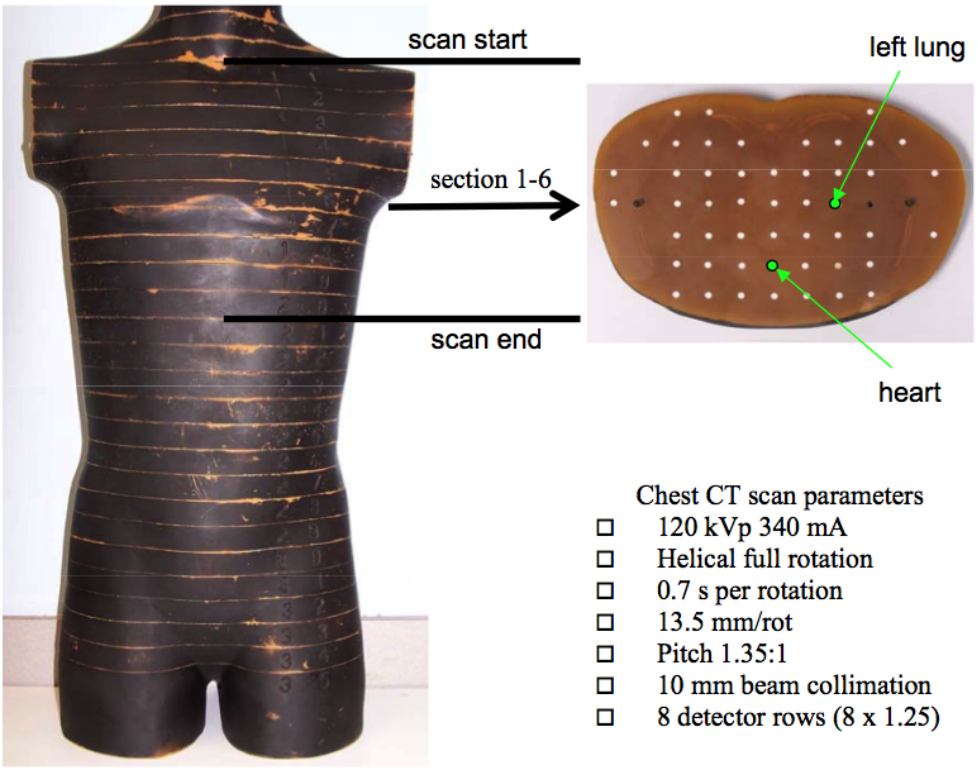


**Figure 5.23** Photograph of Rando® phantom used for testing performance under helical scanning during a routine chest exam. The positions of the slice in the phantom, and the dosimeter in the slice, are detailed. Also shown is a list of CT scanning parameters used for the scans. Used with permission from Peakheart (2006).

study, the dosimeter was placed in the 1-6 slice at a position corresponding to the heart. Figure 5.23 shows the dosimeter locations in the slice, the position of the slice on the assembled phantom, and the CT parameters used.

Figure 5.24 shows the initial intensities taken over three consecutive abd/pel scans for each dosimeter position. The shapes of the scans taken at the 2-2 pancreas position show a more abrupt increase on the left side than on the right, which decays to zero smoothly. This is due to the positions of slice 2-2 and of the starting points of the scans being relatively close to one another. The initial intensities obtained from the 2-5 slice show a more symmetric increase and decrease, as the 2-5 slice is more centrally located in the scanning range. All of the results of figure 5.24 also suffer from a shorter term

variability similar to the periodic structures seen in the helical scans of the CT body phantom (figure 5.21). While table attenuation is certainly still a factor in the variability, the Rando® phantoms internal skeleton also attenuates the incoming x-rays, and in a more complicated fashion than the patient table. The average area under the three curves taken at 2-2 pancreas is 5608 counts with an error of 183, or 3.3% of the average. For the 2-5 left kidney, the average was 5977, with an error of 227 (3.8%). Lastly, the average area under the curves obtained at 2-5 linea alba was 7161, with an error of 175 (2.44%).

The results from the routine chest scans can be found in figure 5.25. This looks similar to the results from the abd/pel scans, but the peak OSL intensities are significantly

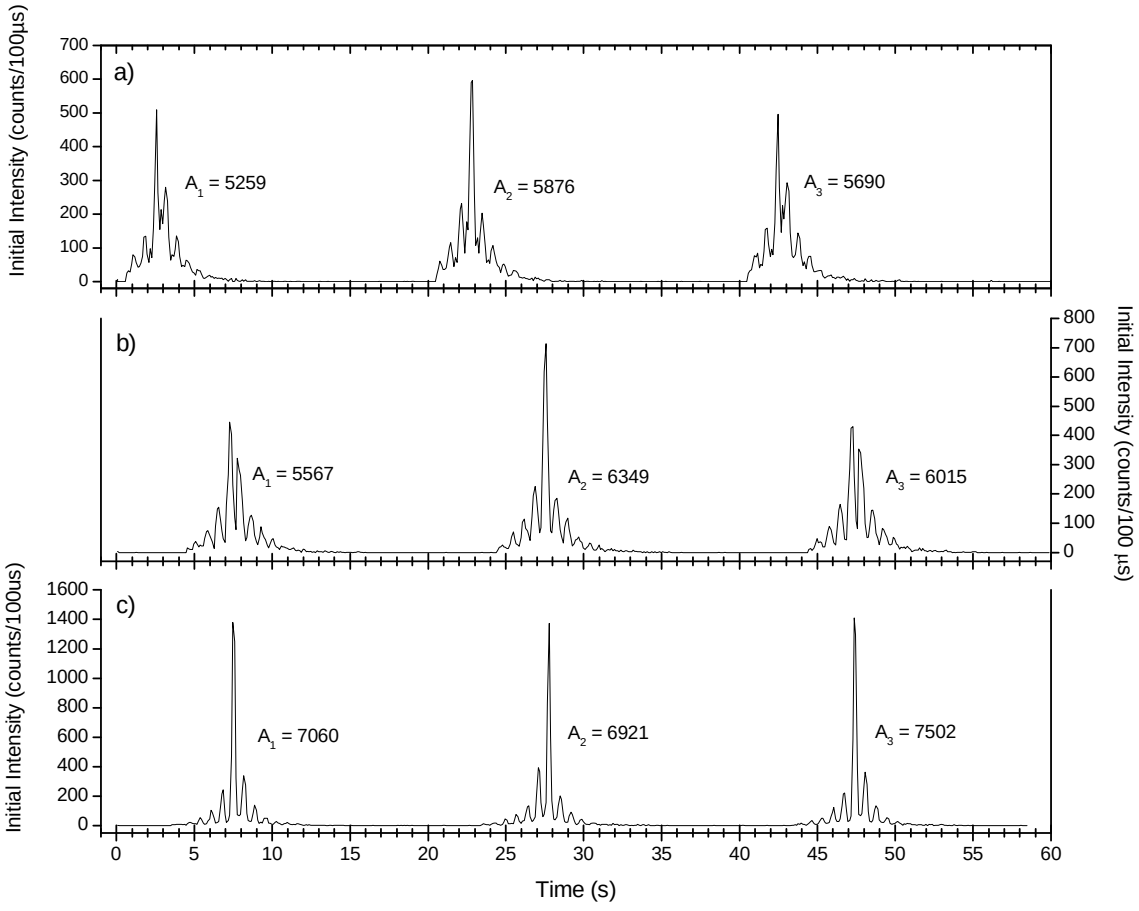


**Figure 5.24** Initial OSL intensity results from simulated abdominal/pelvic scans using the Rando® phantom. The dosimeter was subject to three consecutive scans while placed in the a) pancreas portion of slice 2-2, b) the left kidney area of slice 2-5, and c) the linea alba of slice 2-5. Integrals of the area under the three results from each position in the phantom are shown as $A_{n=1,2,3}$.

higher. Part of the reason for this is that the tube current was increased from 300 mA for the abd/pel, to 340 mA for the chest scans. However, since the OSL signal increases more or less linearly with current (see figure 5.18), the nearly two fold increase in intensity from figure 5.24 to figure 5.25 must be caused by something other than a ~10 % increase in tube current. The main contributor to signal increase is the slower rate of patient table travel during the chest exam. The translation rate is only half that for the simulated abd/pel exam, meaning that the source is close to the dosimeter for twice as long and gives around twice the dose. The three routine chest exam scans gave an average integral of 10901 counts with an error of only 153, or 1.4% of the average.

Even with as complicated a radiation field as that found inside an anthropomorphic Rando® phantom as it undergoes helical CT scanning, the KBr:Eu system was able to reproducibly report dose information with errors ranging from 1.4 % to less than 4 %.

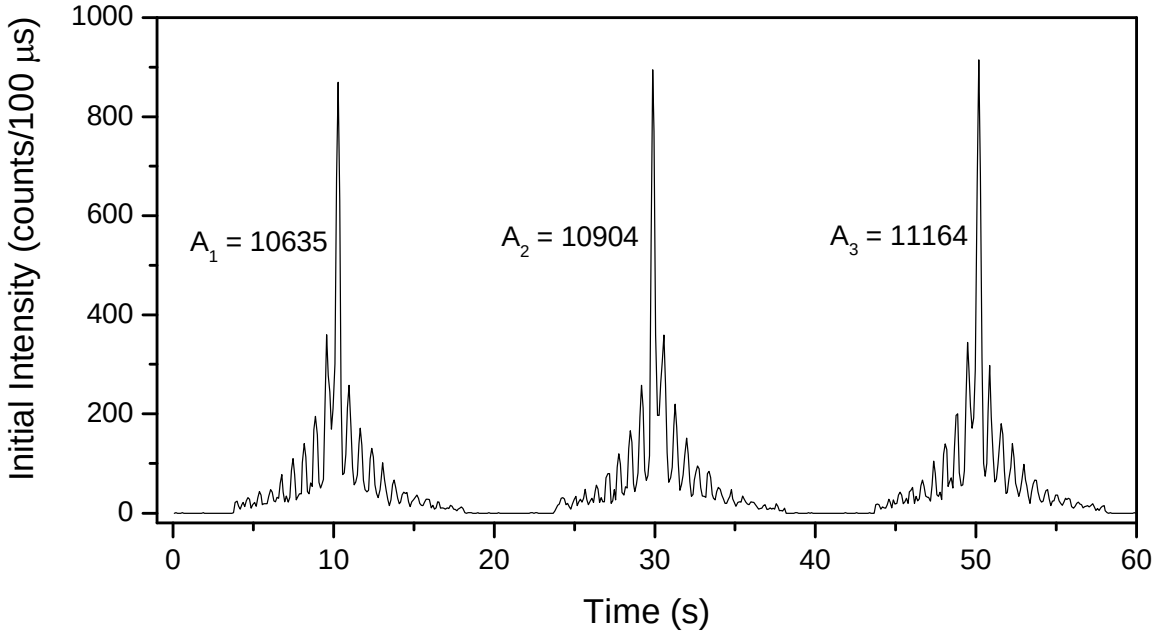


**Figure 5.25** Initial OSL intensity results from simulated routine chest scans using the Rando® phantom, in the fashion of figures 5.21 and 5.24. The dosimeter was subject to three consecutive scans while placed in the heart region of slice 1-6.

## 5.4 Performance under High Dose Rate (HDR) Brachytherapy using an $^{192}$Ir Seed

The KBr:Eu system was also tested using a $^{192}$Ir brachytherapy source ($E_{\gamma,ave}$ = 650 keV) at OUHSC on October 20$^{th}$ and 25$^{th}$ of 2006. The experiments consisted of stability and reproducibility tests of the KBr:Eu system, as well as dose distribution tests to be compared with the dose plans developed by Nucletron's PLATO Brachytherapy (v14.2.5) software. See appendix A for $^{192}$Ir source and dose plan information. Comparisons of the OSL results to the PLATO dose plans are presented, followed by reproducibility results comparing the system's performance on the two different days. Dose plans were constructed after all the measurements on the 20$^{th}$ were performed, and just before measurements started on the 25$^{th}$.

The KBr:Eu fiber probe was placed ~4 mm horizontally away from and parallel to the $^{192}$Ir brachytherapy source applicator (as seen from above in figure 5.26) within a large box water phantom. The KBr:Eu dosimeter was then moved vertically with respect to the $^{192}$Ir source by a motorized translation stage with a step resolution of 0.01 mm. OSL measurements were taken while level with the iridium source, and at vertical displacements away from source center ranging from 5-100 mm above and below the

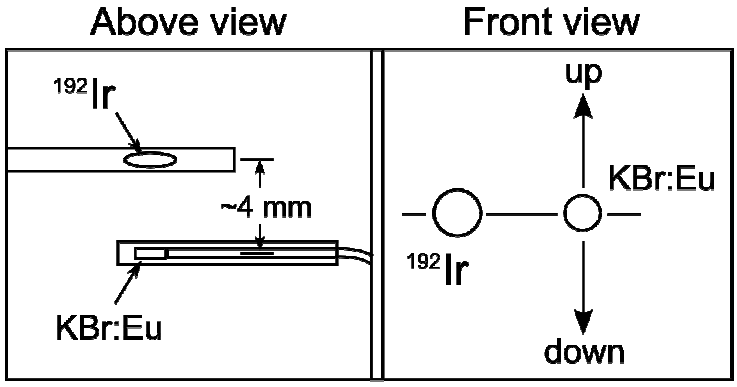


**Figure 5.26** Schematic drawings of initial source and dosimeter positioning.

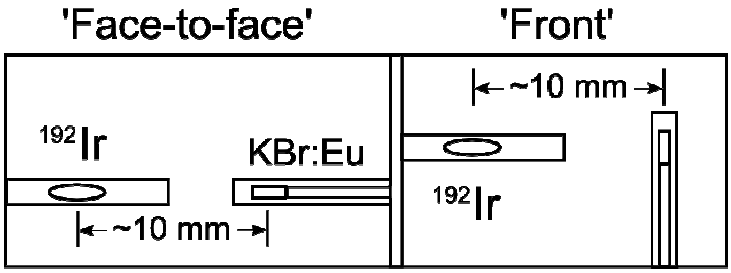


**Figure 5.27** Schematic drawings of alternate positioning schemes.

source in 5 mm or 10 mm steps. The dose profile extending out along the axis of the applicator was measured from 10 to 100 mm with the KBr:Eu probe oriented along the source axis (the so-called 'face-to-face' orientation in figure 5.27) and normal to the source axis (or 'front' in figure 5.27) in 5 mm or 10 mm increments. Measurements on October 20$^{th}$ were taken above and below the sample using the configuration of figure 5.26, as well as along the source axis in the geometries shown in figure 5.27. The measurements taken on October 25$^{th}$ tested only the reproducibility of the dose profile above the $^{192}$Ir source in the configuration of figure 5.26.

Initial positioning was performed by hand using a flexible rule held under water next to KBr:Eu probe and source applicator, and once complete, the translation stage was zeroed in the case of the 'above' and below measurements and set to 10.00 mm in the case of the 'face-to-face' and 'front' measurements. All measurements consisted of a 60 s exposure from the source to the center of the water phantom. The brachytherapy system is designed to advance the $^{192}$Ir seed source, which is attached to a strong but flexible wire, from a shielded chamber into the end of the applicator for a specific treatment period. The system then withdraws the seed back into the chamber. Therefore, for each measurement the real-time acquisition of the dosimetry system was started several seconds before the iridium source began its travel into the end of the applicator and was

not terminated until several seconds after the iridium's retreat out of the water phantom. This was done to ensure proper measurement of background.

The OSL results of the KBr:Eu system are represented using the background-subtracted integral of the area under the OSL signal decay curve (hereafter called BSOSL, after background-subtracted OSL). Though the data were acquired at 10Hz, each datum point in the graphs below represent the integration of data over 1 s. Error bars represent the standard deviation (or propagated standard deviation, in the case of ratios) of the 1 s integrated data over the duration of the measurement.

The first objective of these experiments is to compare the KBr:Eu system's OSL measurements with the dose plan given by the Nucletron software. Figures 5.28 and 5.29 show normalized (to maximum) values of calculated dose plan and OSL results obtained on October 20$^{th}$ for the geometries shown in figures 5.26 and 5.27, respectively. One set of dose plan values was developed and used for both 'above' and 'below' comparisons, since an assumption is made that the dose profile is cylindrically symmetric. A second set

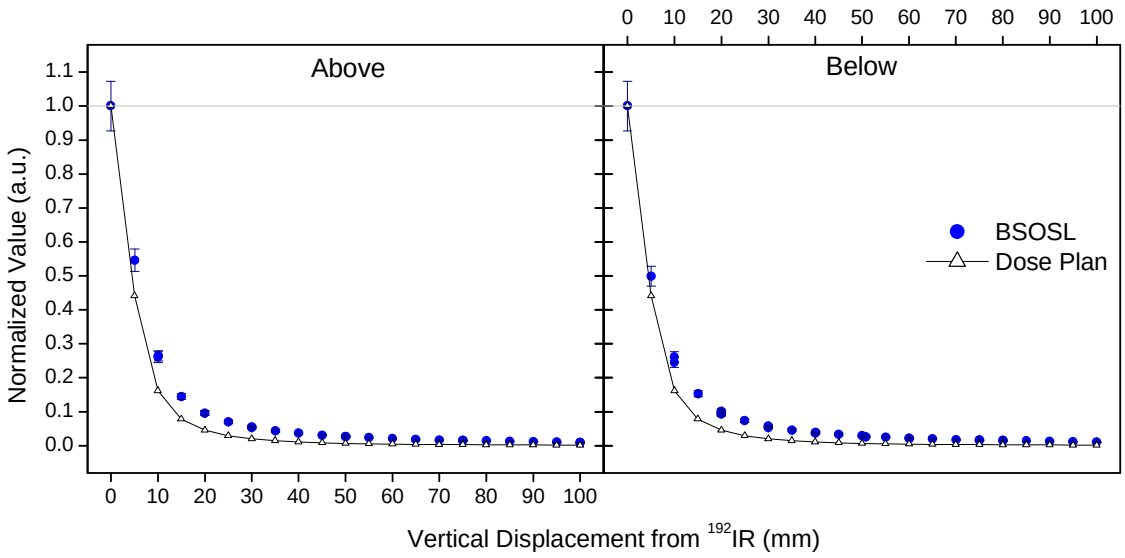


**Figure 5.28** Comparison of 10-20-2006 OSL results to Nucletron dose plan values for the 'above' and 'below' experimental geometries. All data in each curve were normalized to the maximum of the curve.

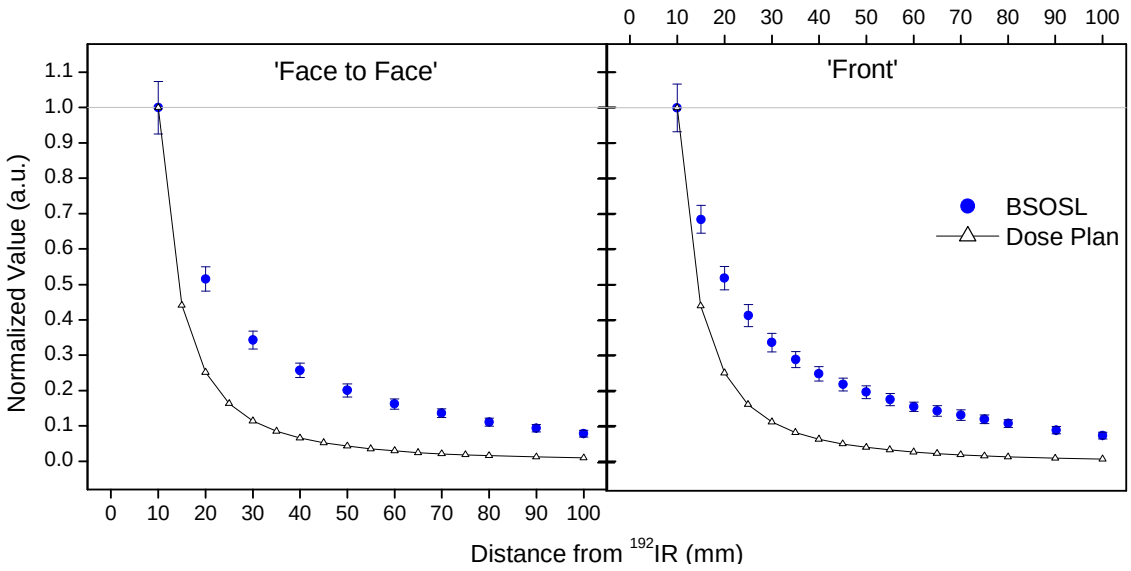


**Figure 5.29** Comparison of 10-20-2006 OSL results to Nucletron dose plan values for the 'face to face' and 'front' experimental geometries. All data in each curve were normalized to the maximum of the curve.

of dose plan values was developed and used for both 'face-to-face' and 'front' comparisons. Figure 5.30 shows the comparison of the OSL results taken on the 25th to the corresponding dose plan. While a slower drop off of the OSL results compared to the dose plan is evident in all of the profile graphs, more significant disparity is found in figure 5.29 in the OSL data taken in the 'face-to-face' and 'front' geometries.

Another comparison between the KBr:Eu system's performance and the dose plan can be made by taking the ratio of the OSL results to the dose plan values. Figure 5.31 shows this ratio using the BSOSL analysis of data taken in all profile geometries and on both days. The ratios resulting from the data and dose plan from Oct. 20th seem to follow a nearly linear relation, with sublinearity occurring at more than 60 mm away from the source. Close to the source, the ratios of the data from the 25th seem to follow a similar trend to that of the 'above' data from Oct. 20th. However, a divergence from the earlier data is seen to start at 40 or 50 mm, with more severe sublinearity and a possible decrease

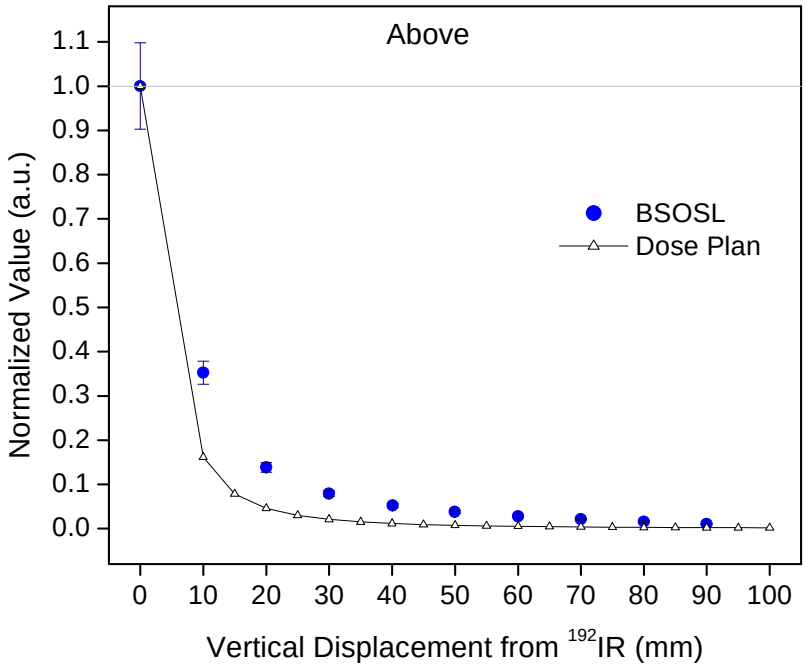


**Figure 5.30** Comparison of 10-25-2006 OSL results to Nucletron dose plan values for the profile above the $^{192}$Ir source as in figures 5.28 and 5.29.

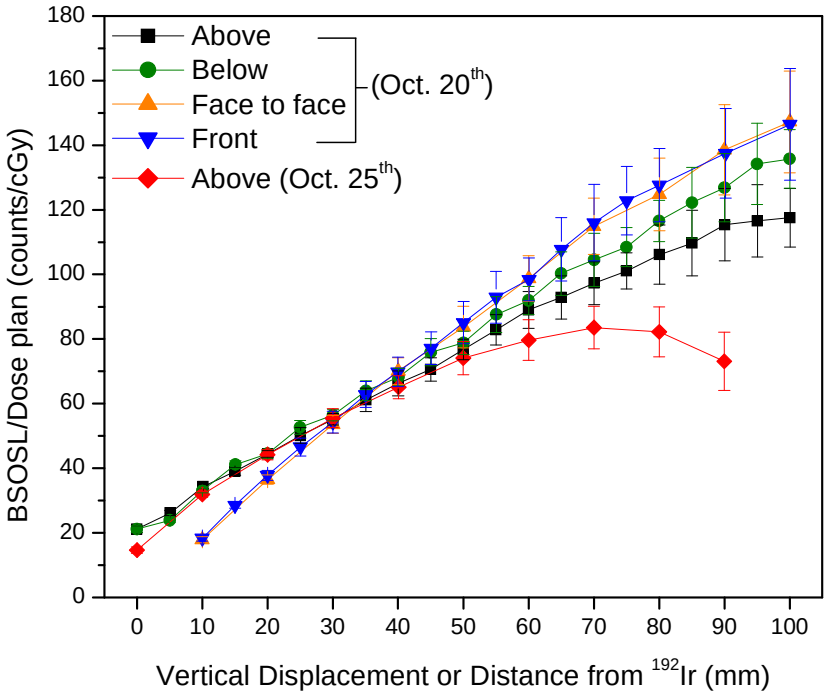


**Figure 5.31** Ratios of BSOSL over dose plan value using dose profile data taken in all positioning geometries on the 20$^{th}$ and above profile data taken on the 25$^{th}$. (Note: Only the profile above the source was taken on the 25$^{th}$, and at lower resolution than on the 20$^{th}$.)

in the ratio after 70 mm. Figure 5.31 may reveal a sensitization effect occurring within the KBr:Eu dosimeter over continued exposure to high dose rates, as the 'above' data were taken first, the 'below' data second, the 'front' data third, and the 'face-to-face' data was taken fourth (and last). This order is followed by an increase in the data in figure 5.31 from Oct. 20$^{th}$, at larger distances from the source. In fact, sensitization of the KBr:Eu was clearly observed over single measurements, and is discussed further in section 5.6. This effect does not satisfactorily explain the behavior of the data from Oct. 25$^{th}$.

The second objective of the experiments is to test the reproducibility of the system. The first test looked at the reproducibility of the system when the position and repositioned at different distances from the source. Figure 5.32 shows the unnormalized results from figure 5.28 ('above') taken as the KBr:Eu dosimeter was raised away from the source in steps of 5 mm. Also shown is a lower resolution repeat of that vertically ascending experiment taken several minutes later. The percent differences of the original and reproduced measurements are shown to range between 0.17 % and 3.63 %. The largest % difference is between the data taken furthest from the source, which is less relevant from a dosimetry perspective than that taken in the high dose regions. The second test looked at dosimeter positioning dependence by comparing the results obtained when the KBr:Eu was oriented in the two manners shown in figure 5.27. Table 5.4 reveals that this orientation dependence is small, with an average percent difference between the two orientations at the same distance from the source being 1.4%. A third experiment tested the reproducibility of the system after a period of just less than five days had passed. Figure 5.33 shows BSOSL from measurements taken at approximately

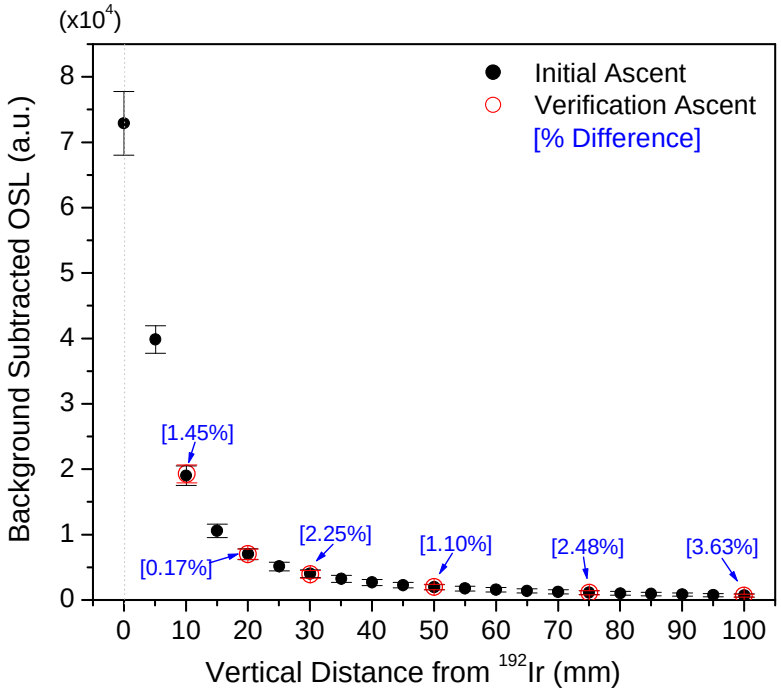


**Figure 5.32** Reproducibilty results after taking repeated OSL measurements at different distances above the $^{192}$Ir source. The error bars represent one standard deviation of the data taken over 60 s.

**Table 5.4** Percent difference comparison of averaged BSOSL data taken in the 'front' and 'face to face' geometries ($\mu_{front}$ and $\mu_{ftof}$, respectively) on October 20$^{th}$.

| Distance (mm) | $\mu_{front}$ | $\mu_{ftof}$ | % Diff. |
|---|---|---|---|
| 10 | 7770.28 | 7561.46 | *2.69%* |
| 20 | 4036.24 | 3897.50 | *3.44%* |
| 30 | 2626.77 | 2591.47 | *1.34%* |
| 40 | 1937.21 | 1944.05 | *0.35%* |
| 50 | 1538.08 | 1513.50 | *1.60%* |
| 60 | 1219.11 | 1222.13 | *0.25%* |
| 70 | 1036.07 | 1026.11 | *0.96%* |
| 80 | 851.19 | 832.55 | *2.19%* |
| 90 | 704.10 | 709.56 | *0.78%* |
| 100 | 585.82 | 589.03 | *0.55%* |

the same positions in the water phantom on the 20th and on the 25th. Percent differences between the results obtained are also given. For this comparison, the experimental conditions cannot be considered identical with respect to the $^{192}$Ir source since it has a half-life of 74 days, and in 5 days the activity has decreased by a non-trivial amount. According to the Nucletron dose plans developed on both days, the sources activity reduced by ~4.8% (see table 5.5). However, even when taking this into account by increasing the data in figure 5.33 (taken on on the 25th) by 5%, only the data between 20 mm and 50 mm approaches the general reproducibility requirements of ≤ 2% difference. The variation in the high dose gradient region close to the source may be due to small errors in placing the dosimeter on the 25th in the same position as it was on the 20th.

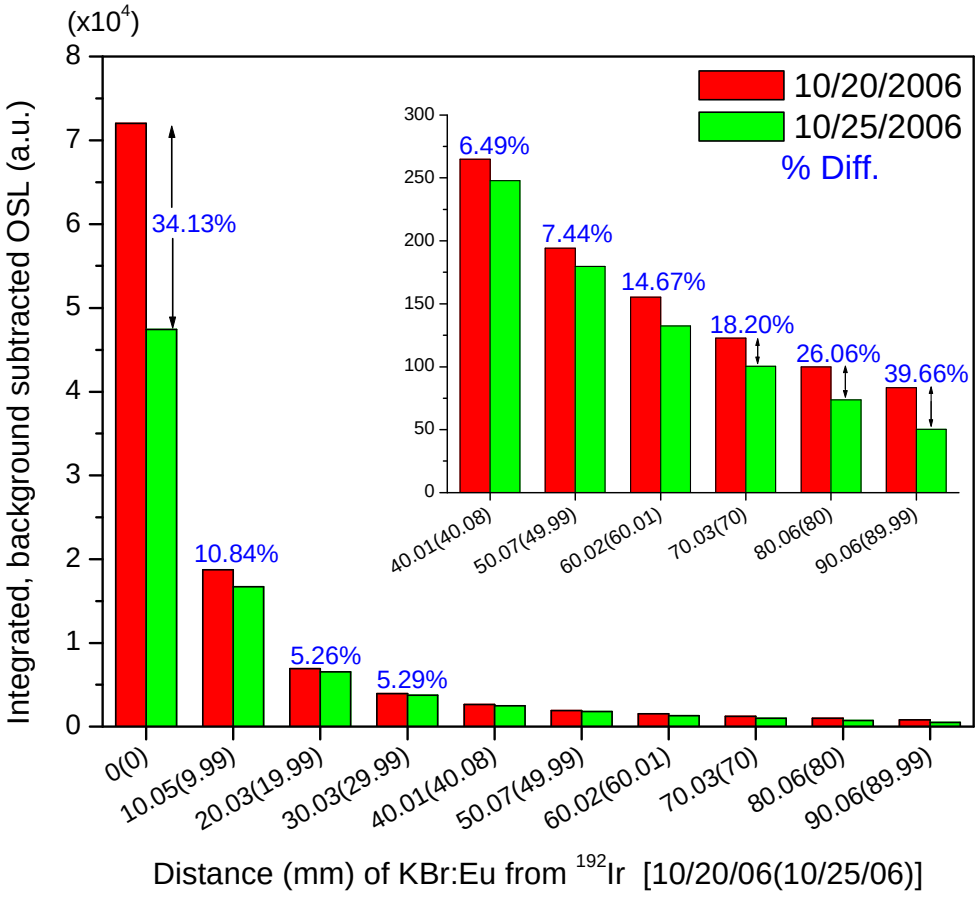


**Figure 5.33** BSOSL values obtained on Oct. 20th compared to the results obtained on Oct. 25th. Inset: Expanded view of results obtained at larger distances.

**Table 5.5.** Data from Nucletron dose planning reports showing different values pertaining to source decay.

| | **10/20/06** | **10/25/06** |
|---|---|---|
| **Air kerma (cGy/h cm$^2$):** | 34773.96 | 33098.70 |
| **% difference:** | *4.82%* | |
| **Decay Factor:** | 0.81 | 0.77 |
| **% difference:** | *4.84%* | |
| **Refer. Dose (cGy):** | 71.80 | 68.40 |
| **% difference:** | *4.74%* | |

## 5.5 Performance under 232 MeV Proton Therapy Beam

The use of protons for the treatment of cancer was first proposed by Robert R. Wilson (1946), as the first machines were being constructed that were capable of accelerating protons to energies that granted sufficient penetration ranges through biological tissues. Since then, proton therapy has flourished with the development of more sophisticated treatment planning and dose delivery techniques. These developments take advantage of the way that protons deposit energy in a medium, which is the key advantage of proton therapy for deep tumor treatment.

Fast moving protons have little time to interact with the atoms in the material through which they pass. Nevertheless, these brief interactions are enough to eventually slow the protons. They interact more severely as they slow down, and impart more and more energy to the atomic electrons and nuclei of the material. Thus, the linear energy transfer (LET) of the protons increases with depth of incident material until the protons are stopped, at which point they no longer deposit energy. The dose deposition (i.e.,

particle energy loss) along the range of 232 MeV protons in water is shown (normalized to the minimum at 3 cm) in figure 5.34. The energy deposited is fairly constant over the beginning of the range, but increases as the protons slow and ends in a sharp increase of very high dose at 33.9 cm known as the Bragg peak, after its discoverer, Sir William Henry Bragg. The dose deposition then falls to zero very quickly as the protons stop. In practice, the entire deposition profile is often referred to as the 'Bragg curve'. Proton radiation therapy takes advantage of the Bragg peak to deliver high doses to cancerous tissues while delivering relatively small entrance doses, and little to no exit dose to the patient.

The performance of the KBr:Eu system under proton beams was investigated over a two day period (July 15-16$^{th}$, 2006) at the Loma Linda University Medical Center (LLUMC), Loma Linda, California. The primary focus of the experiments at LLUMC centered around off-axis neutron scattering experiments conducted by Moyers et al. (2008) The KBr:Eu system was tested (with the dosimeter placed in the proton

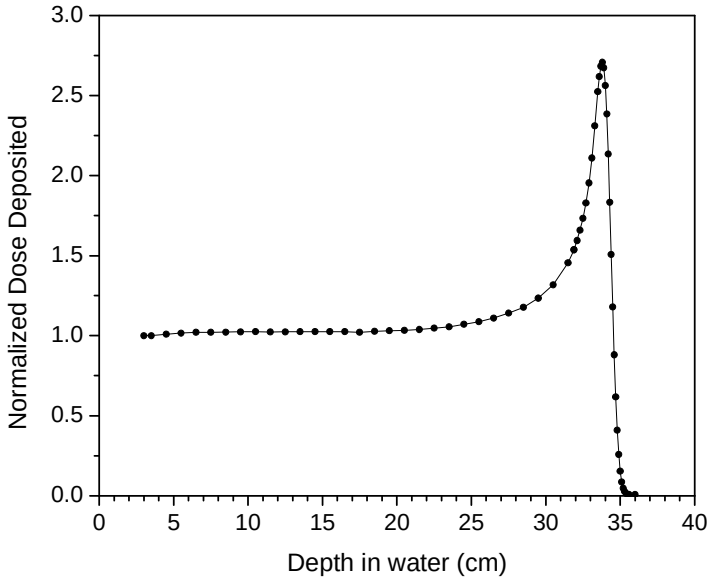


**Figure 5.34** Dose deposition curve (a.k.a. Bragg curve) measured with an ionization chamber for 232 MeV protons in water show the distinct Bragg peak at 33.9 cm.

beam) so that its presence did not interfere with the neutron measurements.

A Zero Gradient Synchrotron (ZGS) accelerated protons to 250 MeV (Coutrakon et al., 1994), The beam was routed to a rotating gantry centered on a patient table, and was output horizontally from a nozzle into a box water phantom 25 cm tall and 36 cm long. Figure 5.35 shows a photograph of the phantom setup inside of the treatment gantry. The protons lost energy traveling from the synchrotron to the nozzle, and so the final output energy was 232 MeV. The KBr:Eu dosimeter was placed on the beam-side surface of, and at various depths within the water phantom. At each position, 50 or 100 ms OSL measurements were triggered using an active RL monitoring scheme similar to that used for pulsed fluoroscopy (see section 5.2.2), since the protons were delivered not continuously, but in bursts (or 'spills') at a rate of 1 spill every 2.2 s. RL from the KBr:Eu crystal RL from the KBr:Eu crystal was observed by interrogating the PMT

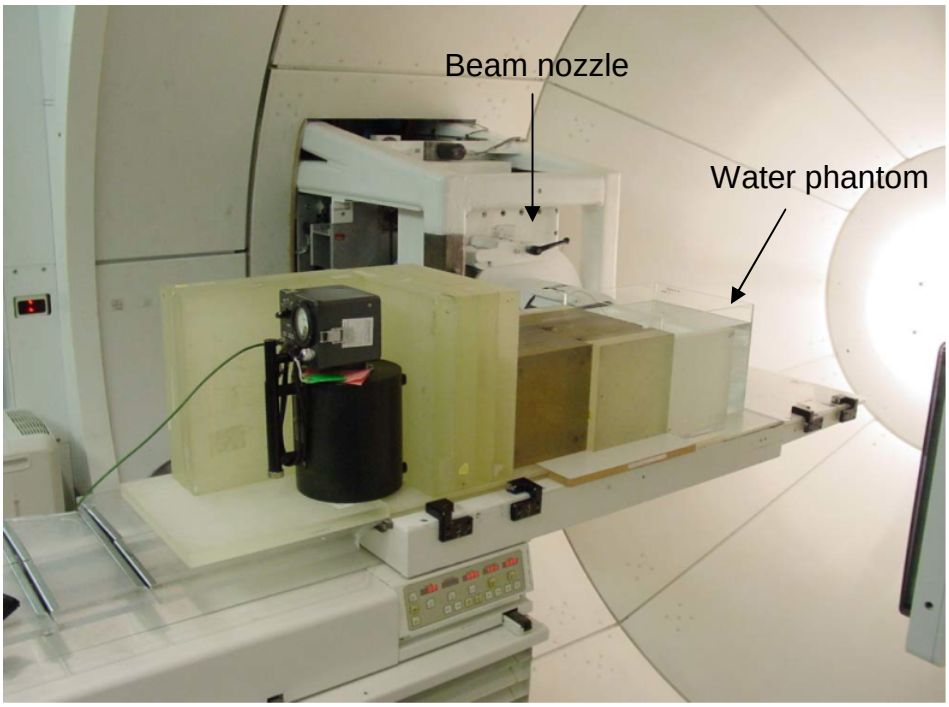


**Figure 5.35** Photograph of gantry #2 at LLUMC set up for off-axis neutron scattering measurements. The water phantom, located at the head of the table, was centered to the beam output nozzle. Plastic shielding blocks and a neutron detector are also shown. Modified from Moyers et al. (2008).

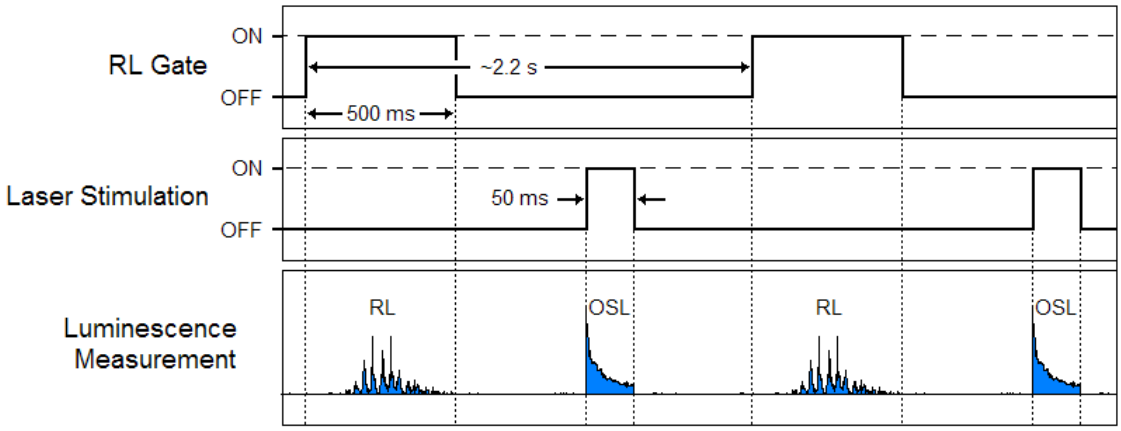


**Figure 5.36** OSL measurement timing scheme (not to scale) used during proton irradiation: proton spills were identified using the RL from KBr:Eu, and then an OSL measurement (50 ms, in this case) was made after a wait period of 500 ms.

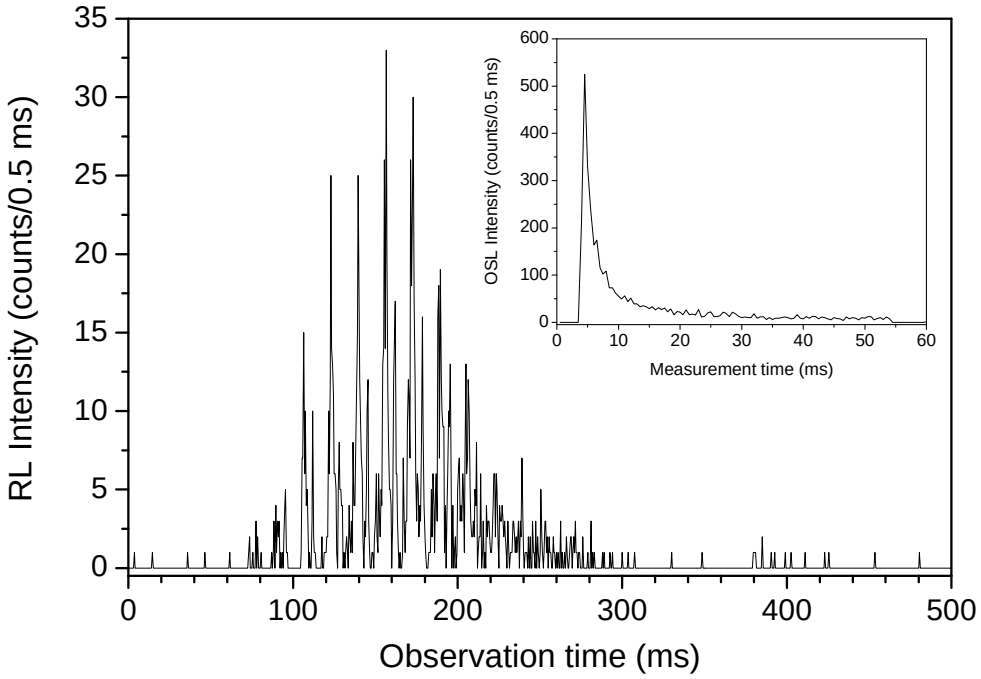


**Figure 5.37** RL signal due to a single proton spill, captured during active RL observation. Inset: The OSL signal from the measurement triggered by the spill RL.

at 2 kHz over consecutive 500 ms periods until a proton spill was identified. Upon the detection of a spill, optical stimulation was initiated after a 500 ms wait period to ensure that the spill period (~250 ms on average) had finished. After the OSL signal was recorded, the active RL monitoring for the next proton spill resumed. A diagram of the timing scheme is given in figure 5.36, while an RL signal due to a proton spill and the subsequent OSL decay, both measured at 5.5 cm depth in water are given in figure 5.37.

One of the most important characteristics of a capable proton dosimetry system is the ability to reproduce the Bragg curve at different depths in a medium. The response of the KBr:Eu system was tested at surface of the water phantom (0 cm) and at four depths inside the water phantom: 5.5, 15, 28.9, and 30.9 cm. The dosimeter was exposed to multiple ~100 s dose periods at each depth. Figure 5.38 shows the results of these dose deposition measurements. Both the averaged BSOSL and initial OSL intensities were obtained from the each data set, and are presented in figure 5.38a ad 5.38b, respectively. The vertical axes were scaled so that the 0 cm OSL data and the first Bragg curve datum matched. The most noticeable feature of the data in figure 5.38 is the rather poor correlation between the OSL results and the Bragg curve. Both the BSOSL and the initial intensities follow a similar pattern, though the initial intensity data at each particular depth are less scattered. Also detailed in figure 5.38a is the order in which the measurements were taken. The data on the surface of the phantom (at 0 cm) was taken late in the evening of July 15$^{th}$, while other data were taken throughout the day on the 16$^{th}$, starting in the morning. The over-response of the KBr:Eu to the proton irradiation may be due to sensitization effects similar to those possibly seen under $^{192}$Ir exposure (see figure 5.31), as the differences between the OSL data and the Bragg curve appear to

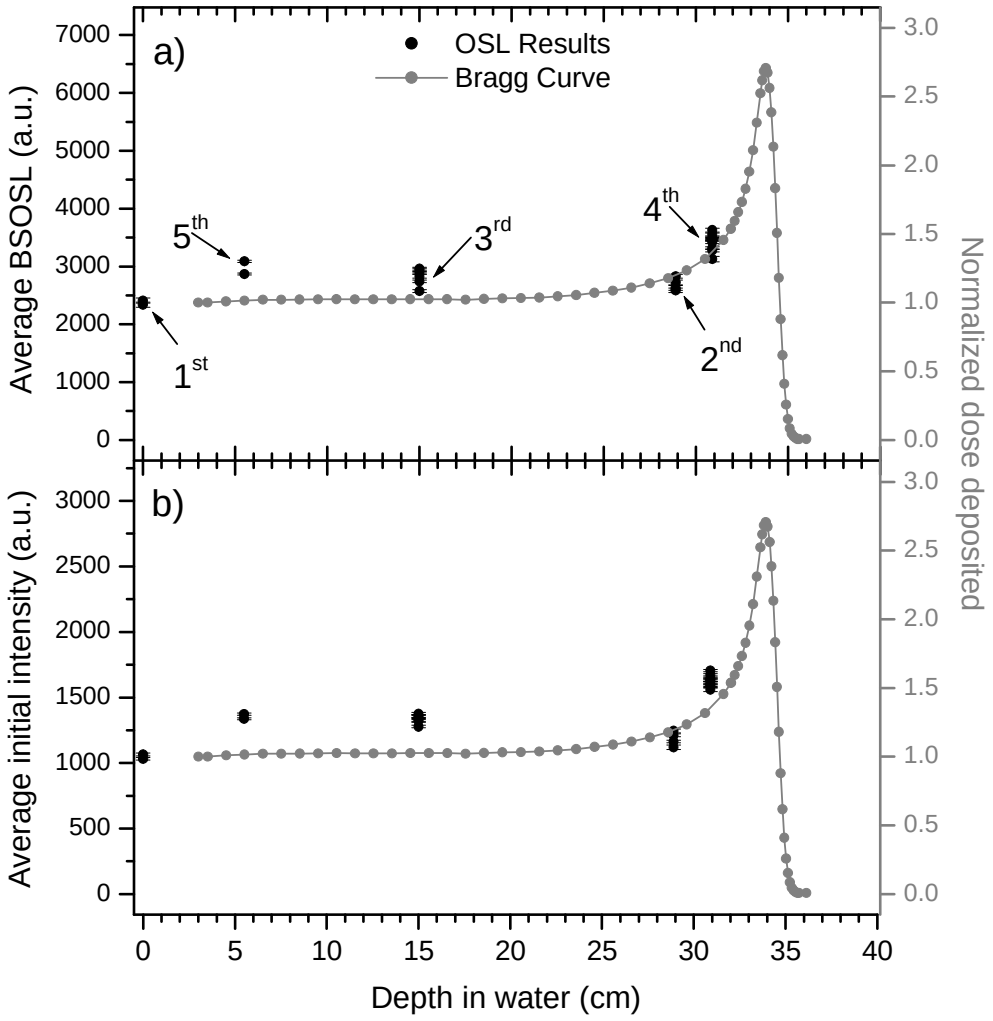


**Figure 5.38** Average a) BSOSL and b) initial OSL intensity results show sub-optimal dose deposition response when plotted against the normalized Bragg curve.

increase as the order of OSL measurement increases.

During the initial OSL measurements, the RL observation acquisitions were used solely for the triggering of an OSL measurement. However, over the course of the experimentation the control software for the KBr:Eu was modified in order to save the data acquired during the RL observation period. This would provide a record of how the dose rate to the KBr:Eu varied over the lifetime of the proton spill, and integration over the entire RL signal would give a value proportional to dose that could be compared to

the results of the following OSL measurement. Many of the RL acquisitions only captured part of the spill, which worked fine for triggering an OSL measurement, but were not useful for extracting dose information. However, other RL observations resulted in signals that captured an entire spill event. Examples of partial and complete spill captures are given in figure 5.39.

A correction to the apparent sensitization of the OSL signals was made by normalizing the average OSL results by the average of the total integrals of the RL signals. For this correction, only those RL and subsequent OSL signals that corresponded to a complete spill captured were used, all other RL and OSL data was ignored. Unfortunately, the RL signal data were only recorded during the final two measurements at 30.9 cm, and for the two measurements at 5.5cm. These normalized OSL results are presented in figure 5.40 as solid black points overlaying the Brag curve. The average of the two results at each depth is also given as hollow points. The scaling of the vertical axes in this case was chosen so that the average of the two 5.5 cm data would match the 5.5 cm data of the Bragg curve. Figure 5.40 shows a clear improvement in conforming to the Bragg curve at these depths when compared to figure 5.38. The initial intensity data is

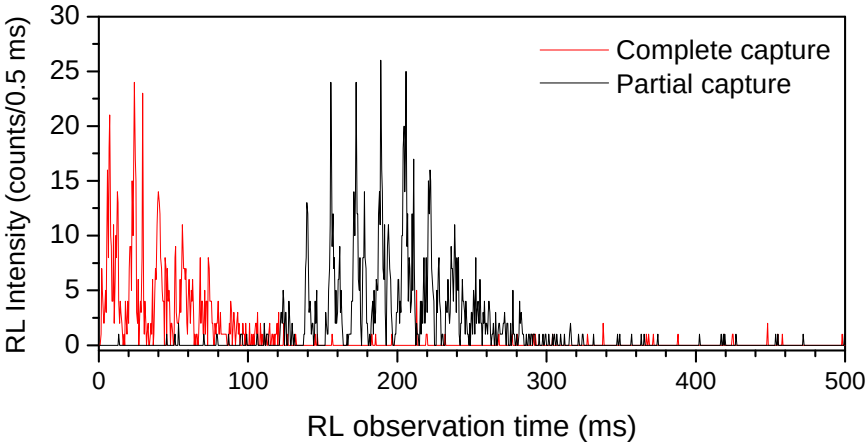


**Figure 5.39** Examples of RL signals obtained as the proton spill occurred completely within (black) and partially (red) within the RL observation period.

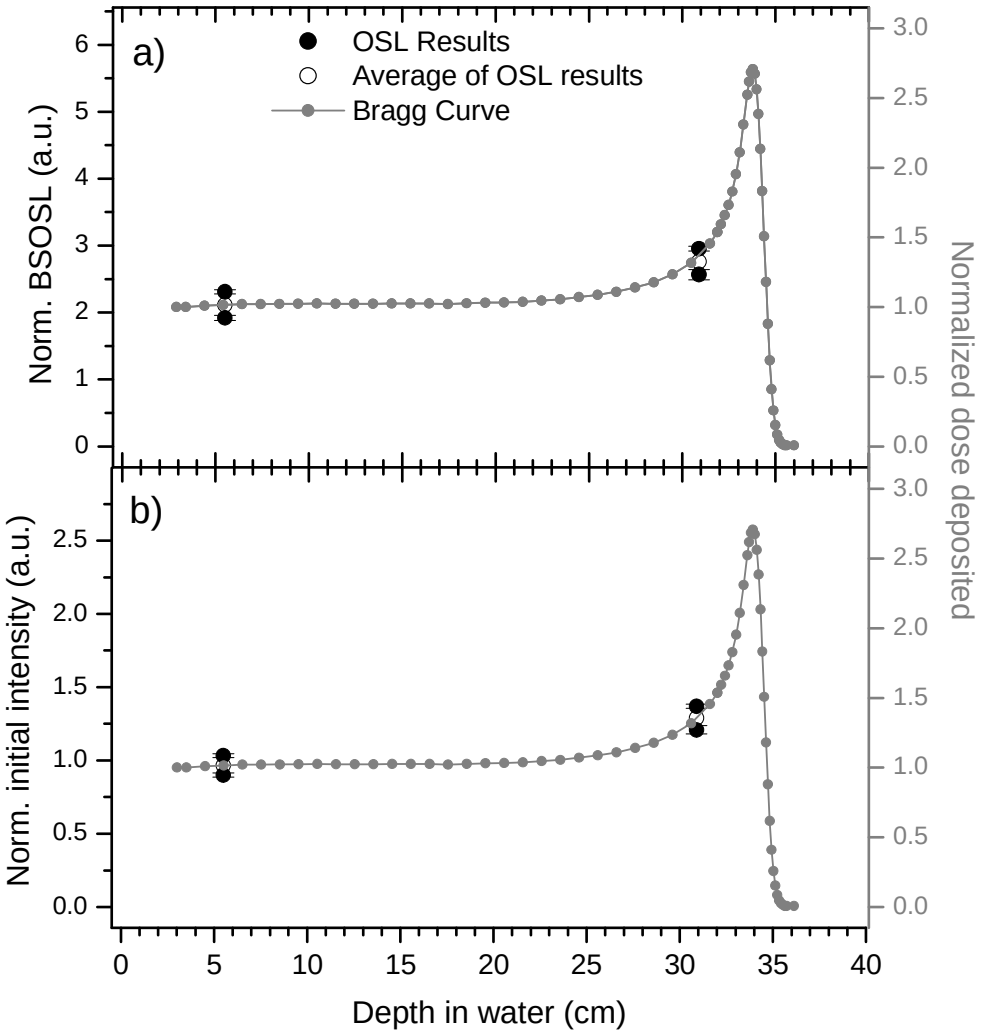


**Figure 5.40** Average a) BSOSL and b) initial OSL intensity results that have been normalized RL signal due to previous proton spills. The data show much better correlation than the data of figure 5.38 when plotted against the normalized Bragg curve. Hollow points represent the averages of the solid points.

again less scattered than the BSOSL data, and also show a closer matchto the Bragg peak at 30.9 cm. Though the data in figure 5.40 seem promising, no definite conclusions can be made towards the efficacy of this correction due to the minimal amount of data.

The results of the testing the KBr:Eu system under proton irradiation, while far from comprehensive, show that the system has potential for application as a capable, near-real-time dosimetry system in these radiation fields. High-resolution proton spill 'imaging' like that shown in figures 5.37 and 5.39 is by itself a capability that most commonly used

radiation detectors (such as TLDs and ionization chambers) do not possess, and could be of great use with respect to proton beam quality assurance. Sensitization of the KBr:Eu dosimeter in this high dose rate environment was observed over single 100 s exposures, much like it was observed under HDR brachytherapy source exposure, and is discussed further in the following section.

## 5.6 Further Characterization of KBr:Eu Towards a Simple Model for Describing OSL Mechanisms

The KBr:Eu system had thus far been tested under various medical radiation fields as an alternative, near-real-time dosimetry system for patients undergoing radiation therapy or radiodiagnosis, and as a radiation quality assurance device. Analysis of data taken close to an $^{192}$Ir brachytherapy source and near the Bragg peak position in a water phantom exposed to an energetic proton beam revealed that the acquired OSL signal exhibits complex sensitization effects. The OSL signal is thought to be composed of multiple components representing different luminescence mechanisms, and these components appear to sensitize at different rates with continued exposure.

Figure 5.41 shows OSL data from single, room-temperature measurements taken at OUHSC using a 10.57 Ci $^{192}$Ir brachytherapy seed, and at LLUMC under irradiation from a 232 MeV proton beam. See sections 5.4 and 5.5 for experimental details concerning the brachytherapy and proton beam experiments, respectively. Two different representations of the data are shown (each normalized to the average over the entire measurement); one

being the initial OSL intensities, and the other being the total integral over the entire OSL decay. The data in figure 5.41a are the average initial intensities and total integrals of 10 OSL measurements taken over 1 full second; while in figure 5.41b, the initial intensity data represent the sum of the first 2 ms of the OSL decay, and initial intensities and integrals are taken from single OSL signals. No background subtraction was used in this analysis, as the highest measured laser-on background while outside of a radiation field was low in comparison to the initial intensities or total integrals, accounting for less than 1% in either analysis.

In each of the plots in figure 5.41, if no sensitivity changes were occurring, then the data would be flat over time. Clearly this is not the case, as both types of OSL signal analysis show increases over time. Furthermore, the response of the total integral of the signal increases faster than that of the initial intensity under both radiation types. This is indicative of component specific sensitization, as the initial intensity is believed to be influenced mainly by a single fast decaying OSL component, while the total integral is governed by all OSL components.

The observed effect was most pronounced in regions of high dose rate. It is important to characterize this effect especially since the higher dose rate regions are of most interest to radiation oncologists and medical dosimetrists. Thus, in order to gain a better understanding of what processes may be responsible, additional characterization of KBr:Eu using related TL and OSL experiments were designed. An examination of the relationship between TL and OSL, specifically the effects of thermal annealing on the OSL signal and the effects of optical bleaching on the TL signal, follows.

KBr:Eu samples (~6×6×1mm in size) were cleaved from existing bulk material.

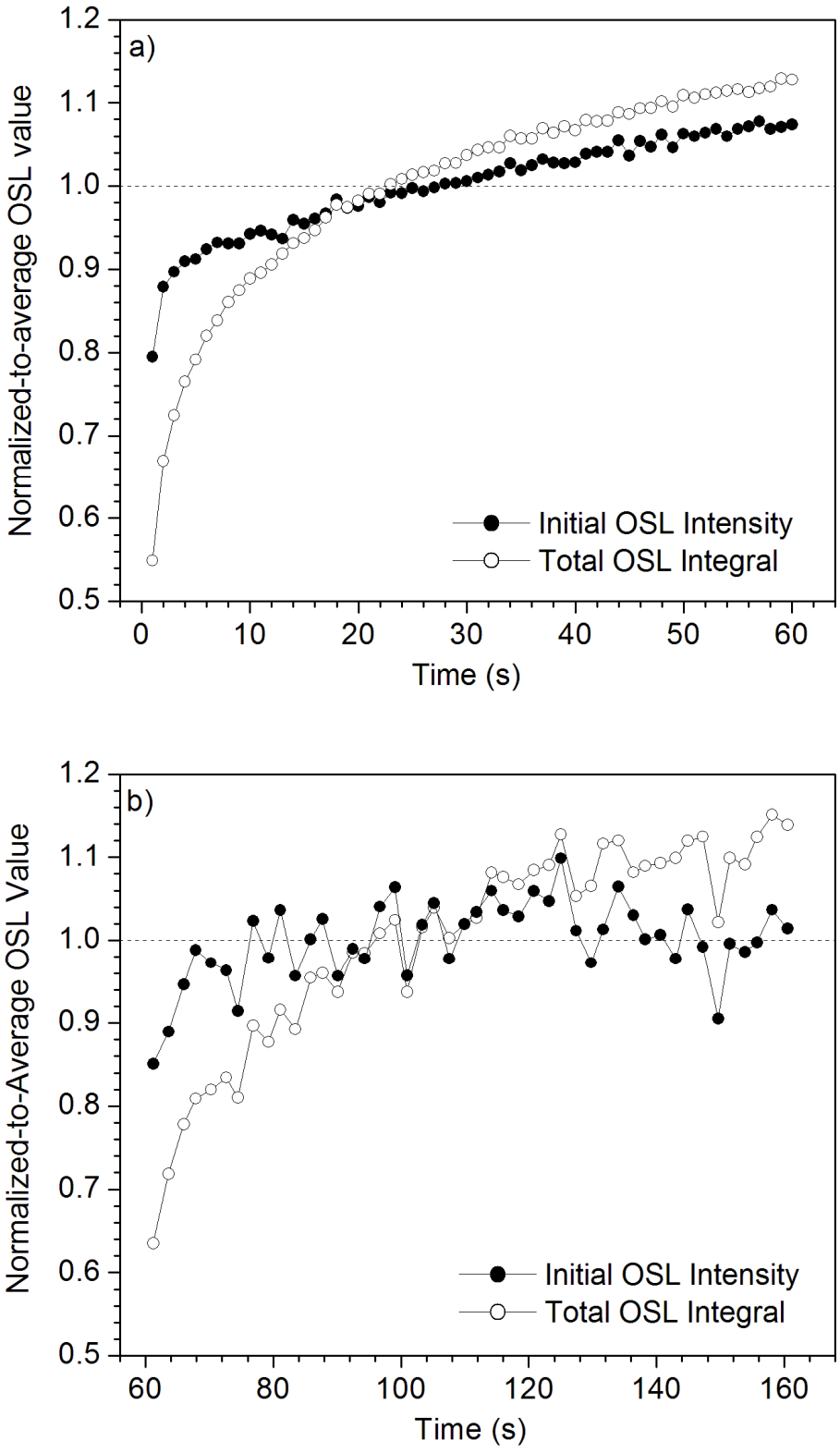


**Figure 5.41** Normalized initial intensity and total integral data for single measurements under a) $^{192}$Ir gamma and b) proton irradiation show sensitivity changes that occur at different rates.

Laboratory TL and OSL measurements were made using a Risø TL/OSL-DA-15 reader with an integrated $^{90}Sr/^{90}Y$ beta source. Doses of 350 mGy were given for all laboratory OSL and TL measurements using the integrated source. OSL was measured in the Risø reader for 100 s using stimulation from a broadband lamp filtered first with a 700 nm Chroma band-pass filter having a 50 nm FWHM, and later with a 650 nm narrow band pass filter from CVI (10 nm FWHM, model F10-650.0-5-1.00) to more closely match the diode laser ($\lambda$ = 658 nm) used in the KBr:Eu system. Three Kopp 5-58 filters were used in front of the Risø readers PMT. These configurations were also used for optical bleaching of the samples. After 700 nm bleaching, TL was performed by heating the samples from room temperature to 673 K at 1 K/s, with 3 x BG-39 placed before the PMT. The filters were changed to 3 x 5-58s after 650 nm bleaching to reduce unnecessary room light exposure to the PMT. TL measurements were performed in the dark, and the KBr:Eu was reset by annealing to 673 K and allowing to cool to room temperature prior to every laboratory OSL and TL measurement.

For the thermal annealing studies, OSL measurements were performed after the KBr:Eu samples had been β-irradiated, pre-heated at 5 K/s to a temperature between room temperature (~296 K) and 623 K, and allowed to cool to room temperature. Representative OSL signals following annealing to various temperatures are shown in figure 5.42, for both 700 and 650 nm stimulation. Also shown in figure 5.42 (insets) are the total integral of the OSL signal versus annealing temperature results. For 700 nm stimulation, the OSL signal is nearly unchanged until the annealing temperature approaches 363 K. At 363 K and above, the signal diminishes quickly until at 423 K no OSL signal remains. The OSL signal obtained using 650 nm stimulation light starts to

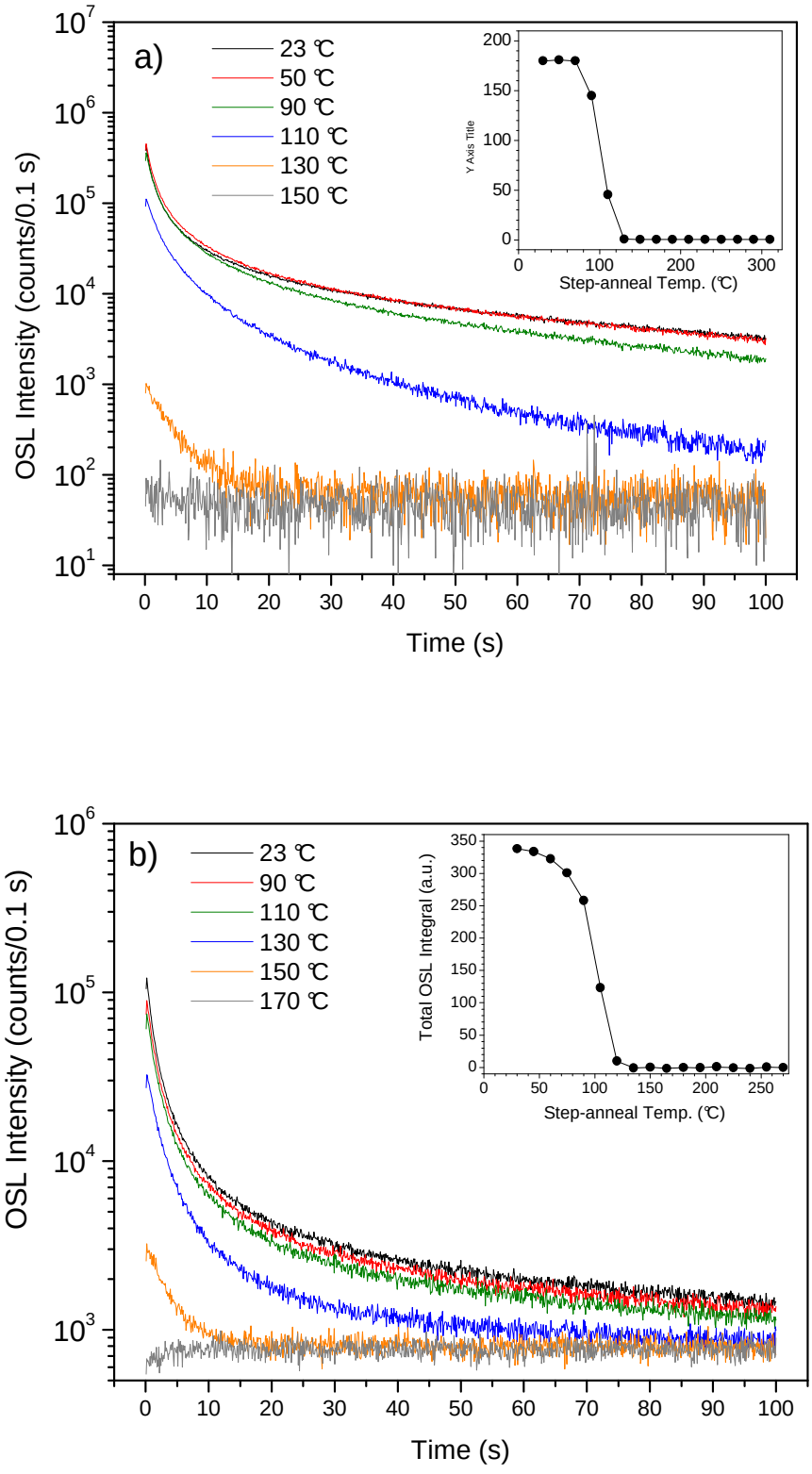


**Figure 5.42** OSL curves taken after step-annealing to various temperatures and stimulated with a) 700 nm and b) 650 nm light from a broadband lamp. Inset: Integrated area under the OSL curves as a function of anneal temperature.

decrease at ~358 K, and is totally annealed out by 408 K. Also, the OSL signal does not maintain its shape as the sample is annealed. A faster initial component appears to survive to higher temperatures than the slower component(s), such as that shown after annealing to 403 K (figure 5.42a) or 393 K (figure 5.42b).

For the step-bleaching experiments, TL was measured immediately after the sample had been β-irradiated and then optically bleached for periods ranging between 0 s and 1500 s. The data taken immediately after bleaching with 700 nm light are shown in figure 5.43a, and after 650 nm bleaching in figure 5.44a. The step-bleached TL results support the findings from the step-annealed OSL, and show that only those TL peaks below 420 K are depleted by bleaching with 700 and 650 nm light. However, with these bleach times of up to 1500s, and since short-term thermal fading effects on the OSL of KBr:Eu has been previously reported (Douguchi et al., 1999, Pedroza-Montero et al., 2000), it was also necessary to determine what effect room temperature fading had on these TL measurements. During each optical stimulation period, room temperature fading may have been assisting the bleach in depleting the TL signal. Thus, another step-bleached TL experiment was conducted such that instead of performing the TL measurement immediately after the bleach period as in figures 5.43a and 5.44a, an additional wait period was added after each bleach period so that the TL was always measured 1500 s after irradiation. For example, the first measurement consists of no bleach period, so the sample would be irradiated and TL would be recorded after a 1500 s wait. The second measurement would use a 5 s bleach period, so after the bleach was finished an additional 1495 s wait would take place before the TL measurement. This ensured that for each step-bleached TL curve, the KBr:Eu sample would be subject to

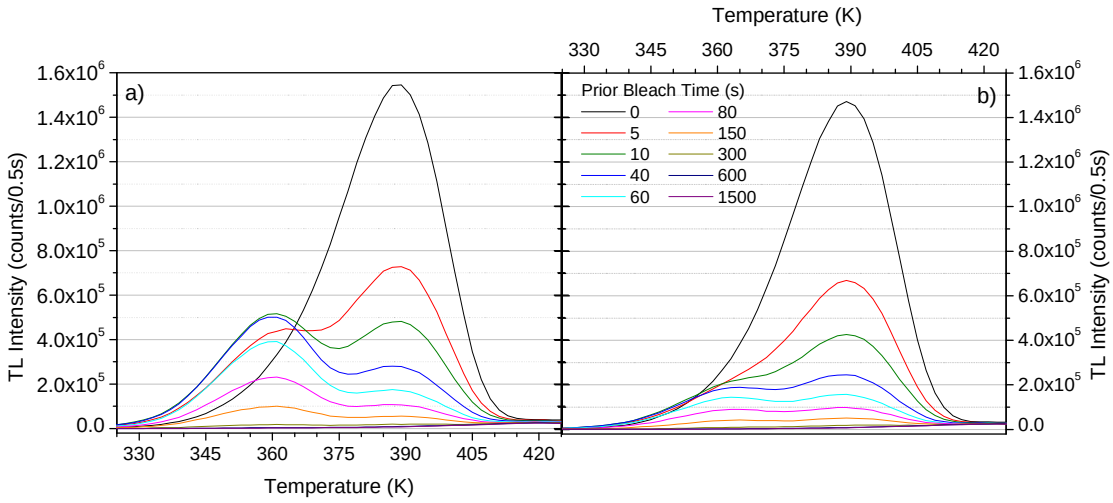


**Figure 5.43** Representative TL curves taken after step-bleaching with **700** nm light show both increasing and decreasing features. TL was measured a) immediately after bleaching and b) 1500 s after irradiation, regardless of bleach period.

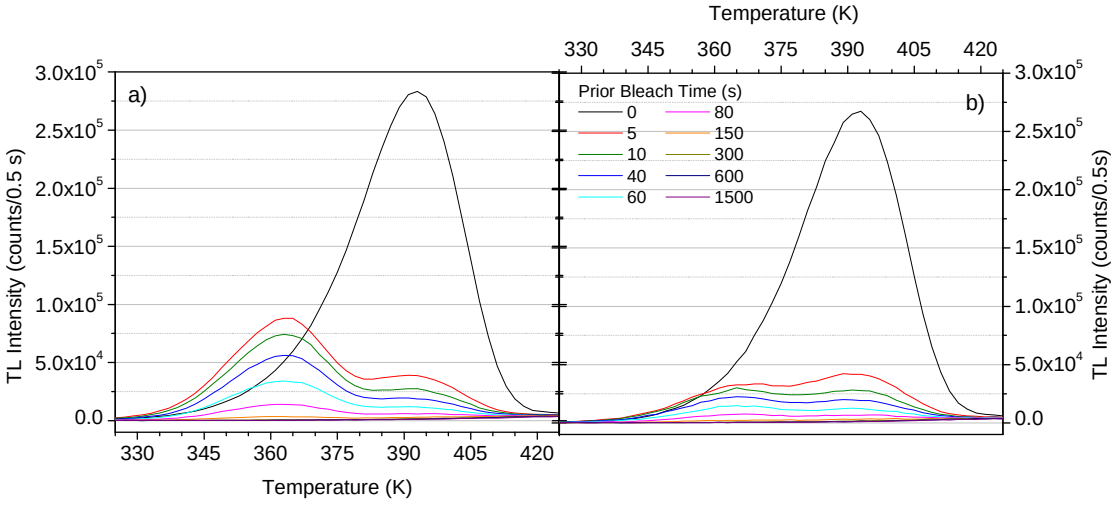


**Figure 5.44** Representative TL curves taken after step-bleaching with **650** nm light show both increasing and decreasing features. TL was measured a) immediately after bleaching and b) 1500 s after irradiation, regardless of bleach period.

fading over identical periods. Results of this second experiment are presented in figures 5.43b and 5.44b, for direct comparison to the TL measurements taken immediately after the end of the bleach periods. Figures 5.43 and 5.44 show that with no prior bleach period, the TL curves are dominated by a peak centred at 390 K. After just 5 s of bleaching, this peak is reduced significantly, while a lower temperature peak at 360 K has increased in intensity significantly above its previous level with no prior bleaching.

For the 700 nm bleached TL in figure 5.43a, the 390 K (from now on called peak 2) decreases rapidly while the 360 K peak (peak 1) continues to increase to a maximum after 10 s, which remains even after 40 s of bleach time. After 60 s, both peaks decrease at different rates and ultimately empty after several hundred seconds of bleaching. In figure 5.43b, peak 1 is reduced significantly more in each post-bleach measurement than in figure 5.43a, due to the additional fading. Peak 2 is only very slightly affected by the added fading period. In general, bleaching with 650 nm light (figure 5.44) gives similar results to those observed using 700 nm light. However, there are some differences that merit discussion. Peak 2 is depleted much faster using 650 nm light than with 700 nm light. Also, peak 1 reaches its apparent maximum after only a 5 s of 650 nm stimulation, and is quickly depleted over longer bleach times. Under 700 nm stimulation, peak 1 grows to a maximum after 10 s, and does not begin to reduce until more than 40 s of stimulation is applied. The bleach-plus-fading results in figure 5.44b show identical traits as that found using 700nm light – peak 1 is greatly reduced over 1500 s, while peak 2 is not.

During irradiation, electron hole pairs are formed such that some electrons are trapped and form F-centers, while some holes are captured by $Eu^{2+}$ ions to form $Eu^{3+}$.

Under optical stimulation, electrons are released from F-centers and eventually recombine with holes at the $Eu^{3+}$ ions. This in turn produces $Eu^{2+}$ ions in an excited state, which relaxes and emits 420 nm light via the $4f^{6}5d \rightarrow 4f^{7}$ transition (see section 3.2). Component-specific sensitivity changes of the OSL signal shown in figure 5.41 may be due to changes in and/or interactions between electron traps rather than hole traps (europium ions). Figure 5.45 illustrates the proposed electronic processes responsible for the different sensitization rates of the fast and slow components of KBr:Eu during an OSL measurement, and further explanation and description of the model follows.

Figure 5.42 shows that the slower OSL component (which itself may be comprised of multiple components) is more susceptible to thermal annealing at lower temperatures than the faster component, which remains even after the slower tail component has been totally annealed. These OSL results show that the electron traps responsible for the slow component have lower thermal stabilities than the fast component traps. As a result, the slow OSL component trap would be expressed in a TL curve as a peak at a lower temperature than the peak expressing the fast component traps. This is illustrated this in the model of figure 5.45 with the electron traps located close to the conduction band labeled 1 (shallow, responsible for the slow component) and2 (for the fast component). The step-bleaching TL signals in figure 5.43a and 5.44a show a steep rise in luminescence intensity of peak 1 after short bleach periods followed by a slow fall in intensity relative to peak 2, which decreases in intensity rapidly from the start. It appears that the electron trap represented by peak 2 (trap 2) has a much higher electron capture cross-section than trap 1, and so more charge is collected by trap 2 during irradiation. This explains the shapes of the TL peaks after no prior bleach. The rise

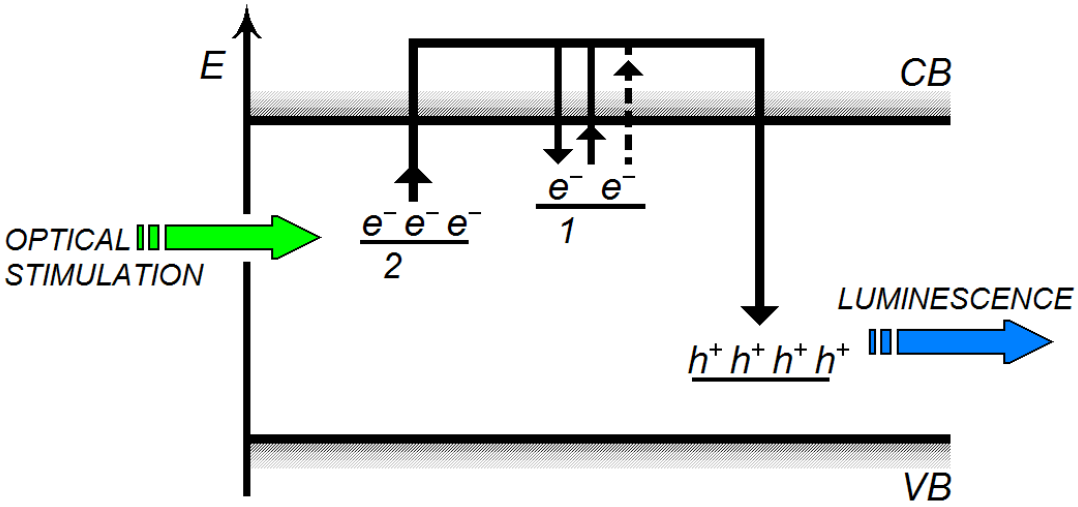


**Figure 5.45** Energy band diagram representing the proposed model of electronic processes during the measurement of OSL from KBr:Eu. Solid lines represent optical transitions of electrons ($e^-$) out of and into electron traps 1 and 2 and into the recombination center, which is populated with holes ($h^+$). The dotted line represents fading of trap 1 due to thermal detrapping of electrons.

in peak 1 intensity after 5 s of bleaching from its nearly insignificant level after 0 s bleach suggests that though trap 1 is not filled effectively during irradiation, it is filled considerably during optical stimulation. Since trap 2 is efficiently emptied during optical stimulation, it is essentially removed from the electron capture competition that took place between the two traps during irradiation, and trap 1 is allowed to accumulate charge, as represented in figure 5.45 by the downward solid arrow into trap 1. Comparing figure 5.43a to 5.43b and 5.44a to 5.44b reveals that peak 1 is vulnerable to room temperature fading. The two charge-release processes from trap 1 are depicted in figure 5.45 by a dotted upward line, representing thermal fading, and a solid upward line, representing detrapping due to optical stimulation. All released charge is depicted as recombining at a hole trap (e.g., a $Eu^{3+}$ ion) located near the valence band leading to excitation of $Eu^{2+}$ ions and luminescence at 420 nm.

The net result of these processes is that the total OSL signal is given as a sum of a fast decaying component (from trap 2) and a component that rises initially and then

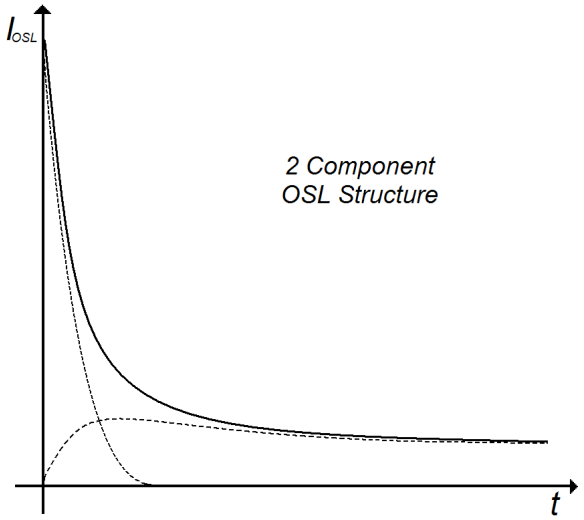


**Figure 5.46** Schematic illustration of OSL signal including the fast and slow components (dotted lines). The fast component is due to the release of charge from trap 2, and decays quickly. The slow component is due to trap 1, and grows initially due to charge transfer from trap 2. It then decreases slowly after trap 2 empties and charge transfer stops. Note: Illustration is not based on numerical evaluations of the proposed model.

decays slowly (from trap 1). A hypothetical OSL signal produced by theses simultaneous processes is depicted schematically in figure 5.46. The initial intensity is comprised almost solely of the fast component, since the slow component has not yet been filled. Trap 1 generates the slow component which is present at longer times. Though trap 1 undergoes photoionization and fadingover the entire length of the OSL measurement, these two processes only begin to slowly empty the trap after the fast component has decayed and the rapid charge transfer into trap 1 has stopped. It is clear that the slow component may not be completely bleached at end of each OSL measurement and that there may be an accumulation of charge in trap 1 surviving each subsequent measurement. This will produce an apparent sensitization of the OSL signal as the irradiation proceeds. The effect will clearly be more pronounced for the slower component (i.e. the total OSL integral) than for the faster component (the initial intensity).

# CHAPTER VI

# CONCLUSIONS AND FUTURE WORK

Two remote radiation dosimetry systems have been developed and tested under various conditions with the goal of providing alternative dosimetry techniques for environmental and medical applications. The work focused primarily on assessing the performance of these systems under ionizing radiation fields that closely match those found at nuclear waste storage sites, and in hospital radiodiagnostic or radiotherapy facilities. Based on this performance, it was necessary, in some cases, to modify or further characterize the systems to better adapt to the various radiation fields.

Modifications were made that allowed the $Al_2O_3$:C-based environmental system to maintain a high sensitivity while being made fully portable. Preliminary development of a high-sensitivity environmental monitoring system showed that doses as low as 1-5 μGy could be detected using the POSL of $Al_2O_3$:C. This level of performance was determined using radionuclides that are commonly found in high-level nuclear waste such as $^{60}Co$, $^{90}Sr/^{90}Y$ and $^{137}Cs$. Based on the limit of contaminant concentration at which soil can be released for unrestricted use (1.85 $Bq/cm^3$), it was determined that the system would be capable of measuring signals from $^{137}Cs$ and $^{90}Sr/^{90}Y$ in only a few days. This provides a significant improvement in temporal resolution compared to quarterly soil sampling.

The capability of the bench-top system was encouraging, and so the environmental

monitoring system was rebuilt into a consolidated, portable form. This system was then tested against other common environmental radionuclides: $^{232}$Th and $^{226}$Ra. Both of these sources are considered to be calibration standards, with the $^{232}$Th presented in the form of silica-filled epoxy blocks acting as a standard soil stimulant. The performance of the portable environmental system shows a detection limit of ~3 μGy, which is at least as good as that of the bench-top system (MDD ≈ 5 μGy).

Two simple computer models were developed using geometries that closely matched those of the experimental conditions using the $^{232}$Th and $^{226}$Ra sources. The dose given to the dosimeter was determined by first finding the mass attenuation of emitted photons through the source and detector probe materials, and then calculating the energy deposited in the dosimeter volume using the mass-energy absorption coefficients provided by NIST (see footnote on p 81).

The $^{232}$Th model produced an average dose that was 26.6% less than that actually measured using the portable system. This discrepancy is due mainly to the fact that the composition of the epoxy blocks that contain the $^{232}$Th is largely unknown. This is particularly problematic for this model since the vast majority of the distance traveled by the photons emitted by the thorium and its daughters is in the block material. The model is therefore very sensitive to the choice of mass attenuation coefficients pertaining the epoxy blocks. Little to no record exists of the exact construction methods used to build the blocks. However, further improvement to this model could be made by obtaining accurate compositional information using x-ray microanalysis of a fragment of one of the blocks. The model pertaining to the radium, on the other hand, consists of materials that are all well-known. The radium model reports a dose that is only 7.2% less than that

actually measured using the portable system. This shows that the two models - which are essentially the same, the only significant difference being the geometries used – are capable of validating the measurements of the portable environmental monitoring system, as long as the correct coefficients are used.

Suggested future work with the environmental monitoring system is to gain further sensitivity improvements. This includes finding an optimal coupling scheme between the $Al_2O_3$:C dosimeter and the reader system. Using a tapered fiber optic cable improves the light collection, but commercial off-the-shelf tapers are limited to ~3 mm diameter. Using dosimeters with reduced diameters of 3 mm instead of the standard 5 mm, but increased thicknesses may increase stimulation and luminescence collection efficiency while maintaining a sizeable dosimeter volume. The use of refractive index-matching gels between the dosimeter ($n$ = 1.77) and the silica fiber taper ($n$ = 1.45) has been investigated in the past, but the gels tested introduced an increased background to the OSL signal. Further investigation of other types of gels may provide some benefit. Using a gated PMT for luminescence detection may also increase sensitivity. Less optical filtration would then be needed between the dosimeter and the PMT since the PMT would be effectively turned off during the laser pulse.

Further testing of the portable environmental system should include the installation and periodic interrogation of ground probes in a real outdoor environment. The soil surrounding the ground probe could be analyzed using gamma spectroscopy, so that the local radionuclide distribution could be verified and used as a control against the POSL measurements.

The KBr:Eu OSL system has been tested under a variety of medical radiation sources. The system's near-real-time capabilities have allowed the system to record and present dose information as fast as the radiation was delivered, and represent an alternative to passive dosimeters (such as TLDs) that can only provide dose information some time after the irradiation has finished. Near-real-time dose reporting permits faster quality assurance (QA) testing, Faster testing may also result in more thorough QA, as more radiation delivery conditions could be tested in the same (or less) time as with passive detectors. The small dosimeter volume (~2 $mm^3$) grants a higher-resolution spatial dose profiling capability that is not easily obtained with other active detectors like ionization chambers.

The results presented in this work show that fine structural detail may be discerned using the KBr:Eu system, particularly for the highly dynamic fields of helical CT scanning and synchrotron-produced high-energy proton beams. Also, modifications made for active monitoring of the RL from KBr:Eu show that reproducible OSL acquisition is possible under continuous irradiation, or under pulsed irradiation of arbitrary pulse width and frequency.

The KBr:Eu dosimeter exhibited an energy dependence under exposure to fluoroscopic x-rays with peak voltages ranging from 60 kVp to 120 kVp. This response is due to a combination of the mass-energy absorption of KBr and the spectral distribution of x-rays emitted from the fluoroscopy machine. The mass-energy absorption of KBr is well-known. However, x-ray spectra between medical systems can vary, depending on the filtration used between the x-ray tube and the patient (see figure 5.5). So, in order to properly correct the OSL data, the equivalent photon energy of the x-ray machine is

needed. The equivalent photon energy represents the single x-ray energy that best correlates to the output of the entire x-ray spectrum, and can be determined by finding the half-value layer of a material placed under the x-ray source (Johns and Cuningham, 1983; Trout et al., 1960).

Characterization of the OSL and TL of KBr:Eu was performed to investigate the causes of sensitization of the OSL signals that has been observed under many different medical radiation fields. The OSL from KBr:Eu was found to result from the interaction of two charge traps with differing thermal stabilities and photo-ionization cross-sections. A simple model was developed to describe electronic processes that may be responsible for the component-specific sensitization of the OSL decay curve under high dose rate irradiation and red light stimulation. Numerically solving rate equations describing this model and a comparison between the solutions to the measured OSL data could provide verification of this model, or lead to refinements that improve the accuracy of the model. Development of KBr:Eu crystals with fewer shallow traps may also solve the OSL sensitization problem.

The KBr:Eu reader system may be improved by replacing the existing diode laser with a higher power light source. This would increase initial OSL intensity and decrease the amount of time it takes to acquire a full OSL decay, and would allow for an increase in measurement rate from the current 10 Hz. A higher laser power may also grant a sensitivity comparable to the existing system, but with an even smaller dosimeter volume.

Overall, the results of developing and characterizing the two remote dosimetry systems have shown that both systems represent potential useful alternatives to existing environmental and medical dosimetry techniques.

# REFERENCES


Akselrod, M. S., Kortov, V. S., Kravertsky, D. J., Gotlib, V. I. Highly sensitive thermoluminescent anion-defective $\alpha$-$Al_2O_3$:C single crystal detectors. *Rad. Prot. Dosim.* **32**, 15-20, 1990.

Akselrod, M. S., Kortov, V. S., Gorelova, E. A. Preparation and properties of $\alpha$-$Al_2O_3$:C. *Rad. Prot. Dosim.* **47**, 159-164, 1993.

Akselrod, M. S., Lucas, A. C., Polf, J. C., McKeever, S. W. S. Optically stimulated luminescence of $Al_2O_3$. *Rad. Meas.* **29**, 391-399, 1998.

Akselrod, M. S., McKeever, S. W. S. A radiation dosimetry method using pulsed optically stimulated luninescence. *Rad. Prot. Dosim.* **81**, 167-176, 1999.

Akslelrod, A. E., Akselrod, M. S. Correlation between OSL and the distribution of TL traps in $Al_2O_3$:C. *Rad. Prot. Dosim.* **100**, 217-220, 2002.

Andersen, C. E., Aznar, M. C., Bøtter-Jensen, L., Bäck, S. Å. J., Mattson, S., Medin, J. Development of optical fiber luminescence techniques for real time in vivo dosimetry in radiotherapy. *Proc. Int. Symp. Vienna Standards and Codes of Practiec in Medical Radiation Dosimetry.* **2**, 353-360, 2003.

Bøtter-Jensen, L., Bulur, E., Duller, G. A. T., Murray, A. S. Advances in luminescence instrument systems. *Radiat. Meas.* **32**, 523-528, 2000

Bøtter-Jensen, L., McKeever, S. W. S., Wintle, A. G. *Optically stimulated luminescence dosimetry.* Elsevier Science B. V., Amsterdam, 2003.

Braunlich, P. F., Kelly, P., Fillard, J.-P. Thermally stimulated luminescence and conductivity. *Thermally stimulated relaxation in solids.* Springer-Verlag, Berlin, 1979.

Braunlich, P. F., Jones, S. C., Sweet, J. A. A remote fibre-optic microdosimetry reader. *Rad. Prot. Dosim.* **6**, 103-107, 1983.

Brewer, J. D., Jeffries, B. T., Summers, G. P. Low-temperature fluorescence in sapphire. *Phys. Rev. B* **22**, 4900-4906, 1980.

Buenfil, A. E., Brandan, M. E. Dosimetric properties of europium-doped potassium bromide thermoluminescent crystals. *Health Phys.* **62**, 341-343, 1992.

Bull, R. K., McKeever, S. W. S., Chen, R., Mathur, V. K., Rhodes, J. F., Brown, M. D. Thermoluminescence kinetics for multipeak glow curves produced by the release of electrons and holes. *J. Phys. D: Appl. Phys.* **19**, 1321-1334, 1986.

Bulur, E. An alternative technique for optically stimulated luminescence (OSL) experiment. *Rad. Meas.* **26**, 701-709, 1996.

Castañeda, B., Pedroza-Montero, M., Meléndrez, R., Barboza-Flores, M. Potassium halide detectors: novel results and applications. *Phys. Stat. Sol. B.* **220**, 663-669, 2000.

Chen, R., McKeever, S. W. S. *Theory of thermoluminescence and related phenomena.* World Scientific Publishing Co., Singapore, 1997.

Chruścińska, A. The influence of trap coupling effect on the shape of optically stimulated luminescence decay. *Radiat. Meas.* **43**, 213-217, 2008.

Coutrakon, G., Hubbard, J., Johanning, J., Maudsley, G., Slaton, T., Morton, P. A performance study of the Loma Linda proton medical accelerator. *Med. Phys.* **21**, 1691-1701, 1994.

Curie, D. *Luminescence in crystals.* (G. F. J. Garlick, Trans) Methuen and Co., Ltd/Wiley and Sons, Inc., London, 1963.

DOE. Long-term, post-closure radiation monitoring system (LPRMS). *Innovative technology summary report DOE/EM-0613.* Industry programs subsurface contaminants focus area, 2001.

Douguchi, Y., Nanto, H., Sato, T., Imai, A., Nasu, S., Kusano, E., Kinbara, A. Optically stimulated luminescence in Eu-doped KBr phosphor ceramics. *Radiat. Prot. Dosim.* **84**, 143-148, 1999.

Draeger, B. G., Summers, G. P. Defects in unirradiated $\alpha$-$Al_2O_3$:C. *Phys. Rev. B* **19**, 1172-1177, 1979.

Dussel, G. A., Bube, R. H.. The theory of thermally stimulated conductivity in a previously photoexcited crystal. *Phys. Rev.* **155**, 764-779, 1967.

Edmund, J. M. Effects of temperature and ionization density in medical luminescence dosimetry using $Al_2O_3$:C. *Doctoral Dissertation*, Risø National Laboratory/Technical University of Denmark. Roskilde, Denmark, 2007.

Eisberg, R., Resnick, R. *Quantum physics of atoms, molecules, solids, nuclei, and particles.* John Wiley and Sons, Inc., New York, 1985.

Evans, B. D., Stapelbroek, M. Optical properties of the $F^+$ center in crystalline $Al_2O_3$:C. *Phys. Rev. B* **18**, 7089-7098, 1978.

Garlick, G. F. J., Gibson, A. F. The electron trap mechanism of luminescence in sulphide and silicate phosphors. *Proc. Phys. Soc.* **60**, 574-590, 1948.

Gaza, R. A fiber-optics, real-time dosimeter based on optically stimulated luminescence of $Al_2O_3$:C and KBr:Eu, for potential use in the radiotherapy of cancer. *Doctoral Dissertation,* Oklahoma State University. Stillwater, Oklahoma, 2004.

Gaza, R., McKeever, S. W. S. A real-time, high-resolution optical fibre dosemeter based on optically stimulated luminescence (OSL) of KBr:Eu, for potential use during the radiotherapy of cancer. *Rad. Prot. Dosim.* **120**, 14-19, 2006.

Gerber, M. S. *On the home front – The cold war legacy of the Hanford Nuclear Site*. University of Nebraska Press, Lincoln, 2002.

Goldman, L. W. Principles of CT: radiation dose and image quality. *J. Nucl. Med. Tech.* **35**, 213-225, 2007.

Grimmeiss, H. G., Ledebo, L. A. Photo-ionization of deep impurity levels in semiconductors with non-parabolic bands. *J. Phys. C: Solid State Phys.* **8**, 2615-2626, 1975.

Hernandez ,A. J., Cory, W. K., Rubio, O. J. Optical investigation of divalent europium in the alkali chlorides and bromides. *J. Chem. Phys.* **72**, 198-205, 1980.

Hernandez ,A. J., Lopez, F. J., Murrieta S. H., Rubio, O. J. Optical absorption, emission, and excitation spectra of $Eu^{2+}$ in the alkali halides. *J. Phys. Soc. Jap* . **50**, 225-229, 1981.

Hobbs, L. W., Hughes, A. E., Pooley, D. Nature of interstitial clusters in alkali halides. *Phys. Rev . Lett.* **28**, 234-236, 1972.

Hult, M., Preuße, W., Gasparro, J., Köhler, M. Underground gamma-ray spectrometry. *Acta Chim. Slov*. **53**, 1-7, 2006.

Huston, A. L., Justus, B. L., Falkenstein, P. L., Miller, R. W., Ning, H., Altemus, R. Remote optical fiber dosimetry. *Nucl. Inst. Methods Phys. Res. B.* **184,** 55-67, 2001.

ICRP. Non-stochastic effects of irradiation. ICRP Publication 41. *Ann. ICRP* **14**, 1-33, 1984.

ICRP. 1990 Recommendations of the International Commission on Radiological Protection. ICRP Publication 60, *Ann. ICRP* **21**, 1990.

ICRP. The 2007 recommendations of the International Commission on Radiological Protection. ICRP Publication 103. *Ann. ICRP* **37**, 2007.

Jennings, W. A. Evolution over the past century of quantities and units in radiation dosimetry. *J. Radiat. Prot.* **27**, 5-16, 2007.

Johns, H. E., Cunningham, J. R. *The physics of radiology, 4th ed*. Charles C. Thomas • Publisher, Illinois, 1983.

Kelly, P., Braunlich, P. Phenomenological theory of thermoluminescence. *Phys. Rev. B* **1**, 1587-1595, 1970.

Klein, D. M., Yukihara, E. G., McKeever, S. W. S., Durham, J. S., Akselrod, M. S. *In-situ*, long-term monitoring system for radioactive contaminants. *Rad. Prot. Dosim.* **119**, 421-424, 2006.

Lee, K. H., Crawford, Jr., J. H. Luminescence of the *F* center in sapphire. *Phys. Rev . B* **19**, 3217-3221, 1979.

Lewandowski, A. C., McKeever, S. W. S. Generalized description of thermally stimulated processes without the quasiequilibrium approximation. *Phys. Rev. B* **43**, 8163-8178, 1991.

Lewandowski, A. C., Markey, B. G., McKeever, S. W. S. Analytical description of thermally stimulated luminescence and conductivity without the quasiequilibrium approximation. *Phys. Rev. B* **49**, 8029-8047, 1994.

Lucas, A. C. *Private communication*, October 2008.

May, C. E., Partridge, J. A. Thermoluminescent kinetics of alpha-irradiated alkali halides. *J. Chem. Phys.* **40**, 1401-1409, 1964.

McCollough, C. H., CT dose: how to measure, how to reduce. *Health Phys.* **95**, 508-517, 2008.

McKeever, S. W. S. *Thermoluminescence of solids.* Cambridge University Press, Cambridge, 1985.

McKeever, S. W. S., Markey, B. G., Akselrod, M. S. Pulsed optically-stimulated luminescence dosimetry using $\alpha$-$Al_2O_3$:C *Rad. Prot. Dosim.* **65**, 267-272, 1996.

McKeever, S. W. S., Agersnap Larsen, N., Bøtter-Jensen, L., Mejdahl, V. OSL sensitivity changes during single aliquot procedures: computer simulations *Radiat. Meas.* **27**, 75-82, 1997a.

McKeever, S. W. S., Bøtter-Jensen, L., Agersnap Larsen, N., Duller, G. A. T. Temperature dependence of OSL decay curves: experimental and theoretical aspects *Radiat. Meas.* **27**, 161-170, 1997b.

McKeever, S. W. S., Akselrod, M. S., Colyott, L. E., Agersnap Larsen, N., Polf, J. C., Whitley, V. Characterisation of $Al_2O_3$ for use in thermally and optically stimulated luminescence dosimetry. *Rad. Prot. Dosim.* **84**, 163-168, 1999.

Milman, I. I., Kortov, V. S., Nikiforov, S. V. Luminescence of the *F* center in sapphire. *Rad. Meas.* **29**, 401-410, 1998.

Molnár, G., Benabdesselam, M., Borossay, J., Iacconi, P., Lapraz, D., Akselrod, M.S. Influence of the irradiation temperatire on the dosimetric and high-temperature TL peaks of $Al_2O_3$:C. *Rad. Prot. Dosim.* **100**, 139-142, 2002.

Morgan, K. Z. Rolf. M. Sievert: The pioneer in the field of radiation protection. *Health Physics.* **31**, 263-264, 1976.

Moyers, M. F., Benton, E. R., Ghebremedhin, A., Coutrakon, G. Leakage and scatter radiation from a double scattering based proton beamline. *Med. Phys.* **35**, 128-144, 2008.

Nanto, H., Miyazaki, M., Imai, I., Komori, H., Douguchi, Y., Kusano, E., Kinabara, A. New photostimulable phosphor materials for digital radiography. *IEEE Trans. Nuc. Sci.* **47**, 1620-1624, 2000.

NRC. *Radioactive waste: production, storage, disposal*. (NUREG/BR-0216, Rev. 2) Office of public relations, Washington, D. C., 2002

NRC. Licensing requirements for land disposal of radioactive waste. *Code of Federal Regulations* Title 10, Pt. 61.55-56, 2007.

Pais, A. *Inward bound: of matter and forces in the physical world.* Oxford University Press, New York, 1986.

Peakheart, D. W. Evaluation of clinically feasible dosimetry systems for CT quality assurance and dose optimization. *Masters Thesis, The University of Oklahoma Health Sciences Center Graduate College.* Oklahoma City, Oklahoma, 2006

Pedroza-Montero, M., Castañeda, B., Meléndrez, R., Piters, T. M., Barboza-Flores, M. Thermoluminescence, optical stimulated luminescence and defect creation in europium doped KCl and KBr crystals. *Phys. Stat. Sol. B.* **220**, 671-676, 2000.

Pérez-Salas, R. Meléndrez, R., Aceves, R., Rodriguez, R., Barboza-Flores, M. Room temperature effects of UV radiation in KBr:$Eu^{2+}$ crystals. *J. Phys.: Condens. Matter*, **8**, 4983-4992, 1996.

Polf, J. C. The role of oxygen vacancies in thermoluminescence processes in $Al_2O_3$:C. *Masters Thesis*, Oklahoma State University. Stillwater, Oklahoma, 2002.

Polf, J. C., Yukihara, E. G., Akselrod, M. S., McKeever, S. W. S. Real-time luminescence from $Al_2O_3$:C fiber dosimeters. *Radiat. Meas.* **38**, 227-240, 2004.

Pollack, A., Zagars, G. K., Starkschall, G., Antolak, J. A., Lee, J. J., Huang, E., von Eschenbach, A. C., Kuban, D. A., Rosen, I. Prostate cancer radiation dose response: results of the M. D. Anderson phase III randomized trial. *Int. J. Radiat. Oncol., Biol., Phys.* **53**, 1097-1105, 2002.

Ranchoux, G., Magne, S., Bouvet, J. P., Ferdinand, P. Fiber remote optoelectronic gamma dosimetry based on optically stimulated luminescence of $Al_2O_3$:C. *Radiat. Prot. Dosim.* **100**, 255-260, 2002.

Randall, J. T., Wilkins, M. H. F. Phosphorescence and electron traps I: The study of trap distributions. *Proc. Roy. Soc. Lond.* **184**, 366-389, 1945.

Rasheedy, M. S. On the general-order kinetics of the thermoluminescence glow peak. *J. Phys.: Condensed Matter* **5**, 633-636, 1993.

Rieke, J. K., Daniels, F. Thermoluminescence studies of aluminum oxide. *J. Phys. Chem.* **61**, 629-633, 1957.

Rubio, O. J. Doubly-valent rare-earth ions in halide crystals. *J. Phys. Chem. Solids* **52**, 101-174, 1991.

Son, C., Ziaie, B. A micromachined electret-based transponder for in situ radiation measurement. *IEEE Electron Dev Letters.* **27**, 884-886, 2006.

Suit, H. Contributions of L. H. Gray to radiation physics, biology and oncology. *Int. J. Radiation Oncology Biol. Phys.* **53**, 795-797, 2002.

Tao, L., Kalend, A. M., Rakfal, S. M. Dose responses of a MOSFET detector for in-vivo dosimetry of clinical electron beams. *Eng. Med. And Biol. Soc, 2000. Proc of the 22nd Ann. Int. Conf. of the IEEE.* **1**, 506-507, 2000.

Townsend, P. D., Kelly, J. C. *Colour centres and imperfections in insulators and semiconductors.* Sussex University Press, London, 1973.

Trout, D., Kelley, J. P., Lucas, A. C. Determination of half-value layer. *Amer. J. Roent. Rad. Therapy, and Nuc. Med.* **84**, 729-740, 1960.

Warren-Forward, H. M., Bradley, D. A. A pilot study of chest x-ray doses and dose variability within the West Midlands Regional Health Authority. *J. Radiol. Prot.* **13**, 267-274, 1993.

Weast, R. C., ed. *CRC handbook of chemistry and physics.* CRC Press, Inc., Boca Raton, Florida, 1987.

Whitley, V., McKeever, S. W. S. Photoionization of deep centers in $Al_2O_3$. *J. Appl. Phys.* **87**, 249-256, 2000

Wilson, R. R. Radiological use of fast protons. *Radiology.* **47**, 487-491, 1946.

Yukihara, E. G., Whitley, V., Polf, J. C., Klein, D. M., McKeever, S. W. S., Akselrod, A. E., Akselrod, M. S. The effects of deep trap population on the thermoluminescence of $Al_2O_3$:C. *Rad. Meas.* **37**, 627-638, 2003.

Yukihara, E. G., Whitley, V., McKeever, S. W. S., Akselrod, A. E., Akselrod, M. S. Effect of high-dose irradiation on the optically stimulated luminescence of $Al_2O_3$:C. *Rad. Meas.* **38**, 317-330, 2004.

# APPENDICES

## A. $^{192}$Ir Dose Plans Calculated for October 20$^{th}$ and 25$^{th}$

The following dose plans were calculated by Dr. George Mardirossian of the Oklahoma University Health Sciences Center (OUHSC) in conjunction with performance testing of the KBr:Eu-based remote medical dosimetry system. The plans include information regarding the type and activity of the $^{192}$Ir source seed used for the irradiation of the KBr:Eu dosimeter in the dose mapping and reproducibility experiments discussed in section 5.4 of this dissertation. Two different dose plans were constructed on October 20$^{th}$, 2006 for the different positioning schemes shown in figure 5.27, and one dose plan was made on October 25$^{th}$ to coincide with the positioning used in figure 5.27a only. All patient information has been blacked out, along with the plan name and ID. Isodose maps of the radiation field around the $^{192}$Ir source are also given, and these show the points in space used for calculating the doses delivered using the 'front' and 'face-to-face' positional schemes of figure 5.27b.

For above & below

Nucletron PLATO BRACHYTHERAPY v14.2.5

Institute : HCA Presbyterian Hospital
Patient name : [redacted]
Patient birthdate : [redacted]
Patient ID : [redacted]
Plan name and ID : [redacted] - 20/10/2006-15:03:14

Planned by :

Approval :

## Case and study

Notes : No notes available.

## Customization

Customization file name : presbyhdrv2

| | |
|---|---|
| Treatment unit name | : mHDR |
| Treatment unit type | : microSelectron_HDR |
| Nucletron source | : Ir-192-mHDR |
| Source timestamp | : 20-Oct-2006 14:54:06 |
| Isotope | : Ir-192 |
| Air kerma strength | : 43146.738 cGy/h cm^2 |
| Reference exposure rate | : 49231.789 R/h cm^2 |
| Apparent source activity [mCi] | : 10570.000 mCi |
| Apparent source activity [MBq] | : 391090.000 MBq |
| At date/time of calibration | : 27-Sep-2006 11:00:00 |
| Air kerma rate constant | : 4.08200 cGy / h / mCi * cm^2 |
| Stepsize | : 5.0 mm |
| Air kerma strength | : 34773.957 cGy/h cm^2 |
| At treatment date/time | : 20-Oct-2006 10:30:00 |

Interval between calibration and treatment date/time : 22.98 days
Decay factor : 0.806

## Shield information

No shielding.

## Optimization

No optimization.

## Dose prescription

Reference dose : 71.8 cGy

Based on 100.0 % of the mean dose in the applicator points.

| Point | Description |
|---|---|
| | |

Nucletron PLATO BRACHYTHERAPY v14.2.5

Institute : HCA Presbyterian Hospital
Patient name : [redacted]
Patient birthdate : [redacted]
Patient ID : [redacted]
Plan name and ID : [redacted] - 20/10/2006-15:03:14

| Point | Description |
|---|---|
| 1 | A210 |

Source positions

```
Cath.  1   5   9  13  17  21  25  29  33  37  41  45  Indexer
.      |   |   |   |   |   |   |   |   |   |   |   |  length
001:   A.....................................................  1500
.      |   |   |   |   |   |   |   |   |   |   |   |
.      0   2   4   6   8  10  12  14  16  18  20  22 cm
```

Source position separation: 5.0 mm

Catheter times

| | #Active pos. | Cath. time (sec.) |
|---|---|---|
| Cath. 1 | 1 | 60.0 |

Total treatment time: 60.0 (sec.)

Per cent of total time, lost due to rounding off: 0.03 %

Source times

Cath. 1

| Pos. | Rel. time | Abs. time (sec.) |
|---|---|---|
| 1 | 1.00 | 60.0 |

Marker points

No points.

Patient points

No points.

Applicator points

Nucletron PLATO BRACHYTHERAPY v14.2.5

Institute : HCA Presbyterian Hospital
Patient name : [redacted]
Patient birthdate : [redacted]
Patient ID : [redacted]
Plan name and ID : [redacted] - 20/10/2006-15:03:14

| Point | X (mm) | Y (mm) | Z (mm) | Norm dose | Dose (%) | Dose (cGy) |
|---|---|---|---|---|---|---|
| A1 | 0.0 | 4.0 | 5.0 | 100.00 | 2123.56 | 1524.71 |
| A2 | 0.0 | 4.0 | 10.0 | 100.00 | 777.49 | 558.24 |
| A3 | 0.0 | 4.0 | 15.0 | 100.00 | 377.86 | 271.30 |
| A4 | 0.0 | 4.0 | 20.0 | 100.00 | 220.05 | 158.00 |
| A110 | 0.0 | 4.0 | 25.0 | 100.00 | 142.96 | 102.64 |
| A210 | 0.0 | 4.0 | 30.0 | 100.00 | 100.00 | 71.80 |
| A310 | 0.0 | 4.0 | 35.0 | 100.00 | 73.68 | 52.91 |
| A410 | 0.0 | 4.0 | 40.0 | 100.00 | 56.41 | 40.50 |
| A11 | 0.0 | 4.0 | 45.0 | 100.00 | 44.48 | 31.94 |
| A12 | 0.0 | 4.0 | 50.0 | 100.00 | 35.89 | 25.77 |
| A13 | 0.0 | 4.0 | 55.0 | 100.00 | 29.49 | 21.17 |
| A14 | 0.0 | 4.0 | 60.0 | 100.00 | 24.61 | 17.67 |
| A15 | 0.0 | 4.0 | 65.0 | 100.00 | 20.81 | 14.94 |
| A16 | 0.0 | 4.0 | 70.0 | 100.00 | 17.78 | 12.77 |
| A17 | 0.0 | 4.0 | 75.0 | 100.00 | 15.31 | 10.99 |
| A18 | 0.0 | 4.0 | 80.0 | 100.00 | 13.28 | 9.54 |
| A19 | 0.0 | 4.0 | 85.0 | 100.00 | 11.60 | 8.33 |
| A20 | 0.0 | 4.0 | 90.0 | 100.00 | 10.20 | 7.32 |
| A21 | 0.0 | 4.0 | 95.0 | 100.00 | 9.00 | 6.46 |
| A22 | 0.0 | 4.0 | 100.0 | 100.00 | 7.98 | 5.73 |
| A23 | 0.0 | 4.0 | 0.0 | 100.00 | 4805.50 | 3450.35 |

Reference points

No points.

Dose points

For . front + 'five to five'

Nucletron PLATO BRACHYTHERAPY v14.2.5

Institute : HCA Presbyterian Hospital
Patient name : [redacted]
Patient birthdate : [redacted]
Patient ID : [redacted]
Plan name and ID : [redacted] - 20/10/2006-15:19:00

Planned by :

Approval :

## Case and study

Notes : No notes available.

## Customization

Customization file name : presbyhdrv2

| | |
|---|---|
| Treatment unit name | : mHDR |
| Treatment unit type | : microSelectron_HDR |
| Nucletron source | : Ir-192-mHDR |
| Source timestamp | : 20-Oct-2006 14:54:06 |
| Isotope | : Ir-192 |
| Air kerma strength | : 43146.738 cGy/h cm^2 |
| Reference exposure rate | : 49231.789 R/h cm^2 |
| Apparent source activity [mCi] | : 10570.000 mCi |
| Apparent source activity [MBq] | : 391090.000 MBq |
| At date/time of calibration | : 27-Sep-2006 11:00:00 |
| Air kerma rate constant | : 4.08200 cGy / h / mCi * cm^2 |
| Stepsize | : 5.0 mm |
| Air kerma strength | : 34726.379 cGy/h cm^2 |
| At treatment date/time | : 20-Oct-2006 14:00:00 |

Interval between calibration and treatment date/time : 23.12 days
Decay factor : 0.805

## Shield information

No shielding.

## Optimization

No optimization.

## Dose prescription

Reference dose : 48.4 cGy

Based on 100.0 % of the mean dose in the applicator points.

| Point | Description |
|---|---|
| | |

Nucletron PLATO BRACHYTHERAPY v14.2.5

Institute : HCA Presbyterian Hospital
Patient name : [redacted]
Patient birthdate : [redacted]
Patient ID : [redacted]
Plan name and ID : [redacted] - 20/10/2006-15:19:00

| Point | Description |
|---|---|
| 1 | A310 |

Source positions

```
Cath.  1   5   9  13  17  21  25  29  33  37  41  45  Indexer
.      |   |   |   |   |   |   |   |   |   |   |   |  length
001:   A.....................................................  1500
.      |   |   |   |   |   |   |   |   |   |   |
.      0   2   4   6   8  10  12  14  16  18  20  22 cm
```

Source position separation: 5.0 mm

Catheter times

| | #Active pos. | Cath. time (sec.) |
|---|---|---|
| Cath. 1 | 1 | 60.0 |

Total treatment time: 60.0 (sec.)

Per cent of total time, given extra due to rounding off: 0.02 %

Source times

Cath. 1

| Pos. | Rel. time | Abs. time (sec.) |
|---|---|---|
| 1 | 1.00 | 60.0 |

Marker points

No points.

Patient points

No points.

Applicator points

Nucletron PLATO BRACHYTHERAPY v14.2.5

Institute : HCA Presbyterian Hospital
Patient name : [redacted]
Patient birthdate : [redacted]
Patient ID : [redacted]
Plan name and ID : [redacted] - 20/10/2006-15:19:00

| Point | X (mm) | Y (mm) | Z (mm) | Norm dose | Dose (%) | Dose (cGy) |
|---|---|---|---|---|---|---|
| A1 | 10.0 | 0.0 | 0.0 | 100.00 | 876.27 | 424.11 |
| A4 | 15.0 | 0.0 | 0.0 | 100.00 | 386.36 | 187.00 |
| A110 | 20.0 | 0.0 | 0.0 | 100.00 | 220.69 | 106.81 |
| A210 | 25.0 | 0.0 | 0.0 | 100.00 | 142.83 | 69.13 |
| A310 | 30.0 | 0.0 | 0.0 | 100.00 | 100.00 | 48.40 |
| A410 | 35.0 | 0.0 | 0.0 | 100.00 | 74.14 | 35.88 |
| A11 | 40.0 | 0.0 | 0.0 | 100.00 | 57.32 | 27.75 |
| A12 | 45.0 | 0.0 | 0.0 | 100.00 | 45.74 | 22.14 |
| A13 | 50.0 | 0.0 | 0.0 | 100.00 | 37.36 | 18.08 |
| A14 | 55.0 | 0.0 | 0.0 | 100.00 | 30.67 | 14.84 |
| A15 | 60.0 | 0.0 | 0.0 | 100.00 | 25.57 | 12.38 |
| A16 | 65.0 | 0.0 | 0.0 | 100.00 | 21.61 | 10.46 |
| A17 | 70.0 | 0.0 | 0.0 | 100.00 | 18.46 | 8.93 |
| A18 | 75.0 | 0.0 | 0.0 | 100.00 | 15.89 | 7.69 |
| A19 | 80.0 | 0.0 | 0.0 | 100.00 | 13.78 | 6.67 |
| A20 | 90.0 | 0.0 | 0.0 | 100.00 | 10.57 | 5.12 |
| A21 | 100.0 | 0.0 | 0.0 | 100.00 | 8.27 | 4.00 |

Reference points

No points.

Dose points

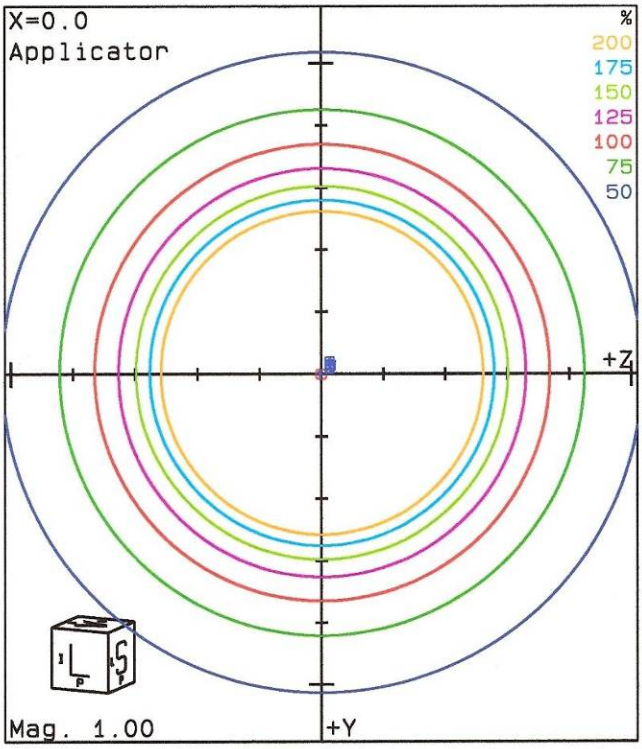


PLATO BRACHY-THERAPY v14.2.5

Name : [redacted]
Pat ID: [redacted]
PlanID: 20/10/2006-15:19:00
Inst: HCA Presbyterian Hospital
Srce: Ir-192-mHDR
Isot: Ir-192
AKS : 34726 cGy/h cm2
Act : 8507 mCi
Opt : None
Date: 20-Oct-2006 14:00:00

Planner:

Approval:

a: A1
b: A4
c: A110
d: A210
e: A310
f: A410
g: A11
h: A12
i: A13
j: A14
k: A15
l: A16
m: A17
n: A18
o: A19
p: A20
q: A21

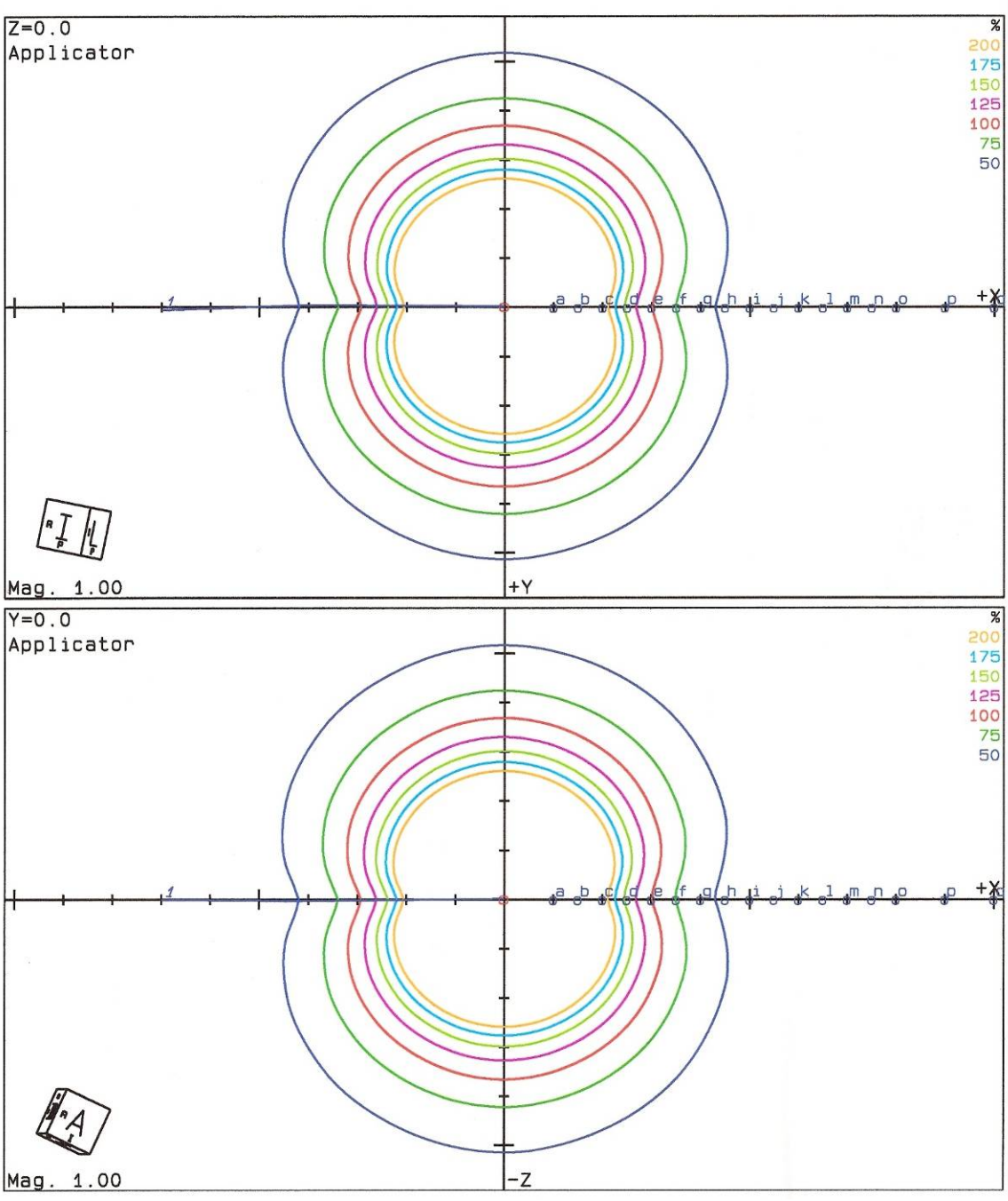
Z=0.0
Applicator
%
200
175
150
125
100
75
50
+X
+Y
Mag. 1.00
Y=0.0
Applicator
%
200
175
150
125
100
75
50
+X
-Z
Mag. 1.00

Nucletron PLATO BRACHYTHERAPY v14.2.5

Institute : HCA Presbyterian Hospital
Patient name : [redacted]
Patient birthdate : [redacted]
Patient ID : [redacted]
Plan name and ID : [redacted] - 25/10/2006-17:04:41

Planned by :

Approval :

## Case and study

Notes : No notes available.

## Customization

Customization file name : presbyhdrv2

Treatment unit name : mHDR
Treatment unit type : microSelectron_HDR
Nucletron source : Ir-192-mHDR
Source timestamp : 25-Oct-2006 16:48:45
Isotope : Ir-192
Air kerma strength : 43146.699 cGy/h cm^2
Reference exposure rate : 49231.742 R/h cm^2
Apparent source activity [mCi] : 10569.990 mCi
Apparent source activity [MBq] : 391089.625 MBq
At date/time of calibration : 27-Sep-2006 11:00:00
Air kerma rate constant : 4.08200 cGy / h / mCi * cm^2
Stepsize : 5.0 mm

Air kerma strength : 33098.695 cGy/h cm^2
At treatment date/time : 25-Oct-2006 16:43:00

Interval between calibration and treatment date/time : 28.24 days
Decay factor : 0.767

## Shield information

No shielding.

## Optimization

No optimization.

## Dose prescription

Reference dose : 68.4 cGy

Based on 100.0 % of the mean dose in the applicator points.

| Point | Description |
|---|---|
| | |

Nucletron PLATO BRACHYTHERAPY v14.2.5

Institute : HCA Presbyterian Hospital
Patient name : [redacted]
Patient birthdate : [redacted]
Patient ID : [redacted]
Plan name and ID : [redacted] - 25/10/2006-17:04:41

| Point | Description |
|---|---|
| 1 | A310 |

Source positions

```
Cath.  1   5   9  13  17  21  25  29  33  37  41  45  Indexer
.      |   |   |   |   |   |   |   |   |   |   |   |  length
001:   A.....................................................  1500
.      |   |   |   |   |   |   |   |   |   |   |   |
.      0   2   4   6   8  10  12  14  16  18  20  22 cm
```

Source position separation: 5.0 mm

Catheter times

| | #Active pos. | Cath. time (sec.) |
|---|---|---|
| Cath. 1 | 1 | 60.1 |

Total treatment time: 60.1 (sec.)

Per cent of total time, given extra due to rounding off: 0.05 %

Source times

Cath. 1

| Pos. | Rel. time | Abs. time (sec.) |
|---|---|---|
| 1 | 1.00 | 60.1 |

Marker points

No points.

Patient points

No points.

Applicator points

Nucletron PLATO BRACHYTHERAPY v14.2.5

Institute : HCA Presbyterian Hospital
Patient name : [redacted]
Patient birthdate : [redacted]
Patient ID : [redacted]
Plan name and ID : [redacted] - 25/10/2006-17:04:41

| Point | X (mm) | Y (mm) | Z (mm) | Norm dose | Dose (%) | Dose (cGy) |
|---|---|---|---|---|---|---|
| A1 | 0.0 | 4.0 | 10.0 | 100.00 | 777.49 | 531.81 |
| A4 | 0.0 | 4.0 | 15.0 | 100.00 | 377.86 | 258.45 |
| A110 | 0.0 | 4.0 | 20.0 | 100.00 | 220.05 | 150.52 |
| A210 | 0.0 | 4.0 | 25.0 | 100.00 | 142.96 | 97.78 |
| A310 | 0.0 | 4.0 | 30.0 | 100.00 | 100.00 | 68.40 |
| A410 | 0.0 | 4.0 | 35.0 | 100.00 | 73.68 | 50.40 |
| A11 | 0.0 | 4.0 | 40.0 | 100.00 | 56.41 | 38.59 |
| A12 | 0.0 | 4.0 | 45.0 | 100.00 | 44.48 | 30.43 |
| A13 | 0.0 | 4.0 | 50.0 | 100.00 | 35.89 | 24.55 |
| A14 | 0.0 | 4.0 | 55.0 | 100.00 | 29.49 | 20.17 |
| A15 | 0.0 | 4.0 | 60.0 | 100.00 | 24.61 | 16.83 |
| A16 | 0.0 | 4.0 | 65.0 | 100.00 | 20.81 | 14.23 |
| A17 | 0.0 | 4.0 | 70.0 | 100.00 | 17.78 | 12.16 |
| A18 | 0.0 | 4.0 | 75.0 | 100.00 | 15.31 | 10.47 |
| A19 | 0.0 | 4.0 | 80.0 | 100.00 | 13.28 | 9.08 |
| A20 | 0.0 | 4.0 | 85.0 | 100.00 | 11.60 | 7.94 |
| A21 | 0.0 | 4.0 | 90.0 | 100.00 | 10.20 | 6.97 |
| A25 | 0.0 | 4.0 | 95.0 | 100.00 | 9.00 | 6.16 |
| A26 | 0.0 | 4.0 | 100.0 | 100.00 | 7.98 | 5.46 |
| A27 | 0.0 | 4.0 | 0.0 | 100.00 | 4805.51 | 3286.97 |

Reference points

No points.

Dose points

## B. Energy Absorption Computer Models for $^{232}$Th and $^{226}$Ra Experiments

Two models were developed to calculate the energy absorbed in the dosimeter - one under $^{232}$Th irradiation and one under $^{226}$Ra irradiation. The geometries of each experimental setup are described in chapter 4, section 2, and the models attempt to incorporate these geometries in a simplified, but accurate manner. The two codes generate linear paths that start at the point of gamma radiation emission in the source and end at an exit point on the surface the dosimeter (see figure 4.15). Linear mass-attenuation is calculated through each material along the path preceding the dosimeter. The mass-energy absorption is then calculated for the path length obtained through the dosimeter. A third code calculates the efficiency of radiation interaction with the dosimeter volume, and this is used by both of the energy absorption codes. The source radiation energies, probabilities of emission, linear mass attenuation coefficients, and mass-energy absorption coefficients relevant to each model and for all radionuclides in the decay chains (see figure 4.14) are listed in tables preceding the codes. Other relevant parameters can be found in the codes themselves.

**Table B1** Coefficients for Thorium-232 and Daughters

| Emission energy (MeV) | Probability of emission | Mass attenuation ($cm^2/g$) | | | Mass-energy absorption for water ($cm^2/g$) |
|---|---|---|---|---|---|
| | | Epoxy Block * | Steel | Teflon | |
| 6.670E-03 | 1.000E-06 | 3.559E+01 | 1.399E+02 | 2.289E+01 | 1.738E+01 |
| 1.030E-02 | 7.686E-02 | 1.004E+01 | 1.542E+02 | 6.248E+00 | 4.499E+00 |
| 1.060E-02 | 1.039E-02 | 9.243E+00 | 1.427E+02 | 5.747E+00 | 4.108E+00 |
| 1.080E-02 | 1.549E-01 | 8.761E+00 | 1.357E+02 | 5.442E+00 | 3.873E+00 |
| 1.110E-02 | 4.310E-04 | 8.100E+00 | 1.260E+02 | 5.025E+00 | 3.551E+00 |
| 1.170E-02 | 3.965E-03 | 6.966E+00 | 1.093E+02 | 4.310E+00 | 3.006E+00 |
| 1.230E-02 | 8.390E-02 | 5.995E+00 | 9.551E+01 | 3.726E+00 | 2.567E+00 |
| 1.230E-02 | 9.559E-02 | 5.995E+00 | 9.551E+01 | 3.726E+00 | 2.567E+00 |
| 1.300E-02 | 3.911E-01 | 5.077E+00 | 8.225E+01 | 3.171E+00 | 2.154E+00 |
| 3.986E-02 | 1.023E-02 | 3.475E-01 | 3.586E+00 | 2.664E-01 | 7.020E-02 |
| 5.778E-02 | 5.014E-03 | 2.273E-01 | 1.305E+00 | 1.929E-01 | 3.380E-02 |
| 5.900E-02 | 1.900E-03 | 2.232E-01 | 1.234E+00 | 1.902E-01 | 3.273E-02 |
| 7.083E-02 | 3.310E-04 | 1.961E-01 | 7.872E-01 | 1.731E-01 | 2.835E-02 |
| 7.280E-02 | 7.312E-03 | 1.928E-01 | 7.362E-01 | 1.708E-01 | 2.780E-02 |
| 7.287E-02 | 5.600E-04 | 1.927E-01 | 7.346E-01 | 1.707E-01 | 2.778E-02 |
| 7.482E-02 | 1.069E-01 | 1.900E-01 | 6.889E-01 | 1.685E-01 | 2.727E-02 |
| 7.497E-02 | 1.235E-02 | 1.898E-01 | 6.854E-01 | 1.683E-01 | 2.723E-02 |
| 7.686E-02 | 3.550E-04 | 1.873E-01 | 6.450E-01 | 1.663E-01 | 2.675E-02 |
| 7.711E-02 | 1.800E-01 | 1.870E-01 | 6.400E-01 | 1.660E-01 | 2.669E-02 |
| 7.929E-02 | 5.950E-04 | 1.843E-01 | 5.979E-01 | 1.637E-01 | 2.617E-02 |
| 8.107E-02 | 1.259E-03 | 1.822E-01 | 5.690E-01 | 1.622E-01 | 2.597E-02 |
| 8.260E-02 | 2.480E-04 | 1.805E-01 | 5.472E-01 | 1.611E-01 | 2.593E-02 |
| 8.378E-02 | 2.092E-03 | 1.792E-01 | 5.312E-01 | 1.602E-01 | 2.590E-02 |
| 8.437E-02 | 1.210E-02 | 1.785E-01 | 5.235E-01 | 1.598E-01 | 2.588E-02 |
| 8.490E-02 | 5.486E-03 | 1.779E-01 | 5.167E-01 | 1.594E-01 | 2.587E-02 |
| 8.730E-02 | 8.035E-02 | 1.754E-01 | 4.874E-01 | 1.578E-01 | 2.580E-02 |
| 8.980E-02 | 2.670E-04 | 1.731E-01 | 4.595E-01 | 1.561E-01 | 2.574E-02 |
| 8.995E-02 | 2.133E-02 | 1.730E-01 | 4.579E-01 | 1.560E-01 | 2.574E-02 |
| 9.335E-02 | 3.485E-02 | 1.700E-01 | 4.238E-01 | 1.539E-01 | 2.565E-02 |
| 9.490E-02 | 9.480E-04 | 1.688E-01 | 4.094E-01 | 1.530E-01 | 2.562E-02 |
| 9.945E-02 | 1.302E-02 | 1.654E-01 | 3.713E-01 | 1.503E-01 | 2.551E-02 |
| 1.050E-01 | 1.612E-02 | 1.620E-01 | 3.401E-01 | 1.476E-01 | 2.574E-02 |
| 1.152E-01 | 6.025E-03 | 1.564E-01 | 2.944E-01 | 1.431E-01 | 2.621E-02 |
| 1.250E-01 | 4.200E-04 | 1.516E-01 | 2.591E-01 | 1.392E-01 | 2.664E-02 |
| 1.291E-01 | 2.770E-02 | 1.497E-01 | 2.465E-01 | 1.377E-01 | 2.680E-02 |
| 1.316E-01 | 1.240E-03 | 1.486E-01 | 2.391E-01 | 1.369E-01 | 2.690E-02 |
| 1.461E-01 | 2.105E-03 | 1.433E-01 | 2.032E-01 | 1.322E-01 | 2.746E-02 |
| 1.542E-01 | 9.418E-03 | 1.407E-01 | 1.895E-01 | 1.298E-01 | 2.780E-02 |
| 1.725E-01 | 1.148E-03 | 1.354E-01 | 1.688E-01 | 1.250E-01 | 2.860E-02 |
| 1.767E-01 | 5.200E-04 | 1.342E-01 | 1.648E-01 | 1.240E-01 | 2.878E-02 |
| 1.912E-01 | 1.163E-03 | 1.305E-01 | 1.519E-01 | 1.208E-01 | 2.936E-02 |
| 1.997E-01 | 3.324E-03 | 1.286E-01 | 1.452E-01 | 1.191E-01 | 2.969E-02 |
| 2.044E-01 | 1.634E-03 | 1.275E-01 | 1.429E-01 | 1.181E-01 | 2.981E-02 |
| 2.093E-01 | 4.432E-02 | 1.264E-01 | 1.406E-01 | 1.171E-01 | 2.994E-02 |
| 2.100E-01 | 2.161E-03 | 1.262E-01 | 1.403E-01 | 1.170E-01 | 2.996E-02 |
| 2.114E-01 | 6.109E-04 | 1.259E-01 | 1.396E-01 | 1.167E-01 | 2.999E-02 |
| 2.160E-01 | 2.390E-03 | 1.249E-01 | 1.376E-01 | 1.158E-01 | 3.011E-02 |
| 2.334E-01 | 1.114E-03 | 1.214E-01 | 1.305E-01 | 1.126E-01 | 3.052E-02 |
| 2.386E-01 | 4.465E-01 | 1.205E-01 | 1.286E-01 | 1.117E-01 | 3.064E-02 |
| 2.410E-01 | 3.950E-02 | 1.201E-01 | 1.277E-01 | 1.114E-01 | 3.069E-02 |
| 2.526E-01 | 2.874E-03 | 1.182E-01 | 1.237E-01 | 1.095E-01 | 3.095E-02 |
| 2.702E-01 | 3.601E-02 | 1.155E-01 | 1.181E-01 | 1.069E-01 | 3.132E-02 |
| 2.774E-01 | 2.443E-02 | 1.143E-01 | 1.160E-01 | 1.059E-01 | 3.146E-02 |
| 2.790E-01 | 2.216E-03 | 1.141E-01 | 1.156E-01 | 1.057E-01 | 3.150E-02 |
| 2.881E-01 | 3.174E-03 | 1.127E-01 | 1.131E-01 | 1.045E-01 | 3.167E-02 |
| 3.001E-01 | 3.407E-02 | 1.110E-01 | 1.100E-01 | 1.030E-01 | 3.190E-02 |
| 3.217E-01 | 2.410E-03 | 1.080E-01 | 1.059E-01 | 1.002E-01 | 3.212E-02 |
| 3.276E-01 | 3.213E-02 | 1.072E-01 | 1.048E-01 | 9.946E-02 | 3.217E-02 |

| | | | | | |
|---|---|---|---|---|---|
| 3.280E-01 | 1.297E-03 | 1.071E-01 | 1.048E-01 | 9.943E-02 | 3.218E-02 |
| 3.324E-01 | 4.432E-03 | 1.066E-01 | 1.040E-01 | 9.890E-02 | 3.222E-02 |
| 3.383E-01 | 1.136E-01 | 1.059E-01 | 1.030E-01 | 9.821E-02 | 3.227E-02 |
| 3.411E-01 | 4.155E-03 | 1.055E-01 | 1.025E-01 | 9.789E-02 | 3.230E-02 |
| 3.795E-01 | 9.460E-04 | 1.012E-01 | 9.674E-02 | 9.384E-02 | 3.263E-02 |
| 4.095E-01 | 2.133E-02 | 9.804E-02 | 9.291E-02 | 9.101E-02 | 3.282E-02 |
| 4.403E-01 | 1.385E-03 | 9.525E-02 | 8.961E-02 | 8.832E-02 | 3.289E-02 |
| 4.528E-01 | 3.475E-03 | 9.417E-02 | 8.836E-02 | 8.731E-02 | 3.291E-02 |
| 4.630E-01 | 4.432E-02 | 9.332E-02 | 8.739E-02 | 8.651E-02 | 3.293E-02 |
| 4.650E-01 | 1.800E-04 | 9.317E-02 | 8.720E-02 | 8.636E-02 | 3.294E-02 |
| 4.782E-01 | 2.299E-03 | 9.207E-02 | 8.599E-02 | 8.536E-02 | 3.296E-02 |
| 5.036E-01 | 2.050E-03 | 9.007E-02 | 8.381E-02 | 8.354E-02 | 3.299E-02 |
| 5.096E-01 | 4.709E-03 | 8.961E-02 | 8.334E-02 | 8.312E-02 | 3.298E-02 |
| 5.108E-01 | 7.761E-02 | 8.952E-02 | 8.325E-02 | 8.303E-02 | 3.298E-02 |
| 5.230E-01 | 1.163E-03 | 8.862E-02 | 8.232E-02 | 8.220E-02 | 3.295E-02 |
| 5.463E-01 | 2.105E-03 | 8.698E-02 | 8.062E-02 | 8.068E-02 | 3.290E-02 |
| 5.497E-01 | 9.500E-04 | 8.674E-02 | 8.038E-02 | 8.046E-02 | 3.290E-02 |
| 5.623E-01 | 9.418E-03 | 8.591E-02 | 7.952E-02 | 7.969E-02 | 3.287E-02 |
| 5.707E-01 | 1.773E-03 | 8.536E-02 | 7.896E-02 | 7.918E-02 | 3.286E-02 |
| 5.721E-01 | 1.551E-03 | 8.526E-02 | 7.887E-02 | 7.910E-02 | 3.285E-02 |
| 5.831E-01 | 3.032E-01 | 8.455E-02 | 7.816E-02 | 7.845E-02 | 3.283E-02 |
| 5.832E-01 | 1.440E-03 | 8.455E-02 | 7.815E-02 | 7.845E-02 | 3.283E-02 |
| 6.238E-01 | 1.136E-03 | 8.206E-02 | 7.565E-02 | 7.614E-02 | 3.270E-02 |
| 7.015E-01 | 1.884E-03 | 7.787E-02 | 7.144E-02 | 7.219E-02 | 3.242E-02 |
| 7.071E-01 | 1.496E-03 | 7.759E-02 | 7.116E-02 | 7.193E-02 | 3.240E-02 |
| 7.220E-01 | 7.294E-04 | 7.687E-02 | 7.044E-02 | 7.124E-02 | 3.235E-02 |
| 7.270E-01 | 7.756E-03 | 7.663E-02 | 7.020E-02 | 7.102E-02 | 3.233E-02 |
| 7.272E-01 | 1.183E-01 | 7.662E-02 | 7.020E-02 | 7.102E-02 | 3.233E-02 |
| 7.552E-01 | 1.053E-02 | 7.530E-02 | 6.891E-02 | 6.981E-02 | 3.224E-02 |
| 7.631E-01 | 5.892E-03 | 7.493E-02 | 6.856E-02 | 6.947E-02 | 3.221E-02 |
| 7.722E-01 | 1.551E-02 | 7.452E-02 | 6.817E-02 | 6.910E-02 | 3.219E-02 |
| 7.820E-01 | 5.263E-03 | 7.408E-02 | 6.775E-02 | 6.871E-02 | 3.216E-02 |
| 7.855E-01 | 1.969E-02 | 7.393E-02 | 6.760E-02 | 6.857E-02 | 3.214E-02 |
| 7.947E-01 | 4.626E-02 | 7.353E-02 | 6.722E-02 | 6.821E-02 | 3.212E-02 |
| 8.049E-01 | 1.800E-05 | 7.309E-02 | 6.680E-02 | 6.780E-02 | 3.207E-02 |
| 8.305E-01 | 5.900E-03 | 7.201E-02 | 6.577E-02 | 6.681E-02 | 3.191E-02 |
| 8.355E-01 | 1.745E-02 | 7.180E-02 | 6.558E-02 | 6.662E-02 | 3.188E-02 |
| 8.400E-01 | 9.418E-03 | 7.162E-02 | 6.540E-02 | 6.645E-02 | 3.186E-02 |
| 8.404E-01 | 1.286E-03 | 7.160E-02 | 6.539E-02 | 6.644E-02 | 3.185E-02 |
| 8.604E-01 | 4.484E-02 | 7.081E-02 | 6.463E-02 | 6.570E-02 | 3.174E-02 |
| 8.934E-01 | 6.522E-03 | 6.954E-02 | 6.344E-02 | 6.454E-02 | 3.155E-02 |
| 9.045E-01 | 8.310E-03 | 6.912E-02 | 6.305E-02 | 6.417E-02 | 3.149E-02 |
| 9.111E-01 | 2.770E-01 | 6.888E-02 | 6.283E-02 | 6.395E-02 | 3.145E-02 |
| 9.276E-01 | 4.489E-04 | 6.829E-02 | 6.227E-02 | 6.341E-02 | 3.137E-02 |
| 9.441E-01 | 1.025E-03 | 6.772E-02 | 6.173E-02 | 6.289E-02 | 3.128E-02 |
| 9.478E-01 | 4.117E-02 | 6.759E-02 | 6.161E-02 | 6.277E-02 | 3.126E-02 |
| 9.480E-01 | 1.163E-03 | 6.759E-02 | 6.161E-02 | 6.276E-02 | 3.126E-02 |
| 9.521E-01 | 3.133E-03 | 6.745E-02 | 6.147E-02 | 6.264E-02 | 3.124E-02 |
| 9.585E-01 | 3.019E-03 | 6.724E-02 | 6.127E-02 | 6.244E-02 | 3.121E-02 |
| 9.646E-01 | 5.208E-02 | 6.703E-02 | 6.108E-02 | 6.225E-02 | 3.118E-02 |
| 9.691E-01 | 1.662E-01 | 6.689E-02 | 6.094E-02 | 6.211E-02 | 3.115E-02 |
| 9.827E-01 | 7.078E-04 | 6.645E-02 | 6.052E-02 | 6.171E-02 | 3.109E-02 |
| 9.878E-01 | 1.828E-03 | 6.628E-02 | 6.037E-02 | 6.156E-02 | 3.106E-02 |
| 1.033E+00 | 2.161E-03 | 6.481E-02 | 5.900E-02 | 6.020E-02 | 3.081E-02 |
| 1.065E+00 | 1.413E-03 | 6.390E-02 | 5.809E-02 | 5.929E-02 | 3.063E-02 |
| 1.074E+00 | 2.810E-04 | 6.365E-02 | 5.784E-02 | 5.904E-02 | 3.058E-02 |
| 1.079E+00 | 9.527E-03 | 6.353E-02 | 5.771E-02 | 5.891E-02 | 3.055E-02 |
| 1.094E+00 | 1.329E-03 | 6.311E-02 | 5.730E-02 | 5.850E-02 | 3.047E-02 |
| 1.096E+00 | 1.274E-03 | 6.306E-02 | 5.725E-02 | 5.845E-02 | 3.046E-02 |
| 1.110E+00 | 3.324E-03 | 6.262E-02 | 5.686E-02 | 5.806E-02 | 3.038E-02 |
| 1.154E+00 | 1.523E-03 | 6.132E-02 | 5.575E-02 | 5.695E-02 | 3.016E-02 |
| 1.246E+00 | 5.401E-03 | 5.898E-02 | 5.358E-02 | 5.478E-02 | 2.972E-02 |
| 1.288E+00 | 1.136E-03 | 5.799E-02 | 5.273E-02 | 5.387E-02 | 2.947E-02 |
| 1.459E+00 | 9.972E-03 | 5.442E-02 | 4.957E-02 | 5.051E-02 | 2.851E-02 |
| 1.496E+00 | 9.972E-03 | 5.368E-02 | 4.897E-02 | 4.987E-02 | 2.832E-02 |
| 1.502E+00 | 5.540E-03 | 5.357E-02 | 4.888E-02 | 4.977E-02 | 2.829E-02 |
| 1.513E+00 | 5.563E-03 | 5.337E-02 | 4.871E-02 | 4.958E-02 | 2.823E-02 |
| 1.557E+00 | 1.939E-03 | 5.259E-02 | 4.805E-02 | 4.883E-02 | 2.801E-02 |
| 1.580E+00 | 6.925E-03 | 5.220E-02 | 4.771E-02 | 4.845E-02 | 2.789E-02 |
| 1.588E+00 | 3.546E-02 | 5.207E-02 | 4.760E-02 | 4.833E-02 | 2.785E-02 |

| | | | | | |
|---|---|---|---|---|---|
| 1.621E+00 | 2.750E-02 | 5.153E-02 | 4.715E-02 | 4.781E-02 | 2.769E-02 |
| 1.625E+00 | 3.047E-03 | 5.147E-02 | 4.709E-02 | 4.775E-02 | 2.767E-02 |
| 1.630E+00 | 1.861E-02 | 5.137E-02 | 4.702E-02 | 4.766E-02 | 2.764E-02 |
| 1.638E+00 | 5.263E-03 | 5.125E-02 | 4.691E-02 | 4.755E-02 | 2.761E-02 |
| 1.666E+00 | 1.994E-03 | 5.081E-02 | 4.654E-02 | 4.712E-02 | 2.748E-02 |
| 1.680E+00 | 1.215E-03 | 5.059E-02 | 4.636E-02 | 4.692E-02 | 2.741E-02 |
| 1.806E+00 | 1.982E-03 | 4.865E-02 | 4.480E-02 | 4.516E-02 | 2.686E-02 |
| 1.887E+00 | 1.053E-03 | 4.755E-02 | 4.389E-02 | 4.413E-02 | 2.653E-02 |
| 2.615E+00 | 3.593E-01 | 3.997E-02 | 3.829E-02 | 3.719E-02 | 2.387E-02 |

*Epoxy block coefficients used 50/50 mix ratio of epoxy ($[C_{15}H_{16}O_2]_{10}[C_3H_5O]_2$) to silica ($SiO_2$)

**Table B2** Coefficients for Radium-226 and Daughters

| Emission energy (MeV) | Probability of emission | Mass attenuation ($cm^2/g$) | | | | Mass-energy absorption for water ($cm^2/g$) |
|---|---|---|---|---|---|---|
| | | HCl solution | Glass | Steel | Teflon | |
| 1.080E-02 | 2.432E-01 | 3.835E-01 | 1.365E+01 | 1.357E+02 | 5.442E+00 | 3.873E+00 |
| 1.080E-02 | 1.351E-01 | 3.835E-01 | 1.365E+01 | 1.356E+02 | 5.441E+00 | 3.871E+00 |
| 1.110E-02 | 5.213E-03 | 3.830E-01 | 1.260E+01 | 1.260E+02 | 5.025E+00 | 3.551E+00 |
| 1.170E-02 | 8.022E-03 | 3.820E-01 | 1.080E+01 | 1.093E+02 | 4.310E+00 | 3.006E+00 |
| 4.650E-02 | 4.050E-02 | 3.392E-01 | 3.398E-01 | 2.344E+00 | 2.287E-01 | 4.963E-02 |
| 5.323E-02 | 1.105E-02 | 3.321E-01 | 2.799E-01 | 1.625E+00 | 2.041E-01 | 3.834E-02 |
| 7.482E-02 | 6.213E-02 | 3.128E-01 | 2.002E-01 | 6.889E-01 | 1.685E-01 | 2.727E-02 |
| 7.686E-02 | 3.601E-03 | 3.113E-01 | 1.956E-01 | 6.450E-01 | 1.663E-01 | 2.675E-02 |
| 7.711E-02 | 1.046E-01 | 3.111E-01 | 1.951E-01 | 6.400E-01 | 1.660E-01 | 2.669E-02 |
| 7.929E-02 | 6.031E-03 | 3.095E-01 | 1.905E-01 | 5.979E-01 | 1.637E-01 | 2.617E-02 |
| 8.107E-02 | 1.802E-03 | 3.082E-01 | 1.875E-01 | 5.690E-01 | 1.622E-01 | 2.597E-02 |
| 8.378E-02 | 2.994E-03 | 3.061E-01 | 1.840E-01 | 5.312E-01 | 1.602E-01 | 2.590E-02 |
| 8.730E-02 | 4.668E-02 | 3.035E-01 | 1.796E-01 | 4.874E-01 | 1.578E-01 | 2.580E-02 |
| 8.980E-02 | 2.706E-03 | 3.016E-01 | 1.767E-01 | 4.595E-01 | 1.561E-01 | 2.574E-02 |
| 9.490E-02 | 1.357E-03 | 2.978E-01 | 1.711E-01 | 4.094E-01 | 1.530E-01 | 2.562E-02 |
| 1.862E-01 | 3.280E-02 | 2.486E-01 | 1.283E-01 | 1.561E-01 | 1.219E-01 | 2.916E-02 |
| 2.420E-01 | 7.491E-02 | 2.279E-01 | 1.162E-01 | 1.273E-01 | 1.112E-01 | 3.071E-02 |
| 2.588E-01 | 5.527E-03 | 2.225E-01 | 1.132E-01 | 1.217E-01 | 1.086E-01 | 3.108E-02 |
| 2.737E-01 | 1.776E-03 | 2.181E-01 | 1.108E-01 | 1.171E-01 | 1.064E-01 | 3.139E-02 |
| 2.745E-01 | 3.257E-03 | 2.178E-01 | 1.107E-01 | 1.169E-01 | 1.063E-01 | 3.141E-02 |
| 2.807E-01 | 3.267E-03 | 2.161E-01 | 1.098E-01 | 1.151E-01 | 1.055E-01 | 3.153E-02 |
| 2.952E-01 | 1.925E-01 | 2.122E-01 | 1.077E-01 | 1.112E-01 | 1.036E-01 | 3.181E-02 |
| 3.097E-01 | 6.700E-05 | 2.085E-01 | 1.057E-01 | 1.081E-01 | 1.017E-01 | 3.200E-02 |
| 3.519E-01 | 3.721E-01 | 1.990E-01 | 1.004E-01 | 1.008E-01 | 9.669E-02 | 3.240E-02 |
| 3.870E-01 | 3.651E-03 | 1.917E-01 | 9.667E-02 | 9.571E-02 | 9.311E-02 | 3.270E-02 |
| 3.891E-01 | 4.145E-03 | 1.912E-01 | 9.646E-02 | 9.543E-02 | 9.291E-02 | 3.271E-02 |
| 4.057E-01 | 1.677E-03 | 1.879E-01 | 9.484E-02 | 9.333E-02 | 9.136E-02 | 3.281E-02 |
| 4.265E-01 | 1.086E-03 | 1.841E-01 | 9.291E-02 | 9.104E-02 | 8.949E-02 | 3.286E-02 |
| 4.548E-01 | 3.197E-03 | 1.797E-01 | 9.048E-02 | 8.817E-02 | 8.715E-02 | 3.292E-02 |
| 4.621E-01 | 1.678E-03 | 1.787E-01 | 8.988E-02 | 8.747E-02 | 8.658E-02 | 3.293E-02 |
| 4.697E-01 | 1.332E-03 | 1.776E-01 | 8.928E-02 | 8.676E-02 | 8.600E-02 | 3.294E-02 |
| 4.744E-01 | 1.184E-03 | 1.768E-01 | 8.891E-02 | 8.634E-02 | 8.564E-02 | 3.295E-02 |
| 4.804E-01 | 3.395E-03 | 1.759E-01 | 8.845E-02 | 8.579E-02 | 8.520E-02 | 3.296E-02 |
| 4.871E-01 | 4.412E-03 | 1.749E-01 | 8.795E-02 | 8.521E-02 | 8.471E-02 | 3.298E-02 |
| 5.120E-01 | 7.600E-04 | 1.711E-01 | 8.611E-02 | 8.316E-02 | 8.295E-02 | 3.297E-02 |
| 5.337E-01 | 1.905E-03 | 1.679E-01 | 8.458E-02 | 8.153E-02 | 8.149E-02 | 3.293E-02 |
| 5.802E-01 | 3.652E-03 | 1.624E-01 | 8.158E-02 | 7.835E-02 | 7.863E-02 | 3.284E-02 |
| 6.093E-01 | 4.628E-01 | 1.590E-01 | 7.984E-02 | 7.652E-02 | 7.696E-02 | 3.276E-02 |
| 6.655E-01 | 1.569E-02 | 1.532E-01 | 7.669E-02 | 7.330E-02 | 7.394E-02 | 3.255E-02 |
| 7.031E-01 | 4.737E-03 | 1.490E-01 | 7.478E-02 | 7.136E-02 | 7.211E-02 | 3.241E-02 |

| | | | | | | |
|---|---|---|---|---|---|---|
| 7.199E-01 | 4.046E-03 | 1.473E-01 | 7.398E-02 | 7.054E-02 | 7.134E-02 | 3.236E-02 |
| 7.528E-01 | 1.332E-03 | 1.441E-01 | 7.248E-02 | 6.902E-02 | 6.990E-02 | 3.225E-02 |
| 7.684E-01 | 5.043E-02 | 1.427E-01 | 7.181E-02 | 6.833E-02 | 6.926E-02 | 3.220E-02 |
| 7.859E-01 | 1.096E-02 | 1.412E-01 | 7.108E-02 | 6.758E-02 | 6.855E-02 | 3.214E-02 |
| 7.861E-01 | 3.158E-03 | 1.412E-01 | 7.107E-02 | 6.758E-02 | 6.854E-02 | 3.214E-02 |
| 7.973E-01 | 1.040E-04 | 1.402E-01 | 7.061E-02 | 6.711E-02 | 6.811E-02 | 3.211E-02 |
| 8.031E-01 | 1.100E-05 | 1.398E-01 | 7.037E-02 | 6.687E-02 | 6.788E-02 | 3.208E-02 |
| 8.062E-01 | 1.234E-02 | 1.395E-01 | 7.024E-02 | 6.675E-02 | 6.775E-02 | 3.206E-02 |
| 8.212E-01 | 1.510E-03 | 1.384E-01 | 6.963E-02 | 6.614E-02 | 6.717E-02 | 3.197E-02 |
| 8.390E-01 | 5.892E-03 | 1.370E-01 | 6.892E-02 | 6.544E-02 | 6.649E-02 | 3.186E-02 |
| 9.043E-01 | 1.056E-03 | 1.327E-01 | 6.651E-02 | 6.306E-02 | 6.418E-02 | 3.149E-02 |
| 9.341E-01 | 3.207E-02 | 1.309E-01 | 6.549E-02 | 6.206E-02 | 6.320E-02 | 3.133E-02 |
| 9.641E-01 | 3.849E-03 | 1.286E-01 | 6.451E-02 | 6.110E-02 | 6.227E-02 | 3.118E-02 |
| 1.052E+00 | 3.168E-03 | 1.233E-01 | 6.181E-02 | 5.846E-02 | 5.966E-02 | 3.070E-02 |
| 1.070E+00 | 2.862E-03 | 1.225E-01 | 6.129E-02 | 5.795E-02 | 5.915E-02 | 3.060E-02 |
| 1.120E+00 | 1.515E-01 | 1.198E-01 | 5.990E-02 | 5.660E-02 | 5.780E-02 | 3.033E-02 |
| 1.134E+00 | 2.556E-03 | 1.190E-01 | 5.954E-02 | 5.625E-02 | 5.746E-02 | 3.026E-02 |
| 1.155E+00 | 1.697E-02 | 1.178E-01 | 5.898E-02 | 5.571E-02 | 5.692E-02 | 3.015E-02 |
| 1.158E+00 | 3.507E-02 | 1.177E-01 | 5.891E-02 | 5.564E-02 | 5.685E-02 | 3.014E-02 |
| 1.208E+00 | 4.618E-03 | 1.151E-01 | 5.769E-02 | 5.446E-02 | 5.566E-02 | 2.990E-02 |
| 1.238E+00 | 5.941E-02 | 1.136E-01 | 5.697E-02 | 5.376E-02 | 5.496E-02 | 2.976E-02 |
| 1.281E+00 | 1.480E-02 | 1.114E-01 | 5.599E-02 | 5.286E-02 | 5.402E-02 | 2.951E-02 |
| 1.304E+00 | 1.214E-03 | 1.103E-01 | 5.548E-02 | 5.240E-02 | 5.353E-02 | 2.937E-02 |
| 1.378E+00 | 4.105E-02 | 1.074E-01 | 5.392E-02 | 5.099E-02 | 5.203E-02 | 2.895E-02 |
| 1.385E+00 | 7.796E-03 | 1.071E-01 | 5.377E-02 | 5.086E-02 | 5.188E-02 | 2.890E-02 |
| 1.402E+00 | 1.391E-02 | 1.066E-01 | 5.344E-02 | 5.057E-02 | 5.157E-02 | 2.881E-02 |
| 1.408E+00 | 2.487E-02 | 1.064E-01 | 5.332E-02 | 5.045E-02 | 5.145E-02 | 2.878E-02 |
| 1.509E+00 | 2.220E-02 | 1.026E-01 | 5.144E-02 | 4.876E-02 | 4.964E-02 | 2.825E-02 |
| 1.539E+00 | 4.145E-03 | 1.016E-01 | 5.093E-02 | 4.832E-02 | 4.914E-02 | 2.810E-02 |
| 1.543E+00 | 3.553E-03 | 1.014E-01 | 5.085E-02 | 4.825E-02 | 4.906E-02 | 2.807E-02 |
| 1.583E+00 | 7.204E-03 | 9.994E-02 | 5.019E-02 | 4.767E-02 | 4.840E-02 | 2.787E-02 |
| 1.595E+00 | 2.664E-03 | 9.953E-02 | 5.000E-02 | 4.751E-02 | 4.822E-02 | 2.782E-02 |
| 1.599E+00 | 3.355E-03 | 9.937E-02 | 4.993E-02 | 4.745E-02 | 4.815E-02 | 2.779E-02 |
| 1.661E+00 | 1.155E-02 | 9.728E-02 | 4.896E-02 | 4.660E-02 | 4.719E-02 | 2.750E-02 |
| 1.684E+00 | 2.368E-03 | 9.654E-02 | 4.862E-02 | 4.631E-02 | 4.686E-02 | 2.739E-02 |
| 1.730E+00 | 2.970E-02 | 9.509E-02 | 4.795E-02 | 4.573E-02 | 4.620E-02 | 2.719E-02 |
| 1.765E+00 | 1.584E-01 | 9.402E-02 | 4.746E-02 | 4.530E-02 | 4.572E-02 | 2.704E-02 |
| 1.838E+00 | 3.849E-03 | 9.187E-02 | 4.647E-02 | 4.443E-02 | 4.474E-02 | 2.673E-02 |
| 1.847E+00 | 2.092E-02 | 9.162E-02 | 4.636E-02 | 4.433E-02 | 4.463E-02 | 2.669E-02 |
| 1.873E+00 | 2.270E-03 | 9.092E-02 | 4.603E-02 | 4.404E-02 | 4.430E-02 | 2.659E-02 |
| 1.896E+00 | 1.776E-03 | 9.031E-02 | 4.574E-02 | 4.379E-02 | 4.402E-02 | 2.649E-02 |
| 2.119E+00 | 1.174E-02 | 8.475E-02 | 4.320E-02 | 4.171E-02 | 4.153E-02 | 2.560E-02 |
| 2.204E+00 | 4.983E-02 | 8.286E-02 | 4.232E-02 | 4.104E-02 | 4.067E-02 | 2.527E-02 |
| 2.293E+00 | 3.256E-03 | 8.101E-02 | 4.147E-02 | 4.039E-02 | 3.984E-02 | 2.494E-02 |
| 2.448E+00 | 1.559E-02 | 7.802E-02 | 4.009E-02 | 3.933E-02 | 3.850E-02 | 2.440E-02 |

**232Th Model 11.vi**

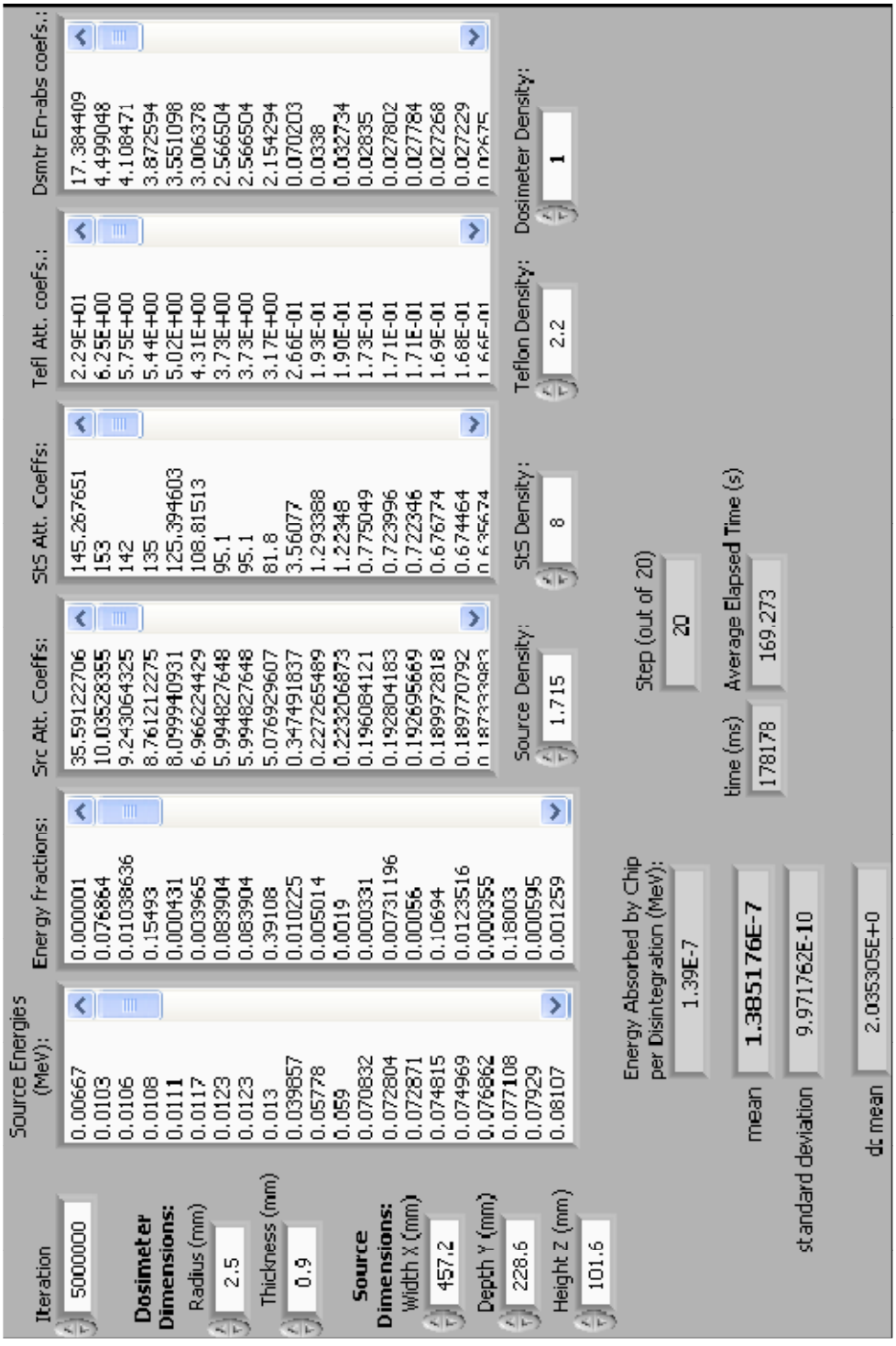

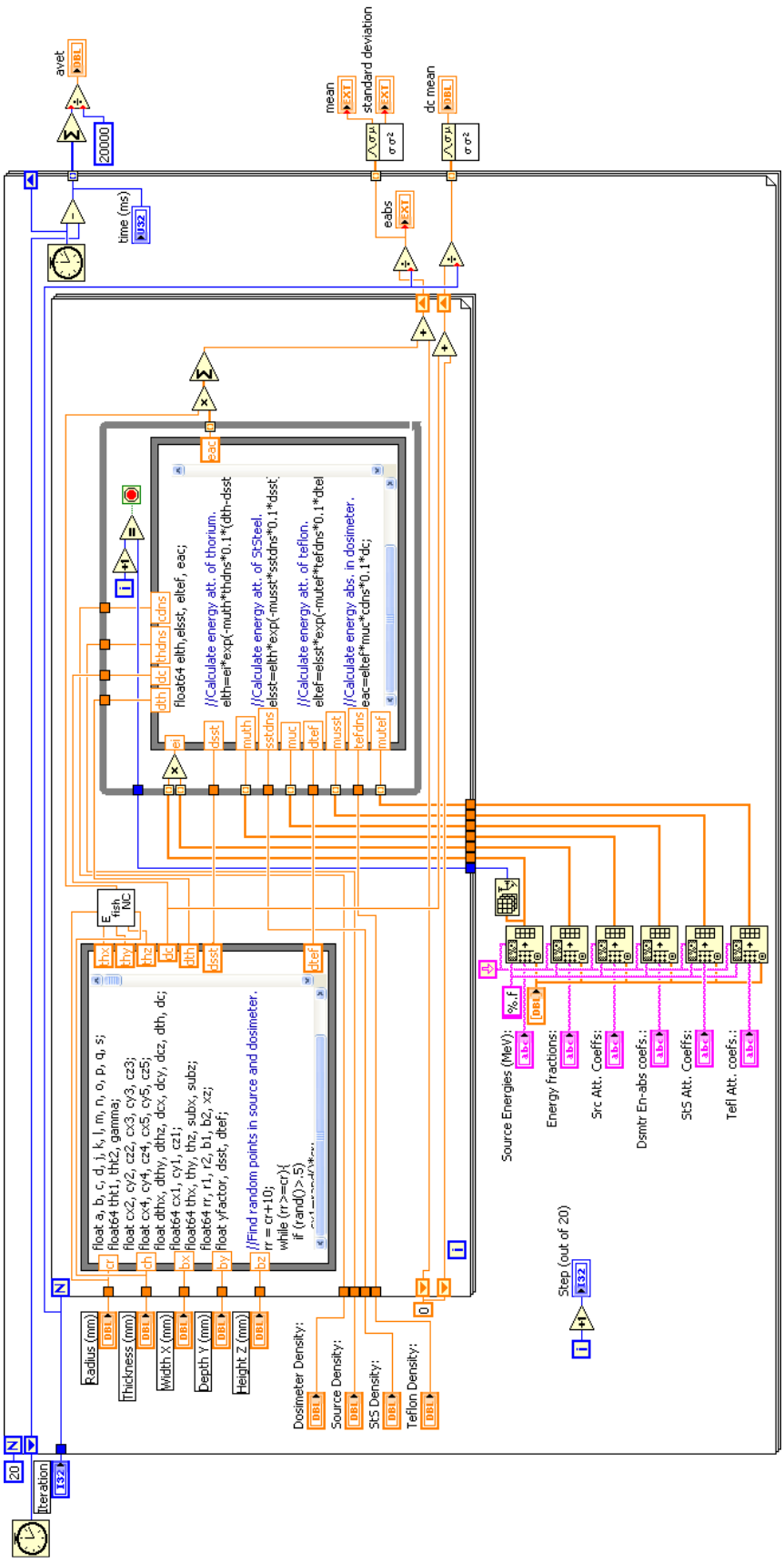
avet
20000
time (ms)
mean
standard deviation
dc mean
eabs
float64 elth,elsst, eltef, eac;
//Calculate energy att. of thorium.
elth=ei*exp(-muth*thdns*0.1*(dth-dsst
//Calculate energy att. of StSteel.
elsst=elth*exp(-musst*sstdns*0.1*dsst;
//Calculate energy att. of teflon.
eltef=elsst*exp(-mutef*tefdns*0.1*dtef
//Calculate energy abs. in dosimeter.
eac=eltef*muc*cdns*0.1*dc;
float a, b, c, d, j, k, l, m, n, o, p, q, s;
float64 tht1, tht2, gamma;
float cx2, cy2, cz2, cx3, cy3, cz3;
float cx4, cy4, cz4, cx5, cy5, cz5;
float dthx, dthy, dthz, dcx, dcy, dcz, dth, dc;
float64 cx1, cy1, cz1;
float64 thx, thy, thz, subx, suby, subz;
float64 rr, r1, r2, b1, b2, xz;
float yfactor, dsst, dtef;
//Find random points in source and dosimeter.
rr = cr+10;
while (rr >=cr){
if (rand()>.5)
Source Energies (MeV):
Energy fractions:
Src Att. Coeffs:
Dsmtr En-abs coefs.:
St5 Att. Coeffs:
Tefl Att. coefs.:
Step (out of 20)
Radius (mm)
Thickness (mm)
Width X (mm)
Depth Y (mm)
Height Z (mm)
Dosimeter Density:
Source Density:
St5 Density:
Teflon Density:
20
Iteration

**Contents of first formula node:**

```
float a, b, c, d, j, k, l, m, n, o, p, q, s;
float64 tht1, tht2, gamma;
float cx2, cy2, cz2, cx3, cy3, cz3;
float cx4, cy4, cz4, cx5, cy5, cz5;
float dthx, dthy, dthz, dcx, dcy, dcz, dth, dc;
float64 cx1, cy1, cz1;
float64 thx, thy, thz, subx, subz;
float64 rr, r1, r2, b1, b2, xz;
float yfactor, dsst, dtef;

//Find random points in source and dosimeter.
rr = cr+10;
while (rr>=cr){
  if (rand()>.5)
    cx1=rand()*cr;
    else cx1=-rand()*cr;
  if (rand()>.5)
    cz1=rand()*cr;
    else cz1=-rand()*cr;
  rr=sqrt(cx1*cx1 + cz1*cz1);}

if (rand()<0.5)
  cy1=-rand()*ch/2;
  else cy1=rand()*ch/2;

rr = 0;
thy = 0;
while  (rr<=4.75 && thy<=26.7){ //outer probe dim.s
if (rand()<0.5)
   thx=-rand()*bx;
   else thx=rand()*bx;
if (rand()<0.5)
   thy=-rand()*by;
   else thy=rand()*by;
if (rand()<0.5)
   thz=-rand()*bz;
   else thz=rand()*bz;
rr=sqrt(thx*thx +thz*thz);}

//Find ray enter/exit points on dosimeter.
a=sqrt((cx1*cx1) + (cz1*cz1));
j=thx/abs(thx);
k=thy/abs(thy);
l=thz/abs(thz);
m=cx1/abs(cx1);
n=cy1/abs(cy1);
o=cz1/abs(cz1);
if (abs(thx)>20) {   // use subx and subz for
  subx=j*20;         // more accurate tht calc
  p=(subx-cx1)/(thx-cx1);
  subz=cz1+p*(thz-cz1);}
  else {
    subx=thx;
    subz=thz;}
```

```
tht1=atan((cz1-subz)/(cx1-subx));
tht2=atan(cz1/cx1);
gamma=abs(tht2-tht1);

if (gamma<0.5*pi)
  d=a*sin(gamma);
  else d=a*sin(pi-gamma);

s=sqrt(a*a - d*d);
q=sqrt(cr*cr - d*d);
b=sin(tht1);
c=cos(tht1);

if (gamma>0.5*pi){
  if(tht1<0){
    cx2=cx1-o*(q-s)*c;
    cz2=cz1-o*(q-s)*b;
    cx3=cx1+o*(q+s)*c;
    cz3=cz1+o*(q+s)*b;}
    else {
      cx2=cx1+o*(q-s)*c;
      cz2=cz1+o*(q-s)*b;
      cx3=cx1-o*(q+s)*c;
      cz3=cz1-o*(q+s)*b;}}
  else {
    cx2=cx1-m*(q+s)*c;
    cz2=cz1-m*(q+s)*b;
    cx3=cx1+m*(q-s)*c;
    cz3=cz1+m*(q-s)*b;}

p=(cx2-thx)/(cx1-thx);
cy2=thy+p*(cy1-thy);
p=(cx3-thx)/(cx1-thx);
cy3=thy+p*(cy1-thy);

n=cy2/abs(cy2);
if (abs(cy2)>0.5*ch)
  cy4=n*0.5*ch;
  else cy4=cy2;
p=(cy4-cy2)/(cy3-cy2);
cx4=cx2+p*(cx3-cx2);
cz4=cz2+p*(cz3-cz2);

n=cy3/abs(cy3);
if (abs(cy3)>0.5*ch)
  cy5=n*0.5*ch;
  else cy5=cy3;
p=(cy5-cy2)/(cy3-cy2);
cx5=cx2+p*(cx3-cx2);
cz5=cz2+p*(cz3-cz2);

//Calculate path distance in source
if (abs(thx-cx4)<abs(thx-cx5))
  dthx=thx-cx4;
  else dthx=thx-cx5;
```

```
if (abs(thy-cy4)<abs(thy-cy5))
   dthy=thy-cy4;
   else dthy=thy-cy5;

if (abs(thz-cz4)<abs(thz-cz5))
   dthz=thz-cz4;
   else dthz=thz-cz5;

dth=sqrt(dthx*dthx+dthy*dthy+dthz*dthz);

//Calculate path distance through steel.
r1=3.861;    // 0.035" wall
r2=4.75;     // < 3/8" steel tubing outer diam.
b1=sqrt(r1*r1 - d*d);
b2=sqrt(r2*r2 - d*d);
xz=sqrt((thx-cx1)**2 + (thz-cz1)**2);
yfactor=sqrt(xz*xz + (thy-cy1)**2)/xz;
if (sqrt(thx*thx + thz*thz) > r2)
   dsst=yfactor*(b2-b1);
   else dsst=8; // apprx. ave. tip thickness.

//Calculate path distance through teflon.
r1=cr;              // inner radius same as cr
r2=cr+0.866;    // 1.3 mm ,threaded wall
b1=sqrt(r1*r1 - d*d);
b2=sqrt(r2*r2 - d*d);
xz=sqrt((thx-cx1)**2 + (thz-cz1)**2);
yfactor=sqrt(xz*xz + (thy-cy1)**2)/xz;
if (sqrt(thx*thx + thz*thz) > r2)
   dtef=yfactor*(b2-b1);
   else dtef=1.3; //apprx. teflon cap thickness

//Calculate path distance through dosimeter.
dcx=cx5-cx4;
dcy=cy5-cy4;
dcz=cz5-cz4;
dc=sqrt(dcx*dcx+dcy*dcy+dcz*dcz);
```

**Contents of second formula node:**

```
float64 elth,elsst, eltef, eac;

//Calculate energy att. of thorium.
elth=ei*exp(-muth*thdns*0.1*(dth-dsst-0.495-dtef));

//Calculate energy att. of StSteel.
elsst=elth*exp(-musst*sstdns*0.1*dsst);

//Calculate energy att. of teflon.
eltef=elsst*exp(-mutef*tefdns*0.1*dtef);

//Calculate energy abs. in dosimeter.
eac=eltef*muc*cdns*0.1*dc;
```

**Radium Calc4.vi**

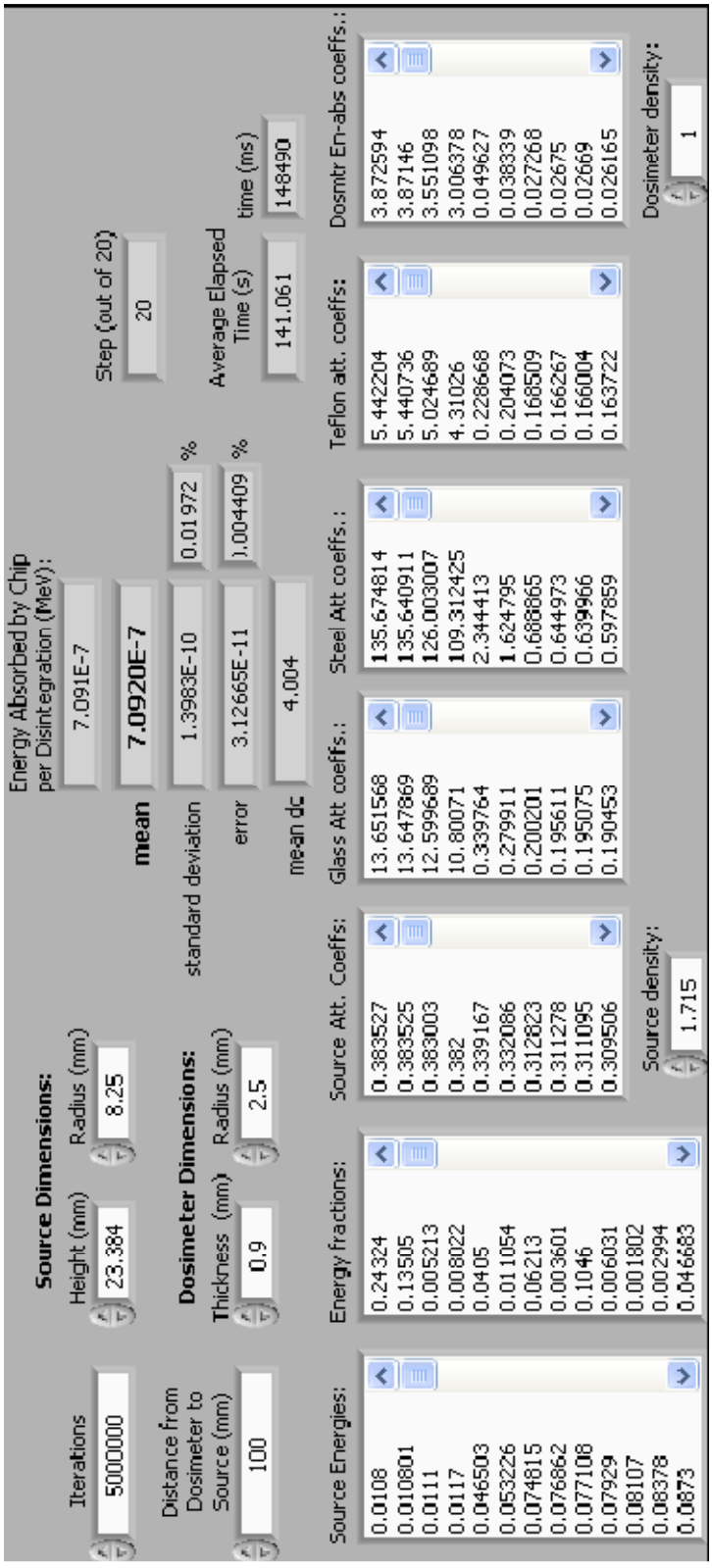

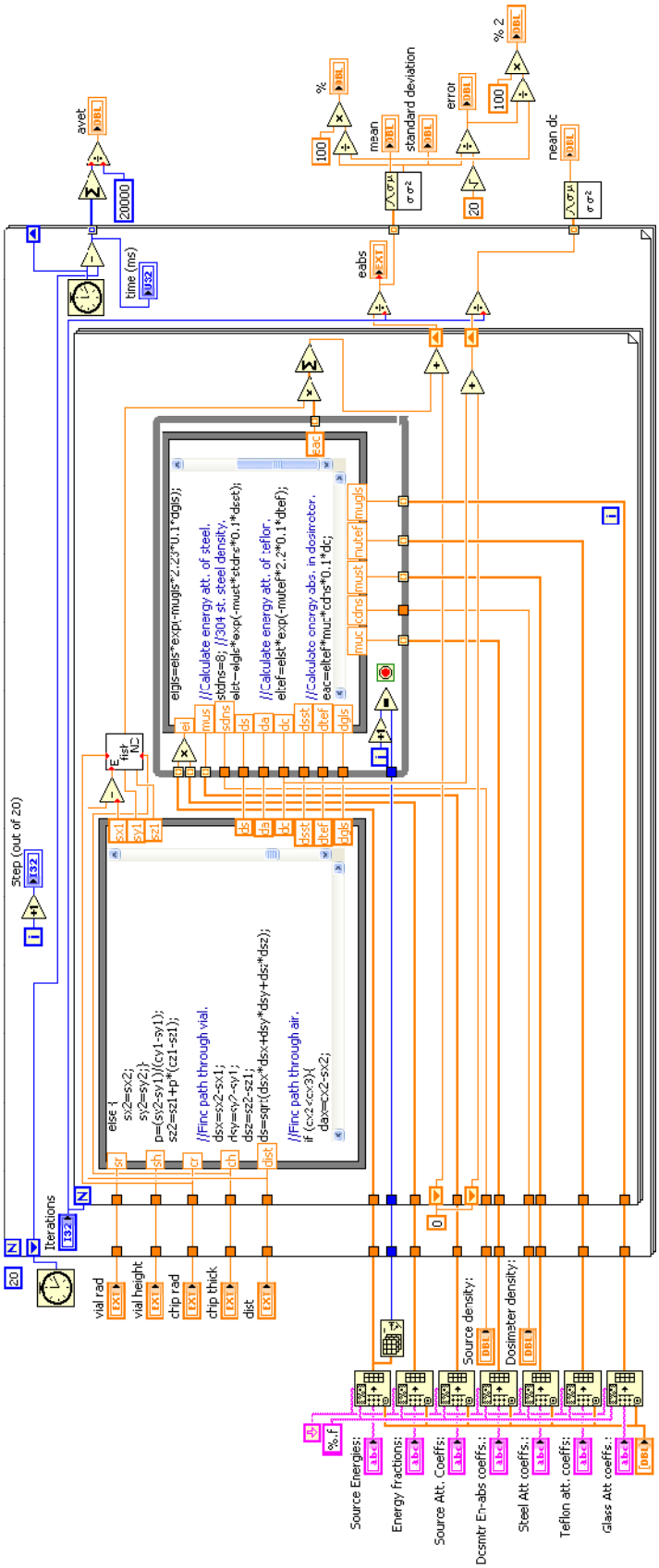
avet
20000
time (ms)
%
100
mean
standard deviation
error
% 2
100
mean dc
eabs
20
Step (out of 20)
Iterations
20
vial rad
vial height
chip rad
chip thick
dist
Source density:
Dosimeter density:
Source Energies:
Energy fractions:
Source Att. Coeffs:
Dosmtr En-abs coeffs:
Steel Att coeffs:
Teflon att. coeffs:
Glass Att coeffs:
%.f
elgls=els*exp(-mugls*2.23*0.1*dgls);
//Calculate energy att. of steel.
stdns=8; //304 st. steel density.
elst=elgls*exp(-must*stdns*0.1*dst);
//Calculate energy att. of teflon.
eltef=elst*exp(-mutef*2.2*0.1*dtef);
//Calculate energy abs. in dosimeter.
eac=eltef*muc*cds*0.1*dc;
else {
sx2=sx2;
sy2=sy2;}
p=(sy2-sy1)/(cy1-sy1);
sz2=sz1+p*(cz1-sz1);
//Find path through vial.
dsx=sx2-sx1;
dsy=sy2-sy1;
dsz=sz2-sz1;
ds=sqrt(dsx*dsx+dsy*dsy+dsz*dsz);
//Find path through air.
if (cx<2<cx<3){
dax=cx2-sx2;

**Contents of first formula node:**

```
float a, b, c, d,  l, m, n, p, s, q, x;
float e, f, g, h, i, j, k, t, u;
float64 tht1, tht2, tht3, tht4;
float64 gamma1, gamma2;
float cx1, cy1,cz1, cx2, cy2, cz2, cx3, cy3, cz3;
float cx4, cy4, cz4, cx5, cy5, cz5;
float sx1, sy1, sz1, sx2, sy2, sz2, sx3, sy3, sz3;
float dsx, dsy, dsz, ds;
float dcx, dcy, dcz, dc;
float dax, day, daz, da, e1, e2;
float64 rr, r1, r2, b1, b2, xy, xz, yfactor, zfactor;
float elv, ela, eac, dsst, dtef, dgls;

//Find random points in vial and dosimeter
rr = sr+10;
while (rr>sr){
  if (rand() > 0.5)
    sx1=rand()*sr;
    else sx1=-rand()*sr;
  if (rand() > 0.5)
    sy1=rand()*sr;
    else sy1=-rand()*sr;
  rr=sqrt(sx1*sx1 + sy1*sy1);}

if (rand() > 0.5)
  sz1=0.5*rand()*sh;
  else sz1=-0.5*rand()*sh;

rr=cr+10;
while (rr>cr){
  if (rand() > 0.5)
    cx1=rand()*cr;
    else cx1=-rand()*cr;
  if (rand() > 0.5)
    cz1=rand()*cr;
    else cz1=-rand()*cr;
  rr=sqrt(cx1*cx1 + cz1*cz1);}
cx1=cx1+dist;

if (rand() > 0.5)
  cy1=0.5*rand()*ch;
  else cy1=-0.5*rand()*ch;

//Find ray enter/exit points on dosimeter
x=cx1-dist;
a=sqrt(x*x + cz1*cz1);
l=x/abs(x);
m=cy1/abs(cy1);
n=cz1/abs(cz1);
tht1=atan((cz1-sz1)/(cx1-sx1));
tht2=atan(cz1/x);
gamma1=abs(tht2-tht1);
```

```
if (gamma1>0.5*pi)
  d=a*sin(pi-gamma1);
  else d=a*sin(gamma1);

s=sqrt(abs(a*a - d*d));   //NaN for sqrt(-)!!
q=sqrt(abs(cr*cr - d*d));
b=sin(tht1);
c=cos(tht1);

if (gamma1>0.5*pi){
  if(tht1<0){
    cx2=cx1-n*(q-s)*c;
    cz2=cz1-n*(q-s)*b;
    cx3=cx1+n*(q+s)*c;
    cz3=cz1+n*(q+s)*b;}
    else {
      cx2=cx1+n*(q-s)*c;
      cz2=cz1+n*(q-s)*b;
      cx3=cx1-n*(q+s)*c;
      cz3=cz1-n*(q+s)*b;}}
  else {
    cx2=cx1-l*(q+s)*c;
    cz2=cz1-l*(q+s)*b;
    cx3=cx1+l*(q-s)*c;
    cz3=cz1+l*(q-s)*b;}

p=(cz2-sz1)/(cz1-sz1);
cy2=sy1+p*(cy1-sy1);
p=(cz3-sz1)/(cz1-sz1);
cy3=sy1+p*(cy1-sy1);

m=cy2/abs(cy2);
if (abs(cy2)>0.5*ch)
  cy4=m*0.5*ch;
  else cy4=cy2;
p=(cy4-cy2)/(cy3-cy2);
cx4=cx2+p*(cx3-cx2);
cz4=cz2+p*(cz3-cz2);

m=cy3/abs(cy3);
if (abs(cy3)>0.5*ch)
  cy5=m*0.5*ch;
  else cy5=cy3;
p=(cy5-cy2)/(cy3-cy2);
cx5=cx2+p*(cx3-cx2);
cz5=cz2+p*(cz3-cz2);

//Find ray origin/exit points in source.
e=sqrt(sx1*sx1 + sy1*sy1);
i=sx1/abs(sx1);
j=sy1/abs(sy1);
k=sz1/abs(sz1);
tht3=atan((cy1-sy1)/(cx1-sx1));
tht4=atan(sy1/sx1);
gamma2=abs(tht4-tht3);
```

```
if (gamma2>0.5*pi)
   h=e*sin(pi-gamma2);
   else h=e*sin(gamma2);
u=sqrt(abs(e*e - h*h));
t=sqrt(abs(sr*sr - h*h));
f=sin(tht3);
g=cos(tht3);

if (gamma2>0.5*pi){
   if(tht3<0){
      sx2=sx1-j*(t-u)*g;
      sy2=sy1-j*(t-u)*f;
      sx3=sx1+j*(t+u)*g;
      sy3=sy1+j*(t+u)*f;}
      else {
         sx2=sx1+j*(t-u)*g;
         sy2=sy1+j*(t-u)*f;
         sx3=sx1-j*(t+u)*g;
         sy3=sy1-j*(t+u)*f;}}
  else {
      sx2=sx1-i*(t+u)*g;
      sy2=sy1-i*(t+u)*f;
      sx3=sx1+i*(t-u)*g;
      sy3=sy1+i*(t-u)*f;}

if (sx3>sx1){
   sx2=sx3;
   sy2=sy3;}
   else {
      sx2=sx2;
      sy2=sy2;}
p=(sy2-sy1)/(cy1-sy1);
sz2=sz1+p*(cz1-sz1);

//Find path through vial.
dsx=sx2-sx1;
dsy=sy2-sy1;
dsz=sz2-sz1;
ds=sqrt(dsx*dsx+dsy*dsy+dsz*dsz);

//Find path through air.
if (cx2<cx3){
   dax=cx2-sx2;
   day=cy2-sy2;
   daz=cz2-sz2;}
   else {
      dax=cx3-sx2;
      day=cy3-sy2;
      daz=cz3-sz2;}
da=sqrt(dax*dax+day*day+daz*daz);

//Calculate path distance through steel.
r1=3.8735;       // 0.035" wall ~ 0.889 mm.
r2=4.7625;       // 3/8" steel tubing outer diam.
b1=sqrt(abs(r1*r1 - d*d));
b2=sqrt(abs(r2*r2 - d*d));
```

```
xz=sqrt((sx1-cx1)**2 + (sz1-cz1)**2);
yfactor=sqrt(xz*xz + (sy1-cy1)**2)/xz;
dsst=yfactor*(b2-b1);

//Calculate path distance through teflon.
r1=cr;              // inner radius same as cr
r2=cr+0.866;    // 1.3 mm ,threaded wall
b1=sqrt(r1*r1 - d*d);
b2=sqrt(r2*r2 - d*d);
dtef=yfactor*(b2-b1);

//Calculate path distance through vial wall.
r1=7.65;          //vial diam = 16.5 mm
r2=8.25;          //wall thickness = 0.6 mm
b1=sqrt(abs(r1*r1 - h*h));
b2=sqrt(abs(r2*r2 - h*h));
xy=sqrt((sx1-cx1)**2 + (sy1-cy1)**2);
zfactor=sqrt(xy*xy + (sz1-cz1)**2)/xy;
dgls=zfactor*(b2-b1);

//Find path through dosimeter (chip).
dcx=cx5-cx4;
dcy=cy5-cy4;
dcz=cz5-cz4;
dc=sqrt(dcx*dcx+dcy*dcy+dcz*dcz);
```

**Contents of second formula node:**

```
float64 els, elgls, elst, eltef, eac, stdns;

//Calculate energy att. of 226Ra sol.
els=ei*exp(-mus*sdns*0.1*ds);

//Calculate energy att. of vial.
elgls=els*exp(-mugls*2.23*0.1*dgls);

//Calculate energy att. of steel.
stdns=8;          //304 st. steel density.
elst=elgls*exp(-must*stdns*0.1*dsst);

//Calculate energy att. of teflon.
eltef=elst*exp(-mutef*2.2*0.1*dtef);

//Calculate energy abs. in dosimeter.
eac=eltef*muc*cdns*0.1*dc;
```

**efficiency3.vi**

**Connector Pane**

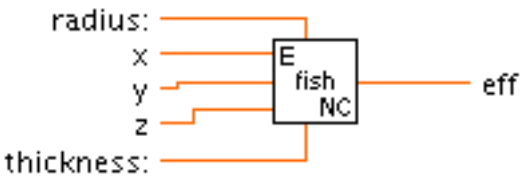


**Front Panel**

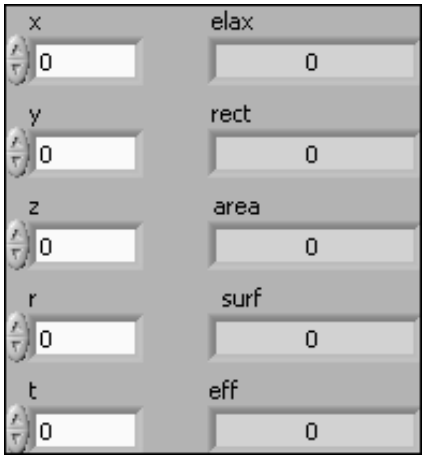


**Block Diagram**

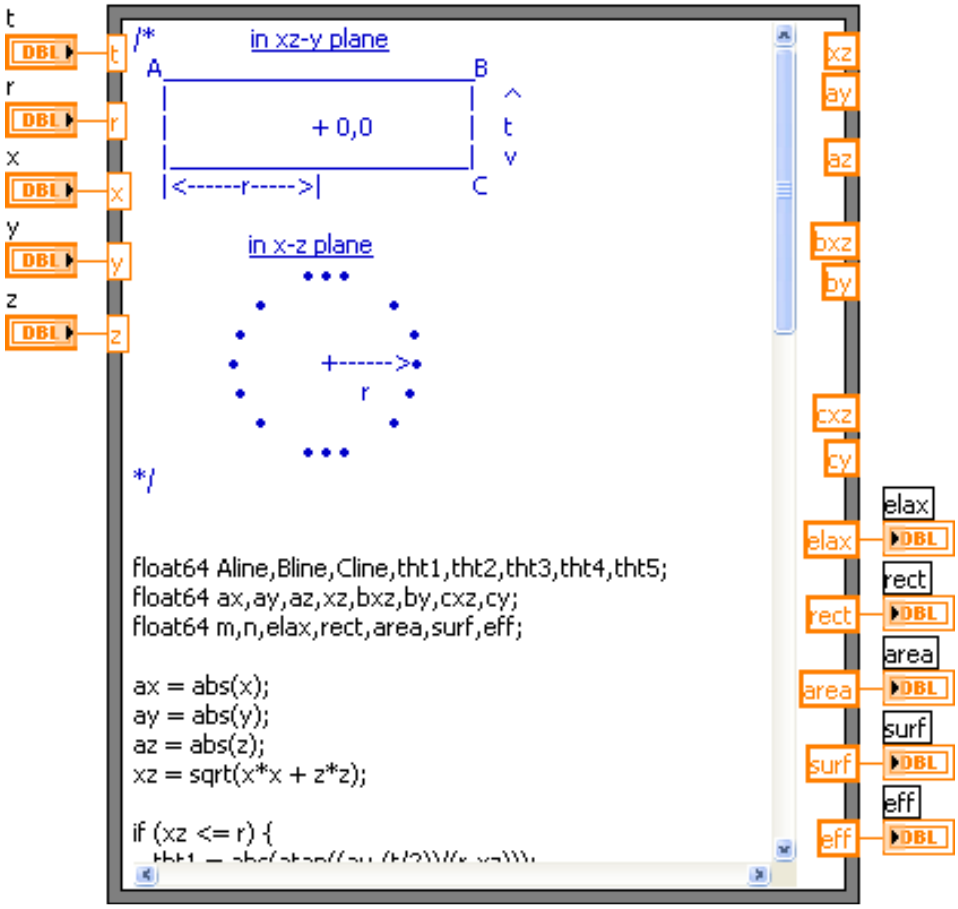

```
/*            in xz-y plane

A_____________________________B
  |                           |  ^
  |                + [0,0]    |  t
  |___________________________|  v
  |<------r------->|          C
```

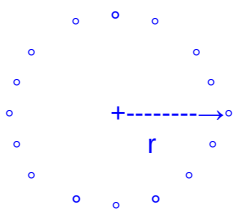


```
*/


float64 Aline,Bline,Cline,tht1,tht2,tht3,tht4,tht5;
float64 ax,ay,az,xz,bxz,by,cxz,cy;
float64 m,n,elax,rect,area,surf,eff;

ax = abs(x);
ay = abs(y);
az = abs(z);
xz = sqrt(x*x + z*z);

if (xz <= r) {
   tht1 = abs(atan((ay-(t/2))/(r-xz)));
   tht2 = abs(atan((ay-(t/2))/(r+xz)));
   tht3 = pi-tht1-tht2;
   Aline = sqrt((r+xz)**2 + (ay-t/2)**2);
   Bline = sqrt((r-xz)**2 + (ay-t/2)**2);
   m = Bline/Aline;
   bxz = (xz+r)-m*(xz+r)-r;
   by = (ay-t/2)-m*(ay-t/2)+t/2;
   elax= sqrt(2*(Bline**2)*(1-cos(tht3)));
   area = pi*r*elax/2;
   surf = 4*pi*Bline**2;
   eff = area/surf;}
   else
      if (ay <= t/2) {
         tht1 = abs(atan((t/2-ay)/(xz-r)));
         tht2 = abs(atan((t/2+ay)/(xz-r)));
         tht3 = tht1+tht2;
         Bline = sqrt((t/2-ay)**2 + (xz-r)**2);
         Cline = sqrt((t/2+ay)**2 + (xz-r)**2);
         m = Bline/Cline;
         cxz = (xz-r)-m*(xz-r)+r;
         cy = (ay+t/2)-m*(ay+t/2)-t/2;
```

```
rect= sqrt(2*(Bline**2)*(1-cos(tht3)));
area = rect*2*r;
surf = 4*pi*Bline**2;
eff = area/surf;}
else {
  tht1 = abs(atan((ay-t/2)/(xz-r)));
  tht2 = abs(atan((ay-t/2)/(xz+r)));
  tht3 = tht1-tht2;
  tht4 = abs(atan((ay+t/2)/(xz-r)));
  tht5 = tht4-tht1;
  Aline = sqrt((r+xz)**2 + (ay-t/2)**2);
  Bline = sqrt((xz-r)**2 + (ay-t/2)**2);
  Cline = sqrt((xz-r)**2 + (ay+t/2)**2);
  m = Bline/Aline;
  n = Bline/Cline;
  bxz = (xz+r)-m*(xz+r)-r;
  by = (ay-t/2)-m*(ay-t/2)+t/2;
  cxz = (xz-r)-n*(xz-r)+r;
  cy = (ay+t/2)-n*(ay+t/2)-t/2;
  elax= sqrt(2*(Bline**2)*(1-cos(tht3)));
  rect= sqrt(2*(Bline**2)*(1-cos(tht5)));
  area = rect*2*r + pi*r*elax/2;
  surf = 4*pi*Bline**2;
  eff = area/surf;}
```

VITA

David Matthew Klein

Candidate for the Degree of

Doctor of Philosophy

Thesis: DEVELOPMENT AND CHARACTERIZATION OF REMOTE RADIATION DOSIMETRY SYSTEMS USING OPTICALLY STIMULATED LUMINESCENCE OF $Al_2O_3$:C and KBr:Eu

Major Field: Physics

Biographical:

Personal Data: Born in Tulsa, Oklahoma, on August 8th, 1979, the son of Fred and Theresa Klein. U.S. citizen. Married since December, 2004 to Helen T. Klein.

Education: Graduated from Bishop Kelley High School in May, 1997; studied at the University of Tulsa in Tulsa, Oklahoma, as a Physics and Music double-major from the fall of 1997 to the spring of 1998; began studies in Physics at Oklahoma State University in the fall of 1998; received Bachelor of Science degree in Physics from Oklahoma State University, Stillwater, Oklahoma in the summer of 2002. Completed the requirements for the Doctor of Science in Physics at Oklahoma State University in December, 2008.

Experience: Undergraduate research assistant under Dr. S.W.S. McKeever in the Optically and Thermally Stimulated Phenomena Laboratory from spring 2001 – summer 2002; Research Experience for Undergraduates (REU) scholarship recipient (summer, 2001; summer 2002); graduate teaching assistant to Dr. David Lien for PHYS 1114 – General Physics in spring, 2003; Oklahoma Space Grant Consortium (OSGC) grant recipient (spring, 2004; spring, 2005); graduate research assistant to Dr. S.W.S. McKeever (fall 2002 – present).

Professional Memberships: American Physical Society (APS)

Name: David Matthew Klein Date of Degree: December, 2008

Institution: Oklahoma State University Location: Stillwater, Oklahoma

Title of Study: DEVELOPMENT AND CHARACTERIZATION OF REMOTE RADIATION DOSIMETRY SYSTEMS USING OPTICALLY STIMULATED LUMINESCENCE OF $Al_2O_3$:C AND KBr:Eu

Pages in Study: 220 Candidate for the Degree of Doctor of Philosophy

Major Field: Physics

Scope and Method of Study: To develop and test the performance of two different dosimetry systems; one for in situ, high-sensitivity, inexpensive environmental monitoring, and another for near-real-time medical dosimetry. The systems are based on remote interrogation of the optically stimulated luminescence (OSL) from $Al_2O_3$:C and KBr:Eu single crystal dosimeters (exposed to environmental and medical radiation fields, respectively) via fiber optic cables. The environmental system was tested in lab conditions using various radioactive sources including $^{60}$Co, $^{90}$Sr, $^{137}$Cs, and $^{226}$Ra, as well as with $^{232}$Th-enriched soil stimulant. The medical system was tested under various diagnostic x-ray systems, including fluoroscopy and computed tomography (CT) machines, as well as with high dose rate $^{192}$Ir brachytherapy sources and 232 MeV proton therapy beams under simulated treatment conditions.

Findings and Conclusions: The environmental system was shown to achieve sensitivity high enough for measuring an OSL signal resulting from a dose of ~1 μGy, which is equivalent to ~12 hours of natural background radiation. This sensitivity allows for monitoring of the radiation characteristics of a natural environment more rapidly and/or less expensively than existing methods, such as soil sampling and in situ gamma spectroscopy. The KBr:Eu-based medical system results show that the near-real-time data acquisition during irradiation allows for rapid quality assurance (QA) measurements that benefits from high spatial resolution. These features are not present in most current standard dosimeters such as thermoluminescent detectors and pencil ionization chambers. The dosimeter does exhibit energy dependence, and a sensitization during high dose rate procedures. As a result, a model has been proposed that provides a description of the possible mechanisms that govern the transfer of electrons and holes within KBr:Eu during OSL measurement at room temperature. Correction factors for these effects must be investigated for the system to become relevant for accurate dosimetry, rather than rapid QA.

ADVISER'S APPROVAL: Dr. Stephen W. S. McKeever